

Non-Radiative Recombination Losses in Perovskite Solar Cells: From Fundamental Understanding to High Efficiency Devices



Cumulative Dissertation

doctor rerum naturalium (Dr. rer. nat) in Experimental Physics

University of Potsdam
Institute of Physics and Astronomy
Soft Matter Physics

Helmholtz-Zentrum Berlin
für Materialien und Energie

Pietro Caprioglio

Potsdam May 2020

Cumulative Dissertation

Supervisors:

Prof. Dr. Dieter Neher
Prof. Dr. Bernd Rech

Scientific Advisor:

Prof. Dr. Steve Albrecht

Author:

Pietro Caprioglio

Published online on the
Publication Server of the University of Potsdam:
<https://doi.org/10.25932/publishup-47763>
<https://nbn-resolving.org/urn:nbn:de:kobv:517-opus4-477630>

Acknowledgments

Firstly, I want to thank all the people in my life who made me become passionate for science and art, making me understand the importance of culture in our lives, the real driving force in this world.

My gratitude goes to my family, my siblings and my friends for their unconditional and never-ending support. Without their constant physiological and economical help, all this would not have been possible.

Especially, I want to express my gratitude to my partner Katherine, who supported me in every single step of this long journey with love, patience and help, giving me constant inspiration.

I will be forever thankful to my scientific mentor Prof. Dieter Neher, who mindfully guided me through this beautiful scientific journey teaching me not only his vast scientific knowledge, but most importantly, how to be a true scientist. His genuine passion and curiosity for the scientific research will always resonate in me.

I want to deeply thank Prof. Steve Albrecht for his constant support in every aspect and decision-making situation of my doctoral path. Without his precious advices and help in every critical moment, I would not have been able to achieve what is reported in this thesis work.

My deepest respect and gratitude go to Martin Stolterfoht, my every day companion and advisor. His guidance and never-ending help have been crucial in defining me as a scientist. Without him, my scientific journey would have been impaired.

I want to thank Prof. Bernd Rech for his wise guidance and constant support, providing me always with important advices for my scientific career. His presence in my doctoral path has been crucial.

Last, but not least, I want to thank the HyperCells graduate school for providing me with full economic support during the complete duration of my doctoral studies.

The author,
Pietro Caprioglio

Declaration by the Author

This thesis is composed of my original work, and contains no material previously published or written by another person except where due reference has been made in the text. I have clearly stated the contribution by others to jointly-authored works that I have included in my thesis.

The author,

8/5/2020 Pietro Caprioglio

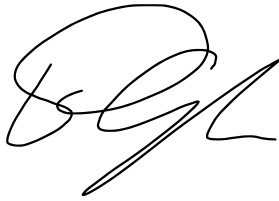
A handwritten signature in black ink, appearing to be 'P. Caprioglio', written in a cursive style.

Table of Content

Abstract	1
Symbols	3
Contribution Statement.....	5
1. Introduction	9
1.1 Solar Energy	10
1.2 Perovskite Semiconductors	11
1.3 Metal Halide Perovskite Properties.....	12
1.3.1 Crystal Structures and Compositions.....	13
1.3.2 Defects and their Passivation.....	15
1.3.3 Optoelectronic Properties.....	16
1.4 Perovskite in Solar Cells.....	18
1.4.1 Deposition Methods	18
1.4.2 Device Architectures	19
1.4.3 Photovoltaics Behaviour	21
1.5 Current Challenges	22
1.6 Aim of this work	24
2. Theoretical Background	25
2.1 Solar cells working principles	26
2.2 Free Carriers in a Semiconductor and quasi-Fermi Level Splitting	29
2.3 Drift and Diffusion Currents	32
2.4 Theoretical Efficiency	34
2.5 Practical Limitations	37
2.5.1 Recombination Losses.....	37
2.5.2 Transport Losses	41
2.6 From Photoluminescence Efficiencies to quasi-Fermi Level Splitting	43
2.7 The Ideality Factor.....	46
2.8 Recombination in Perovskite Solar Cells.....	48
3. Experimental Framework	51
3.1 Photoluminescence Quantum Yield	52
3.2 Drift-Diffusion Simulations.....	54

3.3 Solar Cell Devices.....	57
4. Impact of Energy Alignment and Interface Recombination	59
5. On the Relation between Open Circuit Voltage and quasi-Fermi Level Splitting	73
6. On the Origin of the Ideality Factor	84
7. High Open Circuit Voltages through Strontium Addition	96
8. Bifunctional Interfaces Through Poly-Ionic Liquid Surface Modification	113
9. Microscopic emission properties and optical reciprocity failure in MA-free large bandgap halide-segregated perovskites.....	124
10. Discussion and Conclusions	137
List of Publications.....	142
11. Supporting Material.....	145
11.1 Appendix 1	146
11.2 Appendix 2	161
11.3 Appendix 3	169
11.4 Appendix 4	179
11.5 Appendix 5	192
11.6 Appendix 6	203
12. Materials and Methods.....	212
12.1 Experimental Details Chapter 4	213
12.2 Experimental Details Chapter 5	217
12.3 Experimental Details Chapter 6	218
12.4 Experimental Details Chapter 7	220
12.5 Experimental Details Chapter 8	222
12.6 Experimental Details Chapter 9	226
Bibliography.....	229

Abstract

In the last decade the photovoltaic research has been preponderantly overturned by the arrival of metal halide perovskites. The introduction of this class of materials in the academic research for renewable energy literally shifted the focus of a large number of research groups and institutions. The attractiveness of halide perovskites lays particularly on their skyrocketing efficiencies and relatively simple and cheap fabrication methods. Specifically, the latter allowed for a quick development of this research in many universities and institutes around the world at the same time. The outcome has been a fast and beneficial increase in knowledge with a consequent terrific improvement of this new technology. On the other side, the enormous amount of research promoted an immense outgrowth of scientific literature, perpetually published. Halide perovskite solar cells are now effectively competing with other established photovoltaic technologies in terms of power conversion efficiencies and production costs. Despite the tremendous improvement, a thorough understanding of the energy losses in these systems is of imperative importance to unlock the full thermodynamic potential of this material. This thesis focuses on the understanding of the non-radiative recombination processes in the neat perovskite and in complete devices. Specifically, photoluminescence quantum yield (PLQY) measurements were applied to multilayer stacks and cells under different illumination conditions to accurately determine the quasi-Fermi levels splitting (QFLS) in the absorber, and compare it with the external open-circuit voltage of the device (V_{OC}). Combined with drift-diffusion simulations, this approach allowed us to pinpoint the sites of predominant recombination, but also to investigate the dynamics of the underlying processes. As such, the internal and external ideality factors, associated to the QFLS and V_{OC} respectively, are studied with the aim of understanding the type of recombination processes taking place in the multilayered architecture of the device. Our findings highlight the failure of the equality between QFLS and V_{OC} in the case of strong interface recombination, as well as the detrimental effect of all commonly used transport layers in terms of V_{OC} losses. In these regards, we show how, in most perovskite solar cells, different recombination processes can affect the internal QFLS and the external V_{OC} and that interface recombination dictates the V_{OC} losses. This line of arguments allowed to rationalize that, in our devices, the external ideality factor is completely dominated by interface recombination, and that this process can alone be responsible for values of the ideality factor between 1 and 2, typically observed in perovskite solar cells. Importantly, our studies demonstrated how strong interface recombination can lower the ideality factor towards values of 1, often misinterpreted as pure radiative second order recombination. As such, a comprehensive understanding of the recombination loss mechanisms currently limiting the device performance was achieved. In order to reach the full thermodynamic potential of the perovskite absorber, the interfaces of both the electron and hole transport layers (ETL/HTL) must be properly addressed and improved. From here, the second part of the research work is devoted on reducing the interfacial non-radiative energy losses by optimizing the structure and energetics of the

relevant interface in our solar cell devices, with the aim of bringing their quasi-Fermi level splitting closer to its radiative limit. As such, the interfaces have been carefully addressed and optimized with different methodologies. First, a small amount of Sr is added into the perovskite precursor solution with the effect of effectively reducing surface and interface recombination. In this case, devices with V_{OC} up to 1.23 V were achieved and the energy losses were minimized to as low as 100 meV from the radiative limit of the material. Through a combination of different methods, we showed that these improvements are related to a strong n -type surface doping, which repels the holes in the perovskite from the surface and the interface with the ETL. Second, a more general device improvement was achieved by depositing a defect-passivating poly(ionic-liquid) layer on top of the perovskite absorber. The resulting devices featured a concomitant improvement of the V_{OC} and fill factor, up to 1.17 V and 83% respectively, reaching efficiency as high as 21.4%. Moreover, the protecting polymer layer helped to enhance the stability of the devices under prolonged maximum power point tracking measurements. Lastly, PLQY measurements are used to investigate the recombination mechanisms in halide-segregated large bandgap perovskite materials. Here, our findings showed how few iodide-rich low-energy domains act as highly efficient radiative recombination centers, capable of generating PLQY values up to 25%. Coupling these results with a detailed microscopic cathodoluminescence analysis and absorption profiles allowed to demonstrate how the emission from these low energy domains is due to the trapping of the carriers photogenerated in the Br-rich high-energy domains. Thereby, the strong implications of this phenomenon are discussed in relation to the failure of the optical reciprocity between absorption and emission and on the consequent applicability of the Shockley-Queisser theory for studying the energy losses such systems. In conclusion, the identification and quantification of the non-radiative QFLS and V_{OC} losses provided a base knowledge of the fundamental limitation of perovskite solar cells and served as guidance for future optimization and development of this technology. Furthermore, by providing practical examples of solar cell improvements, we corroborated the correctness of our fundamental understanding and proposed new methodologies to be further explored by new generations of scientists.

Symbols

J	Current density
J_0	Dark recombination current
J_G	Generation current
J_{SC}	Short circuit current
q	Elementary charge
V	Voltage (or volume when specified)
V_{OC}	Open circuit voltage
k_B	Boltzmann constant
T	Temperature
FF	Fill factor
n_e	Electron density
n_h	Hole density
E_e	Electron energy
E_h	Hole energy
D_e	Density of states (or diffusion constant where specified)
N_e	Electron states
N_h	Hole states
N_C	Electron effective density of states
N_V	Hole effective density of states
E_C	Conduction band energy
E_V	Valence Band energy
h	Plank constant
E_F	Fermi level (or Fermi energy where specified)
m_e^*	Electron effective mass
m_h^*	Hole effective mass
π	Pi
c	Speed of light
E_{Fe}	Electron quasi-Fermi level
E_{Fh}	Hole quasi-Fermi level
F_e	Electron free energy
F_h	Hole free energy
η_e	Electron electrochemical potential
η_h	Hole electrochemical potential
η	Efficiency (when specified)
μ_e	Electron chemical potential (or mobility when specified)

μ_h	Hole chemical potential (or mobility when specified)
φ (or ψ)	Electrostatic potential
n_i (or n_e^0)	Intrinsic carrier density
E_G	Band gap energy
χ_e	Electron affinity
ϕ	Photon flux
ϕ_{BB}	Black-body radiation
U_{rad}	Radiative thermal voltage
R	Recombination rate
N_T	Trap density
k_1	First order recombination constant
k_2	Second order recombination constant
k_3	Auger recombination constant
C_e	Electron capture coefficient
C_h	Hole capture coefficient
σ	Capture cross section
v_{th}	Thermal velocity
β_e	Electron detrapping rate
β_h	Hole detrapping rate
S	Interface recombination velocity
R_S	Series resistance
R_{Sh}	Shunt resistance
n_{id}	Ideality factor
I	Signal intensity
C_{int}	Intensity factor
ϵ_0	Vacuum dielectric permittivity
ϵ	Dielectric constant
N_A^- (or N_D^+)	Doping density
τ	Carrier lifetime
α	Absorption coefficient

Contribution Statement

Authors contribution statement for the publications presented in **Chapter 4, 5, 6, 7, 8, 9** as core of this thesis work. The full list of publications can be found at the end of the document.

1. Stolterfoht, M., Caprioglio, P., Wolff, C. M., Márquez, J. A., Nordmann, J., Zhang, S., Rothhart, D., Hörmann, U., Amir, Y., Redinger, A., Kegelmann, L., Zu, F., Albrecht, S., Koch, N., Kirchartz, T., Saliba, M., Unold, T., Neher, D., The impact of energy alignment and interfacial recombination on the open-circuit voltage of perovskite solar cells. *Energy Environ. Sci.* **12**, 2778–2788 (2019)

M.S. planned the project and drafted the manuscript. M.S. and I divided the experimental work in a 50-50 contribution for the following tasks: fabrication of the cells and films, development and calibration of the PL setup, measurement of absolute PL, drift-diffusion simulations, and analysis and interpretation of all the collected data. I also contributed during the drafting of the manuscript and performed SEM measurements. C. M. W. provided important conceptual ideas regarding the identification of the recombination losses, cell fabrication and electrical characterization. J. A. M. performed PL measurements and performed corresponding data analysis and interpretation. J. N. helped during PL measurements on cells and films and contributed to electrical measurements. S. Z. performed PESA and UV-Vis measurements and analysis of this data. D. R. fabricated cells and films, and contributed to electrical measurements. U. H. provided important conceptual ideas regarding the development of the PL setup and corresponding data analysis. Y. A. performed TPC, TPV and differential charging measurements with C. M. W. and M. S. A. R. contributed to the analysis of PL data and development of the setup. L. K. fabricated SnO₂ based cells and films and performed corresponding electrical characterizations. F. Z. performed UPS measurements and interpreted corresponding data. S. A. developed SnO₂ based cells and films. N. K. performed UPS measurements and interpreted corresponding data. T. K. contributed to the analysis of recombination losses and analyzed the simulation results. M. Sa. fabricated TiO₂ based cells and films and performed corresponding electrical characterizations. T. U. performed initial numerical simulations and analyzed simulation results, contributed to the analysis of PL measurements and recombination losses. D. N. contributed to project planning, manuscript drafting and analysis of all electro-optical measurements. All co-authors contributed to proof reading of the manuscript.

2. Caprioglio, P., Stolterfoht, M., Wolff, C. M., Unold, T., Rech, B., Albrecht, S. & Neher, D. On the Relation between the Open-Circuit Voltage and Quasi-Fermi Level Splitting in Efficient Perovskite Solar Cells. *Adv. Energy Mater.* **9**, 1901631 (2019).

I planned the project and drafted the manuscript. The experimental work I performed comprises the fabrication of solar cells and films, electrical measurements,

development and calibration of the PL setup, measurement of the absolute PL. Moreover, I performed drift-diffusion simulations and analyzed and interpreted all the collected data. I also took part actively during the revision of all version of the manuscript. M. S. contributed to the manuscript drafting, data analysis and performed simulations, C. M. W. provided important conceptual ideas and helped during the simulations. T. U. contributed important conceptual ideas for the data analysis and the simulations. B. R. contributed during the drafting of the manuscript and project planning. S. A. and D. N. contributed to project planning, manuscript drafting and analysis of all measurements and simulations performed in the work. All co-authors contributed to proof reading of the manuscript.

3. Caprioglio, P., Wolff, C. M., Sandberg, O. J., Armin, A., Rech, B., Albrecht, S., Neher, D., Stolterfoht, M. On the Origin of the Ideality Factor in Perovskite Solar Cells. Accepted in *Adv. Energy Mater.* (2020)

I planned the project and drafted the manuscript. The experimental work I performed comprises the fabrication of solar cells and films, electrical measurements, development and calibration of the PL setup, measurement of the absolute PL. Moreover, I performed drift-diffusion simulations and analyzed and interpreted all the collected data. I also took part actively during the revision of all version of the manuscript. C. M. W. contributed in the data analysis and cells fabrication. O. J. and A. A. contributed with important conceptual ideas for data analysis and contributed to the manuscript drafting. S. A. contributed in the project planning. D. N. contributed to project planning and manuscript drafting, provided important conceptual ideas for data analysis and developed the recombination model. M. S. contributed to project planning, manuscript drafting, and analysis and interpretation of all measurements and simulations performed in the work. All co-authors contributed to proof reading of the manuscript.

4. Caprioglio, P., Zu, F., Wolff, C. M., Prieto, J. A. M., Stolterfoht, M., Koch, N., Unold, T., Rech, B., Albrecht, S., Neher, D., Márquez Prieto, J. A., Stolterfoht, M., Becker, P., Koch, N., Unold, T., Rech, B., Albrecht, S. & Neher, D. High Open Circuit Voltages in pin-Type Perovskite Solar Cells through Strontium Addition. *Sustain. Energy Fuels* **3**, 550–563 (2019)

I planned the work and drafted the manuscript. The experimental work I performed comprised the fabrication of all solar cell devices and films, PV characterization, TRPL, absolute PL and absolute EL measurements, analysis and interpretation of all data. I analyzed all UPS/IPES and XPS data as well as the SIMS results. Moreover, I performed all SEM characterization. I also took part actively during the revision of all version of the manuscript. F. Z. performed photoemission measurements and helped during interpretation of the results. C. M. W. helped during cell fabrication and planning of the project. J. A. M. P. performed PL imaging and analyzed the data. M. S. helped during electrical characterization. N. K. contributed with conceptual idea for photoemission results interpretation. T. U. contributed to PL imaging analysis. B. R.

contributed to the project planning. S. A. and D. N. contributed to project planning, manuscript drafting and interpretation of all measurements performed in the work.

5. Caprioglio P., Saul-Cruz D., Caicedo-Dávila S., Zu F., Sutanto A.A., Kegelman L., Wolff C.M., Perdigón-Toro L., Koch N., Rech B., Grancini G., Abou-Ras D., Nazeeruddin M.K., Stolterfoht M., Albrecht S., Antonietti M., Neher D., *Bi-functional Interfaces by Poly-Ionic Liquid Treatment in Efficient pin and nip Perovskite Solar Cells* (under revision)

I planned the project and drafted the manuscript. I fabricated all the *pin* devices, measured absolute PL, absolute EL, TRPL, SEM, and performed MPP stability measurement. I characterized also all PV properties of the devices, including intensity dependent measurements. I performed the AFM and C-AFM measurements and data analysis. I finally interpreted all the additional measurements coming from the other co-authors. I also took part actively during the revision of all version of the manuscript. D.S.C synthesized all the PILs and performed XRD and contact angle measurement; S.C.D. performed the EDX and CL measurements and analysis; F.Z. performed XPS and UPS measurements; A.A.S. and L.K. fabricated the *nip* devices; L.P.T. performed the conductivity measurements; C.M.W. helped during the stability measurements and assembled the experimental setup; N.K. supervised the XPS and UPS measurements and helped during the interpretation of the results; B.R. supervised the fabrication of *nip* cell at HZB and helped during the interpretation of the results; G.C. supervised the *nip* cell fabrication at EPFL and helped during the interpretation of the results; D.A. supervised the EDX and CL analysis and helped during the interpretation of the results; M.K.N. supervised the *nip* cell fabrication at EPFL and helped during the interpretation of the results; M.S. helped during photoluminescence measurements, the interpretation of the results and contributed in writing the manuscript; S.A. supervised all the work and helped during the interpretation of the results; M.A. supervised all the work and helped during the interpretation of the results; D.N. supervised all the work, helped during the interpretation of the results and contributed in writing the manuscript.

6. Caprioglio P., Caicedo-Dávila S., Yang C.J., Rech B., Ballif C., Abou-Ras D., Stolterfoht M., Albrecht S., Jeangros Q., Neher D., *Microscopic emission properties and optical reciprocity failure in MA-free large bandgap halide-segregated perovskites* (submitted)

I planned the project and drafted the manuscript. I performed all the PL studies, including intensity dependent measurements and all data analysis, including the interpretation of the results. I performed the intensity dependent data analysis with the associated recombination model. I also took part actively in all the revision version of the manuscript. S.C.D performed the SEM and CL measurements including data analysis; C.J.Y. fabricated all the perovskite films; B.R. contributed during the planning of the project; C.B. contributed during the planning of the project; D.A.R. contributed in the interpretation of the CL and SEM results; M.S. contributed during manuscript drafting and interpretation and the results; S.A. contributed during project planning and interpretation of the results; Q.J. contributed during manuscript drafting and

interpretation of the results, as well as during project planning, D.N. contributed during project planning, interpretation of the results and manuscript drafting.

Chapter 1.

1. Introduction

This chapter serves as a general overview on the perovskite photovoltaic and material research. Here, only the most established and at-the-present known properties of perovskite solar cells and material will be introduced. Given the enormous amount of scientific literature on the matter, in this chapter, we will focus exclusively of the aspects relevant for the core of this thesis work.

1.1 Solar Energy

In the past decades, humanity has faced an important paradigm shift regarding the consumption and production of energy. The ramping development of the every-day technology, which availability touches every corner of the globe, lead to a constant increase in energy consumption. To cope with the high demands of a fast-developing world, the human kind has procured with more and more production of usable energy. Unfortunately, for decades, the leading technologies implemented in the energy production have been statically bounded to what inherited from the 19th century, mostly due to political and economic reasons. Indeed, the conceptual development, in the framework of large-scale energy production, has not followed the energy demand at the same speed. Although, at the present, many alternative technologies exist, and are in fact used by many countries, the market has been, and still is, dominated by usage of fossil fuels. The reckless consumption of fossil fuels has brought the world in the proximity of a predictable energetic and environmental crisis. The natural reservoir of fossil fuels provided by the hearth are doomed to be finished in the foreseeable future and the devastating amount of CO₂ emissions are effectively harming the climate equilibria of the hearth, sadly already observable in our every-day life. The planet is currently on an unsustainable path and the constant growing carbon emissions underscores the urgency for the world to change. Clearly, decarbonizing the power sector while at the same time meeting the rapidly expanding demand of energy is the primary challenge that has to be faced. In response to this, renewable energies are on a continuous growth both on a research and industrial level, led by wind and solar power.

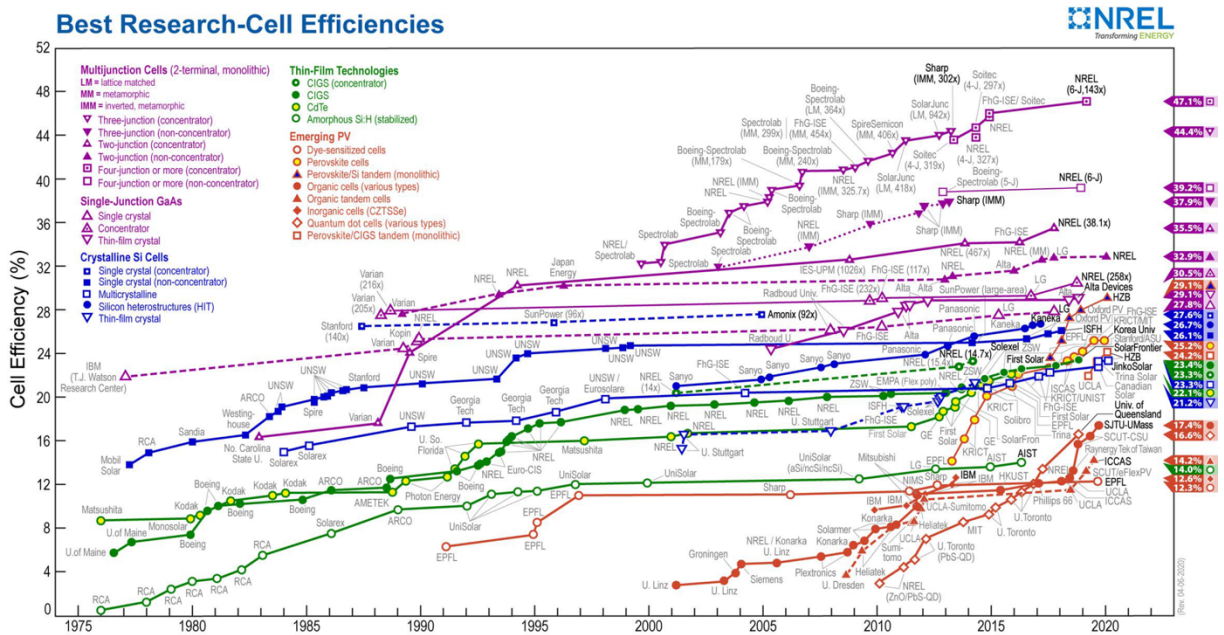


Figure 1.1: Best photovoltaic efficiency chart at research level. The data and the image are provided by the Nation Renewable Energy Laboratory (NREL). Downloaded on 2/5/2020 at: <https://www.nrel.gov/pv/cell-efficiency.html>

In this respect, the most powerful source of energy available on our planet is undoubtedly the sun, which with its inexhaustible irradiation energy (120,000 TW/hours), in 2 hours provides the earth with the equivalent of the energy needs of the entire planet for 1 year. For this reason, photovoltaic is one of the most promising green alternatives to fossil fuels. Since the first discovery of the photovoltaic effect in 1839 for Selenium,^[1] many materials have been investigated with this purpose. Silicon has led the panorama for many decades, starting from efficiencies of 4.5% 1953^[2] to efficiency now surpassing 26%.^[3,4] To date, GaAs has reached the record for the best efficiency on a single junction device, with an efficiency approaching 29%.^[5] Another class of materials widely studied is chalcogenides, as CIGS and CdTe, which exhibited efficiencies around 23%.^[6] Organic solar cells, in the form of conjugated polymers in bulk heterojunction systems, currently occupy a large portion of the photovoltaic research with recent promising results of efficiencies exceeding 18%.^[7] Generally, the need for materials and processing methods capable of efficiently delivering low-cost electricity is of mandatory importance. Solar cell based on organometal halide perovskites have entered the game relatively late compared to other above-mentioned technologies. However, their development in efficiencies has been sky-rocketing, as shown in the efficiency chart in **Fig. 1.1**. Since firstly demonstrated with photovoltaic behavior in 2009,^[8] and later in solid state solar cell devices in 2012,^[9,10] now they have reached efficiencies exceeding 25%.^[5] The ability of this class of material of enabling high efficiencies rather easily, together with the approachable and rather forgiving fabrication procedure, brought this technology to be the new center of interest of academic research. In particular, intriguing material properties^[11–13] and promising low-cost production,^[14,15] have triggered many different scientific fields and opened doors for a wide spectrum of research topics. The large availability of the material precursors and the easy deposition techniques, from evaporation or solution, are keeping the production costs low, although resulting in high efficiency devices. Thereby, this research has moved rapidly from a pure academic level to industry, and the prevision of foreseeable large-scale production is currently discussed. In the next section, we will explore some of key features which brought this material to be one of the top research topics of the last decade.

1.2 Perovskite Semiconductors

Perovskite minerals have been discovered for the first in the form of Calcium Titanite CaTiO_3 by Gustav Rose in Russia in 1839. The new material was named after mineralogist Lev Perovski, thus the name Perovskite. The general formula for oxide perovskites follows the nomenclature ABO_3 , as described by Victor Goldschmidt in 1926.^[16] His original work identifies a tolerance factor r which described the ability of a certain element to fit in the given crystal structure. Usually, values of $r = 0.7 - 1.0$ allows for a stable crystal lattice. Within this range, a vast number of metals are able to form a classical perovskite structure. Of large interest have been, for example, BaTiO_3 and SrTiO_3 especially for energy storage, fuel cells, as well as to generate

hydrogen fuel via photocatalysis process.^[17] Besides metal oxide perovskite, more recently, the halide version of this materials has gain attention as semiconductor for optoelectronic application. In this type of perovskites, with the formula ABX_3 , the X position is occupied by halide atoms. One particular aspect of this type of perovskites is that they can be in the form of organic-inorganic compounds, where, for most photovoltaic application, the A site is commonly occupied by an organic cation. Recently, many different compositions have been investigated by mixing different elements in A and X position with different ratios. Among the most studied ones, we can find, for the A site, the organic compounds Methylammonium (MA) and Formamidinium (FA), but also alkali metals such as Cesium (Cs) and, for the X site, Iodide (I), Chloride (Cl) and Bromide (Br). Moreover, for the majority of the cases, the B site is occupied by Lead (Pb). Although, more recently, different compositions using Tin (Sn) has gain strong interested, as well as introducing Strontium (Sr). The classical structure and the list of commonly studied elements are presented in **Fig. 1.2**.

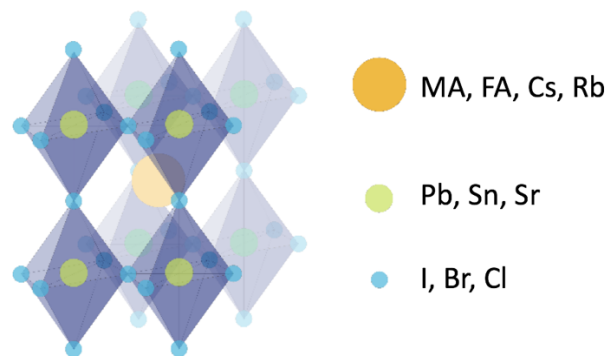


Figure 1.2: Cubic corner sharing metal halide perovskite structure of a unit cell in the form ABX_3 . The most commonly elements studied for photovoltaic within this structure are listed on the left.

The crystal structure presented in **Fig. 1.2** depicts a corner sharing cubic unit cell, called α phase. However, three phases of Bravais lattices can be generally identified depending on the temperature: orthorhombic (γ phase), tetragonal (δ phase) and cubic.^[18] Importantly, each composition would be subjected to change in phases at different temperatures and pressures, following its specific phase diagram. Each of these phases is characterized by different properties and the only photoactive “black-phase” wanted for photovoltaic application is the α phase.

1.3 Metal Halide Perovskite Properties

The extensive investigation of metal halide perovskite started not more than ten years ago. Although many of the general properties have been well understood, many topics are currently still under debate. However, given the vast interest of the scientific community, a large variety of material aspects have been thoroughly covered. In this

section, we will limit to describe the most general and well-known material properties relevant for photovoltaic application. Although, many other aspects and properties can be found in literature, but not of primary interest for this work.

1.3.1 Crystal Structures and Compositions

Metal halide perovskites are ionic crystals in the formula ABX_3 , where the size of the A cation is of crucial importance to determine the crystal structure energetically favourable. If the atom in the A site is characterized by a small ionic radius, the tolerance factor r decreases to values lower than 1 and the formation of the unwanted orthorhombic and tetragonal structures can be more favorable. On the other hand, if the A site is too large, layered 2D or 1D structure can be formed.^[19] The latter structures attracted the interested of the photovoltaic community due to their increased robustness to moisture compared to the classical 3D structure. However, the rather forgiving stability window of the 3D structures allowed for the investigation of a wide range of compositions. The standard starting point in the photovoltaic field is $MAPbI_3$, with an optical bandgap of 1.6 eV. However, in the last years the research has moved toward significantly more complicated compositions, in order to expand the material properties and improve the absorber quality.

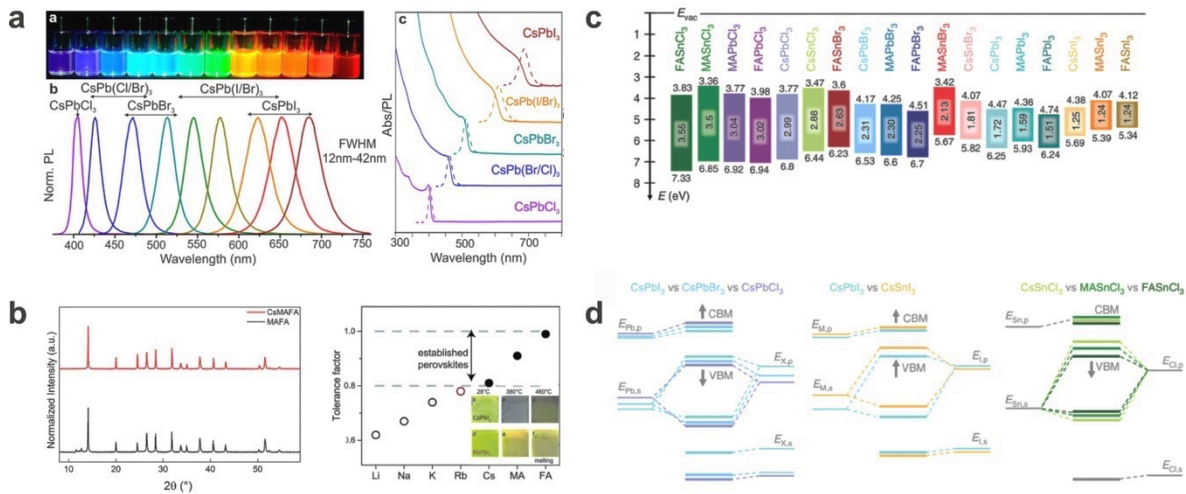


Figure 1.3.1: a) Perovskite bandgap tuning by halide substitution visible in photoluminescence and absorption. Image adapted from Ref^[20]. b) Effect of A-cation substitution in relation to the tolerance factor. On the left panel the effect of Cs addition on the phase purity is highlighted through X-ray diffraction patterns. Image adapted from Ref^[21,22]. c) Effect of bandgap tuning for different perovskite composition where also the B metal is substituted. d) Three examples of composition from c) where here the orbital contribution to the bandgap is detailed. c) and d) are adapted from Ref^[23].

Probably one of the biggest advantages of metal halide perovskites is the ability of optimizing the spectral range of photo-response by tuning the optical band gap (E_G).

Early experimental and theoretical studies^[24,25] showed that the metal ion and the halides contribute mostly to density of states close to the band edges. In lead-containing perovskites, the conduction bands mostly originate from unoccupied Pb p orbitals while the upper states of the valence band are formed by halogen p orbitals and the Pb s orbitals.^[26] Accordingly, different types of halogen anions, commonly I and Br, can be accommodated at a low energy cost in the crystal lattices and homogeneously intermixed with highly tolerant mixing ratios.^[20,27] Specifically, simply increasing the amount of Br present in the crystal structure induces an enlarging of the optical E_G . Theoretically, only by changing the I⁻ to Br⁻ ratio in MAPbI₃, a E_G range of 1.57–2.27 eV could be potentially achieved.^[28] This happened to be of particular interest for using this absorber in multijunction tandem devices, either Si-perovskite or perovskite-perovskite, where an accurate selection of the E_G is of mandatory importance. Moreover, substitution of I with Cl is also possible and the resulting bandgap can reach even larger values close to 3 eV.^[20] Generally, while the size of the halide in the X site decreases and the electronegativity increases, the bandgap of crystal increases. The increase in electronegativity induces a downward shift of the valence band position, while having only a small effect of the conduction band position overall increasing the E_G , as shown in **Fig. 1.3.1c-d**. Furthermore, the monovalent cation MA⁺ in the A site has been partially exchanged with the slightly larger FA⁺.^[29] This time, as expected, the impact of the lattice expansion due to the insertion of the new cation on the E_G is rather small. This experimental evidence is in line with DFT calculations which have demonstrated the negligible contribution of MA⁺/FA⁺ on the band edges.^[30] Despite the instability of the cubic phase at room temperature of pure FA-based perovskite, the introduction of FA⁺ in combination with MA⁺ results in improved structural and thermal stability compared to the pure MA and FA perovskite component.^[31] Also, the appropriate mixing of the two cations has been found to be beneficial during the crystal formation.^[32] Moreover, a simultaneous exchange of MA⁺ and FA⁺ in the A site and I⁻ and Br⁻ in the X site has proven to deliver an ideal compromise of photovoltaic performance, band gap tuning and phase stability.^[33] However, as we will discuss in details in **Chapter 9**, the practical tunability of the E_G is limited by the intrinsic material instability under illumination when a certain amount of Br⁻ content is surpassed.^[34–41] A considerable step forward has been achieved by the addition of the inorganic cation Cs⁺ in combination with MA⁺ and FA⁺.^[22] Also in this case, despite the instability of the cubic phase at room temperature of the pure Cs-based perovskite, this resulted in a substantial suppression of the contribution of photoinactive “yellow δ and γ phases” with beneficial effects in efficiency and stability, mostly due to entropic effects.^[21,42] While MA⁺, FA⁺ and Cs⁺ are still contained within a $r = 0.8 - 1.0$, a few examples demonstrated the beneficial effects of addition cations outside this range. Specifically, the implementation of small amount of Rubidium (Rb⁺) or Potassium (K⁺),^[43,44] has shown significant improvements in the solar cell performance. However, no evidence of true intercalation of these two elements in the crystal structure has been found and studies pointed out different type of effects, as for example, defect passivation. The partial substitution of the divalent metal B and its impact on the optoelectronic properties have not been investigated thoroughly

compared to the substitution of the other components. As explained above, a partial substitution of Pb^{2+} with a different metal can induce a considerable modification of the electronic structure and bandgap, possibly beneficial for the photovoltaic properties of the resulting devices. Some studies have shown that a partial substitution of Pb^{2+} with Sr^{2+} ,^[45] Cd^{2+} , and Ca^{2+} in MAPbI_3 is possible.^[46] Also, the preparation of completely lead-free perovskite solar cells has been achieved, e.g. with Sn^{2+} or Bi^{3+} .^[47,48] Interestingly, it has been reported that a partial substitution of the divalent metal with Co^{2+} can induce an advantageous change in the energetics without changing the band gap or intrinsically doping the material.^[49] Given that it has been shown that the band gap decreases along with the increasing of the B cation electronegativity,^[50,51] recently, a combination of Sn^{2+} and Pb^{2+} achieved efficient low-bandgap perovskites, of particular importance for all-perovskite tandem devices.^[52,53]

1.3.2 Defects and their Passivation

Since the use of halide perovskites in photovoltaic, the most common type of defects studied in perovskite are the point defects in archetypal MAPbI_3 . Within this category, we can find vacancies and interstitials defects of MA, Pb and I or anti-site occupations of the various elements.^[11,54] Importantly, theoretical studies revealed that the point defects that would contribute to deep levels in the band gap have high formation energies, whereas point defects with low formation energies contribute only to shallow energy states.^[55] However, although shallow defects may not be detrimental for carrier recombination, they could contribute to unintentional doping at room temperature.^[56] These defects can be either donors or acceptors type, with the consequence of causing the perovskite to be *p*- or *n*-doped. However, the ionic nature of the crystal structure allows for a compensation of these vacancies with an opposite charge, effectively reducing the doping densities, found to be $10^9 - 10^{14} \text{ cm}^{-3}$.^[57,58] Regardless the nature of these defect, perovskite materials are commonly characterized by rather low electroluminescence and photoluminescence quantum yield, suggesting a significant contribution of non-radiative recombination through defects. In this respect, the density of states within the band has been estimated to be roughly $10^{16} - 10^{19} \text{ cm}^{-3}$.^[59,60] Indeed, a larger type of defects is actually present in perovskite crystals in addition to point defects. Namely, impurities, mainly from the precursor materials, two-dimensional defects, as grain boundaries and surface defects, and three-dimensional defects, as remaining lead cluster after crystallization. Importantly, due to the ionic nature of the crystal and the high ion-migration speed, also charge point defects can migrate to the interfaces, surface or grain boundaries, and strongly affecting the recombination.^[61] Here, these defects can be responsible for local doping and band bending,^[62,63] current density - voltage hysteresis,^[64,65] phase segregation,^[36,66,67] and degradation processes.^[68] Moreover, at these locations, a large variety of defects can be found, possibly causing deep energy level traps. Specifically, undercoordinated halides ions and Pb^{2+} , migrated point defects and Pb clusters can be located at the surface of the crystal. Again, the ionic nature of the crystal, in this case, constitute an advantage in terms of passivation strategies for these defects. The charged nature of

the defects enables passivation methods that are based on coordinate bonding or ionic bonding to neutralize the deep level traps resulting from charge defects. For examples, negatively charged undercoordinated I⁻ and Pb-I anti-site can be passivated by Lewis acids or other cations, through coordination and ionic bonding respectively.^[69] For examples, fluorine atoms, contained in small molecules or polymers, can potentially passivate these defects through halogen bond. Moreover, in these regards, oxygen has proven to an effective passivate agents.^[70] On the other hand, Lewis bases are capable of coordinate and passivate undercoordinated Pb²⁺ defects or Pb clusters. In this case, the lone pair electrons in nitrogen (N), sulphur (S) or phosphorus (P) functionalities can neutralize the extra positive charge, acting as efficient passivating agents.^[71,72] A recent great example is the passivation via trioctylphosphine oxide (TOPO),^[73] which demonstrated drastic reduction of non-radiative recombination in perovskite films. Other similar results have been obtained with compounds containing amines (-NH₂).^[74] Moreover, conceptually similarly as in Si, surface dangling bonds and grain boundaries can be passivated by the addition of a wide E_G , as Polystyrene (PS) or Polymethylmethacrylate (PMMA).^[75,76] A summary of the common defects and their passivation is shown in **Fig. 1.3.2**.

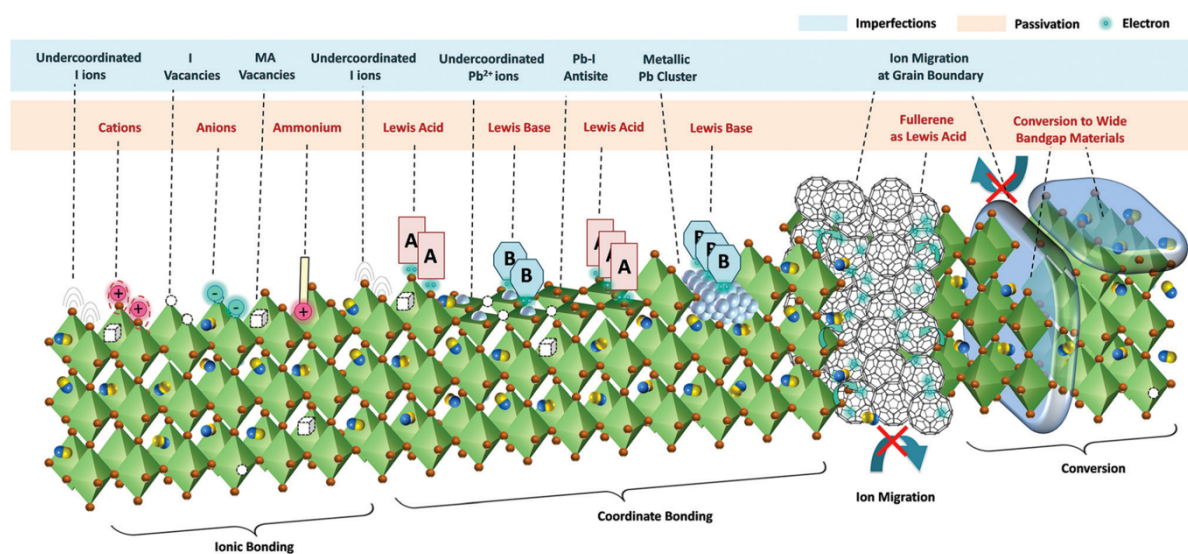


Figure 1.3.2: Schematic representations of the most common defects and their passivation possible presents at the surface of perovskite materials. Image adapted from Ref^[69].

1.3.3 Optoelectronic Properties

Regardless the large number of possible defects that can be found in perovskites, these materials are characterized by exceptionally good optoelectronic properties. Lead halides perovskites are direct bandgap semiconductor with high absorption coefficient $\alpha = 10^4 - 10^5 \text{ cm}^{-1}$, which allows efficient panchromatic absorption of the solar spectrum.^[77] This allows for effective absorption of light and large photocurrent generation, with layer thicknesses smaller than 500 nm. Additionally, the optical E_G ,

generally around 1.6 eV, places these absorbers in a convenient position with respect to the absorption of light in the range of maximum intensity of the sun irradiation. The absence of a high density of defects with energy states deep in the band gap, allows for a very sharp absorption onset and relatively small Urbach energies of around 15 meV, denoting high material purity.^[12] The combination of this properties is summarized in **Fig. 1.3.3**. Moreover, polycrystalline perovskites are generally characterized by very long diffusion lengths, to which is partially attributed the high efficiency of the solar cell devices. Several studies have shown diffusion lengths exceeding 100 nm for simple MAPbI₃ and over 1 μm the mixed halide variant with Cl.^[78] Additionally, in single crystals these values have reach incredibility long values up to 175 μm.^[79] It is important to note that the film formation, processing procedure and crystal quality have a drastic impact of these values and the consequent photovoltaic performance. Furthermore, the carrier mobility, which represent the ability charges to move under an applied field, has been found with significantly good values. In the specific, balanced hole and electron mobilities exceeding 10 cm²V⁻¹s⁻¹ have been measured in perovskite films and above 100 cm²V⁻¹s⁻¹ for single crystals.^[80] Interestingly, both carrier mobility and diffusion lengths seem not be affected by the perovskite composition.^[77] It is also worth to mention that, similarly to other inorganic semiconductors, in 3D perovskites at room temperature the absorption of photons generates spontaneously unbound electron-hole pairs.^[81] On the contrary, for 2D low dimensional perovskites, excitons contribution starts to be significant and must be taken into account.^[19] The combination of all these properties allowed to use 3D perovskite absorber directly in contact with hole-accepting and electron-accepting contacts in the solar cell architecture.

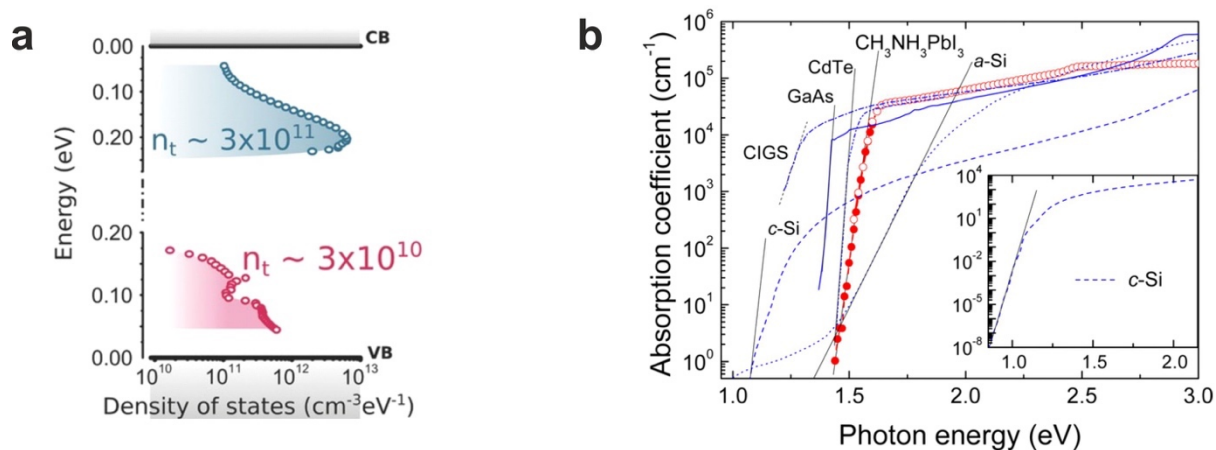


Figure 1.3.3: a) Sub-bandgap density of defect states for MAPbI₃. Image adapted from Ref ^[57]. b) Absorption coefficient and Urbach energy fitting for different photovoltaic materials. The sharp onset of MAPbI₃ correlates with low Urbach energies and low density of sub-bandgap defect states. Image adapted from Ref ^[12].

1.4 Perovskite in Solar Cells

1.4.1 Deposition Methods

One significant advantage of perovskite materials is that they can be deposited via various relatively easy methods. One particularly interesting approach is the deposition via thermal evaporation, which, in principle, allows the deposition of perovskite layers on large flat or uneven surfaces. This method usually consists in the co-evaporation of PbI_2 and MAI from two different sources at precisely controlled rates, in order to end up with the correct stoichiometry composition, as presented in **Fig. 1.4.1a**. However, the tedious control of the precursor ratio is a critical step, which commonly limits the successful deposition of high-quality films. Moreover, the lack of appropriate control on the rates often brings to a scarce reproducibility. Consequently, the complexity of this approach increases drastically with the increase of the perovskite components, such as FA-MA and Br-I mixtures. Notably, this approach is of high interest in Si-perovskite tandem application and industrial production but, at an academic level, it has not been extensively explored and mastered yet, as other more common deposition techniques.

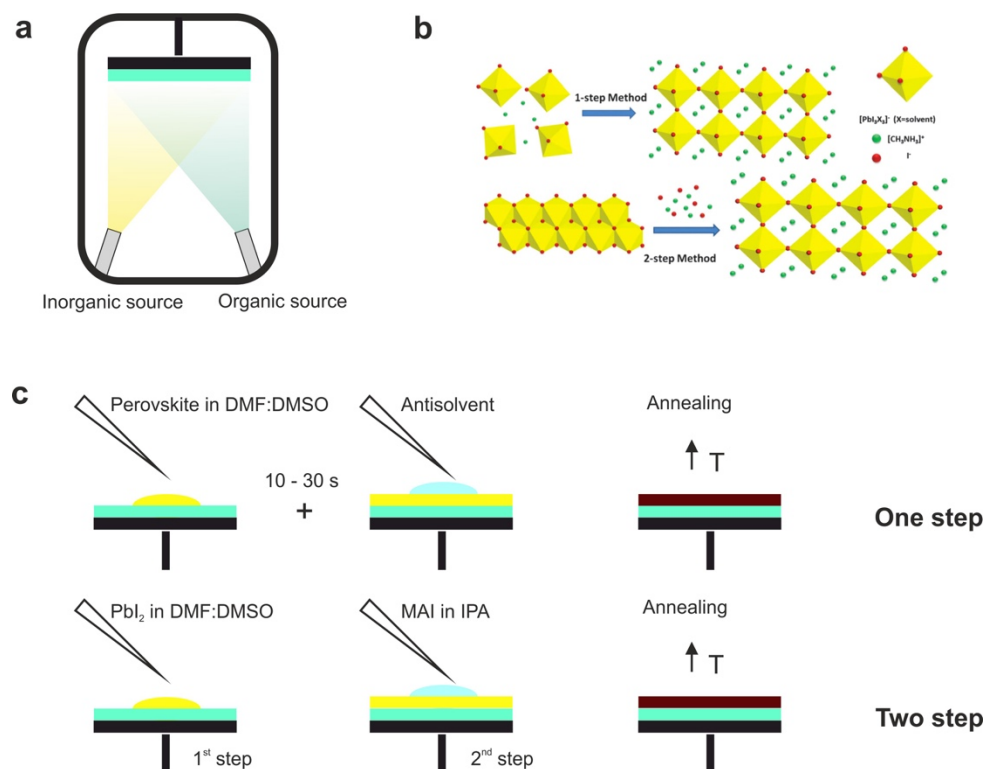


Figure. 1.4.1: Schematic representation of different deposition steps. Co-evaporation deposition method in a). In b) perovskite precursors and solvent interaction are presented for one or two step spin coating deposition method. Panel b) adapted from Ref^[82]. c) Step by step representation of the spin coating deposition for one or two step method.

A much easier method, more approachable in a laboratory scale, is the deposition of a precursors' solution via spin coating. In this case, tremendous efforts have been devoted in order to optimize the process, which is currently able to deliver high efficiencies with high degree of reproducibility. The solution deposition techniques can be grouped in two main categories: one-step and two-step methods. The one-step method encompasses the direct deposition of the precursor solution whereas, the two-step method consists firstly in the deposition of a PbI_2 layer, which is later converted into perovskite with an additional deposition step of MAI, as indicated in **Fig. 1.4.1b-c**. One challenge in the one-step method is the ability to obtain uniform smooth layer. This is related to film shrinkage during the crystal formation, caused by the rapid and simultaneous evaporation of the solvent and perovskite crystallization.^[82] The solution of this problem has been achieved by adding certain amount of dimethyl sulfoxide (DMSO) to the dimethyl formamide (DMF) solution. In fact, DMSO can interact with PbI_2 to form complexes, which can retard the rapid crystallization of the film during the spin coating.^[83] An additional advance in this methodology has been achieved by forcing the rapid precipitation of the perovskite precursor during spin coating by solvent engineering.^[84] Here, an anti-solvent, commonly toluene, chlorobenzene, diethyl ether or ethyl acetate, is quickly dripped during the spin coating of the perovskite solution at a specific time. The anti-solvent does not dissolve the perovskite, but it is still miscible with the precursors' solvent. In this way, the concentration of the perovskite is drastically increased uniformly across the entire substrate, where it crystallizes. In the two-step method, the main precursor PbI_2 can be easily deposited in a uniform and compact film. This layer structure facilitates the intercalation of MA or FA, which is additionally spin coated on top, in order to form for the actual perovskite. Notably, in this case, the final morphology it is largely dominated by the initial PbI_2 film and the reaction rate is entirely dominated by the diffusion of MAI (or FAI) in the lattice.^[82] Importantly, it seems that both methodologies can be applied to different type of perovskite mixtures. Other techniques for the two-step conversion of PbI_2 , as the low-pressure vapor assisted diffusion of MAI or solvent assisted via deep coating.^[85,86] In most of the deposition methods, after the deposition, an additional annealing step is necessary to complete the crystallization of the film and to induce the complete evaporation of the solvents. Commonly, this step is conducted at 100°C for 1h, but many different variations can be found in literature. Usually, all the depositions steps are carried in water free inert atmosphere. Notably, one limitation of the deposition via solution is the wettability and roughness of the bottom substrate.

1.4.2 Device Architectures

The large diffusion length and the low recombination rates allow perovskite solar cells to be fabricated by simply sandwiching the perovskite absorber between two selective transport layers. The role of the transport layers is that of selectively transport electrons or holes to the metal contact, without allowing the passage of the oppositely charged carriers. Given that the perovskite absorber is generally intrinsic and the transport of carriers is dominated by diffusion, the choice the transport layers is of crucial

importance in order to achieve efficient devices. Historically, the first perovskite device was fabricated in a dye-sensitized solar cell fashion, where the perovskite was infiltrated in a TiO₂ scaffold. However, because of the liquid electrode and the consequent dissolution of the perovskite, this architecture has been quickly changed.^[31] A fundamental improvement has been achieved by mesoporous TiO₂ devices with a solid state hole transport layer (HTL), namely Spiro-OMeTAD.^[87,88] These devices were able to achieve high efficiency and relatively good stability. More recently, devices with planar TiO₂ or SnO₂ have been introduced and are currently use.^[89] The advantage of the latter is to avoid the tedious and time-consuming preparation of the mesoporous TiO₂ scaffold and more stable efficiency. Importantly, this type of devices, which are the most common and widely studied, are called regular architecture, abbreviated *n-i-p*. As above mentioned, they commonly use TiO₂ or SnO₂ as bottom electron transport layer (ETL) and Spiro-OMeTAD doped with lithium (Li) and cobalt (Co) salts as top HTL.

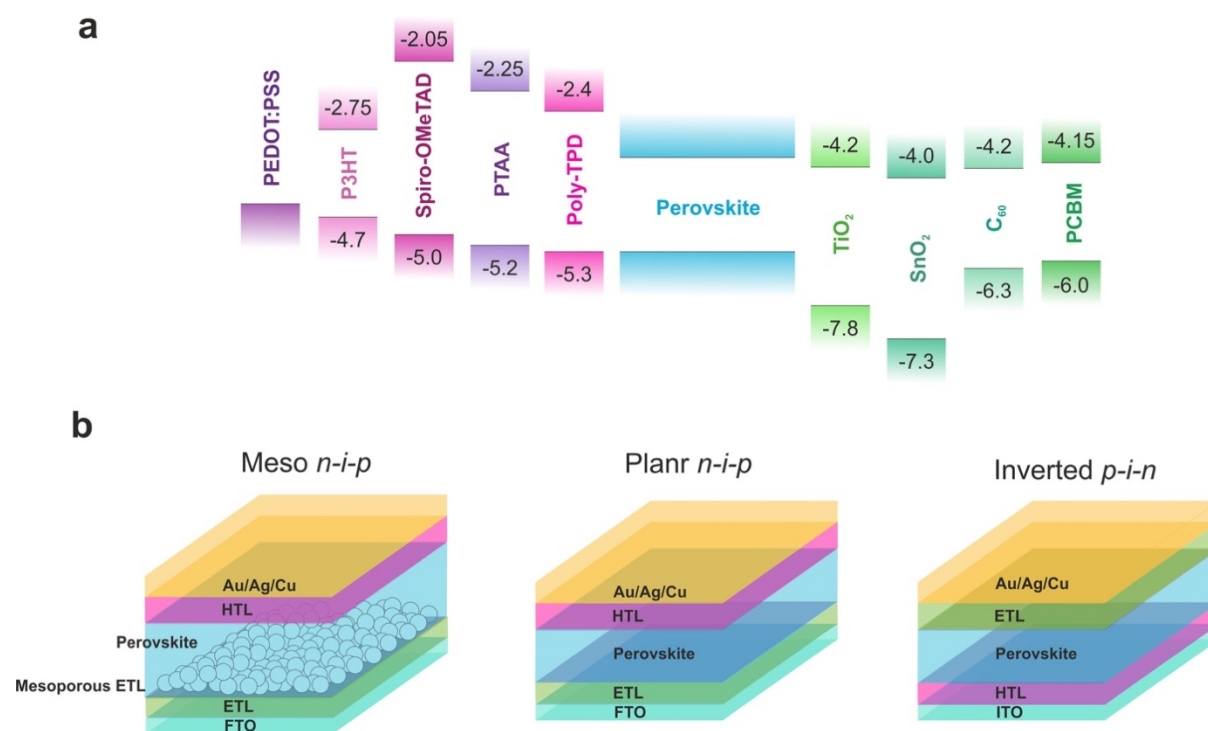


Figure 1.4.2: a) Representation of the energy levels with respect to the vacuum level of the common electron and hole transport layers used in *n-i-p* and *p-i-n* perovskite solar cells. The energy levels of the perovskite are not specified since it can vary depending on the composition. b) Schematic representation of the three common architectures used in perovskite solar cells.

Another type of architecture, yet so far less popular, takes the name of inverted architecture and it is abbreviated with *p-i-n*. In these devices, the bottom layer is constituted by the HTL and the top layer by the ETL. Inverted solar cells are prone to reduced hysteresis,^[90,91] low processing temperatures and recently gained strong

interest in perovskite based multijunction devices.^[92] Where the selection of ETL in these devices is mostly limited to fullerenes, C₆₀ or PCBM, the variety of HTL that can be implemented is significantly larger. Generally, the HTL used consistent in organic semiconductor. The use of small molecules has the advantage that they can be processed either by solution or evaporation. Also, the optoelectronic properties can be easily chemically tuned. Although, small molecules usually require chemical doping in order to increase the effectiveness of carrier transport. On the other hand, conjugated polymers are characterized by higher intrinsic hole mobilities and can easily form homogenous thin layers via spin coating.^[31] In this work, we will mostly focus on *p-i-n* type devices utilizing polymers as HTL. The standard device investigated throughout this thesis work implements poly[bis(4-phenyl)(2,4,6-trimethylphenyl)amine] (PTAA). However, many other polymers can be used as HTL, such as poly(3-hexylthiophene) (P3HT), poly(3,4-ethylenedioxythiophene) polystyrene sulfonate (PEDOT:PSS) or Poly(N,N'-bis-4-butylphenyl-N,N'-bisphenyl)benzidine (PolyTPD). The summary of all architectures and common transport layer is presented in **Fig. 1.4.2**. A common characteristic of all transport layers is the ability to efficiently transport the majority carriers while effectively blocking the minority carriers. This is very much connected to their bandgap and energetic of the material, which constitute the essential parameter in the choice of the right selective contact. Throughout this work, we will see how small changes in these values can drastically affect the efficiencies of the devices.

1.4.3 Photovoltaics Behaviour

As predicted by the exceptional absorber properties, perovskite solar cells are generally characterized by close-to-ideal photovoltaic behavior. Although, many important limitations still have to be overcome. One peculiarity of the current-voltage ($J - V$) characteristic is the presence of hysteresis phenomena. Specifically, reverse and forward $J - V$ scans may result in two different traces. The first implication of this is that the extraction of power conversion efficiencies at maximum power point can be ambiguous. This behavior has been extensively investigated and it resulted to be a transient phenomenon, which depends on the scan rate. Therefore, it is strictly dependent on the measurement conditions. Generally, *n-i-p* devices exhibit large hysteresis in a larger scan rate windows,^[65,93] while *p-i-n* cells are found to be less affected by hysteresis, due to the usage of fullerene derivatives as ETLs.^[90,91] A general consensus agrees on associating the hysteresis phenomena with migrations of ionic defects, like iodine vacancies, which are able to accumulate on one side of the cell under an electric field and, consequently, to screen the internal voltage. An ongoing debate questions the relevance of this particular aspect under normal operational conditions in devices which do not present large hysteric behavior.^[90,94] Very much related to this question is what ion densities are actually needed to effectively introduce a limitation in the photovoltaic performance.^[95] Current works are devoting on this important aspect. Due to the high absorption coefficient, high photocurrents in perovskite solar cells, reported as the short-circuit current J_{SC} (explained in details in **Chapter 2**), are theoretically achievable by relatively thin layers, as detailed above.

However, the device structure itself can have an influence on the values actually observed in real devices. Given the multilayered architecture and the different layers being characterized by different refractive indexes, reflective photocurrent losses can be present. Moreover, the usage of other semiconductor as transport layer can additionally bring parasitic absorption of the incoming light. Usually, the reported values of J_{SC} can vary in the range of 22 – 24 mA/cm² for a nominal bandgap of 1.6 eV, depending on the architecture. A strategy applicable to perovskite is the narrowing of the bandgap in order to achieve higher J_{SC} , even exceeding 25 mA/cm² improving the final efficiencies.^[96] Being perovskite solar cells characterized by relatively low density of detrimental defects, in principle, it is possible to achieve open-circuit voltages (V_{OC}) close to the thermodynamic limit (we will explain this point in details in **Chapter 2**), which are calculated to be around 1.33 V for a bandgap of 1.60 eV. Realistically, due to the usage of transport layers, in addition to the intrinsic limitation of the perovskite absorber, perovskite solar cells exhibit lower V_{OC} values that can vary from around 1.10 V to the best ever reported values for the given bandgap of 1.26 V.^[97] Throughout the manuscript we will discuss in details all the parameters which can influence the V_{OC} and what are the strategies to improve these values. Lastly, the fill factor FF (explained in details in **Chapter 2**), is predominantly affected by how effectively the charges are extracted from the solar cell device. Given that perovskites are characterized by excellent carrier mobilities, the primary limitations are caused by the attached transport layers. Here, usually the carrier mobilities are generally smaller, especially in the organic components, slowing the transport of carriers. Additionally, general series resistance in the device due to the extraction and the transport at the contacts can further limit the FF values. However, also the polycrystalline nature of the perovskite films used in solar cells can have a certain degree of transport limitation, due to the presence of grain boundaries.^[77] Nevertheless, also in this case, exceptionally good values in the range of 70 – 80 %, are commonly observed, depending on the architecture. Record FF values of 84 – 85 % are also reported.^[98] The combination of the photovoltaic behavior allowed for achieving astonishingly high power conversion efficiencies, with a current record of 25.2 % for *n-i-p* architectures.^[5] Commonly, *p-i-n* devices are limited to lower efficiencies due to lower J_{SC} values. In this case, efficiencies rarely approach 21%, however, the current record exceeded 23%.^[99] Specific details on the general working principle of a solar cell can be found in **Chapter 2**.

1.5 Current Challenges

Despite the fact that this technology has witnessed tremendous improvements in the last decade^[100] and that the advance in understanding of the physical processes governing the photovoltaic behavior of perovskite solar cells has increased at rapid pace, the theoretical efficiencies are far to be reached and long term stability is still an issue.^[101,102] In particular, the lack of a fully complete picture of the non-radiative and transport losses in perovskite solar cells keeps their efficiencies still away from their predicated theoretical limit.^[101] Therefore, a thorough understanding of the aspects

influencing the strength of non-radiative recombination in such multilayered architecture devices is of mandatory importance. The work presented in this thesis is strongly devoted to the investigation of these mechanisms. Furthermore, important aspects of the working principle of these devices still have to be clarified, such as the origin of the built-in-field and the exact energy alignment between the different layers. This is particularly true for *p-i-n* devices, which currently dominates the tandem research, lack behind their *n-i-p* counterparts in terms of efficiency and stability. Currently, researchers around the world are addressing these problematics in order to exploit the full potential of this class of materials and to achieve stable devices, suitable for a desirable industrial production. Through the years, diverse approaches have been introduced with the purpose of increasing the efficiencies of perovskite solar cells. For instance, several works focused on reducing the energy losses in the devices and consequently increasing the open-circuit voltages (V_{OC}) by using passivating agents^[73,103,104], introducing interlayers^[75,105] or by surface modifications.^[106] Other approaches, instead, focused directly on improving the material quality through compositional engineering^[43,49,107] or by the usage of additives.^[72,108] Finally, work has been devoted to the optimization of the charge transport layers (CTL) by minimizing transport losses or reducing the energetic offset between the layers.^[109,110] On the other hand, various methodologies have been implemented aiming to improve the intrinsic stability of the material, as well as devices. For example, low-dimensional (2D) perovskites,^[19,111,112] or a combination of high and low dimensional structures,^[113,114] have been successfully implemented improving the water and humidity resilience, while also hindering the out-diffusion of volatile organic cations, and finally leading to significantly improved long-term stability.^[115] Other successful approaches allowed for better device stability by implementing self-assembled amphiphilic monolayers (SAMs)^[116–118] or by sandwiching the perovskite between diffusion and water resistant layers^[76,119,120], blocking the penetration of water and oxygen and the diffusion of the organic cation at the same time. The ability of tuning the bandgap the perovskite absorber makes this technology highly applicable for tandem application. Already the classic bandgap of 1.6 eV is a suitable match to be combined with the 1.1 eV bandgap of Si. The combination of the two material allows to exploit almost the full spectrum of the incident photons by absorbing the low energy photons in the perovskite and the high energy photons, which energy would be otherwise lost by thermalization in the Si. Tandem solar cells comprising Si and perovskite have demonstrated outstanding efficiencies in the recent years, at the present exceeding 29%.^[5] The calculated perovskite bandgap to achieve the maximum efficiency in combination with Si, is roughly 1.7 eV, which could be potentially achieved by increasing the Br content in a mixed halide composition. However, these mixtures have shown intrinsic instability due to the demixing of the initial phases and generally higher non-radiative losses.^[35] Currently the community is devoting efforts to understanding thoroughly these intrinsic limitations and optimizing these systems accordingly.^[39] **Chapter 9** will be focused on understanding these phenomena. Additionally, tandem device can be fabricated from all-perovskite absorbers. Specifically, Sn based perovskite here can serve as low bandgap absorber and Pb based perovskite as large bandgap absorber. Recently,

several works focused on the improvement on the low bandgap bottom cell, managing to achieve outstanding results with efficiencies approaching 25%.^[52,53]

1.6 Aim of this work

As perovskite solar cells continue to experience a rapid improvement from different aspects, a more fundamental insights are of imperative importance to completely unlock the full thermodynamic potential of these materials. In particular, this work aims for a deeper understanding of the interfacial non-radiative recombination processes and their influence on the V_{OC} of the solar device and the radiative potential of the neat material. This knowledge is then ultimately used to reduce the non-radiative recombination in actual devices and to improve further their efficiencies. The experimental and theoretical work done as active part of this thesis work is collected from **Chapter 4** to **9**. This work will be essentially divided in two main parts. Firstly, in **Chapter 4, 5** and **6**, we will investigate the non-radiative recombination processes and energy losses in different types of perovskite devices. Here, we extend our understanding on the device physics and on the general working mechanisms of perovskite solar cells. Devices with different transport layers and characterized by different energy losses are investigate with the aim of understanding what are the effects of the recombination at the interfaces on the overall performance of the solar cells. To complete the picture recombination models will be proposed in order to rationalized the types of the losses mechanisms commonly observed. After exploring and understanding in details the physics of perovskite solar cells, in **Chapter 7** and **Chapter 8**, we will move on the actual optimization of the latter by using the knowledge learned in the previous chapters. We will show two examples of effective reduction of non-radiative losses by addressing the interface between the perovskite and the transport layers. After successful surface and interface modification, we will demonstrate non-radiative losses as low as 100 meV from the theoretical thermodynamic limit and generally improved efficiencies exceeding 21%. These two chapter corroborates the understanding achieved in **Chapter 5** and **Chapter 6**, and serves as base for future strategies for device improvement and development. Lastly, in **Chapter 9**, we will investigate in detail some peculiar optoelectronic properties of halide-segregated large bandgap perovskite systems. Also in this case, a recombination model will be provided and a deeper understanding of the physical properties of these systems achieved.

Chapter 2.

2. Theoretical Background

This chapter provides the knowledge to the reader in order to follow what is presented in the following chapters. This theoretical background serves as the base for the models and conclusions presented throughout this work. Part of the content here is related to well-known classic semiconductor physics. Whereas, other parts describe important relations and conclusions for perovskite solar cells, published in literature during the last decade.

2.1 Solar cells working principles

In a semiconductor absorber, when irradiated with light, the incident photons with energy equal or larger than the bandgap are absorbed exciting electrons from the valence band to the conduction band, leaving behind a positive carrier. The creation of an electron-hole pair by absorption of a photon, in a solar cell device, generates a photocurrent and a photovoltage, and this is called photovoltaic effect. The detailed description of this phenomena will be presented in the following sections of this chapter. However, here we will limit the discussion to the macroscopic effect of this phenomena on a solar cell device. In order produce electrical work, the photogenerated charges have to be extracted to an external circuit by a cathode and an anode. The total flow of carriers J_{tot} in the solar cell device can be, for now, approximated to the classic Shockley diode equation

$$J_{\text{tot}} = J_0 \left[\exp\left(\frac{qV}{k_B T}\right) - 1 \right] - J_G \quad \text{Eq.2.1.1}$$

where here the terms J_G is added to account for the current generated by the photovoltaic effect and J_0 is the recombination current in the dark and with no bias applied. **Eq.2.1.1** generally describes the relation between current and voltage ($J - V$) of photovoltaic device.

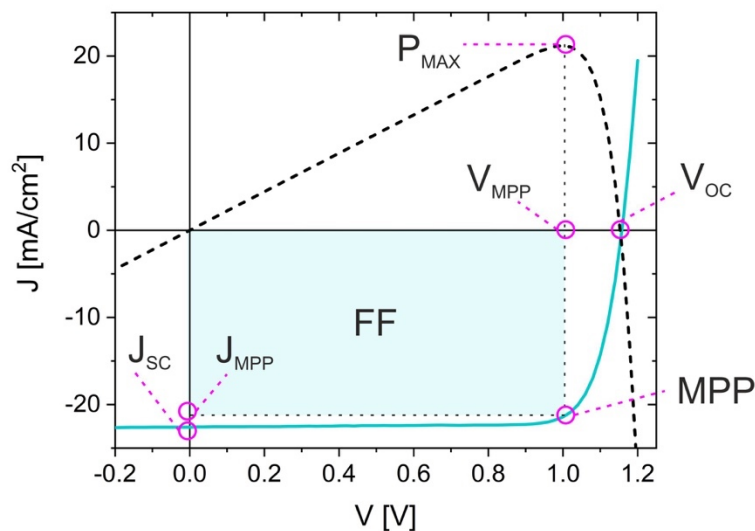


Figure 2.1.1: Exemplary perovskite solar cell experimental J - V characteristics with all parameters highlighted. In blue, solar cell J - V trace and in dotted black, the calculated power output.

The $J - V$ characteristics of a solar cell defines a few essential parameters used for efficiency calculation. Firstly, the short-circuit current is defined as the current flowing in the device at $V = 0$. In the ideal case, this current is equal to the generation current in the device and **Eq.2.1.1** will become

$$J_{SC} = J_{tot} = -J_G \quad \text{Eq.2.1.2}$$

In this situation, the conduction and valence bands in the device are tilted and the internal field of the solar cells is large, leading to efficient extraction of all photogenerated charges.

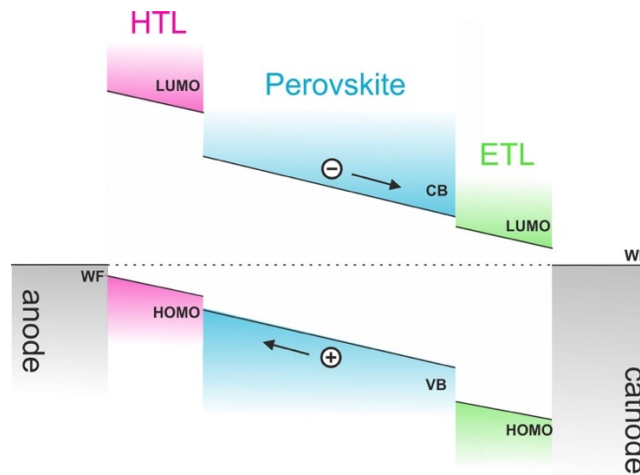


Figure 2.1.2: Schematic energy diagram of an exemplary perovskite solar cell at short circuit condition.

Similarly, the second important parameter is defined by the voltage in the device when zero net current is flowing in the device. In this situation the solar cell is at open circuit condition and the voltage is called open circuit voltage V_{OC} . In this case, $J_{tot} = 0$ and **Eq.2.1.1** will become

$$V_{OC} = \frac{k_B T}{q} \ln \left(\frac{J_G}{J_0} + 1 \right) \quad \text{Eq.2.1.3}$$

In this situation, the conduction and valence bands in the device are flat and the internal field of the solar cells is at minimum and the internal voltage at maximum.

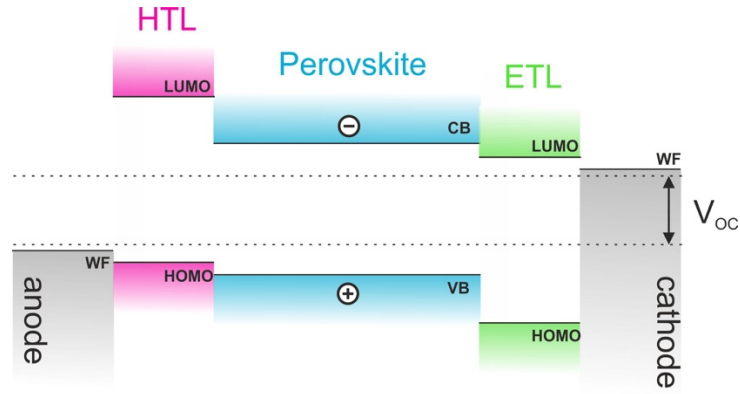


Figure 2.1.3: Schematic energy diagram of an exemplary perovskite solar cell at open circuit condition.

Generally, the power output of a solar cell is given by the product of J and V . Although, the J_{SC} and the V_{OC} represent the maximum current and voltage achievable, the power at either of these points is zero. This power output has a maximum at a specific current and voltage location, which is denoted a maximum power point (MPP). The exact values are then defined by the J_{MPP} and the V_{MPP} . In order to define the real efficiency of the solar cells a new parameter has to be introduced. The fill factor (FF) is defined as the ratio of the maximum power point to the product of J_{SC} and V_{OC}

$$FF = \frac{V_{MPP} \cdot J_{MPP}}{V_{OC} \cdot J_{SC}} \quad \text{Eq.2.1.4}$$

Graphically, this can be depicted as the “squareness” of the $J - V$ curve and it is essentially the area of the largest rectangle that can be subtended under the $J - V$ curve. As a consequence, the FF is generally influenced by the extraction behavior in the device in the presence of small fields, in the proximity of the V_{OC} . Practically, the higher the series resistance in the device, the lower the FF will be. Thereby, the power conversion efficiency (PCE) of the solar cell device can be defined as the ratio of the maximum power output and the power input P_{input} follow

$$PCE = \frac{V_{OC} \cdot J_{SC} \cdot FF}{P_{input}} \quad \text{Eq.2.1.5}$$

The standard input power used for the solar cell efficiency calculation is $P_{input} = 100 \text{ mW/cm}^2$.

2.2 Free Carriers in a Semiconductor and quasi-Fermi Level Splitting

The density of electrons in a semiconductor dn_e with a given energy E_e within an energy interval dE_e is generally described by the density of states $D_e(E_e)$ and the distribution function describing the occupation of electron states $f_e(E_e)$. Thereby, this density can be defined as such

$$dn_e(E_e) = D_e(E_e)f_e(E_e)dE_e \quad \text{Eq.2.2.1}$$

Here, the density of states $D_e(E_e)$ in a crystalline semiconductor depends on the number of states N_e in the conduction band per volume V which are available for electrons between a given energy E_e and the conduction band minimum E_C

$$N_e(E_e) = \frac{8\pi V(2m_e^*)^{3/2}}{3h^3} \cdot (E_e - E_C)^{3/2} \quad \text{Eq.2.2.2}$$

Then, $D_e(E_e)$ as the number of electron states per volume V and per energy interval at a given energy E_e is given by

$$D_e(E_e) = \frac{1}{V} \frac{dN_e(E_e)}{dE_e} = 4\pi \left(\frac{2m_e^*}{h^2} \right)^{3/2} \cdot (E_e - E_C)^{1/2} \quad \text{Eq.2.2.3}$$

Because electrons are Fermions, the occupation function $f_e(E_e)$ for electrons in steady state at a given energy E_e follows the Fermi-Dirac statistic

$$f_e(E_e) = \frac{1}{\exp[(E_e - E_F)/k_B T] + 1} \quad \text{Eq.2.2.4}$$

Here, E_F is the Fermi level. For a condition where $E_e - E_F > k_B T$, combining **Eq. 2.2.3** and **Eq. 2.2.4** and integrating over the electron energy, the density of free electrons over all energies in the conduction band can be calculated as follow

$$\begin{aligned} n_e(E_e) &= 2 \left(\frac{2\pi m_e^* k_B T}{h^2} \right)^{3/2} \cdot \exp \left[\frac{-(E_C - E_F)}{k_B T} \right] \\ &= N_C \cdot \exp \left[\frac{-(E_C - E_F)}{k_B T} \right] \end{aligned} \quad \text{Eq.2.2.5}$$

where N_C is defined as the effective density of states. Analogously, using the same degree of approximation used for electrons, we define the hole density as such

$$n_h(E_h) = \int_{-\infty}^{E_V} D_h(E_h)[1 - f_h(E_h)]dE_h = N_V \cdot \exp\left[\frac{-(E_F - E_V)}{k_B T}\right] \quad \text{Eq.2.2.6}$$

One important relation is given by the product of electron and hole density

$$n_h n_e = N_V N_C \cdot \exp\left[\frac{(E_C - E_V)}{k_B T}\right] = n_i^2 \cdot \exp\left[\frac{E_G}{k_B T}\right] \quad \text{Eq.2.2.7}$$

where the intrinsic carrier density n_i is related solely to the effective densities of states in the conduction and valence band. In a solar cell, when irradiated by the sun, an additional population of electrons and holes is generated by the absorption of photons. Initially, electron and hole pairs are generated in the form of Coulombically bound excitons. However, in a semiconductor with large dielectric constant as metal halides perovskites, at room temperature excitons are unstable and electron and holes can be considered as free carriers. Under light irradiation, given that now the electron density in the conduction band is larger than in the dark, the Fermi energy describing this population must be closer the conduction band, compared to the intrinsic Fermi level position in dark condition. At the same time, also the hole density in the valence band will be larger than in the dark and therefore, the Fermi energy describing this population must be closer to the valence band. Consequently, to describe such a picture, two Fermi distributions must be used, one quasi-Fermi level for electron E_{Fe} in the conduction band and one quasi-Fermi level for holes (missing electrons in the valence band), E_{Fh} . Consequently, the electron and hole densities under light are now defined as

$$n_e = N_C \cdot \exp\left[\frac{-(E_C - E_{Fe})}{k_B T}\right] \quad \text{Eq.2.2.8a}$$

$$n_h = N_V \cdot \exp\left[\frac{-(E_V - E_{Fh})}{k_B T}\right] \quad \text{Eq.2.2.8b}$$

with their product being equal to

$$\begin{aligned}
n_e n_h &= N_C N_V \cdot \exp\left[\frac{-(E_C - E_V)}{k_B T}\right] \exp\left[\frac{(E_{Fe} - E_{Fh})}{k_B T}\right] \\
&= n_i^2 \cdot \exp\left[\frac{(E_{Fe} - E_{Fh})}{k_B T}\right]
\end{aligned}
\tag{Eq.2.2.9}$$

In this work, we will refer to the quantity $E_{Fe} - E_{Fh}$ as quasi-Fermi level splitting, abbreviated as QFLS. The tremendous importance of this quantity is related to the fact that it can directly describe the population of the free carriers in the absorber. Moreover, if the number of electron-hole pairs is increased upon illumination by dN , this is associated to an increase in the free energy of the semiconductor according to:

$$dF = dF_e + dF_h = (\eta_e + \eta_h)dN = (E_{Fe} - E_{Fh})dN \tag{Eq.2.2.10}$$

Here, η_e and η_h is the electrochemical potential of electrons and holes, respectively. **Eq. 2.2.10** highlights the equality between the electrochemical potential and the quasi-Fermi level, which is connected with the change in entropy of the system. The full derivation of this relation is not of the interest of this work. The electrochemical energy of an electron-hole pair is the sum of their specific electrochemical potential. If the carrier populations are considered at the same position, the two carrier types will have the same electrical potential. Being the electrochemical potential the sum of electrical ($q\phi$) and chemical (μ) potential the energy of an electron-hole pair with both charges at the same position is equal only to the sum of their chemical potentials

$$\eta_e + \eta_h = \mu_e + q\phi + \mu_h - q\phi = \mu_e + \mu_h \tag{Eq.2.2.11}$$

Combining **Eq. 2.2.10** and **Eq. 2.2.11** we can now rewrite **Eq. 2.2.9** as follow

$$n_e n_h = n_i^2 \cdot \exp\left[\frac{(\mu_e + \mu_h)}{k_B T}\right] = n_i^2 \cdot \exp\left[\frac{\text{QFLS}}{k_B T}\right] \tag{Eq.2.2.12}$$

This equation relates the QFLS to the free energy that can be delivered by a semiconductor upon the release of an electron-hole pair. Moreover, as the electrical energy a solar cell can deliver to the outside per electron-hole pair is qV , the splitting of the quasi-Fermi levels $E_{Fe} - E_{Fh}$ at the external contacts of a solar cell is equal to qV . This, finally, defines the open circuit voltage of the solar cell when no net current is flowing the device

$$\begin{aligned}
qV_{OC} &= E_{Fe} - E_{Fh} = (E_C - E_V) + k_B T \cdot \ln\left(\frac{n_e(V_{OC})n_h(V_{OC})}{N_C N_V}\right) \\
&= E_G + k_B T \cdot \ln\left(\frac{n_e(V_{OC})n_h(V_{OC})}{N_C N_V}\right)
\end{aligned}
\tag{Eq.2.2.13}$$

Importantly, from **Eq. 2.2.13** it is intuitive that the V_{OC} is described by the QFLS and it will always be smaller than E_G , since $n_e n_h < N_C N_V$. Moreover, the dependence on the electron and holes density makes it clearly dependent on the illumination intensity. The stronger the illumination intensity, the larger the number of photogenerated free carriers and the larger the V_{OC} .

2.3 Drift and Diffusion Currents

Once free carriers are generated in the conduction and valence band, drift and diffusion processes will drive these carriers across the semiconductor generating a current. The motion of these charge is dependent on the electric field E across the material and the gradient of carrier density ∇n . Therefore, we can exemplarily express the total electron current J_e as such a sum of the drift and diffusion contribution

$$J_e = J_{\text{drift},e} + J_{\text{diff},e} = qn_e\mu_e E + qD_e\nabla n_e \tag{Eq.2.3.1}$$

We will now derive a form for the contribution of both components, which allow to relate the current densities to the quasi-Fermi levels. Firstly, the electric field across the layer can be express as the gradient of the electrostatic potential $q\varphi$, therefore the resulting drift current for electrons can be expressed as such

$$J_{\text{drift},e} = qn_e\mu_e\nabla(q\varphi) \tag{Eq.2.3.2}$$

Then, to treat the diffusion current, now we express the chemical potential of electrons as function of carrier density and electron affinity χ_e

$$\mu_e = \chi_e + k_B T \ln\left(\frac{n_e}{N_C}\right) \tag{Eq.2.3.3}$$

now expressing in form of n_e

$$n_e = N_C \exp\left(\frac{\mu_e - \chi_e}{k_B T}\right) \tag{Eq.2.3.4}$$

Using **Eq.2.3.4**, the variation in carrier density across the space can be expressed as such, given that only μ_e depend on x

$$\frac{dn_e}{dx} = \frac{n_e}{k_B T} \frac{d\mu_e}{dx} \quad \text{Eq.2.3.5}$$

Combining now the **Eq.2.3.5**, with the diffusion components of the current expressed in **Eq.2.3.1**, we obtain

$$J_{\text{diff},e} = qD_e \frac{dn_e}{dx} = \frac{qD_e n_e}{k_B T} \frac{d\mu_e}{dx} \quad \text{Eq.2.3.6}$$

The diffusion coefficient D_e is defined by the Einstein relation, where we expressed the mobility of electrons as b_e in order not to be confused with chemical potential

$$D_e = \frac{k_B T}{q} b_e \quad \text{Eq.2.3.7}$$

Combining with **Eq. 2.3.6**, this then results in

$$J_{\text{diff},e} = b_e n_e \frac{d\mu_e}{dx} \quad \text{Eq.2.3.8}$$

Combining now equation **Eq. 2.3.2** and **Eq. 2.3.8** with **Eq.2.3.1** we obtain

$$J_e = n_e b_e \nabla(q\varphi) + n_e b_e \nabla(\mu_e) = n_e b_e \nabla(q\varphi + \mu_e) \quad \text{Eq.2.3.9}$$

Using **Eq.2.2.10** and **Eq.2.2.11** we rewrite **Eq.2.3.9** as follow

$$J_e = n_e b_e \nabla(\eta_e) = n_e \mu_e \nabla(E_{Fe}) \quad \text{Eq.2.3.10}$$

Analogously, the same approach is valid for holes. Thereby, the total current in devices with contribution of both electrons and holes then result in

$$J_{\text{tot}} = n_e \mu_e \nabla E_{Fe} + n_h \mu_h \nabla E_{Fh} \quad \text{Eq.2.3.11}$$

This relation will define an essential relation which will constitute the base of the drift-diffusion simulations treated in this work.

2.4 Theoretical Efficiency

The first limitation that a solar cell is encountered when treated as heat engine transforming thermal energy into electrical work. The efficiency of this process is set by the thermodynamic limitation of heat exchange described using an ideal Carnot engine. The absorption efficiency of a black body absorber irradiated by the sun, where absorption and emission occur at the same solid angle, essentially depends on the temperature T of the two bodies and it is maximized for a low temperature of the absorber T_A

$$\eta_{\text{abs}} = 1 - \frac{\Omega_{em} T_A^4}{\Omega_{abs} T_S^4} \quad \text{Eq.2.4.1}$$

Here, Ω_{em} and Ω_{abs} are the solid angles of light absorption and emission, respectively. In the ideal case, $\Omega_{em} = \Omega_{abs}$. Now if the heat produced by the absorption process is extracted and conducted through an ideal heat engine, we can define the maximum thermodynamic efficiency as

$$\eta_{\text{th}} = \eta_{\text{abs}} \cdot \eta_{\text{Carnot}} = \left(1 - \frac{T_A^4}{T_S^4}\right) \left(1 - \frac{T_0}{T_A}\right) \quad \text{Eq.2.4.2}$$

This equation requires for a low T_A for efficient absorption which is in contrast to the requirements for a high Carnot efficiency in the right part of the equation. The ideal combination of these temperatures can still set a maximum efficiency for the conversion of solar heat energy at 82% for an absorber with $T_A = 2500$ K with the given temperature of the sun $T_S = 5800$ K. The impracticability of this limit is rather clear. However, this relation highlights the great potential of solar energy conversion due to the elevated temperature of the sun. Notably, one main problem is related to the fact that, $\Omega_{em} \gg \Omega_{abs}$, since radiation enters through a small cone while emission is into the full half space.

A true efficiency limit for operational solar cells is identified with the detailed balance principle, firstly theorized by Shockley and Queisser (S.Q.).^[121] To derive the maximum efficiency of an idealized solar cell it necessary to consider three main assumptions: 1) perfect absorption of photons with energy greater than the threshold energy gap E_G and each photon creates an electron-hole pair, 2) perfect collection of the photogenerated carriers at the electrodes, assuming infinite electron and hole mobility in the absorber, 3) band-to-band radiative recombination of free carriers is the only

recombination process allowed. Within these boundaries, the only parameters effectively influencing the solar cells are the E_G , temperature T , and the spectrum and intensity of the incident light. Given assumption 1), the absorption of photons is described by a step function where the absorptivity $\alpha(E)$ is zero for energies below E_G and unity for energies greater than E_G . Therefore, we can now define the maximum short circuit current J_{SC}^{\max} in relation to the sun spectrum ϕ_{sun} as follow

$$J_{SC}^{\max} = q \int_{E_G}^{\infty} \phi_{\text{sun}}(E) dE \quad \text{Eq.2.4.3}$$

On the other hand, if the solar cell is in the dark and no voltage is applied, it's in thermal equilibrium with its environment. According to detailed balance, every process involved in establishing this thermal equilibrium has to be in equilibrium with the inverse process at the same rate. Kirchhoff derived a thermodynamic law for the thermal equilibrium condition of a grey body which states that the absorptivity $a(h\nu)$ must be equal to the emissivity $e(h\nu)$ of the absorber at any photon energy. The implication of this important law is that, in the dark, the amount of black body radiation that is absorbed must be equals to be amount of radiation emitted if the absorber and the device are in thermal equilibrium. We make use of Wülfel's generalized Planck law to described the non-thermal emission of the black body in terms of photon flux as follow

$$\phi_{\text{BB}} = \frac{1}{4\pi^2 \hbar^3 c^2} \frac{E^2}{\exp\left(\frac{E}{k_B T}\right) - 1} \quad \text{Eq.2.4.4}$$

According to Kirchhoff's law, the fraction of ϕ_{BB} absorbed by the solar cell in the dark must be reemitted given that thermal equilibrium condition is established and no work is produced. This emission has to occur via recombination of photogenerated electron-hole pairs, which generates a recombination current J_R . Considering assumption 3), the only recombination mechanism allowed is the radiative recombination of free carriers which, in thermal equilibrium, has to be equal to the photocurrent generated by the absorption of the ϕ_{BB} . Within the boundary of the step function absorption, we can now define the minimum radiative current $J_{0,\text{rad}}$, which a solar cell produces in the dark due the absorption of the ϕ_{BB} allowed as function of the E_G as in described in assumption 1)

$$q\phi_{\text{dark,em}} = J_{0,\text{rad}} = q \int_{E_G}^{\infty} \phi_{\text{BB}}(E) dE \quad \text{Eq.2.4.5}$$

The importance of this recombination current originates from the fact that this recombination is responsible for setting the upper limit of the maximum V_{OC} potentially achievable in a solar cell for a given E_G .

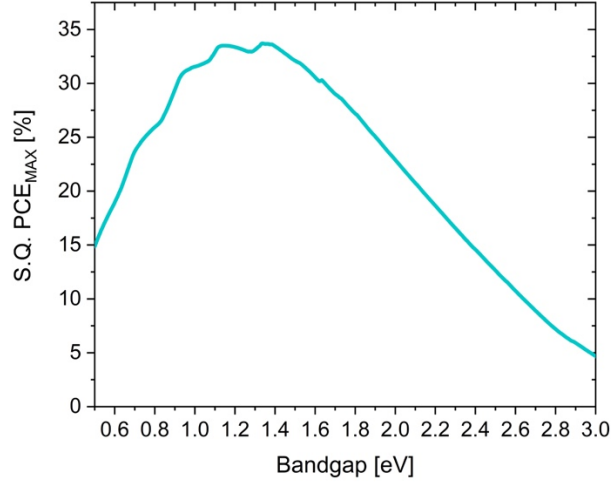


Figure 2.4.1: Calculated theoretical Shockley-Queisser power conversion efficiencies as function of the bandgap of the absorber.

We express now the Shockley ideal diode equation for a solar cell under illumination in terms of dark recombination current J_0 and generation due to the absorption of sun photons current J_G as follow

$$J = J_0 \left[\exp\left(\frac{qV}{k_B T}\right) - 1 \right] - J_G \quad \text{Eq.2.4.6}$$

Within the S.Q. discussion, J_0 is equal to dark radiative current $J_{0,\text{rad}}$ since only radiative processes are allowed. Thereby, we can now express the voltage V in **Eq.2.4.6** under open circuit condition in the case of only radiative processes

$$V_{OC,\text{rad}} = \frac{k_B T}{q} \ln\left(\frac{J_G}{J_{0,\text{rad}}}\right) \quad \text{Eq.2.4.7}$$

The radiative voltage $V_{OC,\text{rad}}$ set the maximum voltage achievable for a given E_G in a solar cell in which only radiative recombination processes are taking place. Consequently, the maximum FF achievable can be approximated using the following relation, as function of the radiative reduced voltage $U_{\text{rad}} = V_{OC,\text{rad}}/k_B T$, as follow

$$FF^{\max} = \frac{U_{\text{rad}} - \ln(1 + U_{\text{rad}})}{1 + U_{\text{rad}}} \quad \text{Eq.2.4.8}$$

As we will discuss in the next chapter, these theoretical limits are far from the realistic output achieved in real life operational conditions.

2.5 Practical Limitations

In real life, the S.Q. conditions are not entirely fulfilled and the violation of its assumptions results in a limitation of the efficiencies that can be reached by the solar cell. For example, the violation of assumption 1) has as main consequence the reduction of the short circuit current J_{SC} potentially achievable. First of all, in a real absorber, the absorption onset cannot be described by a step function, but, on the contrary, it will depend on the distribution of states in the proximity of the band edge. Moreover, solar cells generally comprehend the implementation of different layers in addition to the absorber. Each of this layer is characterized by a different diffractive index, which could cause reflection of the incident light and limiting the amount of absorbed photons from the absorber in specific regions of the spectrum. Overall, the sum of these effects will result in a lower J_{SC} and consequently a lower efficiency. Furthermore, the violation of assumption 1) is connected with the presence of sub-band gap states, which implies that there is a certain degree of absorption of photons also for energies below E_{G} . As explained above, this directly translates in a higher $J_{0,\text{rad}}$ and a consequent lower implied theoretical $V_{\text{OC},\text{rad}}$. Assumption 2), which implies perfect extraction of the photogenerated carriers, is likely to be violated as well in real life scenarios. A certain degree of losses due to inefficient charge extraction and Ohmic series resistance in the complete solar cell device, will introduce transport limitations, which eventually will limit the efficiency of the device. To some extent, the violation of assumption 3) is strongly visible on the FF of a real device. Finally, assumption 3), which allows only radiative recombination processes, is always violated in a realistic absorber. In fact, in any semiconductor, in parallel to radiative recombination, there will be always a significant presence of non-radiative recombination processes. The implication of this is that the density of free carriers in the device is effectively reduced by this additional recombination processes and the V_{OC} limited to lower values. In the interest of this work, we will focus on discussing in depth the violation of assumption 2) and 3) in a real-life scenario.

2.5.1 Recombination Losses

In crystalline semiconductors, like perovskite solar cells, there will always be certain number of defects and impurities in the lattice, which will act as centers for non-radiative recombination. At these locations, there are available energy states which extend inside the bandgap of the material and are able to capture the free carriers

present in the conduction and valence bands. This event will eventually mediate a non-radiative recombination of charges. The direct consequence of lowering the density of free carriers in the conduction and valence band is the limitation of the splitting of the quasi-Fermi levels $E_{Fe} - E_{Fh}$ and consequently the V_{OC} .

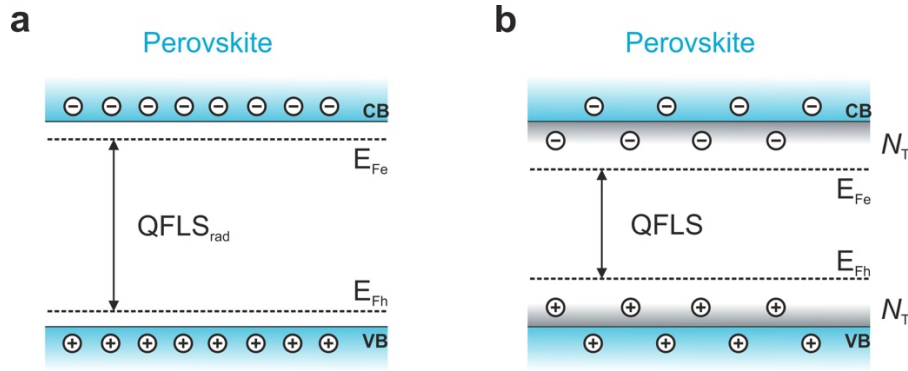


Figure 2.5.1.1: Schematic representation of electrons and holes in the conduction and valence bands respectively, and the respective QFLS in a perovskite absorber in the case of: a) no impurities and radiative limit conditions and b) realistic condition of reduction of free carriers and QFLS due to carrier trapping by defect states N_T present in the bandgap.

Generally, band-to-band radiative recombination processes can be defined as second order (or bimolecular), since the involvement of two carriers is mandatory and the rate of recombination depends quadratically on the carrier density for $n_e = n_h$

$$-\frac{dn}{dt} = R = k_2 n_e n_h = k_2 n_e^2 \quad \text{Eq.2.5.1}$$

On the other hand, the non-radiative recombination mediated via trap states of density N_T is defined as a first order process (or monomolecular) and its rate of recombination depends linearly on the carrier density

$$-\frac{dn}{dt} = R = k_1 n_e N_T \propto k_1 n_e \quad \text{Eq.2.5.2}$$

Therefore, in a realistic picture, the total recombination rate relevant for moderate carrier densities will be

$$-\frac{dn}{dt} = R = k_1 n_e N_T + k_2 n_e^2 \quad \text{Eq.2.5.3}$$

The strength of the contribution of first and second order strongly depends on the strength of their respective recombination coefficient k_1 and k_2 . In perovskite solar cells, it has been found that first order non-radiative processes are of great importance over the total recombination of charges.^[122] Usually, small values of external $k_2 = 10^{-10} - 10^{-11} \text{ s}^{-1}$ have been reported, while much larger values of $k_1 = 10^6 - 10^8 \text{ s}^{-1}$ are commonly observed.^[123–125] Where k_2 is mostly an intrinsic property of the material, k_1 is strongly influenced by the degree of defect present in the material. In order to understand properly what are the actual parameter influencing this type of recombination we need to relate to Shockley-Read-Hall (SRH) theory.^[126]

First of all, the nature of this impurities can be categorized as acceptor trap states, when a state is negatively charged if occupied by an electron, or donor trap state, when a state is positively charged if unoccupied. As such, a preferential trapping of electrons or holes can occur. Besides the density of these trap states, the ability of the latter to capture the surrounding free carriers is of significant importance for the effectiveness of this processes. This is called capture coefficient C . Notably, C depends on the capture cross section σ and the thermal velocity of the carrier v_{th} , as $C = \sigma v_{\text{th}}$. Moreover, after a trapping event takes place, there is the probability for the trapped carrier to escape the trap, if the energy involved in this process is not too large. The detrapping rate is define as β and become more effective when the trap location is in the proximity of the conduction or valence band, and the energy costs for detrapping is comparable to $k_B T$. The SRH formalisms, which full derivation is not of the interest of this work, allows to express the recombination rate in terms of the above-mentioned parameters

$$-\frac{dn}{dt} = R_{\text{SRH}} = \frac{C_e C_h (n_e n_h - n_i^2)}{[C_e n_e + \beta_e] + [C_h n_h + \beta_h]} \cdot N_T \quad \text{Eq.2.5.4}$$

If we are in a situation of an intrinsic semiconductor, with the energy of impurities E_{imp} located at middle of the bandgap, the detrapping rate is negligible and at the recombination site $n_e = n_h$ and $C_e = C_h$, the SRH recombination rate in **Eq.2.5.4** can be simplified into

$$-\frac{dn}{dt} = R_{\text{SRH}} = \frac{C_e^2 n_e^2}{2[C_e n_e]} \cdot N_T = \frac{C_e n_e}{2} \cdot N_T \propto n_e \quad \text{Eq.2.5.5}$$

Importantly, in a perovskite absorber, defects can be located at different positions. It has been found that a larger concentration of impurities is located at the grain boundaries and at the surface of the material, mostly due to a wrong termination of the crystal lattice. To disentangle the precise location in the absorber where most of the recombination takes place is a task of great difficulty and it is very hard to safely address the bulk, the grain boundaries or the surface as main source of non-radiative

recombination separately. However, for the sake of this work, the precise location of recombination inside the perovskite absorber is not essential. Thereby, we will refer to all non-radiative recombination processes occurring in the perovskite absorber, generally, as bulk recombination. This is with the aim distinguishing the latter from other recombination of processes taking place in the actual solar cell device. Perovskite materials are able to achieve rather forgiving non-radiative recombination rates, limiting the amount of energy losses present in the material itself. However, given that in perovskite solar cells CTLs has to be implemented, additional recombination may occur across the new interfaces between perovskite and CTLs.^[122,127–130] Importantly, at these interfaces different types of recombination events could possibly take place, as presented in **Figure 2.5.1.2**. For examples, the trap states located at the interface could simply mediate the non-radiative recombination of carriers contained in the perovskite and carriers present in the CTL **(1)**. Moreover, electrons (holes) in the perovskite could in principle manage to recombine with holes (electrons) in the HTL (ETL) **(2)**. Furthermore, if the selectivity of the transport layers is not sufficiently good, some carriers could pass across the wrong interface, e.g. holes (electrons) in ETL (HTL) and recombine here recombine with the carriers of opposite sign **(3)**.

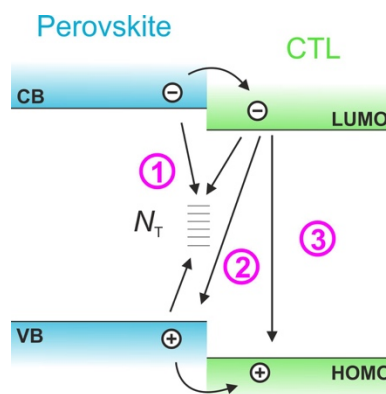


Figure 2.5.1.2: Schematic representation of different possible recombination events happening at the interface between the perovskite and a generic charge transport layer.

Overall, also in this case, the full understanding of these recombination processes across the interfaces has not yet been achieved. Therefore, addressing one or the other mechanism independently is not possible. However, in term of energy losses and recombination rates, the sum of all these possible processes is experimentally measurable and we will refer to them, generally, as interface recombination. The strength of interface recombination can be described by the interface recombination velocity S which is defined as such

$$S = \sigma v_{th} N_T \quad \text{Eq.2.5.6}$$

and it depends on the capture cross section σ , the thermal velocity of the carrier v_{th} and the density of traps at the interface N_T . The investigation of this particular type of non-radiative recombination will be at the center of the core work of this thesis. Furthermore, an additional recombination mechanism can potentially occur in semiconductors. This recombination type takes the name of Auger recombination. In this type of recombination one electron in the conduction band can recombine with a hole in valence band and the released energy given to a third-particle electron in the conduction band, which is consequently excited to a higher energetic state. This electron, successively, can either thermalize or, if close enough to the surface, leave the conduction band.^[24] In the former case, the energy set free upon recombination is lost and the recombination is, therefore, non-radiative. Thereby, this type of recombination involves three different carriers and it is considered as a third order recombination. Indeed, the recombination rate can be simplified as a cubic dependence on the carrier density as such

$$-\frac{dn}{dt} = R = k_3 n_e^3 \quad \text{Eq.2.5.7}$$

Although, the cubic dependence on the carrier density might suggest a large contribution of this recombination processes on the total recombination, the recombination constant k_3 in perovskite is usually as low as $k_3 = \sim 10^{-28} \text{ cm}^6 \text{ s}^{-1}$.^[125] Therefore, the effect of this recombination process can be considered irrelevant unless very high carrier densities are reached or a high degree of doping is present in the system. Since neither of these two conditions is reached in the framework of this thesis work, the discussion of this negligible recombination processes will be intentionally avoided.

2.5.2 Transport Losses

As briefly mentioned above, additionally to the non-radiative energy losses, in a real device also the transport of carriers through the actual device can constitute a source of limitation in terms of efficiency. These types of losses are essentially connected to the ability of extracting the photogenerated carriers from the absorber to the external circuit and to the overall Ohmic series resistance in the complete solar cell device. To better understand the limitation that can occur on the current-voltage characteristic of a solar cell, we rewrite **Eq.2.4.6** adding a new term which account for the series resistance R_s

$$J = J_0 \left[\exp\left(\frac{qV - JR_s}{k_B T}\right) - 1 \right] - J_G \quad \text{Eq.2.5.8}$$

This new term comprehends the effects of the movement of current through the absorber and through the additional layers, the contact resistance between the transport layers and the metal contacts, and the resistance of the contacts themselves.

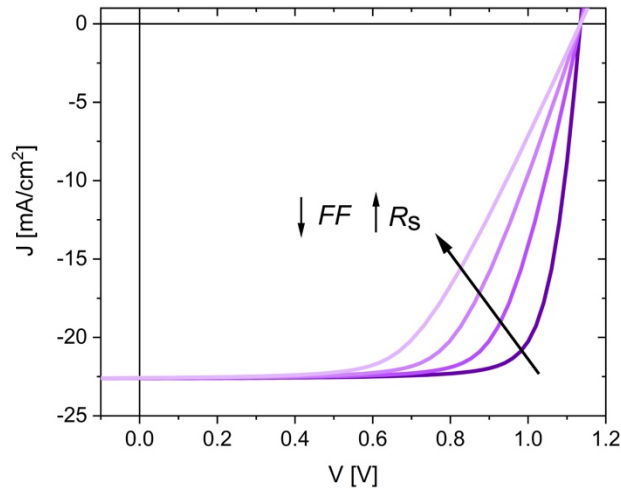


Figure 2.5.2.1: Drift-diffusion simulation of a series of J - V curves representing an exemplary perovskite solar cell with increasing series resistance.

Generally, these limitations could originate, for example, from low carrier mobilities in the absorber or poor transport across the different layers. Perovskite materials are commonly characterized by high carrier mobilities in range of $1 - 10 \text{ cm}^2/\text{s}$ with a diffusion length in the range of microns. On the other hand, the organic transport layers commonly used in actual devices are characterized by carrier mobilities order of magnitude lower, in the range of $10^{-5} - 10^{-2} \text{ cm}^2/\text{s}$. Clearly, it is likely that, commonly, in this type of devices the majority of the transport limitation originates from the multilayered stack architecture rather than the absorber material itself. Moreover, how effectively charge can move across one or the other layer can have a significant impact on this type of losses. We exemplarily show in **Fig. 2.5.2.1** how increasing R_s in a typical perovskite solar cell device can effectively decrease the FF and limit the overall performance. An additional type of resistance which, on the contrary, must be maximized in the solar cell device is the shunt resistance R_{sh} . This term represents the resistance for the photogenerated charges to flow in a current path parallel to solar cell junction. Such an alternative path can reduce the amount of current flowing in the solar cell and it can additionally reduce the voltage. These effects are more pronounced at low light intensity regime, since the photogenerated current is smaller, and at low voltages, where the driving force for charge extraction is lower. It is trivial that these effects must be minimized by an effectively large R_{sh} . Low shunt resistance regions in a solar cell can originate mostly from imperfections during the fabrication procedure, e. g. inhomogeneous coverage of some of the layers or pinholes, which create direct contact points between the electrodes. We can now add this term to **Eq.2.5.8** as follow

$$J = J_0 \left[\exp\left(\frac{qV - JR_S}{k_B T}\right) - 1 \right] - J_G - \frac{V - R_S}{R_{Sh}} \quad \text{Eq.2.5.9}$$

We will now show the effect of lowering the shunt resistance in typical perovskite solar cells for a fixed R_S . Also in this case, as evident from **Fig. 2.5.2.2** the deviation from ideality mainly affects the FF , which is decreased by decreasing R_{Sh} .

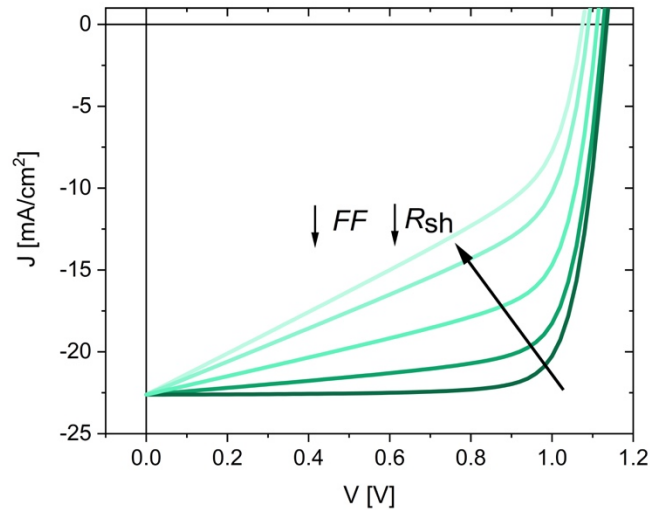


Figure 2.5.2.2: Drift-diffusion simulation of a series of J - V curves representing an exemplary perovskite solar cell with decreasing shunt resistance.

Note that now, **Eq.2.5.9** represent the Shockley diode equation for a real-life solar cell, where most of the deviation from the ideal condition are considered. What is missing here a term which account for the presence of non-radiative losses. This will be discussed below in **Section 2.7**

2.6 From Photoluminescence Efficiencies to quasi-Fermi Level Splitting

As explained in **Section 2.2**, the difference between $E_{F,e}$ and $E_{F,h}$ is the QFLS. While the absolute locations of $E_{F,e}$ and $E_{F,h}$ are generally not accessible, the QFLS can be accessed directly by the measurement of the quantum efficiency of photoluminescence (PLQY) and the external quantum efficiency of electroluminescence (EQE_{EL}) measurements.^[121,131–134] Importantly, measuring the QFLS in an efficient approach for quantifying recombination losses and deviation from the theoretical S.Q. prediction of an absorber or solar cell device. This methodology has been proven to be an efficient approach for quantifying recombination losses in the neat perovskite, multilayer assemblies or even complete perovskite solar cells.^[127,135–137] This methodology relies on the use of the reciprocity between absorption and emission of radiation, based on

Kirchhoff's law and Würfels generalized Planck law for PL, or the optoelectronic reciprocity firstly introduced by Rau for EL.^[138] In the interest of this work, the following discussion will focus entirely on the use of the PLQY. As shown in **Section 2.4**, the $V_{OC,rad}$ is calculated by assuming only radiative recombination processes, which translate in a case where the PLQY (or EQE_{EL}) is equal to unity. Considering that all the photoluminescence stems from the radiative recombination of free charges in the perovskite, the quantum yield of the PL radiation is the ratio between the emitted photon flux ϕ_E from free carrier recombination on the perovskite and the absorbed photon flux ϕ_A or, equivalently, as the ratio between the total radiative recombination current J_{rad} and the generation current J_G .

$$PLQY = \frac{\phi_E}{\phi_A} = \frac{J_{rad}}{J_G} = \frac{J_{rad}}{J_R} = \frac{J_{rad}}{J_{rad} + J_{non-rad}} \quad Eq.2.6.1$$

Therefore, in a realistic scenario where also non-radiative events take places, the PLQY will always be smaller than unity. At V_{OC} conditions, the net current flowing in the device is zero and J_G is equal to the recombination current J_R , which consists in the radiative (J_{rad}) component and all non-radiative recombination processes ($J_{non-rad}$).

To take a step further, now we relate now **Eq.2.2.12** to the radiative recombination current $J_{rad} = edR = ed \cdot kn^2$, which is the current originated exclusively from bimolecular radiative recombination in the perovskite, and the dark radiative recombination current $J_{0,rad} = edR_0 = ed \cdot kn_i^2$, coming from S.Q. theory. The important resulting expressing relates the QFLS of the material of the radiative current J_{rad}

$$J_{rad} = J_{0,rad} \cdot e^{\left(\frac{QFLS}{k_B T}\right)} \quad Eq.2.6.2$$

Furthermore, this relation can be combined with **Eq.2.6.1** to arrive at a direct relation between the PLQY and the QFLS

$$\begin{aligned} QFLS &= k_B T \cdot \ln\left(\frac{J_{rad}}{J_{0,rad}}\right) \\ &= k_B T \cdot \ln\left(PLQY \frac{J_G}{J_{0,rad}}\right) = QFLS_{rad} + k_B T \cdot \ln(PLQY) \end{aligned} \quad Eq.2.6.3$$

Here, $QFLS_{rad} = k_B T \cdot \ln\left(\frac{J_G}{J_{0,rad}}\right)$ is the radiative limit of our semiconducting material, as analogously derived in **Section 2.4** for the $V_{OC,rad}$.

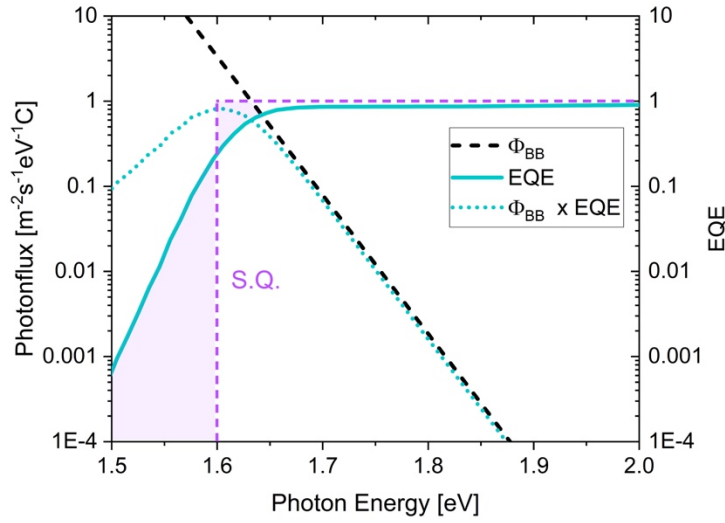


Figure 2.6.1: Example of experimental determination of $J_{0,rad}$ by EQE_{PV} and ϕ_{BB} convolution. In the image, the step-function onset assumed in Shockley-Queisser theory is also presented in order to highlight the deviation from real experimental conditions.

In **Section 2.4** we showed also how $J_{0,rad}$ can be calculated in the frame of S.Q. boundaries by using the detailed balance principle and the back-body radiation. However, in the order to determine realistic QFLS values, a $J_{0,rad}$ associated to the actual material investigated has to be used. As detailed in the same above cited publication by Rau,^[138] one way of calculating this current is to make use of the photovoltaic external quantum efficiency (EQE_{PV}). In this way it is possible to calculate the current generated by absorption of the black body radiation at energies greater than the EQE_{PV} onset. Thereby, similarly to **Eq.2.4.5**, we can define $J_{0,rad}$ as follow

$$J_{0,rad} = q \int EQE_{PV}(E) \phi_{BB}(E) dE \quad \text{Eq.2.6.4}$$

Eq. 2.6.4 takes into account that in the dark, the absorption of photons from the environment generates free charge, and that reemission of photons is through the recombination of free carriers. This reminds of the optical reciprocity between absorption and emission, following the detailed balance principle. Related to that, a fundamental condition that has to be fulfilled in order for **Eq.2.6.3** in combination with **Eq.2.6.4** to be applied, is that the absorption and reemission of photons of the illuminated cell also happens at the same energy and follows the optical reciprocity. We will show in **Chapter 9** that, if this is not the case, the QFLS cannot be calculated with this method. Also, from **Eq.2.6.4** and **Fig. 2.6.1**, it is evident how the steepness of the absorption onset is a decisive factor in determining the values of $J_{0,rad}$. Perovskite absorbers are usually characterized by steep onsets and low Urbach energies and therefore, $J_{0,rad}$ values are commonly low and the $V_{OC,rad}$ high.

2.7 The Ideality Factor

As expressed by **Eq.2.4.6**, the total current flowing in a solar cell can be described by the Shockley diode relation. Note that in that expression, J_0 referred only to the radiative recombination processes occurring in the solar cell in the dark, being the radiative recombination, the only recombination process allowed in S.Q. theory. However, in a realistic picture, the recombination of carriers involved in a solar cell is a combination of all types of radiative and non-radiative events, and as a consequence $J_0 \gg J_{0,\text{rad}}$. Therefore, in order to take into account this additional non-radiative recombination processes, **Eq.2.4.6** has to be rewritten in the form

$$J = J_0 \left[\exp\left(\frac{qV}{n_{\text{id}}k_{\text{B}}T}\right) - 1 \right] - J_{\text{G}} \quad \text{Eq.2.7.1}$$

where n_{id} is a figure of merit introduced to account for the deviation from the ideal condition of pure radiative recombination, and it is called ideality factor. One simple way to determine the ideality factor is to analyze current vs. voltage characteristics in the dark ($J_{\text{G}} = 0$) and extrapolate its values from the slope of the curve. However, depending on the system studies the influence of the shunt resistance at low voltages and the series resistance at high voltages can be significant and the determination of the n_{id} erroneous. An elegant well-established approach to cancel the influence of the series resistance is based on the measurement of the V_{OC} as a function of the light intensity.^[139,140] As the V_{OC} does not dependent on the series resistance, the obtained ideality factor is only influenced by the recombination pathways in the cell, while the influence of the shunt resistance can be readily identified and disregarded in the analysis. Within this approach, **Eq.2.7.1** can be rewritten at V_{OC} conditions as follow

$$V_{\text{OC}} \propto n_{\text{id}}k_{\text{B}}T \cdot \ln(J_{\text{G}}) \quad \text{Eq.2.7.2}$$

Experimentally, in the majority of the cases, J_{G} scales linearly with the illumination intensity I , and thereby the open circuit voltage V_{OC} can be plotted as function of the latter, as $V_{\text{OC}}(I)$. The rather simple experimental methodology makes this approach an easy tool to infer the type of recombination processes taking place in the solar cell. In the case of dominant radiative second order recombination n_{id} is equal to 1 by definition. Simply combining the **Eq.2.7.1** at open circuit condition with the recombination current associated to first order and second order recombination process it is possible to estimate the n_{id} for the specific recombination mechanism. In the case of second order radiative recombination, the recombination current is entirely determined by the QFLS:

$$R = k_2 n_e n_h = k_2 n_0^2 \exp\left(\frac{QFLS}{k_B T}\right) \propto \exp\left(\frac{qV_{OC}}{k_B T}\right) \quad Eq.2.7.3$$

$$J_R = qdR = qdk_2 n_0^2 \exp\left(\frac{qV_{OC}}{k_B T}\right) \equiv J_0 \exp\left(\frac{qV_{OC}}{n_{id} k_B T}\right) \Rightarrow n_{id} = 1 \quad Eq.2.7.4$$

On the other hand, in the case of dominant SRH recombination, the n_{id} can be calculated by expressing **Eq.2.5.5** in relation to the carrier density of electrons (holes). For an intrinsic semiconductor, the density of one specific carrier type, electron or holes, is related to the position of its single quasi-Fermi level, which will be 1/2QFLS in the fully symmetric case. Accordingly, the density of one carrier type is expressed as

$$n_e = n_e^0 \exp\left(\frac{QFLS}{2k_B T}\right) \quad Eq.2.7.5$$

We then rewrite **Eq.2.7.4** for a first order dependence as follow

$$J_R = qdR = qdk_1 n_e \propto \exp\left(\frac{QFLS}{2k_B T}\right) \propto \exp\left(\frac{qV_{OC}}{2k_B T}\right) \equiv \exp\left(\frac{qV_{OC}}{n_{id} k_B T}\right) \quad Eq.2.7.6$$

$$\Rightarrow n_{id} = 2$$

where the ideality factor n_{id} assume values of 2.

Notably, in **Eq.2.7.6**, we can observe that as the n_{id} is directly related to the V_{OC} and the recombination current J_R of the solar cell, it is consequently related also to QFLS of the absorber. Where to determine the V_{OC} it is necessary to have a complete solar cell connected to an external circuit, as we have seen in **Section 2.6**, the QFLS can be obtained from fully optical experiments, e.g. the PLQY. Generally, the PLQY under steady state illumination conditions will be limited by all recombination processes, meaning that there is no trivial relation between the QFLS and J_G . However, within a limited intensity interval, this relation can be written in terms of a modified diode equation^[136]:

$$J_G = J_R = J_0 \cdot e^{\left(\frac{QFLS}{n_{id} k_B T}\right)} \quad Eq.2.7.7$$

Thereby, from **Eq.2.7.7**, similarly as for **Eq.2.7.2**, it is possible to calculate the ideality factor, not only on full solar devices, but also on neat materials or on the combination of absorbers with single transport layers. We will demonstrate in **Chapter 5** and

Chapter 6 that this methodology is an essential tool of great importance to study and decouple the recombination losses in perovskite solar cells.

2.8 Recombination in Perovskite Solar Cells

In the **Section 2.5.1**, we detailed how the different type of non-radiative recombination processes are detrimental for solar cells, limiting the efficiency largely below the theoretical predicted radiative limit from S. Q. theory. The exact source of these non-radiative processes in perovskite materials and solar cells is currently still a debated topic. Although, in **Chapter 1**, we explained that the formation of deep trap states in the bandgap is not favorable, historically, the main center for non-radiative recombination has been addressed to the perovskite bulk and grain boundaries.^[101,141] Indeed, many improvements in terms of reduction of non-radiative losses have been achieved by improving the material quality and the crystallization processes.^[108,142] However, more recent studies have pointed out the greater contribution in non-radiative recombination of the perovskite surfaces rather than the absorber bulk.^[143,144] Again, as introduced in **Chapter 1**, this is in line with the defect nature and their location in perovskite materials. On this note, this finding opened doors to a large number of publications where surface passivation strategies have been successfully demonstrated. Probably on the most effective one is the deposition of the TOPO molecule on the top surface, which allowed simple MAPbI₃ to achieve external PLQY of ca. 20%, enabling a QFLS of 1.28 V.^[73] Achieving values significantly close to the radiative limit, 1.32 V in this case, highlighted, on one hand, the importance of addressing the perovskite surface in order to improve the material and, on the other hand, the small contribution of the non-radiative processes in the bulk to the overall energy losses. Regardless these improvements in the neat material, currently, the V_{OC} 's of perovskite solar cells rarely exceed values of 1.2 V,^[43,145,146] for a bandgap of around 1.6 eV. This indicates that the multilayered architecture of perovskite devices, although essential, is also detrimental in terms of V_{OC} losses, suggesting the recombination at the perovskite/transport layer interfaces as major source of losses. A few pioneer works investigated specifically the effect of interface recombination on the overall energy losses. First the work by Sarritzu et al.,^[136] followed by a second work by Stolterfoht et al.,^[127] extended the use of PLQY measurements, commonly used to characterize the losses in the perovskite absorber, to the perovskite with one of two transport layers attached or on the full device stack. The great advantage of this method lies in the lack of necessity of having an electrical contact in order to estimate the V_{OC} losses. As a result, they studied the effect of the single interfaces on the PLQY and consequently on the QFLS. Essentially, this allowed to quantify the amount of non-radiative losses introduced by the single transport layers. The important conclusion of these two works can be summarized as such: 1) the majority of the non-radiative losses in perovskite solar cells are located at the interfaces with the transport layers and 2) the interface with the larger losses basically determines the overall losses of the device and the final

V_{OC} . Importantly, we will show in **Chapter 4** how the strength of these recombination processes largely depends on the specific transport layer used.

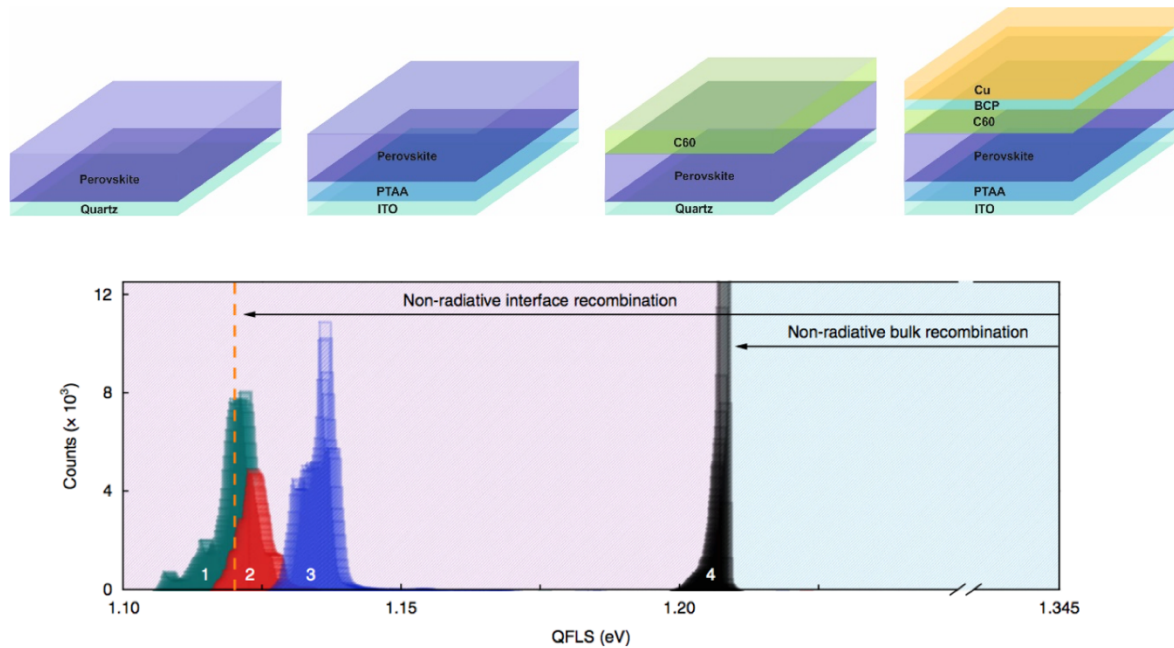


Figure 4.1: On the top, schematic representation of the perovskite layer, single junctions and full devices stack samples that can be independently measure with PLQY. On the bottom, Results from PLQY measurements on series on samples as represented on the top of the figure. Here, in black is represent the neat perovskite, in red and blue the PTAA and C60 interfaces whereas in green the full device stack. Image adapted from Ref^[127].

While this method allows to quantify the energy losses at a specific interface, no information can be extracted regarding the exact mechanism and rate of these recombination processes at these locations. Besides various sophisticated transient techniques, as transient absorption spectroscopy (TAS) or time resolved micro conductivity (TRMC), transient PL (TRPL) constitutes a rather easy and largely used experimental approach to obtain such information. Importantly, also in this case, the fully optical TRPL can be applied to different single parts of the layer stack. Similarly to PLQY, TRPL lifetimes in the neat material are found to reach extremely large values (μs range)^[73,145,147] for optimized systems, whereas the introduction of the transport layer dramatically decrease them. Commonly, lifetimes in the range of 10 – 200 ns are usually observed in unoptimized full devices.^[127,148] From these values, various works managed to estimate the recombination velocities (S) at the interfaces. Depending on the transport layer used, these are found to be in the range of 200 – 2000 cm/s.^[127,148,149] Importantly, one drawback of TRPL is that of being influenced also by charge extraction, since the PL signal depends on the product of hole and electron densities. Therefore, if one of the carriers is extracted from the perovskite absorber, the PL signal us reduced similarly as in the case of non-radiative recombination. Detailed experimental and theoretical studies on this matter^[148]

interpreted the initial fast component of the TRPL decays at low fluences as charge extraction, whereas the slow component was treated in the frame of non-radiative recombination. This picture is also confirmed by TRMC and TAS studies, where transfer kinetics are studied in details and found to be significantly faster than the recombination ones.^[129,150] Overall, the important implication of these findings bring attention on the need of appropriate optimization of the perovskite/CTL interfaces and in particular, highlight the importance of the optimization of the worst interface rather than an arbitrary one. This methodology to investigate the solar cell devices has been extensively used and further developed during this thesis work.

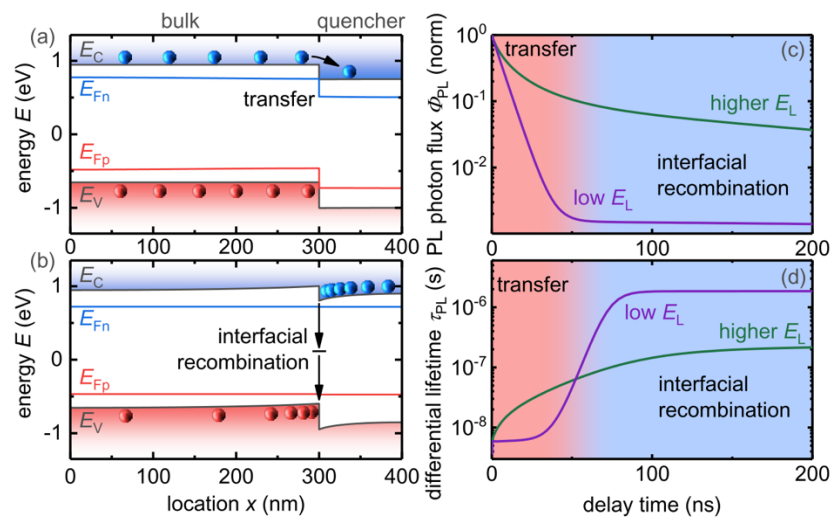


Figure 4.2: TRPL decays at the different injection conditions. The image highlights the fast and slow decay in relation to the transfer or recombination of charges, respectively. Image adapted from Ref^[151].

Chapter 3.

3. Experimental Framework

In this thesis work a vast number of experimental techniques have been used to study perovskite devices and films. The set of experiments range from rather simple opto-electrical characterizations, as $J - V$ under simulated solar radiation, light intensity dependent $J - V$, photovoltaic external quantum efficiency (EQE_{PV}) and electroluminescence quantum efficiency (EQE_{EL}), optical techniques as steady state and transient photoluminescence (PLQY and TRPL respectively), microscopy techniques as atomic force microscopy (AFM) and scanning electron microscopy (SEM), to more advanced characterization method, as cathodoluminescence (CL) imaging, energy dispersive X-ray (EDX) imaging, X-ray photoelectron spectroscopy (XPS), ultraviolet photoemission spectroscopy (UPS), inverted photoemission spectroscopy (IPES), secondary ion mass spectroscopy (SIMS). Additionally, drift-diffusion simulations are extensively used in the first part of the thesis to corroborate the experimental results and derive recombination models. Given the large variety of the experimental approach, this chapter will not discuss every technique in detail. Instead, we will focus exclusively on the methodologies specifically developed during the course of this thesis, being them part itself of the core of the work. In addition, a brief description of the technical details of all the experiments can be found in **Chapter 11**.

3.1 Photoluminescence Quantum Yield

The photoluminescence quantum yield (PLQY) set up used for this work is not part of any commercially available pre-assembled instrument, although some of the components were taken from different pre-existing commercially available setups. This set up has been specifically assembled during this thesis work with the aim of measuring large part of the samples investigated here. In detail, the excitation source is provided by an external CW laser source (Insaneware), being either 445 nm or 530 nm, and coupled into an optical fiber in order to be guided to the inside of a 3.3 inch integrating sphere. The latter was originally part of a Hamamatsu C9920 absolute luminescence set up. However, due to scarce sensitivity of the detector and the low excitation intensity of the monochromator provided by the company, only the integrated sphere has been used. From the sphere, the light is then outcoupled into a second fiber to arrive at an Andor Shamrock 500i spectrometer with integrated low pass filters and equipped with a cooled (-70 °C) Si CCD detector DU420A-BR-DD iDUS. With this new configuration, the sample excitation is completely independent in term of wavelength and intensity and with this specific CCD detector we are highly sensitive also to low luminescence samples. Additionally, as illustrated in **Fig. 3.1**, an optical density (OD) filter wheel is placed in front of the laser source in order to precisely control the illumination intensity. In this configuration, two Si photodiodes, one before and one after the integrated sphere in the laser path, are used to monitor the intensity at different location of the setup. In particular, photodiode 1 is used to generally monitor the laser intensity, and photodiode 2 is used to measure the light intensity in the proximity of the sample and to establish 1 sun condition. Notably, in order to measure with photodiode 2 the sample has to be remove from the sphere.

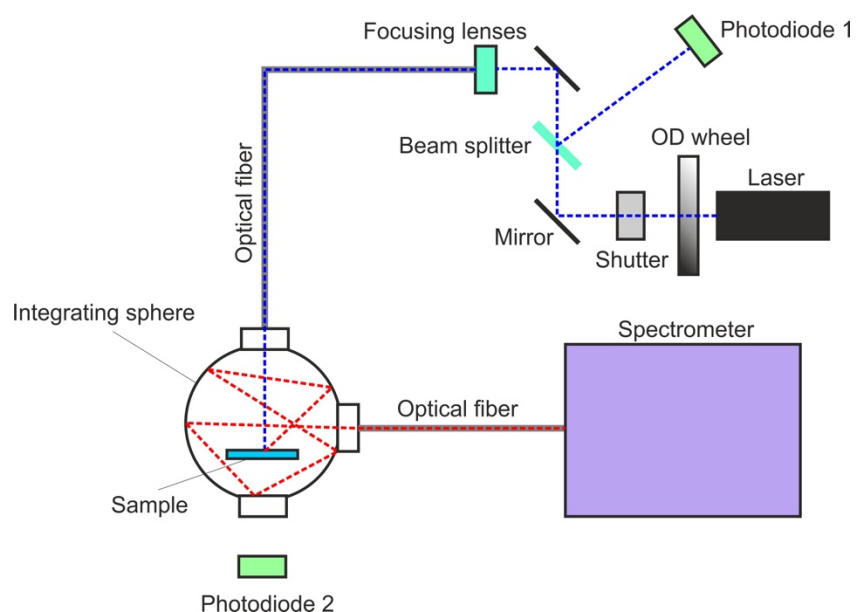


Figure 3.1: Schematic representation of the PLQY setup used in this work.

The setup has been calibrated by using a halogen lamp with known spectra irradiance, in order to be able to take into account the spectral response of all the components of the set up during the analysis of the data. Here a calibration spectrum was obtained by matching the spectral output of the detector with the calibrated spectral irradiance of the lamp. In order to obtain PLQY values of our samples, various measurements steps have to be taken. Firstly, given that the PLQY is calculated as the ratio of the number absorbed photons to the number of emitted photons, we have to be able to calculate how many photons are actually absorbed by our material. To do so, a first spectrum is recorded without any sample inside the integrating sphere, in order to record only the excitation signal. We will call this spectra S1. After that, at the same intensity, a new spectrum is recorded, this time with the sample inside the integrated sphere. We will call this spectra S2. In this way by subtracting the spectrum S2 to the spectrum S1, and integrating the resulting spectrum in the wavelength region of the laser peak, we are able to calculate the amount of light that is actually absorbed by our sample. Here, only the part of the spectrum relevant for the excitation wavelength is considered. Importantly, given the high sensitivity of the detector to prevent saturation, the steps are conducted at low illumination intensities. Now the intensity of the laser is set to 1 sun equivalent by illuminating a perovskite solar under short-circuit condition and matching the current density to the J_{SC} obtained under the sun simulator. Usually, these values are found to be $\sim 22 \text{ mA/cm}^2$ at 100 mW/cm^2 . Once the excitation intensity is adjusted, a low pass filtered is inserted in front of the CCD internally in the Andor Shamrock 500i spectrometer in order to remove the contribution from the excitation light. The filter can be 500 nm for an excitation at 445 nm or 600 nm for an excitation at 520 nm. Now, the actual PL of the sample is finally recorded. We will call this spectra S3. Additionally, a dark measurement is performed to yield the background spectrum, used later as baseline. Importantly, a certain contribution in the recorded PL in spectrum S3 can originate from the filter PL itself or the remaining laser signal after the filter. Therefore, one measurement of 1 sun intensity without samples inside the integrated sphere has to be recorded. We will call this spectra S4. The data analysis is performed within a self-written Matlab routine. Now, we will go through the main calculations step by step. Firstly, to all recorded spectra the dark background is subtracted. After that, the sample PL spectra S3 has to be corrected by subtracting the additional contributions from the setup, recorded in S4. Once all spectra are clean, they are corrected to take into account the spectra response of the setup. This is done by dividing the recorded spectra by the correction spectra obtained during the calibration of the setup.

$$\frac{I_{\text{raw}}(\lambda)}{I_{\text{calibration}}(\lambda)} = I_{\text{corrected}}(\lambda) [\text{Wm}^{-2} \cdot \text{nm}^{-1}] \quad \text{Eq.3.1.1}$$

Now, the original spectra in arbitrary unit are in the unit of spectra irradiance. Therefore, from here the signal is transformed in photon flux by dividing by the photon energy hc/λ .

$$\frac{I_{\text{corrected}}(\lambda)}{\frac{hc}{\lambda}} = I_{\text{corrected}}(\lambda) [\text{\#photons} \cdot \text{m}^{-2} \cdot \text{s}^{-1} \cdot \text{nm}^{-1}] \quad \text{Eq.3.1.2}$$

Now the spectra for the absorbed laser intensity and the emitted PL intensity can be integrated and the PLQY calculated. Importantly, since the absorbed laser intensity was measured at a lower intensity, here an intensity factor C_{int} has to be applied in order to normalize this contribution to 1 sun condition.

$$\text{PLQY} = \frac{\int_{750}^{850} I_{\text{corrected}}^{\text{Emit}}(\lambda) d\lambda}{\int_{400}^{500} C_{\text{int}} \cdot I_{\text{corrected}}^{\text{Abs}}(\lambda) d\lambda} \quad \text{Eq.3.1.3}$$

The integration limits indicated here are for a general perovskite with $E_G = 1.6$ eV and an excitation wavelength of 445 nm. Naturally, these can be adjusted with respect to the perovskite E_G and the different excitation wavelength.

3.2 Drift-Diffusion Simulations

1D Drift-diffusion simulations are carried out using the open source software SCAPS. The program has been developed by the Department of Electronics and Information Systems (ELIS) of the University of Gent, Belgium, and it is freely available online for the scientific community. The basic working principle of SCAPS relies on basic equations commonly implied in drift-diffusion models. Namely, the Poisson equation for the electrostatic potential ψ

$$\frac{\partial^2}{\partial x^2} \psi(x) = \frac{q}{\epsilon \epsilon_0} \left[-n_e + n_h - N_A^- + N_D^+ + \frac{1}{q} \rho_{\text{def}}(n, p) \right] \quad \text{Eq.3.2.1}$$

and the continuity equations

$$\frac{\partial n_e}{\partial t} = -\frac{\partial J_e}{\partial x} + G - R_e \quad \text{Eq.3.2.2}$$

$$\frac{\partial n_h}{\partial t} = -\frac{\partial J_h}{\partial x} + G - R_h \quad \text{Eq.3.2.3}$$

Note that in **Eq.3.2.1**, for our simulations the doping densities N_A^- and N_D^+ are usually negligible or very low and the defect distribution ρ_{def} is approximated as a discrete level. The current density of electron and holes are defined as

$$J_e = -\frac{n_e \mu_e}{q} \frac{\partial E_{Fe}}{\partial x} \quad \text{Eq.3.2.4}$$

$$J_h = +\frac{n_h \mu_h}{q} \frac{\partial E_{Fh}}{\partial x} \quad \text{Eq.3.2.5}$$

The boundary conditions are set at the interfaces between the individual layers and at the metal contacts. Thereby, from the above equations we obtain a system of differential equations in (ψ, n_e, n_h) and (ψ, E_{Fe}, E_{Fh}) . The scheme to solve this set of equations is based on the work by Gummel.^[152] Here, a first guess is made by the program for the electrostatic potential and the carrier density. From the latter, a new correction $\delta\psi$ for the total ψ is calculated from **Eq.3.2.1**. Then, the newly updated ψ is used to calculate a new carrier density with the continuity equations **Eq.3.2.2** and **Eq.3.2.3**. This process is iterated until convergence is reached. In SCAPS, the simulation environment can be defined by specifying a series (or single) layers between to two metal contacts. In each layer the following parameters can be specified: bandgap E_G , electron affinity EA , dielectric permittivity ε , conduction and valence band effective density of states, N_C and N_V respectively, thermal velocities for electron and holes, v_{th}^e and v_{th}^h respectively, and electron and hole mobility, μ_e and μ_h . Additionally, the donor and acceptor doping densities can be defined as well. For each layer, the recombination of charges is defined by the radiative recombination coefficient k_2 , Auger hole and electron coefficient (not relevant for perovskite materials for carrier density regimes studied here) and, most importantly, the defects density N_T . The latter, together with the electron and hole cross section, σ_e and σ_h , define the carrier lifetime in the layer according to the following general relation

$$\tau = \frac{1}{\sigma N_T v_{th}} \quad \text{Eq.3.2.6}$$

A fundamental advantage of SCAPS is that recombination at the interfaces of the different layer can directly accessible and freely adjusted. Here, interface recombination is defined by a recombination velocity defined as such

$$S = \sigma N_T^{\text{int}} v_{th} \quad \text{Eq.3.2.7}$$

where, in this case, N_T^{int} defines the trap density at that specific interface. Importantly, as for bulk defects, defects can be either acceptor or donor type. In all our simulations we have chosen realistically values usually assumed for Si, as $\sigma = 10^{-15} \text{cm}^2$ and $v_{\text{th}} = 10^7 \text{cm/s}$, for both electron and holes. This allow to vary N_T^{int} accordingly in order to obtain realistic values of interface recombination velocities experimentally determined. Importantly, here the recombination via interface traps and their occupation is treated in a way that allows the exchange of electrons (holes) between one interface state and the two adjacent conduction (valence) bands. In this way, recombination can take place from both sides of the interface. The general material properties of the single layers have been chosen by the data available in literature. On the other hand, specific parameters connected to the specific devices studied, as the interface recombination and the bulk lifetimes, had to be determined experimentally. This has been carried out beforehand in the publication by Stolterfoht et al.^[127]

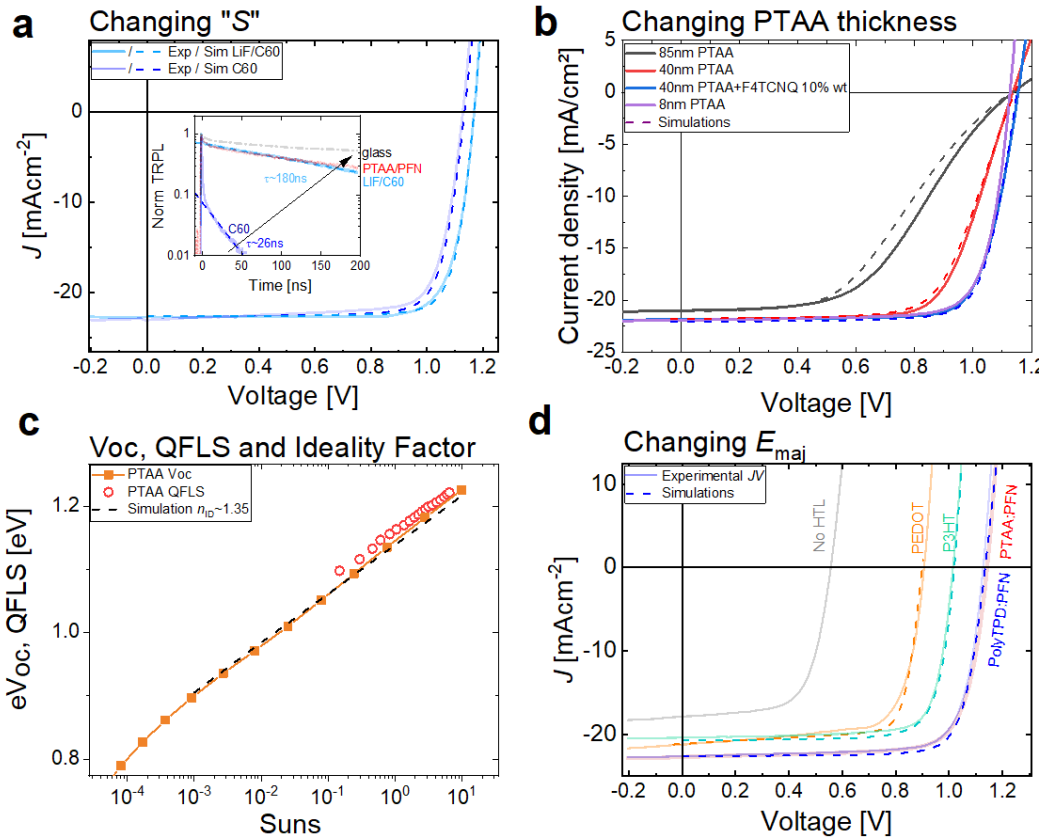


Figure 3.2: a) Inserting LiF between the perovskite and C₆₀ leads to concurrent increased of transient PL (TRPL) lifetime and device V_{oc} . The TRPL results allowed to deduce the interface recombination velocity (S) parameter for both interfaces and the lifetime in the perovskite bulk which allowed us to fit our experimentally obtained JV-curves. Interestingly, S increases 1 order of magnitude upon application of LiF, however, the effect on the V_{oc} is relatively small 35 meV, yet consistent with numerical simulations. b) Based on these simulations, we aimed to fit cells with changing PTAA thickness to finetune the perovskite and the PTAA layer mobility ($\mu_{\text{pero}} = 1 \text{cm}^2/\text{V/s}$, $\mu_{\text{PTAA}} = 1.5 \times 10^{-4} \text{cm}^2/\text{V/s}$). It is clear that the mobility in the PTAA layer has a significant impact on the device fill factor consistent with previous works.^[98] c) Without

further optimization of the simulations, we readily obtained an n_{id} of ~ 1.35 consistent with experimental results. d) Lastly, we fitted cells with different HTLs by varying majority carrier band-offsets as obtained from UPS measurements and the HTL material properties. In principal, we find any majority carrier offsets causes an equal reduction in the device V_{OC} as long as the interface (with the offset) is limiting the overall recombination loss. By implementing offsets for a cell with PEDOT:PSS and P3HT we can well reproduce the experimental JV-curves without further adjustments of the simulation settings. Image adapted from the Supporting Information of the publication presented in **Chapter 6**.

Briefly, using transient PL measurements, we obtained an interfacial recombination velocity of $S = 1000$ cm/s at the perovskite/ C_{60} interface, $S = 100$ cm/s PTAA/PFN/perovskite interface and a bulk lifetime of approximately 500 ns in the absorber layer. With these values, we could accurately reproduce the V_{OC} of our cell by implementing surface recombination velocities and bulk lifetimes in SCAPS. Based on these initial results, we have further optimized the simulation parameters by fitting the simulations to several experimental results, as shown in **Fig. 3.2**. Specifically, in **Fig. 3.2a**, we managed to fit the $J - V$ of a device with improved C_{60} interface characterized by higher V_{OC} by only reducing S at this interface. In **Fig. 3.2b**, we fitted the $J - V$ curves of a series of devices where the PTAA thickness is increases and the resulting FF decreased accordingly. In **Fig. 3.2c**, the ideality factor from V_{OC} vs. intensity measurements has been fitted by simulated intensity dependent $J - V$ measurements. Finally, in **Fig. 3.2d**, the $J - V$ of a series of devices with different HTL has been fitted by specifying different HTLs in the simulation program. All these experiments were fitted based on a “standard simulation” by changing only 1 parameter depending on the particular experiment. In this way, we have a safe and solid simulation model, realistically representing our devices, which can be used to study the recombination mechanisms and fundamental physics governing perovskite devices. Moreover, this simulation tool set the basis for setting up and testing the different recombination models proposed in **Chapter 5** and **Chapter 6**.

3.3 Solar Cell Devices

In this work, we will mostly focus on $p-i-n$ type devices utilizing polymers as HTL. The standard device investigated throughout this thesis work PTAA, which has been optimized to have a thickness of roughly 8 nm by using a diluted solution of 1.5 mg/ml in Toluene.^[98] However, examples with P3HT, PEDOT:PSS and PolyTPD will be also presented. The hydrophobicity of the PTAA surface makes the wetting of the perovskite precursor solution rather difficult. This, results in a poor coverage and formation of pin-holes, with resulting V_{OC} losses and FF losses due to possible shunt paths. Therefore, an additional ultra-thin polymeric layer of Poly(9,9-bis(3'-(N,N-dimethyl)-N-ethylammonium-propyl-2,7-fluorene)-alt-2,7-(9,9-dioctylfluorene))dibromide (PFN-Br) is used on top of PTAA to improve the wettability.^[127] The resulting devices showed improved better perovskite coverage and reproducibility, with a consequent

V_{OC} improvement. The ETL of our devices consists of 30 nm of thermally evaporated C_{60} . On top of that, an additional thin layer (8 nm) of bathocuproine (BCP) is also thermally evaporated to improve the interface with the final Cu top metal contact (90 nm). The resulting structure is presented in **Fig. 3.3**. Throughout this thesis work the perovskite is, for the most part, constituted by a triple cation perovskite with the nominal composition $Cs_{0.05}(MA_{0.17}FA_{0.83})_{0.95}Pb(I_{0.83}Br_{0.83})_3$ with a molarity of 1.2M in DMF:DMSO (4:1). Importantly, in the precursor solution, 10% Pb excess in molar ratio is used. The deposition method follows the one-step approach described in **Chapter 1**, utilizing mostly ethyl acetate (diethyl ether when specified) as antisolvent dropped 10 s after the start of the spin coating (3500 rpm). In the following chapters we will show several examples of the introduction of additional interlayers between the perovskite and C_{60} , as well as different perovskite compositional modifications.



Figure 3.3: Exemplified layer stack of a typical perovskite solar cell studied in this work.

Chapter 4.

4. Impact of Energy Alignment and Interface Recombination

This chapter is an adapted preprint of the publication:

Stolterfoht, M., Caprioglio, P., Wolff, C. M., Márquez, J. A., Nordmann, J., Zhang, S., Rothhart, D., Hörmann, U., Amir, Y., Redinger, A., Kegelman, L., Zu, F., Albrecht, S., Koch, N., Kirchartz, T., Saliba, M., Unold, T., Neher, D., The impact of energy alignment and interfacial recombination on the open-circuit voltage of perovskite solar cells. *Energy Environ. Sci.* **12**, 2778–2788 (2019)

Despite the late date of publication due to the long review process (arXiv:1810.01333), this work sets the fundamental basis and understanding of the effects of the perovskite/transport layer interfaces on the device performance. The results highlight how all the studied transport layers induce a significant amount of non-radiative losses, which consistently lower the QFLS compared to the one potentially achievable by the neat perovskite. Moreover, here we introduce the importance of the relation between the strength of interface recombination and the energy alignment of the perovskite with the transport layers. In particular, we will show how the combination of these two effects can induce a mismatch between the internal QFLS and the external V_{OC} . Importantly, this work constitutes the background knowledge for the research that follows in this thesis work.

Huge endeavors are devoted to understanding and improving the performance of perovskite solar cells, which continue to develop at a rapid pace already outperforming other conventional thin-film technologies on small cells ($< 1\text{cm}^2$).^[120] It is well established that further improvements will require suppression of non-radiative recombination losses to reach the full thermodynamic potential in terms of open-circuit voltage (V_{OC}) and fill factor (FF).^[101] As such, a major focus of the entire field to push the technology forward is targeted at reducing defect recombination in the perovskite bulk with numerous works highlighting the importance of grain boundaries in determining the efficiency losses.^[108,153] In contrast, many other studies highlight the significance of traps at the perovskite surface which is likely chemically distinct from the bulk.^[153–155] In many cases, performance improvements were achieved by mixing additives into the precursor solution including multiple cations and/or halides.^[22,43,107,155] In many studies, a slower transient photoluminescence (TRPL) decay is shown as the figure of merit to prove the suppressed trap-assisted recombination in the bulk while implying its positive impact on the overall device efficiency.^[108,155,156] Significantly fewer publications have focused on the importance of non-radiative recombination of charges across the perovskite/CTL interface.^[75,157,158] Until recently it has been challenging to pinpoint the origin of these free energy losses in complete cells, although there have been some studies with valuable insight.^[75,129,157–159] Methods that have been employed to study interfacial recombination in perovskite stacks include impedance spectroscopy,^[157,160] transient photoluminescence (TRPL)^[75,148,149] or reflection spectroscopy (TRS),^[159] transient microwave conductivity (TRMC),^[129] transient photovoltage (TPV).^[161] Whilst these techniques exhibit in principle the required time resolution to unveil the kinetics of the interface and bulk recombination, the interpretation of these transient measurements can be very challenging. The reasons are related to the inherent fact that extraction and recombination can both reduce the emitting species in the bulk, thus causing the signal decay.^[101] Previously, a more direct approach to decouple the origin of these recombination losses at each individual interface has been introduced based on steady-state photoluminescence measurements.^[107,127,134–137,162] In particular, measurements of the emitted photoluminescence quantum yield (PLQY) on individual perovskite/transport layer junctions have been used to explain the V_{OC} through QFLS losses in the perovskite bulk and at the individual interfaces.^[107,127,136] However, the relation between the internal QFLS and the external V_{OC} remains poorly understood today, especially for different solar cells architectures with different perovskite absorbers and/or charge transport layers. For example, in a recent study, a very high external PLQY (15%) has been reported on a *nip*-stack (i.e. an electron transport layer/perovskite/hole transport layer junction) upon grain boundary passivation using potassium iodide.^[107] Considering, the provided external quantum efficiency (EQE), this high PLQY translates in an internal QFLS of ~ 1.26 eV which is very close to the radiative limit of the given perovskite absorber layer (~ 1.31 eV). Yet, the V_{OC} of the optimized cells was considerably lower (1.17 V). This suggests that interfacial recombination (which impacts the QFLS of the *nip*-stack) is not causing the primary V_{OC} limitation and suggests that losses of ~ 100 mV are of different nature. This raises the

important question whether the external V_{OC} as measured on a complete solar cell truly represents the QFLS in the perovskite bulk and how this depends on the strength of interfacial defect recombination or the energy level alignment between the perovskite and the transport layers. Until today, the importance and impact of energy level alignment remains an important, yet heavily debated topic in perovskite solar cells. For example, several studies showed the benefit or a large impact of energy level alignment between the perovskite and the transport layers,^[75,163–165] which was however challenged in other works.^[166]

In this work, we studied the relation between the QFLS and the V_{OC} by means of absolute PL measurements in “regular” (*nip*-type)^[29,43,167] and “inverted” (*pin*-type)^[98,104,168] perovskite solar cells for a broad range of CTLs including metal oxides, conjugated polymers,^[155,169] small molecules, and fullerenes. First, we aim to compare the selectivity of CTLs used for *nip* and *pin* configurations in triple cation perovskite cells; i.e. for instance TiO_2 or SnO_2 vs. PTAA underneath the perovskite or doped Spiro-OMeTAD vs. C_{60} on top. We note that in this work we define the selectivity of a CTL as its ability to maintain the QFLS of the absorber layer while providing efficient majority carrier extraction. The results suggest that when attached to the perovskite, all studied CTL cause a reduction of the QFLS with respect to the QFLS of the neat perovskite on a fused silica substrate (1.23 eV). The results were also generalized to different perovskite absorber layers. A comparison of the QFLS obtained on CTL/perovskite (or perovskite/CTL) bilayers and *nip*- or *pin*-stacks, suggests a simple superposition principle of non-radiative recombination currents at each individual interface. This implies that the inferior interface dominates the free energy loss in the complete cell. In efficient cells, where the QFLS matches the device V_{OC} , we can further estimate the parallel recombination currents in the bulk, interfaces and/or metal contacts under V_{OC} conditions. However, in poor performing cells we find that the V_{OC} is substantially lower than the corresponding QFLS of the *pin*-stack. Drift diffusion simulations highlight the impact of energy level offsets in causing the mismatch between the internal QFLS and the external V_{OC} which we further confirmed using photoemission spectroscopy (UPS) and transient differential charging capacitance experiments. The results underline that the primary non-radiative recombination loss channel of today’s perovskite cells is interfacial recombination at (or across) the perovskite/CTL interface and that interfacial recombination is often exponentially increased in case of an energy level offset between the perovskite and the TEs. As such, our findings highlight the importance of tailoring the energetics and kinetics at the perovskite/CTL interfaces to harvest the full potential in perovskite solar cells.

The studied CTLs in this work belong to 3 material classes, conjugated polymers, small molecules and metal oxides. Regarding the conjugated polymers, we studied highly selective wide-band gap donors such as PolyTPD and PTAA.^[155,169] PFN was added on top of both materials to improve the wettability. In order to draw correlations between the QFLS and the energetics of the HTL, we also investigated P3HT,^[170,171] as well as highly conductive composite PEDOT:PSS.^[158] As small molecule HTL, we tested Spiro-OMeTAD^[172,173] which requires doping by different ionic salts and other additives.^[173] For the case of small molecule ETLs, we tested the fullerene C_{60} (with

and without the interlayer LiF20) and the solution-processable fullerene derivative PCBM.^[168,174] Lastly, we studied the commonly used transparent metal oxides TiO2 and SnO2. TiO2 is widely considered as an ideal electron transporting layer due to its high selectivity and high charge carrier mobility,^[175] while SnO2 is the preferred platform for planar efficient nip cells.^[157] These chemical structures of the materials are shown in **Fig. 4.1**. As absorber layer we chose the so-called triple cation perovskite (CsPbI₃)_{0.05}[(FAPbI₃)_{0.83}(MAPbBr₃)_{0.17}]_{0.95},^[22] while the results were extended to other perovskite systems as discussed below.

In order to quantify the energy losses at the CTL/perovskite interface, we measured the absolute photoluminescence (PL) yield of perovskite/transport layer heterojunctions, detailed in **Chapter 2**. Here we express the PLQY by highlighting all the different types of recombination currents as such

$$\begin{aligned} \text{PLQY} &= \frac{\phi_{\text{em}}}{\phi_{\text{abs}}} = \frac{J_{\text{rad}}/e}{J_{\text{G}}/e} = \frac{J_{\text{rad}}}{J_{\text{R,tot}}} = \frac{J_{\text{rad}}}{J_{\text{rad}} + J_{\text{non-rad}}} \\ &= \frac{J_{\text{rad}}}{J_{\text{rad}} + J_{\text{B}} + J_{\text{p-i}} + J_{\text{i-n}} + \dots} \end{aligned} \quad \text{Eq. 4.1}$$

$J_{\text{non-rad}}$ is equal to the sum of all non-radiative recombination pathways in the bulk (J_{B}), at the HTL/perovskite ($J_{\text{p-i}}$) and perovskite/ETL ($J_{\text{i-n}}$) interfaces, and potentially other losses (e.g. recombination in the transport layers, or at the CTL/metal interfaces). Using the expression for the radiative recombination current density according to Shockley-Queisser^[121] and **Eq. 4.1**, we can write the QFLS as a function of the radiative efficiency

$$\begin{aligned} J_{\text{rad}} = J_{0,\text{rad}} e^{\mu/kT} \rightarrow \mu &= kT \ln \left(\frac{J_{\text{rad}}}{J_{0,\text{rad}}} \right) = kT \ln \left(\text{PLQY} \frac{J_{\text{G}}}{J_{0,\text{rad}}} \right) \\ &= kT \ln \left(\frac{J_{\text{G}}}{J_0} \right) = kT \ln \left(\frac{J_{\text{rad}}}{J_{\text{rad}} + J_{\text{B}} + J_{\text{p-i}} + J_{\text{i-n}} + \dots} \frac{J_{\text{G}}}{J_{0,\text{rad}}} \right) \end{aligned} \quad \text{Eq. 4.2}$$

We note, that the PLQY depends itself on external conditions such as the illumination intensity or the internal QFLS. This originates from the fact that the non-radiative recombination pathways depend differently on the actual number of charge pairs present in the device compared to radiative recombination.^[139] Thus, in order to predict the QFLS under 1 sun and open-circuit, the PLQY needs to be measured under the same illumination conditions. **Eq. 4.2** also shows that the QFLS depends logarithmically on the non-radiative recombination currents in the bulk, interface etc. In order to quantify the QFLS, the generated current density under illumination (J_{G}) and $J_{0,\text{rad}}$ need to be known, as well as the thermal energy (we measured a temperature of ~26-28°C on the sample under 1 sun equivalent illumination using a digital standard infrared sensor). J_{G} and $J_{0,\text{rad}}$ are obtained from the product of the external quantum efficiency (EQE) and the solar (ϕ_{sun}) and the 300 K - black body spectrum (ϕ_{BB}),

respectively.^[121,131,176,177] As such, we obtained a $J_{0,rad}$ of $\sim 6.5 \times 10^{-21} \text{ A/m}^2$ ($\pm 1 \times 10^{-21} \text{ A/m}^2$) independent of the bottom CTL (**Fig. 11.1.1 Appendix 11.1**) as it is predominantly determined by the tail absorption of the triple cation perovskite absorber layer (with Urbach energies around 15 meV). In all cases, the QFLS was measured by illuminating the films through the perovskite (or the transparent layer in case of *pin* or *nip* stacks) in order to avoid parasitic absorption of the studied CTL (and ϕ_{abs} doesn't equal J_G/e anymore, see **Fig. 11.1.2 Appendix 11.1**). The results of the PL measurements of the different transport layers are summarized in **Table 1** and plotted in **Fig. 4.1b**. All results were obtained as an average of multiple fabricated films (**Fig. 11.1.3 Appendix 11.1**) with representative PL spectra shown in **Fig. 11.1.4 Appendix 11.1**. Details of the measurements conditions are discussed in **Section 12.1**.

Table 1. Optoelectronic quality of several tested perovskite-CTL layer junctions.

Film	Absorption	PLQY	$J_{0,nr}$ [Am^{-2}]	QFLS [eV]
ITO/Pero	0.839	2.0×10^{-5}	3.5×10^{-16}	1.060
PEDOT:PSS/Pero	0.854	7.5×10^{-5}	9.9×10^{-17}	1.092
P3HT/Pero	0.848	7.7×10^{-4}	1.0×10^{-17}	1.152
Pero/Spiro-OMeTAD	0.944	1.4×10^{-3}	4.6×10^{-18}	1.172
PTAA/PFN/Pero	0.852	5.1×10^{-3}	1.3×10^{-18}	1.204
PolyTPD/PFN/Pero	0.851	7.3×10^{-3}	1.1×10^{-18}	1.208
Pero	0.850	1.4×10^{-2}	4.6×10^{-19}	1.231
SnO ₂ /Pero	0.854	5.9×10^{-3}	1.5×10^{-18}	1.201
TiO ₂ /Pero	0.854	2.1×10^{-3}	3.2×10^{-18}	1.181
Pero/PCBM	0.934	5.7×10^{-4}	1.3×10^{-17}	1.145
Pero/C ₆₀	0.927	3.8×10^{-4}	1.8×10^{-17}	1.137
Pero/LiF/C60	0.892	1.3×10^{-3}	4.9×10^{-18}	1.170

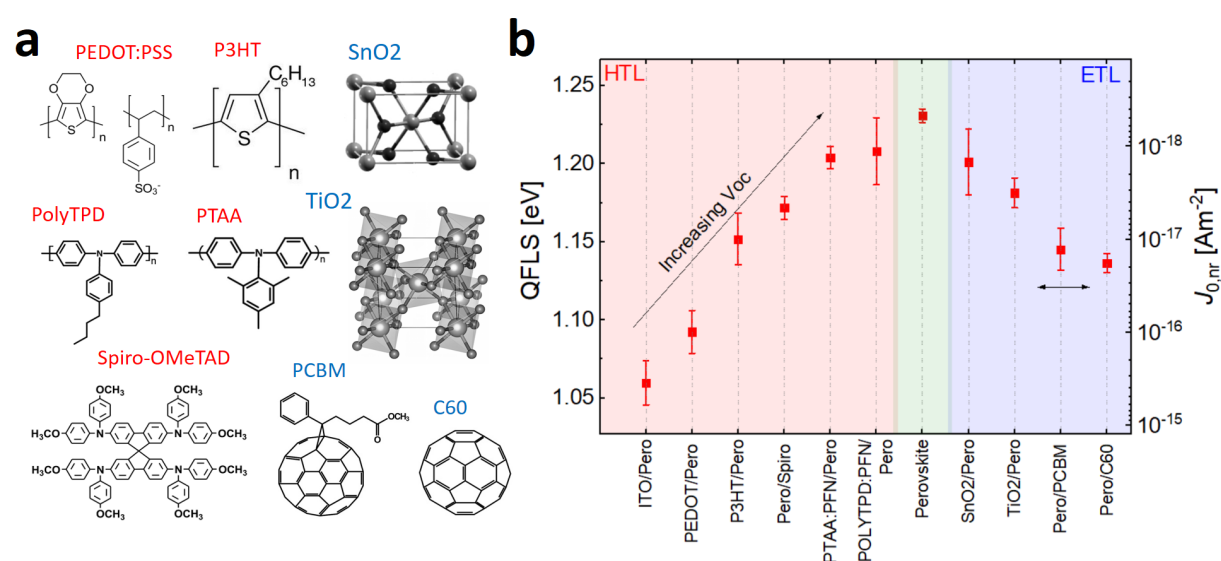


Figure 4.1. a) Materials studied in this paper. b) The calculated quasi-Fermi level splitting of

the studied heterojunctions with different hole and electron transporting materials and of the neat absorber layer based on equation 2 using absolute photoluminescence measurements. The absorber was spin casted from the same solution for all transport layers. The non-radiative dark saturation current is plotted on the right and was obtained from $J_{0,nr} = J_0 - J_{0,rad}$ which allows comparing the strength of non-radiative recombination of different junctions.

Fig. 4.1b shows that the triple cation perovskite on a fused silica substrate limits the QFLS to approximately 1.231 eV, which is ~110 meV below the radiative V_{OC} limit (where the PLQY equals 1). We note that we cannot rule out that this value is limited by recombination at the fused silica/perovskite interface and that we observe a substantially lower QFLS (~40 meV) of the bare perovskite layer on a glass substrate (see **Fig. 11.1.5 Appendix 11.1**). Moreover, significantly higher PLQY values above 20% were observed on methylammonium lead triiodide films where the top surface was passivated with tri-n-octylphosphine oxide (TOPO).^[73] These results highlight the high opto-electronic quality of the perovskite bulk comparable (or already better) than highly pure silicon or GaAs but also indicates substantial recombination losses at the perovskite top surface. For the HTL/perovskite junctions we also tested the influence of the underlying ITO layer, however this did not significantly influence the obtained QFLS within a small error except for samples with SnO_2 (see **Fig. 11.1.3 Appendix 11.1**). Likewise, we tested the influence of the copper metal electrode on top of the C_{60} in perovskite/ C_{60} heterojunctions and of *pin* stacks (**Fig. 11.1.6 Appendix 11.1**). Overall, these tests suggest that there is an essentially lossless charge transfer between the metal electrodes and the HTL. Interestingly, **Fig. 4.1b** shows that the polymers PTAA/PFN and PolyTPD/PFN performed best - even outperforming the omnipresent Spiro-OMeTAD. However, it is clear that the selectivity of a TL can be different underneath or on top of the perovskite. Therefore, we do not aim to quantify the opto-electronic quality of a CTL itself but rather assess the selectivity of the CTL in a particular configuration (i.e. either on top or underneath a particular perovskite layer). Among the studied ETLs, SnO_2 and TiO_2 outperform the organic ETLs C_{60} and PCBM which are usually used in *pin*-type cells. Therefore, this data suggests that the *p*-interface is the limiting interface for *nip* cells, and the *n*-interface for *pin* cells consistent with earlier studies.^[136] Moreover, we observe that the capping CTLs PCBM and C_{60} are worse than Spiro-OMeTAD. Considering that the inferior interface will dominate the final V_{OC} (**Eq. 4.1** and **4.2**), this might be one reason for the superior performance of *nip* cells today. One approach to suppress non-radiative recombination at the perovskite/ C_{60} interface is to insert a thin LiF interlayer as demonstrated earlier²⁰ and in **Tab. 4.1**.

A frequently arising question is how much the perovskite morphology, which potentially varies depending on the underlying CTL, could influence the obtained QFLS and the interpretation of the results. Thus, we performed top scanning electron microscopy and AFM measurements (see **Fig. 11.1.7 Appendix 11.1**). Interestingly, we find the largest grains on a PEDOT:PSS bottom CTL despite it being the worst among the studied transport layers. The largest grain size distribution is visible on perovskite films on TiO_2 while the perovskite morphology on all other substrates appears, at least qualitatively,

similar where we observe relatively small grains ($< 10 - 100$ nm). In addition, AFM measurements reveal root mean square surface roughnesses varying from $12 - 27$ nm, where the perovskite on PolyTPD/PFN and PTAA/PFN appears to be roughest (> 20 nm) while the perovskite film on TiO_2 is the smoothest. We also note the similar Urbach tail of the perovskite absorber layer when processed on different CTLs (**Fig. 11.1.1 Appendix 11.1**) which is related to the density of subgap states. This further indicates a similar opto-electronic quality of the perovskite. Considering these results, it seems unlikely that the perovskite bulk morphology can explain the changes in the non-radiative recombination loss currents which increase by orders of magnitude depending on the underlying substrate (as shown in **Fig. 4.1b**). It is also worth to note that these results do not allow distinguishing whether the critical recombination loss occurs across the perovskite/CTL interface, or at the perovskite surface next to the interface. In any case, the presence of the additional CTL triggers additional (non-radiative) interfacial recombination losses, which are dominating the non-radiative recombination losses.

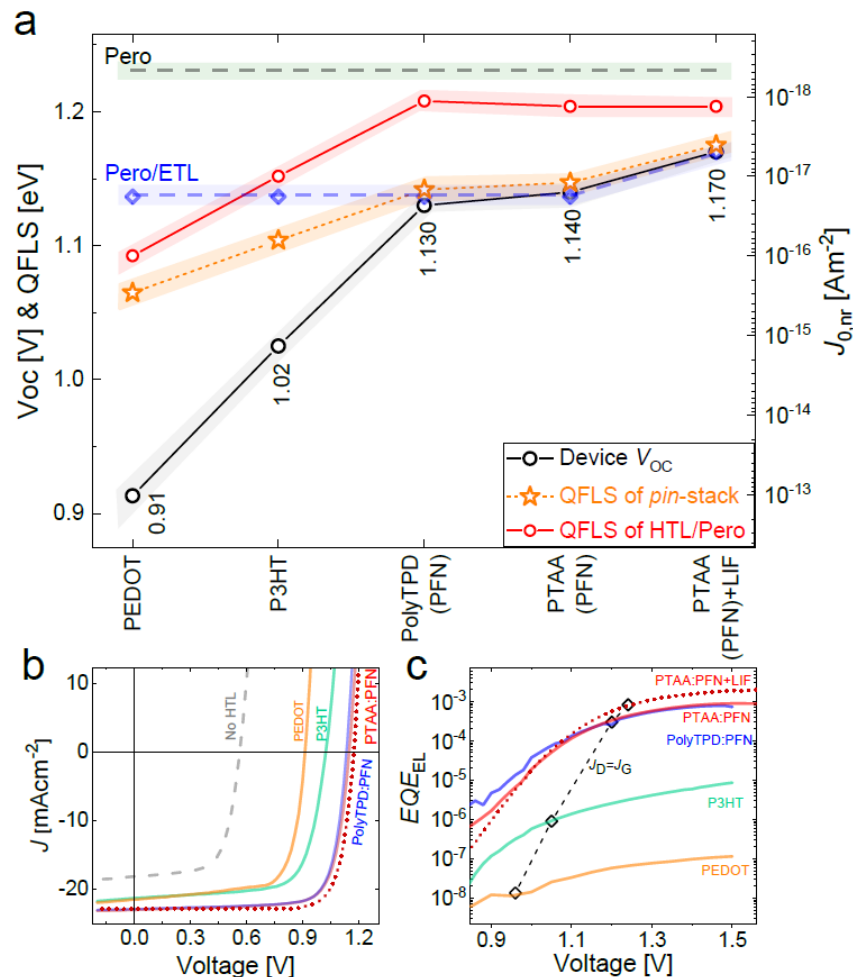


Figure 4.2. a) Average V_{oc} of pin cells employing different conjugated polymers as HTLs and a C_{60} ETL, compared to the average QFLS of the corresponding HTL/perovskite bilayers (red), and of the pin stacks (orange). The QFLS of the perovskite/ C_{60} junction and of the neat perovskite on fused silica are shown in dashed blue and black lines, respectively. The dark

saturation current ($J_{0,nr} = J_0 - J_{0,rad}$) as plotted on the right allows to compare the strength of non-radiative recombination of different junctions. b) Corresponding current density vs. voltage characteristics of the *pin* cells with different HTLs, and c) the external electroluminescence efficiency as a function of voltage. The dashed line shows conditions where the dark injection and light generation currents are equal for each device.

In the following, we aim to compare the non-radiative recombination losses at the *p*- and *n*-interfaces with the QFLS of the *pin* stacks and the V_{OC} of the complete cells with different HTLs and (LiF)/C₆₀ as ETL. **Fig. 4.2a** shows that the device V_{OC} (black line) generally increases with the average QFLS of the *pin*-stack (orange line) which was taken as an average as obtained on 3-4 samples for each configuration. Importantly, for optimized cells with PolyTPD or PTAA, the V_{OC} (black line) matches the QFLS of the stack (orange line) within a small error. This is also nearly identical to the QFLS of the less selective perovskite/C₆₀ interface (blue line). This indicates that for these particular cells, the losses determining the V_{OC} occur almost entirely at the inferior interface to the perovskite while the electrodes are not causing additional V_{OC} losses. On the other hand, in case of the less selective PEDOT:PSS and P3HT bottom layers, the V_{OC} was found to be substantially lower than the corresponding QFLS. This will be discussed further below. The current density vs. voltage (*JV*) characteristics of the corresponding cells are shown in **Fig. 4.2b** which highlight the large differences in the measured V_{OC} s. Device statistics of individually measured stacks are shown in **Fig. 11.1.9 Appendix 11.1**. We note that our devices with LiF/C₆₀ as ETL reach efficiencies of up to 21.4% with a V_{OC} of ~ 1.2 V (for a triple cation perovskite with a bandgap of ~ 1.6 eV), which is among the highest reported values for *pin*-type cells (**Fig. 11.1.10 Appendix 11.1**).^[97,106,178]

Next, we compared the PLQY with the external electroluminescence quantum efficiency (EQE_{EL}) as shown in **Fig. 4.2c**. Under conditions where the dark injection current equals the generation current, the EQE_{EL} of PTAA and PolyTPD cells (3×10^{-4} for both devices) approaches the PLQY of the stack within a factor of two (5.9×10^{-4} for PTAA and 4.6×10^{-4} for PolyTPD). Improving the perovskite/ETL interface by inserting LiF increases both the QFLS of the *pin* stack and the V_{OC} to 1.17 V corresponding to a PLQY of $\sim 1.3 \times 10^{-3}$ and EQE_{EL} of $\sim 8.3 \times 10^{-4}$.²⁰ However, for devices with PEDOT:PSS, the EQE_{EL} ($\sim 1.4 \times 10^{-8}$) is orders of magnitude lower than the PLQY of the stack ($\sim 1 \times 10^{-5}$). We note that the measured EQE_{EL} matches roughly the expected EQE_{EL} value for a V_{OC} of 0.9 V as obtained from the *JV* scan (3.8×10^{-8}). Therefore, we conclude that the inferior interface (PEDOT:PSS/perovskite) limits the QFLS of the stack, however, there is an additional loss which affects the V_{OC} but not the QFLS. This will be addressed further below. Lastly, films with P3HT lie somewhat in between PEDOT:PSS and PTAA (PolyTPD) devices. Here, both interfaces (P3HT/perovskite and perovskite/C₆₀) appear to be equally limiting the QFLS of the stack which also lies below the QFLS of the individual heterojunctions (bilayers). Similar to PEDOT:PSS devices, we observe a considerable mismatch between PLQY of the optical *pin* stack (6.2×10^{-5}) and the EQE_{EL} ($\sim 9 \times 10^{-7}$). We note that the measure EQE_{EL} is again very close to the EQE_{EL} that is expected for a P3HT device with a V_{OC} of ~ 1.0 V ($\sim 1.8 \times 10^{-6}$). As for the *nip*-

cells with SnO₂ and TiO₂ as the ETL, and SpiroOMeTAD as the HTL, we observe a similar trend as in our optimized *pin*-type cells with PTAA or PolyTPD, that is a close match between the average device V_{OC} (~ 1.15 V) and the average internal QFLS (1.161 eV and 1.168 eV for TiO₂ and SnO₂ based cells, respectively) under 1 sun conditions. All results obtained on *nip*-cells are shown in **Fig. 11.1.11 Appendix 11.1**. Regarding the potential impact of the perovskite morphology when the samples are prepared on different hole (electron) transport layers, it is important to note that the losses in the neat material (dashed black in **Fig. 4.2a**) cannot be larger than the cumulative losses observed in the CTL/perovskite bilayers (red). Moreover, the match between the QFLS of the *glass/perovskite/CTL* bilayers (blue) and the *pin* or *nip* stacks (**Fig. 4.2a** and **Fig. 11.1.11 Appendix 11.1**) means that the recombination at the top CTL interface can consistently explain the overall V_{OC} regardless, if the perovskite is deposited on glass or on the CTL (PTAA:PFN, PolyTPD:PFN, TiO₂, SnO₂). This highlights the importance of the top interface in determining the non-radiative recombination current in perovskite solar cells.

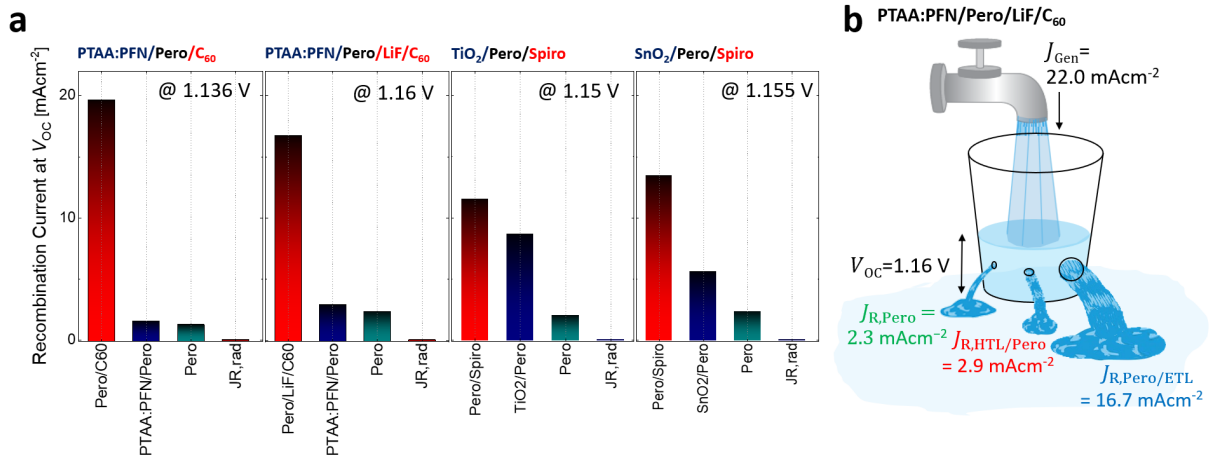


Figure 4.3. a) Bulk and Interfacial recombination currents at open-circuit as obtained on *nip* and *pin* type cells with nearly flat quasi-Fermi levels. In *pin* type cells, the non-radiative recombination current is dominated by the C_{60} interface (blue) – even if optimized with LiF. In *nip*-type cells, the recombination at the upper perovskite/Spiro-interface (red) dominates the recombination loss, although the recombination at the *p*- and *n*-interface are quite similar in case of cells based on TiO₂. In all cases, the non-radiative recombination losses in the neat perovskite (green) are smaller than at the top interface. We note the radiative recombination current density is very small, e.g. $7.8 \mu\text{Acm}^{-2}$ in panel (a). b) Illustrates a solar cell as bucket with holes where the water level represents the cells' V_{OC} .⁵³ The water stream from the tap corresponds to the generation current density from the sun. The holes in the buck represent the recombination losses at V_{OC} in the bulk, interfaces etc. Depending on the exact size of the holes, the water level will change so as the V_{OC} of the device.

The absolute-PL approach allows to further estimate the parallel recombination currents at V_{OC} . To this end, we successively quantify the non-radiative recombination

currents in the neat material and the bottom and top interfaces from the PLQY of the corresponding perovskite/CTL films (Eq. 4.1) and knowledge of J_{rad} (Eq. 4.2). Important to note is that the PLQY needs to be known at the V_{OC} of the complete cell. Moreover, the individual recombination currents must add up to J_{G} which allows to check the consistency of the approach. This is possible in efficient cells where the QFLS in the absorber layer matches the device eV_{OC} within a relatively small error (≈ 20 meV), but the procedure is prone to fail in cells where $\text{QFLS} > eV_{\text{OC}}$. Fig. 4.3a shows the obtained recombination currents for efficient *pin*-type and *nip*-type cells. Fig. 3b illustrates our optimized *pin* cells with LIF/C₆₀ as ETL at V_{OC} by a bucket with holes which represent the recombination losses (see caption). We note again that the recombination current in the neat perovskite (green) is obtained from a film on fused silica and therefore the loss in the neat absorber layer might be slightly different when deposited on top of a CTL. However, as we detail throughout the manuscript, changes in the perovskite morphology when deposited on different CTL cannot explain the V_{OC} of the final cells, and the fact that the recombination currents add up to J_{G} suggests that this loss estimation provides a realistic description of the parallel recombination currents at V_{OC} . The experimental results in the previous sections show that $\text{QFLS} \sim V_{\text{OC}}$ in case of good performing transport layers (PTAA and PolyTPD). This indicates that interfacial recombination in these devices lowers the QFLS throughout the whole bulk equally. However, in case of PEDOT:PSS or P3HT, the device V_{OC} is lower than the QFLS in the perovskite layer. In such cases, at least one QFL bends, presumably at the interfaces or contacts, causing a further reduction in the electrochemical potential of the photogenerated charges. This bending has a much larger effect on the final V_{OC} than on the average QFLS in the perovskite bulk. In order to check whether this phenomenon depends on the charge carrier generation profile, we analysed all samples by illuminating the samples through the bottom glass or top using a 445 nm laser (Fig. 11.1.2 Appendix 11.1) and through intensity and wavelength dependent V_{OC} measurements (Fig. 11.1.12 Appendix 11.1). However, we concluded that neither the QFLS nor the V_{OC} depend significantly on the charge generation profile, which we attribute to the rapid diffusion of charges through the perovskite. In order to understand the spatial distribution of the recombination losses and the QFLS, we simulated our perovskite solar cells using the well-established drift-diffusion simulator SCAPS.^[179] These simulations take into account previously measured interface recombination velocities and perovskite bulk lifetimes.^[127] The simulated electron/hole quasi-Fermi levels ($E_{\text{F,e}}$ and $E_{\text{F,h}}$) at open-circuit are shown along with the conduction and valence bands in Fig. 4.4a for a PTAA/PFN/perovskite/C₆₀ device. Important simulation parameters listed in Tab. 11.1.1 Appendix 11.1. Qualitatively, these simulations confirm that $E_{\text{F,e}}$ and $E_{\text{F,h}}$ are spatially flat in the perovskite bulk and extend to the corresponding electrodes which explains that eV_{OC} is nearly identical to the QFLS (of ~ 1.13 eV) in these devices. Interestingly, to reproduce the comparatively high open-circuit voltages (~ 1.14 V) and FFs up to 80% of these devices, a considerable built-in voltage (V_{BI}) of at least 1.0 V had to be assumed considering realistic interface recombination velocities. Otherwise, a strong backfield would hinder charge extraction in forward bias but also accumulate minority carriers at the wrong contact (Fig.

11.1.13). We note that the role of the V_{BI} across the absorber layer is currently an important topic in the community and further efforts need to be taken to properly consider the impact of ions on the field distribution.^[95] Moreover, we had to assume a small majority carrier band offset ($\Delta E_{maj} < 0.1$ eV) between the perovskite valance/conduction band and the HOMO/LUMO of the HTL/ETL, respectively in order to reproduce the measured device V_{OC} .

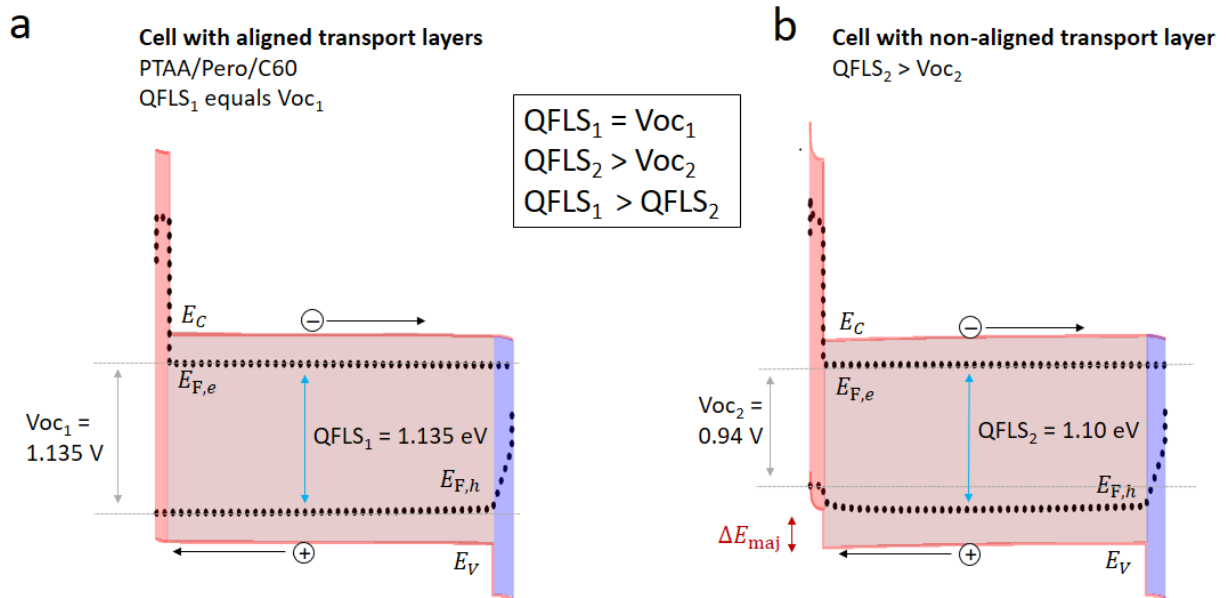


Fig. 4.4. a) The simulated quasi-Fermi level splitting (QFLS) in junctions with aligned transport layers (PTAA/perovskite/C₆₀) is identical to eV_{OC} but not in case of energetically mis-aligned transport layers b) where the hole QFL bends at the interface to the hole transport layer which causes a QFLS - V_{OC} mismatch. The perovskite is represented in brown showing unoccupied states in between the conduction band minimum (E_C) and valence band maximum (E_V), while the dashed lines show the electron and hole quasi-Fermi levels ($E_{F,e}$ and $E_{F,h}$), the resulting QFLS in the absorber and the open-circuit voltage (V_{OC}) at the contacts. The HTL (red) and ETL (blue) are represented by their unoccupied states in between the highest and lowest unoccupied molecular orbitals.

Interestingly, the implementation of a majority carrier band offset at the p -interface causes a considerable bending of the hole quasi-Fermi level close to the interface which explains the QFLS - V_{OC} mismatch (**Fig. 4.4b**). Considering that $E_{F,e}$ and $E_{F,h}$ need to extend throughout the CTLs to the metal contacts in order to produce an external V_{OC} , it is clear that any ΔE_{maj} will cause an exponential increase of the hole population in the HTL. This implies an exponential increase in the recombination rate. Therefore, it is expected that a finite ΔE_{maj} will lead to an equal loss in the device V_{OC} . In order to generalize the conditions under which the V_{OC} deviates from the QFLS, we extended our simulations by studying a wide range of parameters (**Fig. 11.1.1 Appendix 11.1**). We found that at least two requirements must be fulfilled in order to explain the QFLS -

V_{OC} mismatch: (a) a band offset for the majority carrier of at least ~ 0.2 eV, and (b) a sufficiently high recombination velocity (> 1 cm/s), otherwise $E_{F,e}$ and $E_{F,h}$ can remain flat despite the energy offset (**Fig. 11.1.14 Appendix 11.1**). Indeed, these simulations show that the V_{OC} loss scales linearly with the ΔE_{maj} offset as long as the p -interface is limiting. We also note that the minority carrier band offset ΔE_{min} (i.e. the LUMO of the HTL and the perovskite conduction band) is not influencing the results if ΔE_{min} is larger than only 0.1 eV which is further discussed at **Fig. 11.1.15 Appendix 11.1**. We also simulated a pin stack with a PEDOT:PSS bottom layer which we simplified by a metal with a work function of 5 eV, a high surface recombination velocity for holes and an intermediate value for electrons (**Tab. 11.1.1 Appendix 11.1**). Also, for these settings we observed that $E_{F,h}$ bends at the interface, giving rise to the experimentally observed QFLS - V_{OC} mismatch of roughly 150 meV in the PEDOT cell. All results on PEDOT:PSS cells are summarized in **Fig. 11.1.16 Appendix 11.1**. We acknowledge that these simulations only illustrate one possible scenario of the internal device energetics using a set of plausible parameters, and thus different energetic alignments or a morphological issue at the interface cannot be excluded. However, we can conclude that energy level alignment of all layers is a crucial requirement to maximize the V_{OC} while the defect density at the interface is also a critical parameter in determining the non-radiative recombination losses. The findings in the previous sections suggest that the observed mismatch between the internal QFLS and the V_{OC} in cells comprising PEDOT:PSS and P3HT is due to an energy offset at the p -interface. To study the energy level alignment between the perovskite and the transport layer, we first performed photoelectron yield spectroscopy measurements (PYS) on the individual layers of the solar cells (**Fig. 11.1.17 Appendix 11.1**). However, these measurements did not allow a reliable prediction of ΔE_{maj} which is due to the assumption of a constant vacuum level across different layers of the stack. To measure the energetic offsets between the perovskite and the transport layers with respect to the fixed Fermi level (E_F) of the ITO substrate, we performed UPS measurements with background illumination. Recently, it has been shown that the perovskite surface can be considerably n -doped,^[180] which will directly impact the location of the valence band onset with respect to E_F when measuring the top surface of the perovskite film with a He beam (21.1 eV). However, when UPS is performed with an additional background light, the band bending at the surface can be flattened which then allows to access the bulk energy levels. This enabled a direct comparison between the energy levels of the transport layers and the perovskite bulk. Indeed, as shown in **Fig. 4.5** below, by properly taking into account the surface photovoltage (SPV) effect, we found that the valence band of the perovskite is aligned with the HOMO of PTAA and PolyTPD HTLs, while P3HT and PEDOT:PSS exhibited states close to, or at the Fermi-edge. Thus, we conclude that PTAA and PolyTPD allow maintaining the high QFLS that is generated from the perovskite upon illumination which is in agreement with the drift diffusion simulations. In contrast, in case of P3HT, and even worse in case of PEDOT:PSS, carriers will lose part of their free energy once they are transferred from the perovskite to the HTL, thereby causing the additional V_{OC} -loss as numerically predicted and experimentally observed. A further confirmation of this picture comes from the

measurement of the charge carrier density in the bulk (n_{bulk}) at a given V_{OC} using differential charging capacitance measurements. [181,182] In the case of proper energy alignment, n_{bulk} would be a sole function of the V_{OC} , independent of the choice of the TL material. The results in **Fig. 11.1.18 (Appendix 11.1)** show that this is not the case. Instead, for a given V_{OC} , n_{bulk} is substantially larger for the PEDOT:PSS cell than for the P3HT and the PTAA cell with proper energy alignment. This is a direct consequence of the energy offset and the resulting difference between the QFLS and the device V_{OC} (see **Fig. 11.1.18d Appendix 11.1** for a schematic representation of this situation).

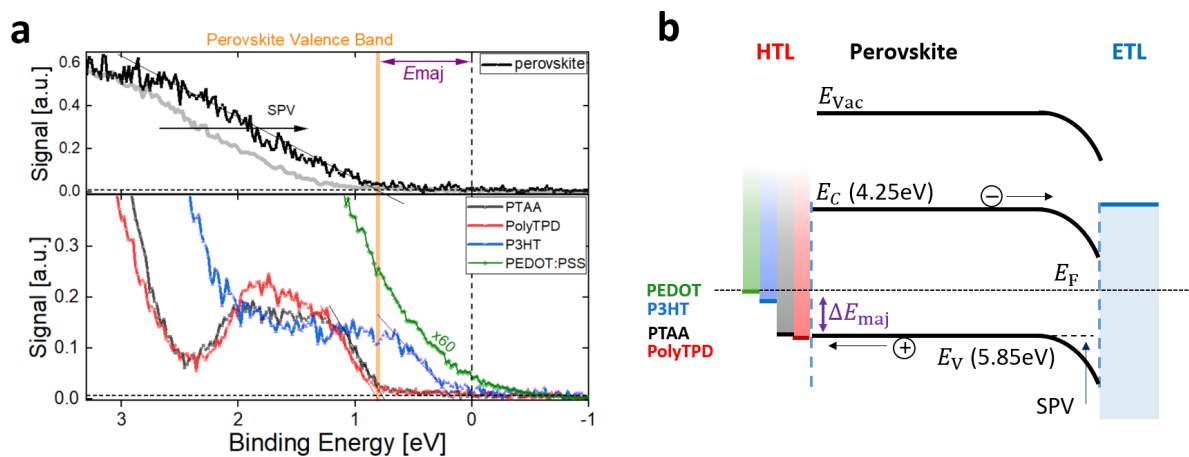


Figure 4.5. a) Ultraviolet photoelectron (UPS) spectra of PTAA, PolyTPD, P3HT and PEDOT:PSS on ITO. The corresponding signal of the perovskite film is shown above. The perovskite surface is n -doped⁵⁶ resulting in an apparent valence band onset of 1.35 eV. Application of a background light (with a 1 sun equivalent intensity) flattens the band bending at the surface which allows accessing the valence band offset in the perovskite bulk (0.8 eV away from the Fermi level).⁵⁶ The spectra of PEDOT:PSS is scaled by a factor of 60 as compared to the other films. As discussed by Hwang et al.,⁵⁹ a high-bandgap PSS layer is present on top of a solution processed film which weakens the photoelectron signal of states at the Fermi-edge of the underlying PEDOT:PSS bulk as shown in several publications.^{59,60} The deduced energy levels are plotted in b). As predicted from the QFLS $-V_{\text{OC}}$ match in these cells, in case of PTAA and PolyTPD hole transport layers, the HOMO of the HTL is aligned with respect to the perovskite valence band. However, considerable majority carrier band offsets exist in case of P3HT and PEDOT:PSS. This causes the observed QFLS $-V_{\text{OC}}$ mismatch as carriers relax to the band edges during their transport to the extracting electrode.

In order to generalize the findings, we also studied QFLS and V_{OC} losses in other currently popular perovskite materials (**Fig. 11.1.19, Appendix 11.1**). The results further confirm our main conclusions: (i) the perovskite bulk usually allows to reach higher V_{OC} s than ultimately achieved in the cell. This is confirmed in a low-gap triple cation perovskite (~ 1.54 eV) which is currently used in the highest efficiency solar cells,^[120] a hybrid vacuum/solution processed MAPbI₃ (~ 1.6 eV) which is relevant for application on textured surfaces in tandem solar cells,^[183,184] a high-gap mixed

perovskite with a bandgap of 1.7 eV which is the ideal bandgap for monolithic Si/perovskite tandem solar cells, as well as two-dimensional perovskites based on *n*-butylammonium^[185] - a popular system which demonstrates increased stability under thermal and environmental stress.^[186] However, in some cases the QFLS of the optical stack is close to the QFLS of the neat absorber layer, e.g. for a solution processed CsFAPbI₃ (~1.47 eV) and MAPbI₃ (~1.6 eV). (ii) In most cases, the QFLS-PL technique can well describe the V_{OC} of the final cell which allows to assess the inferior interface by comparing the QFLS of HTL/perovskite or perovskite/ELT junctions. However, in a high-bandgap (~1.7 eV) mixed perovskite system we observe again a considerable mismatch between the QFLS of the *pin*-stack and the V_{OC} . This highlights the difficulties in increasing the perovskite bandgap while maintaining aligned energy levels and further demonstrates the relevance of our findings for other perovskite systems.

Chapter 5.

5. On the Relation between Open Circuit Voltage and quasi-Fermi Level Splitting

This chapter is an adapted preprint of the publication:

Caprioglio, P., Stolterfoht, M., Wolff, C. M., Unold, T., Rech, B., Albrecht, S. & Neher, D. On the Relation between the Open-Circuit Voltage and Quasi-Fermi Level Splitting in Efficient Perovskite Solar Cells. *Adv. Energy Mater.* **9**, 1901631 (2019).

This chapter is a direct continuation of the work presented in **Chapter 4**. Here, we make use of the intensity dependence of the PLQY to study in details the relation between the internal QFLS and external V_{OC} . The intensity dependent fashion of the approach allows to monitor the evolution of the two quantities at different carrier densities. We will show how the behavior of QFLS and V_{OC} can be different depending on the transport layer used in the device. Moreover, the saturation of the V_{OC} at high carrier concentration, observed for both devices, will be safely attributed to a specific type of recombination process, clarifying a so far rather unclear matter in literature. A combination of experiment and drift-diffusion simulation allowed us to conclude that the V_{OC} can be affected by additional recombination processes and it cannot be used alone to infer the recombination mechanisms happening in the perovskite absorber.

A common approach to study the rate and mechanisms of recombination is to measure specific recombination properties, such as the carrier lifetime or the recombination current density, as a function of the V_{OC} .^[131,139,187,188] Hereby, the V_{OC} is used as a measure of how strongly the carrier distribution of the illuminated sample differs from the thermal equilibrium. For example, the recombination current is commonly written in terms of the classical diode equation and related to the ideality factor, as defined in **Eq.2.7.7**. However, the V_{OC} is a quantity measured externally, at the device's *external* contacts and given the multilayer architecture of the perovskite solar cells it might be not truly representative of the quasi-equilibrium established in the absorber or at the absorber/transport layer interfaces. On the other hand, an *internal* quantity representative of the density of free photogenerated charges in the conduction and valence band of the absorber is the QFLS. As extensively presented in **Section 2.3**, in the S.Q. theory, the QFLS and the V_{OC} are two interchangeable quantities which are considered as equal to each other.^[121,133] However, as briefly introduced in **Chapter 4**, it has been experimentally observed that the magnitude of the *internal* QFLS is not always equal to the *external* V_{OC} .^[189] Moreover, several authors reported that the V_{OC} saturates at high illumination intensities ($> 1\text{sun}$), which is of particular importance for applications of perovskite in solar cell concentrators.^[190] While several mechanism have been proposed to explain the V_{OC} saturation^[139,191,192], it still constitutes a matter of active debate. On the other hand, there are very few publications regarding the intensity dependence of the QFLS, and none of these reported a saturation of the QFLS.^[136] In this chapter, we compare the *external* V_{OC} with the *internal* QFLS of the same solar cell device, obtained using photoluminescence quantum yield (PLQY) measurements, and monitor the evolution of the two quantities with respect to the light intensity. From these data, we calculate two different ideality factors, namely an *internal* ideality factor, obtained from the QFLS measurements, and an *external* ideality factor, obtained from the V_{OC} measurements.

$$V_{OC} \propto n_{id,ext} k_B T \cdot \ln (J_{SC}) \quad \text{Eq.5.1}$$

$$QFLS \propto n_{id,int} k_B T \cdot \ln (J_{SC}) \quad \text{Eq.5.2}$$

The study is performed on two different perovskite solar cell model systems characterized by different energy losses and utilizing different hole transporting layers (HTL), namely PTAA and P3HT. For both systems, the QFLS increases continuously with light intensity, with a constant *internal ideality* factor of ca. 1.3-1.5, while the V_{OC} displays a clear saturation for both types of devices. We also find that the V_{OC} of the poorer performing device lies significantly below the QFLS for all light intensities. This finding challenges the common view that the V_{OC} is a proper measure of the deviation from thermal equilibrium of the illuminated system. Therefore, the measurements of the V_{OC} as function of intensities do not allow to draw reliable conclusions about the mechanism of recombination. By implementing drift diffusion simulations, we elucidate

the possible causes for the V_{OC} saturation and identify its limitations, compared to the QFLS potentially achievable.

Here, the two *pin*-type perovskite solar cells, with the so called “triple cation” $\text{Cs}_{0.05}(\text{MA}_{0.17}\text{FA}_{0.83})_{0.95}\text{Pb}(\text{I}_{0.83}\text{Br}_{0.17})_3$ perovskite absorber^[22] are compared in **Fig. 5.1**. Consistent with our previous reports,^[98,189] the PCE of our P3HT cells is lower compared to the cells with a PTAA hole-transporting layer, which regularly exhibit PCEs exceeding 20%.^[127] Most of the limitation comes from the poor V_{OC} s of below 1 V when utilizing P3HT, while PTAA cells generally exhibit V_{OC} s of 1.14 V and above, depending on the choice of the perovskite and electron-transporting material. The reduction in J_{SC} for P3HT cells is due to its energy gap (E_g) of roughly 2 eV, which allows absorption of light overlapping with the perovskite absorption, consequently reducing the number of photons reaching the perovskite absorber. We also note a slightly reduction of the FF , which we will address further below. All the relevant values are reported in **Tab. 5.1**.

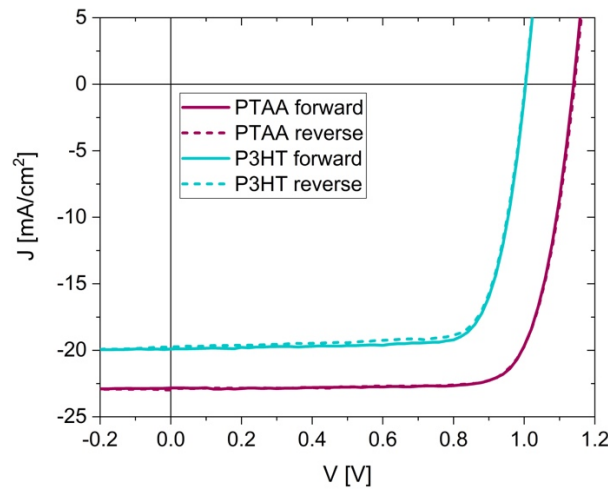


Figure 5.1: *J-V characteristics of forward and reverse scans (0.1 V/s with voltage step of 0.02V) under simulated AM 1.5G illumination calibrated to 100 mW/cm² for two typical devices utilizing PTAA and P3HT as hole-transporting layers.*

Table 5.1: *J-V parameters for the two model devices taken from J-V scans and averaged over 10 cells. Inside the brackets, values for the champion device are reported.*

	V_{oc} [V]	J_{sc} [mA/cm ²]	FF [%]	PCE [%]
P3HT	0.95 ± 0.04 (0.98)	20.4 ± 0.5 (21.2)	73 ± 4 (78)	14.2 ± 1.2 (16.23)
PTAA	1.14 ± 0.01 (1.15)	22.2 ± 0.6 (22.9)	77 ± 2 (78)	19.4 ± 0.6 (20.56)

To study the energy losses in detail, we performed intensity dependent PL and V_{OC} measurements on the very same solar cell device. The PLQY was measured by exciting the complete device, inside an integrated sphere with a 455 nm laser diode, varying its intensity. The V_{OC} of the respective cell was measured with the very same light source,

in the same intensity regime. The laser intensity is normalized to 1 sun when the illuminated cell shows a current density at 0 V equal to the J_{SC} . Importantly, the PLQY, as the calculated QFLS, is an internal quantity, which represent the destiny of the photogenerated charges recombining in the absorber or its interfaces; on the other hand, the V_{OC} is quantity measured at the external contact, therefore taking into account also the possible recombination processes happening in the transport layers or at the contacts. The dependence of the PLQY on the illumination intensities is presented in **Fig.5.2**. In the ideal case of purely radiative recombination, the PLQY is independent of illumination intensity. Instead, both cells show an intensity dependence according to the power law $PL(I) \propto I^k$, suggesting that non-radiative recombination processes of lower order, most likely assisted by traps in the perovskite bulk, at grain boundaries or at the interfaces compete with the second order radiative recombination of free carriers, as described in **Chapter 2**. The larger slope for the lower performing cell with P3HT highlights the importance of this process in limiting the efficiency of our cells.

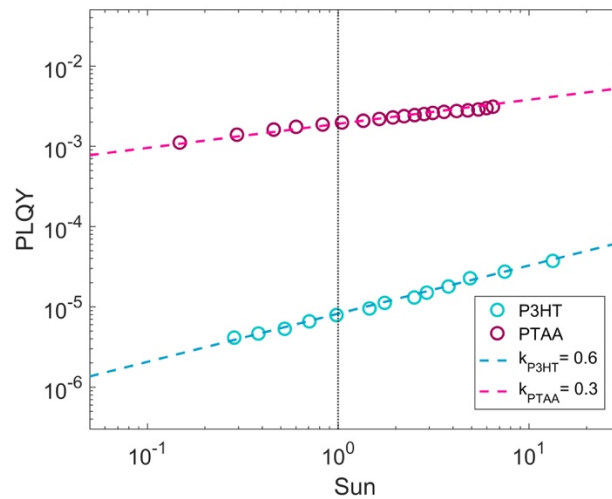


Figure 5.2: Intensity dependent photoluminescence quantum yield (PLQY) measured on two cells with P3HT and PTAA as hole transport layer respectively. The PLQY is generally higher for the PTAA case, indicating less non-radiative losses for this system.

Successively, we calculate the *internal* QFLS, the radiative limit of the QFLS, $QFLS_{rad}$, according to the method presented in **Chapter 2**. The details for these calculations with respect of these specific devices is presented in **Appendix 11.2**. The result is compared with the corresponding $QFLS_{rad}$ and the V_{OC} of the same cell in **Fig. 5.3a**. Several important findings can be discerned. First, the measured $QFLS(I)$ lies significantly below $QFLS_{rad}(I)$ over the entire intensity range and increases with a higher slope. This is also expressed by an $n_{id} > 1$ (compared to $n_{id} = 1$ for $QFLS_{rad}(I)$). Notably, the difference in the overall magnitude is significantly larger for the poorer performing device, which consistently exhibit a larger ideality factor. Second, for low to

intermediate intensity, depending on the system, $qV_{OC}(I)$ and $QFLS(I)$ increase with similar slopes. Notably, in this intensity range, the PTAA cell shows a good match ($< 10\text{meV}$) between V_{OC} and the $QFLS$, while for the P3HT cell, $qV_{OC}(I)$ remains below $QFLS(I)$ by at least 80 meV . When increasing the intensity further, for both devices the $qV_{OC}(I)$ starts to saturate, while the $QFLS(I)$ continues to follow the initial trend. Interestingly, the onset of the saturation is significantly different for the two samples. For all intensities considered here, the difference between $QFLS$ and the qV_{OC} is, however, smaller than the loss in $QFLS$ compared to its radiative limit, limiting the V_{OC} to significantly below its radiative limit even for the well performing device. Overall, the measurements of the $QFLS$ and V_{OC} on the same sample reveal important differences between these two quantities, in particular at higher illumination intensities. This, questions the accuracy of well-established characterization methodologies which make use of the intensity dependence of the V_{OC} as representative of the recombination processes inside the absorber. In the following, we will go step-by-step through the processes determining the intensity dependence of $QFLS$ and V_{OC} , and conclude with the overall recombination picture of the device at different illumination intensities.

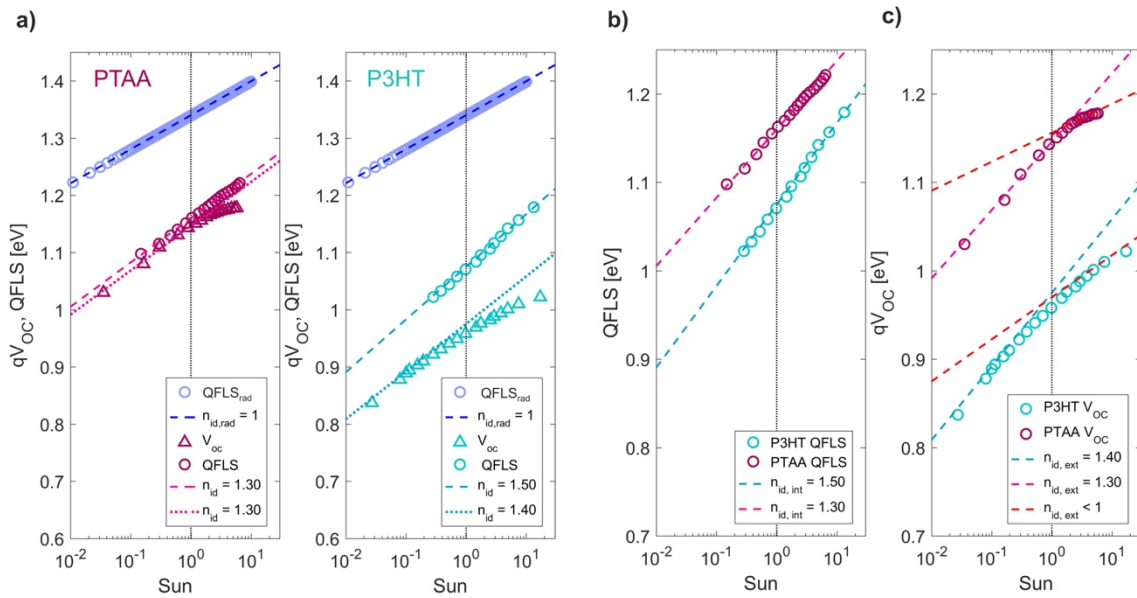


Figure 5.3: a) Comparison between qV_{OC} , $QFLS$ and $QFLS_{rad}$ of the corresponding solar cell using PTAA and P3HT as HTL respectively. The V_{OC} is directly measured, the $QFLS$ is obtained from PLQY measurements through Eq.5 and the $QFLS_{rad}$ is calculated analogously but assuming $PLQY = 1$. The $V_{OC}(I)$ measurements were performed on the same solar cell sample, illuminating the sample at exactly the same illumination intensity and light exposure as in the case of PL measurements. b) Internal ideality factor calculated from the dependence of the $QFLS$ on illumination intensity and c) external ideality factor calculated from the dependence of the V_{OC} on illumination intensity.

It is well established that the QFLS of state-of-the-art perovskite solar cells still lies well below the $QFLS_{rad}$. As detailed in **Chapter 2**, this is due to non-radiative losses, e.g. non-radiative recombination in the bulk and at interfaces and/or parasitic absorption.^[123,136,149] A possible way to look at the nature of these losses is to study the ideality factor.^[139] By definition, an ideality factor equal to 1 refers to only second order bimolecular recombination of free charges whereas, an ideality factor close to 2 is explained by a first order monomolecular recombination processes, e.g. symmetric trap-assisted recombination through mid-gap traps^[193]. Perovskite solar cells generally exhibit values between these extremes. This is usually indicative of a superposition of first and second order recombination mechanism, involving monomolecular and bimolecular recombination.^[194] There are two observations speaking against this interpretation. First, the competition between a first and a second order loss would be in favor for the first (second) order process at low (high) intensities, rendering n_{id} to be a function of intensity. This is in clear contrast to our observation that the measured $QFLS(I)$ has a constant slope throughout the entire intensity range. Second, the PLQY remains well below 1 % for both devices at even the highest intensity, meaning that radiative recombination is of minor importance. We, therefore, conclude that the recombination in our devices is dominated by one particular pathway, that this pathway is non-radiative, and that it is more efficient in the case of P3HT. Recently, $n_{id} = 1.5$ was attributed to non-radiative trap-assisted recombination where free holes recombine predominately with trapped electrons (but not the other way around).^[195–197] Our analysis of $QFLS(I)$ yields $n_{id,int} = 1.30$ and 1.50 for the device with PTAA and P3HT, respectively (we refer to the ideality factor obtained from QFLS as *internal* ideality factor, $n_{id,int}$). These values are below the above prediction of the recombination of free holes with trapped electrons, and they are distinctly different for the two hole-transporting materials. We will show below that our experimental findings are consistent with a model, where recombination of photogenerated charges is predominately across the perovskite/CTL interfaces.

At low to intermediate intensities, $QFLS(I)$ increases almost in the same way as $qV_{OC}(I)$, meaning that $n_{id,ext} \cong n_{id,int}$ (here we denote the ideality factor from V_{OC} as the *external* ideality factor, $n_{id,ext}$). In the case of PTAA the two ideality factors perfectly match, indicating that both V_{OC} and QFLS are determined by the very same recombination mechanism. On the other hand, in the P3HT case, the $n_{id,ext}$ is always a bit lower than the $n_{id,int}$ and qV_{OC} lies always below QFLS. This means that this recombination loss must occur predominately in the vicinity of the perovskite surfaces or near the electrodes, and it is stronger than in the bulk. In a previous study we have explained this finding by an energetic offset between the HOMO (LUMO) of the hole-(electron-) transporting material and the VB (CB) of the perovskite in conjunction with rapid interfacial recombination.^[189] As a result, the density of majority carriers in the perovskite becomes reduced specifically near the respective contacts, causing an upwards (downwards) bending of $E_{F,h}$ ($E_{F,e}$), which finally reduces V_{OC} compared to the QFLS in the perovskite bulk. We note that the exact interfacial offset is not known to us for the studied system, as we have no access to the energetics at buried interfaces. In both samples, at high densities, the V_{OC} starts to saturate and the internal and external

ideality factors deviate. The V_{OC} saturation phenomena has been observed for different type of solar cells, but a common consensus regarding its causes has not been reached in the community.^[139,191,192] Recent studies pointed out that the saturation of the V_{OC} can be explained by an increase in local temperature under high illumination conditions.^[198] However, several of our experimental findings disprove this model. First, measurements of the $V_{OC}(I)$ at different conditions, namely with and without temperature controller, and with different illumination exposure times, yielded the same results, see **Fig. 11.2.2A-B (Appendix 11.2)**. We also monitored the local temperature increase with an infrared sensor at the laser incident spot, which showed an only modest increase of about 2° C at 10 suns, regardless of the presence of the temperature controller. This indicates that the metal sample holder that carries the substrate (2.5 x 2.5 cm²) acts as a heat sink and it is sufficient to dissipate efficiently the heat produced by the rather small illumination spot of ~3x3 mm². Furthermore, from the PL spectra taken at different illumination conditions, it is possible to calculate the local temperature of the emissive volume,^[73,132,137] as presented in **Fig. 11.2.2C (Appendix 11.2)**. These data lack evidence for an appreciable increase in temperature when increasing the illumination intensity from 0.1 to 10 suns, during the short illumination time (~1 s). Finally, and most importantly, QFLS(I) exhibits a constant slope at even the highest intensity range. Given that the illumination conditions are the same when measuring $V_{OC}(I)$ and QFLS(I) on the same sample, and that $n_{id,ext} = n_{id,int}$ at intermediate intensities, Eq. 1 and Eq. 6 predict the very same effect of temperature on QFLS(I) and $V_{OC}(I)$, which is apparently not the case. We conclude that the saturation of the V_{OC} has to be caused by an additional non-radiative recombination loss, which specifically affects the V_{OC} , meaning this process occurs (again) near the perovskite surface and electrodes.

In order to shed more light on this matter, we perform one dimensional drift-diffusion simulations to model our two typical perovskite devices at different illumination conditions, using realistic solar cell parameters. The simulation relies on the model outlined in **Section 3.2**. This includes our complete multilayer stacks, with specific carrier lifetime and specific interface recombination velocities at the interfaces, implemented with mid-gap traps. To keep the number of fit parameters as small as possible, most of them were set constant using reasonable values from the literature or from our own simulation work. **Table 11.2.1 in Appendix 11.2** lists the final set of values, including the parameters that were kept variable to fit the data. This simple model gave a fairly good fit of the observed QFLS(I) and $V_{OC}(I)$ data at low and intermediate intensity, but we were not capable to explain the saturation of the V_{OC} (and the lack of the QFLS saturation) at high intensity. We found out that in order to reproduce the V_{OC} saturation it is necessary to add a new recombination pathway that becomes relevant exclusively at sufficiently high minority carrier density. To account for this, we added a further trap at the perovskite/HTL interface, located above (or at) the perovskite conduction band (CB), outside its band gap. This situation is presented schematically in **Fig. 11.2.3A (Appendix 11.2)**. In the limit that the filling and detrapping of this state is faster than its draining through recombination with a hole on the HTL, the trap occupation, n_T , follows the Fermi-Dirac statistic, meaning that the

density of occupied traps is nearly proportional to the electron density (minority carrier density) at the interface: $n_T \propto n_e$. Then, with an intensity dependent hole density at the interface, $n_h(I)$, the rate of interfacial recombination becomes $R(I) \propto n_h(I) \times n_T \propto n_h(I) \times n_e(I)$, meaning that it's a higher order process. In fact, when we conduct simulations with only the new recombination channel being active, we get an $n_{id} = 1.2$, which is fairly close to the $n_{id} = 1$ obtained with exclusively radiative second order recombination. For the PTAA cell, this model gives an excellent fit to the experimental results, matching nicely the internal and external ideality factors $n_{id,ext} \cong n_{id,int} = 1.3$, as well as the onset and extent of the V_{OC} saturation (**Fig. 5.4a**). Interestingly, when in the simulation model the additional recombination channel is deactivated for the PTAA cell, **Fig. 11.3.3D (Appendix 11.2)**, the QFLS and the V_{OC} matches throughout all the intensity range, with $n_{id,ext} \cong n_{id,int} = 1.4$. A detailed analysis of the rates and internal currents reveals that most recombination proceeds through interfacial states and is non-radiative. As such, an ideality factor of 1.4 is neither characteristics for the competition between radiative ($n_{id,int} = 1$) and trap-assisted ($n_{id,int} = 2$) recombination, nor it allows conclusions about the nature and energy of traps inside the perovskite. Instead, we find that the value of n_{id} depends mainly on the energetics at the interface and the related capture rates for carriers at both side of the heterojunction. A detailed study on these is presented in **Chapter 6**. For the P3HT device, we add an energetic offset of 0.2 eV between the HOMO of the HTL and the VB of the perovskite in order to reproduce the QFLS - V_{OC} mismatch at low-intermediate intensities.^[189] Also, the position of the additional trap state was moved closer to the perovskite CB. This increases the effectiveness of this additional recombination path and leads to an earlier onset of the saturation of the V_{OC} . Additional simulation show how varying the position and the recombination velocity of these trap states is determinant for the onset and degree of V_{OC} saturation, see **Fig. 11.3.3B, Appendix 11.2**. We note here that when the additional trap is removed, the difference between the V_{OC} and the QFLS is maintained due to the majority carrier offset. Here, a modest difference between $n_{id,ext}$ and $n_{id,int}$ is still present. As expected, the implementation of this additional recombination channel has also an overall effect on the QFLS, generally lowering it when active, **Fig. 11.2.5d, in Appendix 11.2**. Interestingly, the difference is more pronounced in the PTAA case, where also a change in slope is observed, compared to the P3HT where the strong surface recombination due to the energetic offset is alleviating the effect of the new channel. Independent of these details, the very good agreement of the simulation results and the experimental data suggests the presence of a recombination channel that allows electrons to enter the HTL via states that are close to the CBM, as schematically represented in **Fig. 4c**. This is equivalent to the situation of a contact with reduced selectivity. We, therefore, modelled a second situation where the contact is completely non-selective. As presented in **Fig. 11.2.4A-B (Appendix 11.2)**, in this scenario, the minority carriers are able to directly enter the HTL and to recombine with the majority carrier either at the contacts or in the HTL. In this extreme case, the V_{OC} is limited by the work function difference between the two metal contacts, i.e. the built-in field. A similar picture has been already proposed in the case of silicon solar cells, where back contact

recombination has been introduced and modelled as an opposite diode activated only at sufficiently high carrier density.^[191] While this model can explain the V_{OC} saturation, the complete unselectivity of the HTL implemented in our simulation can represent an over exaggerated scenario that leads to too low V_{OC} s compared to our devices.

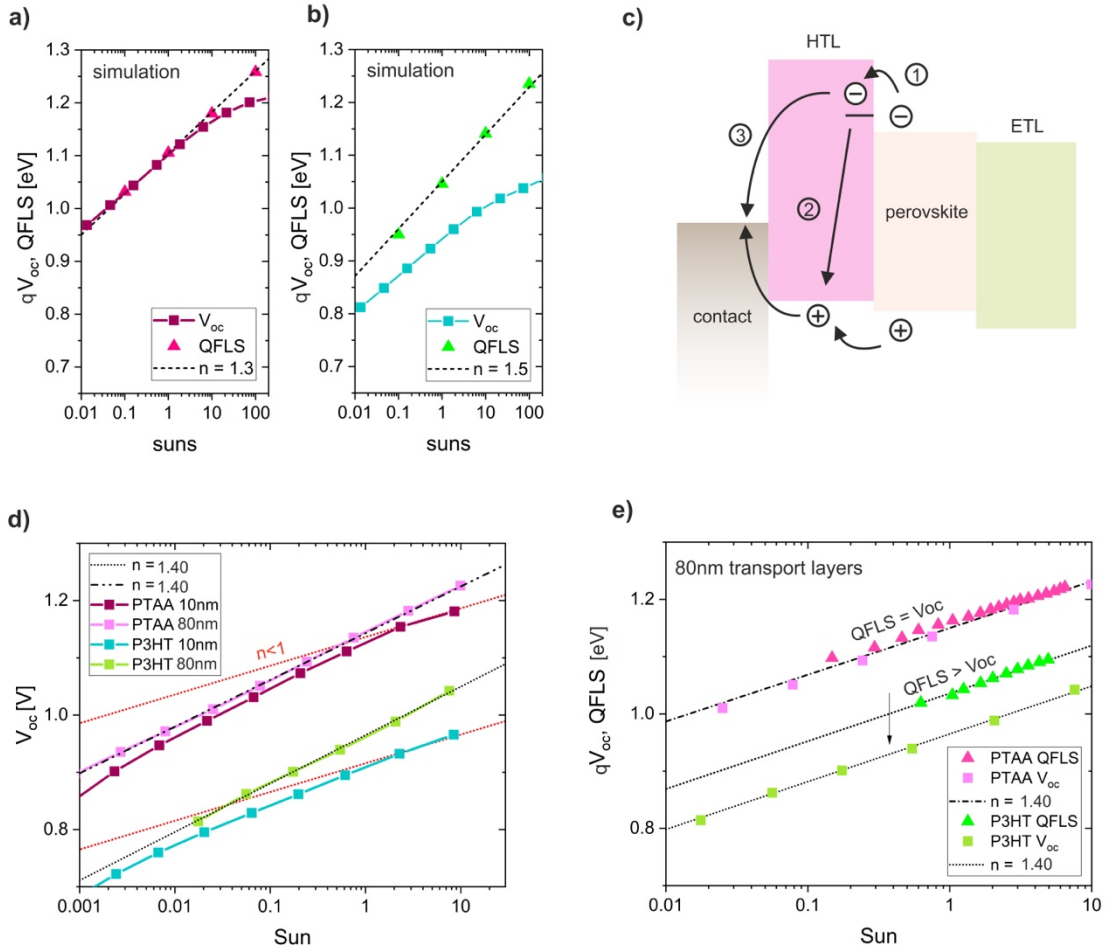


Figure 5.4: Intensity dependent drift diffusion simulation results for two different solar devices utilizing a) PTAA and b) P3HT using the first saturation-model. c) Schematic representation of the possible recombination processes that cause the V_{OC} saturation. (1) Electrons can reach the HTL either by additional high-energy interfacial states or by the lack of selectivity of the HTL at certain points of the substrate. Consequently, the electrons on the HTL now can recombine with the holes in the HTL (2) or they can reach the contacts and undergo recombination there with the holes trying to reach the external circuit (3). d) Experimental results of the effect of the HTL thickness on the $V_{OC}(I)$ and ideality factor measurements. e) Experimental results of the QFLS(I) and $V_{OC}(I)$ comparison for solar cells using 80 nm PTAA and P3HT respectively as HTL.

These simulation results suggest a third option, namely that the non-ideal coverage provided by the very thin HTL layer (~ 10 nm) introduces an additional direct recombination channel between the contact and the perovskite, gradually becoming stronger at high illumination intensities. Motivated by the results of the simulations, we

measured the QFLS(I) and $V_{OC}(I)$ on cells with different thickness of the HTL, with exemplary results shown in **Fig. 5.4d-e**. The usage of thicker transport layers totally prevents the saturation of the V_{OC} across the whole intensity range of the experiment. The *external* ideality factor from the $V_{OC}(I)$ is constant and approaches the same values of the *internal* one for both systems. Notably, in the PTAA case the QFLS and V_{OC} match, whereas for the P3HT the QFLS - V_{OC} energetic mismatch is still present, consistently with the simulation in **Fig. 11.2.4C, Appendix 11.2**. This gives strong empirical evidence that the saturation of the V_{OC} is caused by a recombination process related to the partial loss of selectivity of the hole-extracting contact and not to processes within the perovskite bulk. Possibly, a thicker HTL provides a better coverage of the ITO substrate, preventing direct accessibility of the minority carriers (electrons) to the wrong contact, either by direct contact, by tunneling, or through additional states caused by the interaction between the ITO substrate and the perovskite. Additionally, a thicker polymeric layer can form a smoother surface, reducing the perovskite crystal strain and the probability to have non-ideal crystal formation at the interface, which can conceivably lead to interfacial defects above the perovskite bandgap.^[199,200] This finding indicates that, from an energetic point of view, the selectivity of the HTL used in this work is itself sufficient to block the minority carriers and it's not responsible for the saturation of the V_{OC} .

The two regions identified during the analysis of the *internal* and *external* ideality factor in devices with optimized, extremely thin (~ 10 nm) transport layers represent essentially two different types of recombination mechanisms. Generally, when $n_{id,ext}$ and $n_{id,int}$ are equal this means that the recombination processes affects the QFLS and the V_{OC} in a very similar way, involving the charge carrier distribution in both the perovskite bulk and its interfaces. On the other hand, the transition of $n_{id,ext}$ towards lower values, compared to $n_{id,int}$, implies the presence of an additional recombination pathway near or at the perovskite/TL interface that has a much larger effect on the V_{OC} compared to the QFLS. In this case the extra recombination pathway depletes the carrier reservoir near the perovskite surface faster than it can be replenished from the bulk by photogenerated carriers. As the hole current density towards the contact is given by $J = n_h \mu_h \nabla E_{F,h}$ (with μ_h the hole mobility), the upwards bending of $E_{F,h}$ increase with the hole density n_h in the HTL. This is the situation realized in the sample with a P3HT as HTL. **Fig. 5.5** visualizes schematically the relation between the QFLS and the V_{OC} for different illumination condition in the different type of devices, based on the results of our drift-diffusion simulations in **Fig. 11.2.3C, Appendix 11.2**. The scheme clearly shows that the quasi-Fermi levels $E_{F,e}$ and $E_{F,h}$ propagate flat throughout the bulk of the absorber, but significant bending at the perovskite/HTL interface can occur. This process results eventually in a lower V_{OC} and a consequent mismatch with the QFLS in the bulk, and the consequent failure of the S.Q. theory. This picture strongly highlights that the V_{OC} cannot always be truly representative of the recombination mechanisms occurring in the absorber and at its surfaces, but can lead to a misinterpretation of the recombination behavior. Additionally, this knowledge can be utilized be for future solar cell improvement and development of new transporting layers strategies. In order to exploit the full potential of the material, these additional

losses must be eliminated, especially for operational conditions at high carrier concentration. We propose that a perfectly aligned and fully blocking transport layer, which completely prevent the accessibility of the minority carriers and does not introduce an energetic offset for the majority carriers, is able to prevent the V_{OC} saturation until relatively high intensity and to nullify the QFLS $-V_{OC}$.

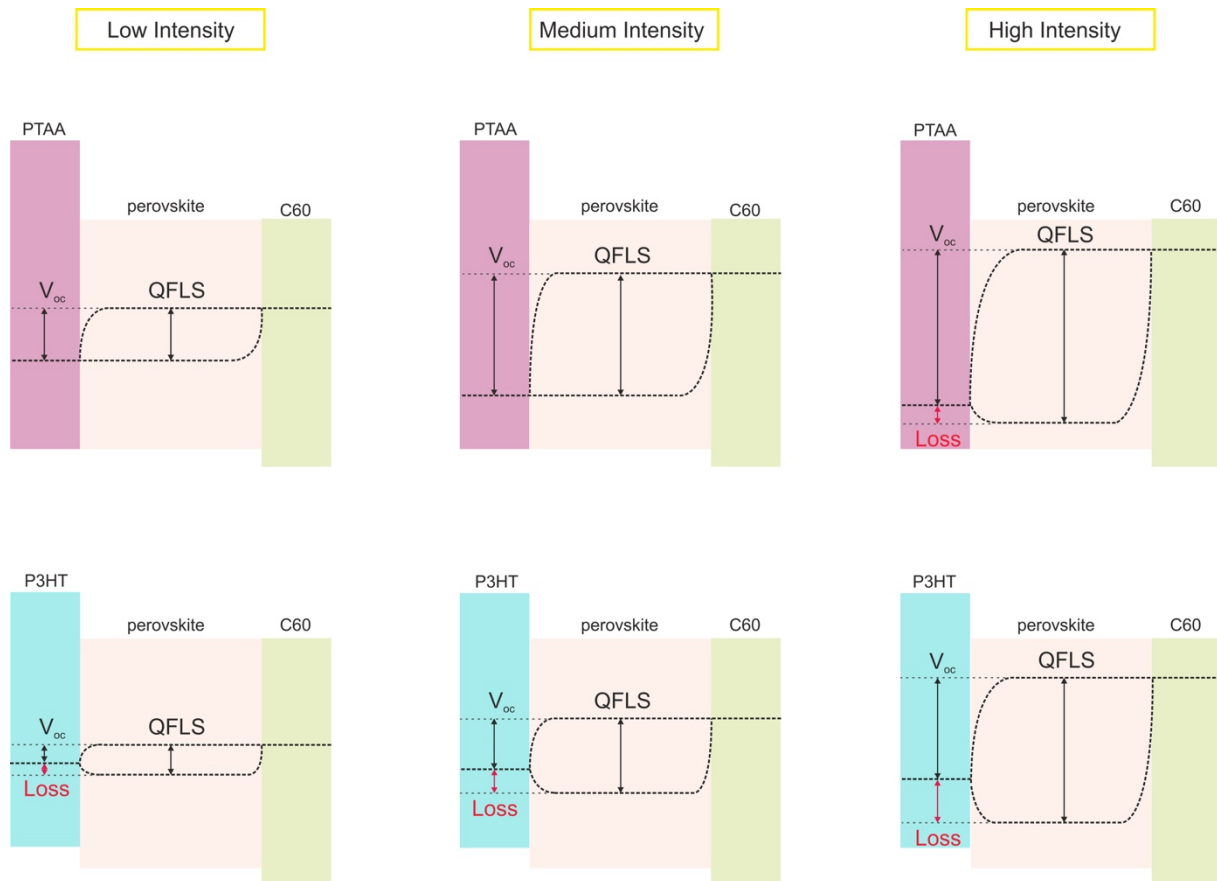


Figure 5.5: Schematic representation of the relation between the QFLS and the V_{OC} for different illumination intensities in the solar cells employing P3HT and PTAA as hole transport layer. The schemes have been derived from the results of drift-diffusion simulations in **Fig. 11.2.3C (Appendix 11.2)** The dashed lines in the perovskite layer represent the $E_{F,e}$ and $E_{F,h}$ defining the QFLS, whereas the external V_{OC} is given by the respective energy levels at the contacts. The graph highlights the detrimental effects of P3HT on the V_{OC} of the cell, especially at high illumination intensities.

Chapter 6.

6. On the Origin of the Ideality Factor

This chapter is an adapted preprint of the publication:

Caprioglio, P., Wolff, C. M., Sandberg, O. J., Armin, A., Rech, B., Albrecht, S., Neher, D., Stolterfoht, M. On the Origin of the Ideality Factor in Perovskite Solar Cells. Accepted in *Adv. Energy Mater.* (2020)

The research presented in this chapter comes as complementary continuation of the research presented in **Chapter 5**. Although in that publication we observed ideality factors between 1 and 2 and attributed this to non-radiative interfacial recombination rather than to radiative bimolecular recombination, no extensive investigation on the origin of these values have been performed nor a physical model has been provided. Here we combine intensity dependence QFLS measurements on the perovskite absorber, perovskite/transport layer junctions and full devices with drift-diffusion simulations in order to investigate the origin of these ideality factor values. We then use an analytical approach to rationalize these values with a recombination model exclusively based on SRH recombination. Here, we explain how an ideality factor of nearly 1 in perovskite solar cells, is usually indicative of strong first order non-radiative interface recombination and that it correlates with a lower device performance.

One of the most popular approaches to assess the dominant recombination mechanism is the measurement of the ideality factor (n_{id}).^[130,141,197,201,202] As introduced in **Chapter 2**, $n_{id} = 1$ is assumed to be representative of a second-order (bimolecular) radiative recombination of free charges, whereas $n_{id} = 2$ is attributed to a first-order (monomolecular) non-radiative recombination process, e.g. trap-assisted recombination through mid-gap trap states.^[193,203] In this picture, reported values of the n_{id} between 1 and 2 in efficient perovskite solar cells suggest a superposition of first- and second-order recombination where the value of n_{id} depends on the relative strength of one or the other process. However, this often-used approach to connect the value of the ideality factor to the order of recombination relies on several critical assumptions. The first one is that the very same carrier reservoir determines all recombination processes, meaning that the recombination current, J_R , can be written as $J_R \propto k_1 n + k_2 n^2 + k_3 n^3 \cong k_\alpha n^\alpha$, where α is the effective recombination order at the respective carrier density n , in the case equal electron and hole density. The second assumption concerns the relation between n and the external voltage (V), which is assumed to follow an exponential dependence $n \propto e^{\left(\frac{qV}{\vartheta k_B T}\right)}$, where ϑ is a parameter describing the density of state distribution at the band edge,^[204,205] $k_B T$ is the thermal energy and q the elementary charge. This approximation, however, requires that the electron density is proportional to the hole density at the sites dominating recombination ($n_e \propto n_h \propto n$). Only then the ideality factor is related to the recombination order via the well-known relation $n_{id} = \vartheta/\alpha$. None of these conditions is fulfilled in perovskite solar cells.

As pointed out above, the recombination under a 1 sun equivalent illumination intensity in *pin*-type perovskite solar cells is mainly a first order non-radiative trap-assisted process at the perovskite/TL interface. Radiative second order recombination, on the other hand, is believed to originate strictly from the perovskite absorber, as there is no evidence for additional interfacial radiative recombination in the EL and PL emission spectra of the complete devices. Therefore, it is likely that first and second order recombination processes are controlled by different carrier reservoirs. Secondly, as we showed in details in **Chapter 5**, a strong interface recombination will drive a current of electrons and holes towards the respective TL even at V_{OC} , potentially causing the V_{OC} to be smaller than the QFLS in the perovskite. Consequently, analyzing the total recombination current as a function of V_{OC} may lead to wrong conclusions about the mechanism of the recombination in the absorber and at its interfaces to the TLs.^[206,207] In **Chapter 5**, we found the ideality factor of devices using PTAA as HTL to be around 1.3, which we could consistently attribute to trap-assisted recombination regardless of involving radiative second order recombination. Moreover, we found that recombination at the metal contacts may lead to a saturation of the V_{OC} despite increasing carrier density in the bulk, resulting in n_{id} approaching a value of 1 (or even decreasing below this value) at high intensities (typically above 1 sun). Nevertheless, in the existing literature only a few successful attempts to interpret and address the origin of the n_{id} values have been reported in literature.^[141,158,208,209]

Here, we extend these studies by utilizing intensity dependent PL measurements on perovskite films with and without transport layers in order to obtain the internal n_{id} (from QFLS) of the individual junctions of the cell and the neat material, with the aim of understanding and rationalizing the origin of the n_{id} values previously observed.^[130,207] This allows us to study the impact of a particular interface on the n_{id} with the aim to ultimately understand which recombination mechanism controls its value in the full cell. In particular, we find that the single perovskite/C₆₀ junction, responsible for the majority of the energy losses, and the complete device exhibit an almost identical ideality factor, which suggests that this interface governs the ideality factor of this cell. On the other hand, despite an overall higher QFLS, a passivated neat perovskite film presents a higher n_{id} value due to reduced surface recombination.^[210] By corroborating our results by drift diffusion simulations, we clarify that a single non-radiative recombination process at the interface can alone cause such *mixed* (between 1 and 2) n_{id} values. We study the impact of a broader range of parameters on the n_{id} , such as the interface recombination velocity and the majority carrier band offset. We thoroughly explain, experimentally and theoretically, that a low ideality factor in many cases correlates to low V_{OC} s and poor device performances. Based on an analytical model, we explain how SRH recombination at the perovskite/TL interface accounts for such low n_{id} values in all devices in this study. In this picture, the ideality factor of the cell depends essentially on the asymmetry of the electron and hole quasi-Fermi levels at the dominant recombination site. As previously observed empirically,^[141,211] here we rationalize how in interface limited solar cells, $n_{id}=1$ is not a result of bimolecular recombination of free charge carriers and does not necessarily correspond to a better performing device, as often assumed.

Our combined experimental/simulation study focusses on *p-i-n* type “triple cation” perovskite solar cells utilizing PTAA and C₆₀ as HTL and ETL, respectively. Also here, the nominal composition of the perovskite absorber is (Cs_{0.05}(MA_{0.17}FA_{0.83})_{0.95})Pb(I_{0.83}Br_{0.17})₃, with an optical bandgap of 1.62 eV.^[22] In the configuration, the devices studied here regularly exhibit PCEs around 20% and they are characterized by V_{OC} s of 1.14 V and FFs of 78%.^[127,207] **Fig. 11.3.1 (Appendix 11.3)** displays *JV*-characteristics measured in forward and reverse direction with different scan speeds. The comparatively small hysteresis at different scan rates suggests a minor effect of ion motion on the device characteristics under operational conditions. As shown in the previous chapter, recombination in such devices is determined by non-radiative interfacial recombination, which limits the PLQY to values well below 1%. Despite the insignificance of radiative recombination in the bulk, these devices have ideality factors of approximately 1.3. If n_{id} would be entirely determined by the competition between non-radiative first order and radiative second order recombination of the same carrier reservoir (see **Section 11.3.5** for full derivation), then

$$n_{id} = \frac{2}{(1 + PLQY)} \quad \text{Eq. 6.1}$$

Note that PLQY will generally differ from the internal PL quantum efficiency (IQE) by the outcoupling efficiency and parasitic losses.^[212,213] For the considered cells, the PLQY is approximately 0.1 %. In this case, **Eq. 6.1** predicts $n_{id} \cong 2$, which is well above the measured value. Therefore, this shows that radiative recombination cannot be responsible for the ideality factor in our devices (~ 1.3). To show how different parts of the device determine the value of n_{id} , we performed intensity dependent photoluminescence (PL) measurements on different layer combinations, including the neat surface-passivated perovskite absorber, different perovskite/transport layer junctions (perovskite/ETL, perovskite/HTL) and the complete device. The neat perovskite is surface-passivated with TOPO^[73,214] in order to probe mainly the recombination in the perovskite bulk (PLQY $\sim 5\%$ under 1 sun conditions). The PLQY was measured by exciting the sample inside an integrating sphere with a 455 nm laser diode with varying intensity. In order to avoid possible effects induced by the illumination exposure time, all measurements have been performed under the exact same conditions with illumination time of ~ 1 s for each point. In these regards, it has been noted that transient effects could influence the determination of n_{id} from $V_{OC}(I)$ measurements.^[202] We, therefore, performed measurement of the PLQY and V_{OC} as function of illumination intensity with different exposure times (see **Fig. 11.3.2, Appendix 11.3**). Importantly, no significant variation was found within the timeframe studied here, confirming the robustness of our results and their relevance for operational conditions. From these results, the QFLS in the perovskite absorber was calculated at each intensity, following the approach as outlined in our previous works,^[207] (see also **Fig. 11.3.3, Appendix 11.3** for further details). Note that the QFLS of the complete device was measured at open circuit conditions. We, finally, determined the internal and external ideality factor by fitting QFLS(I) and $V_{OC}(I)$, respectively, as detailed in **Chapter 5**. Here, $J_R(I)$ is the intensity dependent recombination current density, which is equal to the generation current density at V_{OC} and J_0 is the dark saturation current density.

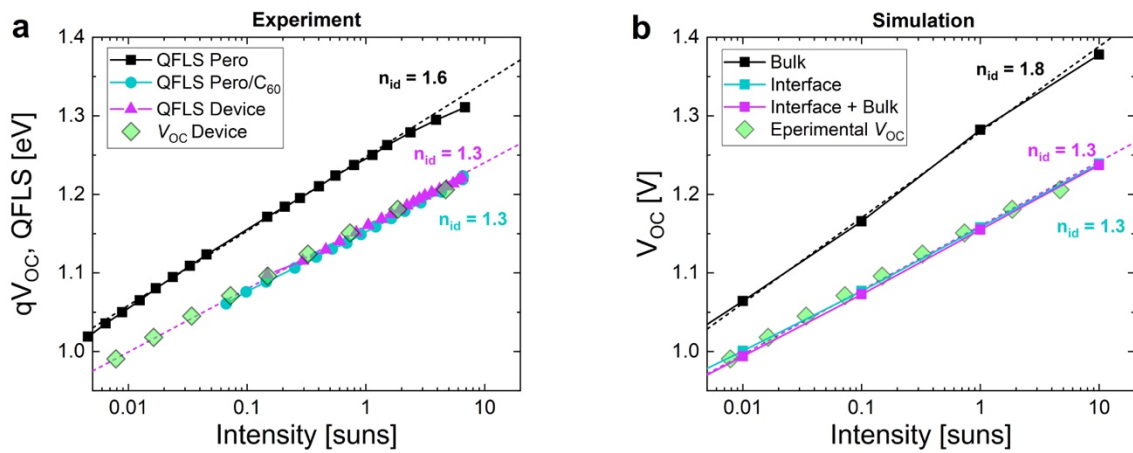


Figure 6.1: a) Intensity dependent quasi-Fermi level splitting, $QFLS(I)$, of a neat TOPO-passivated perovskite, a perovskite/ C_{60} bilayer and a complete device structure (including

electrodes) in addition to the intensity dependent V_{OC} of the device. Dashed lines show fits to an exponential dependence on the illumination intensity, yielding the internal ideality factor. b) $V_{OC}(I)$ as obtained from drift-diffusion simulations of a typical perovskite solar cell utilizing PTAA and C_{60} as HTL and ETL, respectively. The results show the effects of different recombination types on the ideality factor. The ideality factor is largest when only radiative and non-radiative bulk recombination is considered (black) as compared to the case of interface recombination only (turquoise) or a combination of interface and bulk recombination (magenta), in good agreement to the experimental results.

The results are shown in **Figure 6.1a**, together with the intensity dependent V_{OC} of the device. In agreement with previous results, for the complete device the fit of the intensity dependent QFLS yields $n_{id,int} \sim 1.3$, and this value is nearly identical to the value of $n_{id,ext} \sim 1.3$ as deduced from the intensity dependence of the V_{OC} , provided that leakage through the thin PTAA layer can be avoided.^[207] Notably, the neat TOPO passivated perovskite has a $n_{id} \sim 1.6$, which is significantly larger than that of the full device. However, when the C_{60} layer is attached to the perovskite (on glass), the n_{id} value drops to roughly 1.3; the same value as of the complete cell. We have recently shown that the performance of such PTAA/perovskite/ C_{60} *pin*-type cells is dominated by non-radiative recombination at the perovskite/ETL interface.^[127,206] Therefore, we conclude that 1) interfacial recombination leads to lower n_{id} compared to the recombination in the bulk and 2) the recombination at the least optimum interface (here the perovskite/ C_{60} interface) determines the ideality factor of the complete cell. Importantly, for this type of devices, the internal QFLS and external V_{OC} match within the light intensity regime studied here. Lastly, we note that the non-passivated perovskite lies in between with $n_{id} = 1.45$ (**Fig. 11.3.4, Appendix 11.3**). This suggests that the recombination at the perovskite surface results in a similar n_{id} as the C_{60} interface.

To confirm this experimental insight, we performed drift diffusion simulations using our simulation model, detailed in **Section 3.2** and already used in the previous chapter. All simulation parameters are listed in **Table 11.3.1** in **Appendix 11.3.6**. Importantly, values of the interface recombination velocities and bulk lifetimes were determined from transient photoluminescence (TRPL) while energy offsets at the HTL/perovskite interface were measured with Ultraviolet Photoemission Spectroscopy (UPS).^[127,206] For the passivated perovskite we estimated a bulk lifetime of $1\mu s$. Values for the carrier mobilities in the different layers were optimized by fitting the *JV*-curves of samples with different layer thickness. The corresponding data and simulation results are shown in **Figure 11.3.5, Appendix 11.3**. The resulting *JV* curve and the voltage dependent recombination losses (in the bulk, interface, contacts etc.) corresponding to our standard settings are shown in **Fig. 11.3.6, Appendix 11.3**. Although the simulation tool used here does not include ion motion in the absorber layer, given the excellent match of the simulations with a large number of different experiments and the absence hysteresis in our device, we believe that for the particular system studied here, using fullerenes as ETL, the ion movement is not a decisive parameter, consistent with previous reports.^[94] Overall, the simulations can well reproduce the intensity

dependence of the V_{OC} of our cells as shown in **Fig. 6.1b**. Moreover, the ideality factor of the device is identical (~ 1.3) regardless whether recombination in perovskite bulk (both radiative and SRH) is implemented or not. In contrast, if we consider only bulk recombination (device with ideal interfaces), then the ideality factor is considerably higher (~ 1.8). Here, we implemented a SRH lifetime of $1 \mu s$ (for the passivated perovskite) and a $k_2 = 6 \cdot 10^{-11} \text{ cm}^3/\text{s}$ ^[215] (see **Appendix 11.3.6** for other settings). Importantly, as expected from **Eq. 6.1**, k_2 has a certain impact on the ideality factor at high intensities, above 1 sun, when the PLQY becomes significantly large (**Fig. 11.3.7, Appendix 11.3**). It is also important to note that the constant slope of the QFLS vs. I in the case of the device and the perovskite/ C_{60} bilayer suggests that n_{id} is dominated by a single recombination process (within the studied intensity regime). This indicates that n_{id} values between 1 and 2 do not originate from a competition of different recombination mechanisms, which would rather result in a change of slope when a different recombination mechanism takes over. We also note that in the neat passivated perovskite, we observe a bending of the QFLS at high intensities (10 suns) where bimolecular recombination is presumably starting to be the predominant recombination mechanism. Importantly, we have previously ruled out that heating is a determinant factor in causing this deviation at high intensities.^[207]

Considering the relevance of the perovskite/TL interface in determining n_{id} , we performed simulations for a wide range of interfacial recombination velocities (S) and majority carrier band offsets (E_{maj}) at the HTL/perovskite interface. Note that from here on we will discuss the impact of these parameters on the external n_{id} . This was inspired by previous works which revealed a large effect of these parameters on the V_{OC} of *pin* devices.^[206,207] We kept an S of 2000 cm/s with no energy offset at the *n*-interface, while the injection barrier at the metal at both sides was kept constant. In **Fig. 6.2**, we plot the ideality factor (**Fig. 6.2a**) and the device V_{OC} (**Fig. 6.2b**) vs. S and E_{maj} . Several findings are important. First, the ideality factor drops rapidly to one (or even below) when increasing the majority carrier band-offset (the blue region in **Fig. 6.2a**), even for small surface recombination velocities, while the drop of V_{OC} is more continuous. This reminds of the situation of dominant surface recombination.^[139,216,217] On the other hand, when increasing S with an ideal band alignment ($E_{maj} = 0 \text{ eV}$), the decrease of n_{id} is less sudden, and it remains above one. Finally, its only for $E_{maj} \leq 0.1 \text{ eV}$ and $S < 1000 \text{ cm/s}$ that $n_{id} \sim 1.3-1.4$, consistent with our experimental data. Importantly, none of the input parameters yields $n_{id} = 2$, as would have been predicted for predominate trap-assisted recombination by the simple model introduced above. In contrast, reducing the quality of the perovskite/TL interface decreases the value of n_{id} (along with a decrease of the V_{OC}), irrespectively of whether E_{maj} , S or both of them is increased. Therefore, in most cases a small n_{id} indicates the presence of a non-ideal interface rather than predominant radiative recombination. In other words, the plot shows that an n_{id} of 1 is not necessarily representing an efficient cell as often believed (as observed in other works).^[218,219]

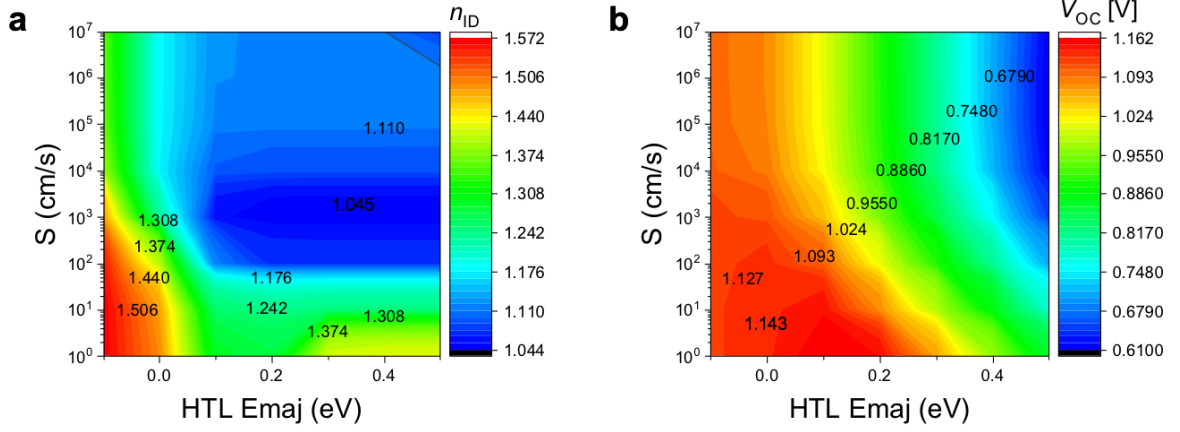


Figure 6.2: a) Numerically simulated external n_{id} and open-circuit voltages b) as a function of the interface recombination velocity S and the majority carrier band offset (E_{maj}) for holes at the HTL/perovskite interface. The blue area in panel a) shows a region with strong interfacial recombination which results in an ideality factor of 1 and a low device V_{OC} b). In contrast, weaker interface recombination (small energetic offsets and low S) cause an ideality factor of $\sim 1.3 - 1.4$ as observed in our optimized cells.

In order to provide further insights into the origin of these ideality factor values, we analyzed the hole (n_h) and electron (n_e) densities at the spatial location in the device where most of the recombination happens. Notably, the recombination rate at this location sets the upper limit for V_{OC} at a given intensity and therefore defines the ideality factor. Given that the PLQY of all of our devices is below 1 %, we consider only SRH trap mediated recombination rate in the bulk and/or at the interfaces. In the case of imbalanced carrier densities (e.g. $n_e \ll n_h$) and mid-gap trap states (with negligible de-trapping), the recombination rate will be almost entirely determined by the minority carrier density (e.g. electrons) (extended derivation in **Appendix 11.3.7**). Then, the recombination rate can be written in terms of the QFLS at the location of predominant recombination as follows:

$$R_{SRH}(I) \propto n_{min}(I) \propto e^{\left(\frac{E_{F,min}(I) - E_F^0}{k_B T}\right)} \propto e^{\left(\frac{\Delta E_{F,min}(I)}{k_B T}\right)} \propto e^{\left(\frac{\theta \times QFLS(I)}{k_B T}\right)} \propto e^{\left(\frac{QFLS(I)}{n_{id} k_B T}\right)} \quad Eq. 6.2$$

where $n_{min}(I)$ is the intensity dependent density of the minority carriers at the recombination site, $E_{F,min}$ is the quasi-Fermi level of the minority carriers, E_F^0 is the intrinsic Fermi level in the dark, $\theta \times QFLS(I)$ is the minority carriers share of the total QFLS increase when increasing I . According to **Eq. 6.2**, this situation leads to

$$n_{id} = 1/\theta \quad Eq. 6.3$$

In other words, the value of n_{id} is given by the share of the QFLS that $E_{F,min}$ gets when the QFLS increases as function of light intensity. In the extreme case where the majority

carrier density is fixed and the increase of the QFLS is only due to the increase of the minority carriers, the ideality factor is 1 despite the fact that all recombination is due to first order non-radiative processes (See **Appendix 11.3.7** for derivation). On the other hand, when n_e and n_h at the recombination site are nearly equal (for example when the recombination happens in the bulk or in case of a near-ideal interface), the quasi-Fermi levels for electron and holes ($E_{F,e}$ and $E_{F,h}$) would share the total QFLS symmetrically, resulting in an n_{id} of 2. **Fig. 6.3** visually depicts the scenarios of the two cases described above. Note that interface recombination may cause a significant bending of the majority quasi-Fermi levels in the perovskite bulk ($E_{F,e}$ at the ETL and $E_{F,h}$ at the HTL), which has its origin in the depletion of the majority carrier density in the perovskite near the TL due to a large energy offset in combination with fast surface recombination. Therefore, the measured V_{OC} will not necessarily be equal to the QFLS at the dominant recombination side, however this is considered in the model. The situation becomes less complicated if this band bending exists only at one of the interfaces and if this is the interface of predominant recombination. The reason is that qV_{OC} is the difference between the Fermi levels at the two contacts, which in this special case, is identical to the QFLS at the dominant recombination region.

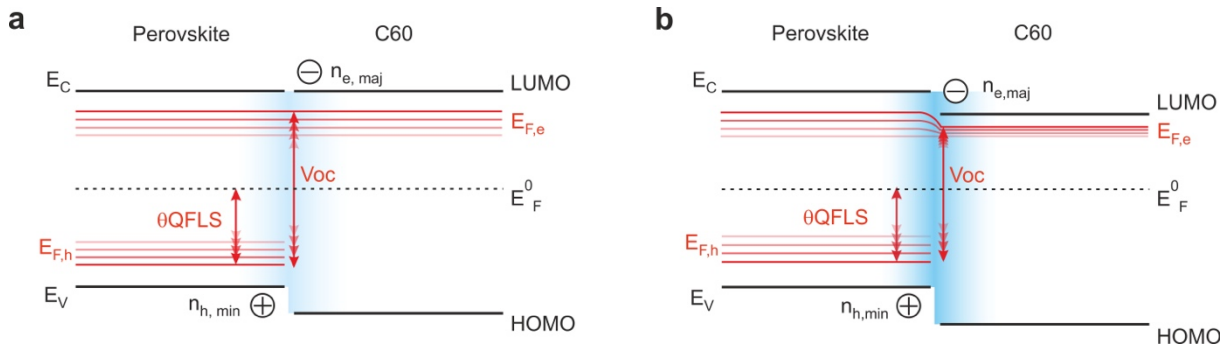


Figure 6.3: Schemes of interfacial energy levels and quasi-Fermi level splitting (QFLS) based on a simulated energy diagram. Importantly, this picture only represents the situation in close proximity to the interface and we acknowledge that inside the individual layers additional space charge effects might be present influencing the internal electric field. a) Exemplified is a scenario with negligible interface recombination and perfect energy alignment, where the electron and hole carrier densities are balanced and the splitting of the quasi-Fermi levels is symmetric. In this case, the minority carrier share of the total QFLS increase (θ) is 0.5. According to Eq. 3, this would give an $n_{id} = 1/\theta = 2$ in the case of dominant SRH recombination through mid-gap states. b) Example of a scenario with fast interface recombination and energetic offset, where the electron and hole carrier densities are unbalanced and the splitting of the quasi-Fermi levels is asymmetric. This scenario would give an n_{id} between 1 and 2 because the QFLS increase steams mostly from minority carriers (θ close to 1).

Numerical simulations and V_{OC} vs. I experiments of systems giving different n_{id} are exemplified in **Figure 6.4a**. For these systems, in **Figure 6.4b-e**, we plot the simulated

n_h (n_e) and $E_{F,e}$ ($E_{F,h}$) at the site of predominant recombination as function of intensity and V_{OC} , respectively, in order to visualize the symmetry of the QFLS and corroborate the validity of our approach to explain the simulated and experimentally determined n_{id} . Here, the study is expanded to perovskite solar cells with different HTLs characterized by different majority carrier energetic offsets and interface recombination at the p -interface, namely undoped P3HT ($E_{maj} \sim 0.2$ eV) and doped PEDOT:PSS ($E_{maj} \sim 0.4$ eV).^[206,207] Consistently with earlier studies, both type of devices show ideality factors approaching 1 and low V_{OC} s.^[101,158] Importantly, given the large energetic offset and the strong interface recombination, these two systems exhibit a significant mismatch between QFLS in the bulk and the V_{OC} . However, in case of predominant recombination at the perovskite/TL interface, the QFLS in the perovskite is irrelevant for the interfacial recombination rate and the recombination rate is determined by the difference of the electron and hole quasi-Fermi levels at the HTL interface, which in case of only one dominant interface is equal to the V_{OC} (see **Fig. 6.3** and **Fig.11.3.8A Appendix 11.3**)

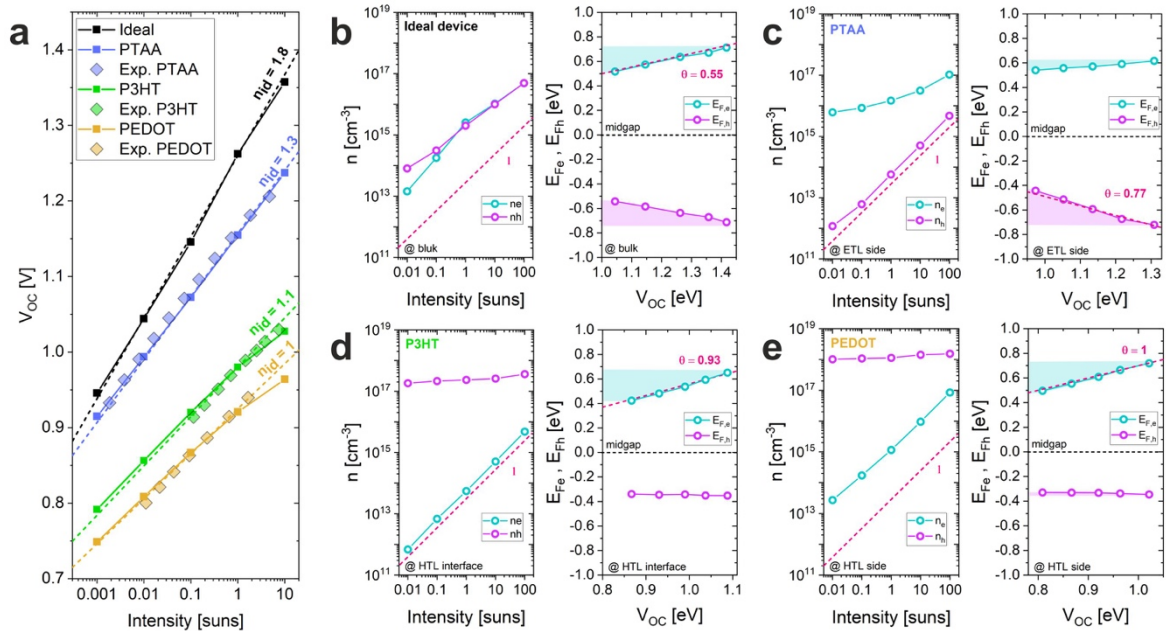


Figure 6.4: a) V_{OC} versus intensity obtained from experimental and numerical simulations of perovskite solar cells utilizing PTAA, P3HT and PEDOT:PSS as hole transport layer (HTL) and C_{60} as electron transport layer (ETL), respectively. We note that where the PEDOT:PSS is slightly thicker (~ 20 nm), the P3HT layer has the same thickness as PTAA. In black a simulated cell with PTAA without interfacial recombination. In purple simulation and experimental results of our reference cell with PTAA with realistic interface recombination. In green simulation and experimental results for the P3HT cell considering misaligned highest occupied molecular orbital with respect to the perovskite valence band ($E_{maj}=0.2$ eV). In yellow the a simulation and experimental results for a cell with a highly p -doped (10^{18} cm^{-3}) PEDOT:PSS layers and $E_{maj}=0.4$ eV. The red line corresponds to a simulation with the standard settings but misaligned energy levels at the HTL-interface ($E_{maj}=0.5$ eV). b)-e) The left panels show the electron and holes densities as function of the light intensity for each of the system shown in a). Here the magenta line indicates a dependence of 1 of carrier density with respect to the light intensity. The right panels show the electron and hole quasi-Fermi

levels at the site of predominant recombination, plotted against the respective V_{OC} of the cell. The series shows how in devices with a large majority carrier energy level offset and faster interface recombination, the majority carrier density in the TL is essentially pinned while the minority carrier density increases linearly with the intensity. This scenario results in an asymmetry of the splitting quasi-Fermi levels. The band diagram of the two extreme cases b) and e) is represented schematically represented in **Fig. 6.3**.

For all cases, we obtain θ from the intensity dependence of $\Delta E_{F,\min}(I) \propto \theta \times QFLS(I)$, where θ is the slope representing the minority carrier share of the QFLS increase. In the case of the ideal device, most of the recombination happens in the bulk. Due to the lack of interface recombination ($S=0$), n_e and n_h are nearly equal and the QFLS splits almost completely symmetrically with respect to the light intensity. In this case, the internal QFLS in the bulk is equal to the external V_{OC} , resulting in n_{id} of nearly two. In contrast, in the standard PTAA/perovskite/ C_{60} cell with no energy offset on both sides, $S_h = 200$ cm/s and $S_e = 2000$ cm/s, we find that $n_e > n_h$ at the ETL interface and therefore the recombination rate depends mostly on n_h . Importantly, both n_e and n_h depend on the illumination intensity, yet the dependence of n_e is weaker. The reason is that electron injection from the cathode leads to a constant background electron density in the ETL (remote doping). On the other hand, because of the negligible energy offset to the perovskite CB, there exists a quasi-equilibrium between electrons in the ETL and in the perovskite, with the electron density in the latter being a function of intensity. Moreover, fast interface recombination at this interface induce a slower increase of n_e in the ETL layer compared to the perovskite bulk. Overall, this can explain the rather small increase of $n_e(I)$ in the ETL and as a consequence, the ratio θ , at which $E_{F,\min}$ increases with respect to the increase of the total QFLS with the light intensity, is 0.77 and equivalent to $n_{id} = 1.3$. In the extreme case of the cell with PEDOT:PSS, the strong p -doping of the HTL in combination with a large majority carrier band offset causes the carrier concentration to be highly unbalanced ($n_h \gg n_e$) at the perovskite/HTL interface but also n_h to be constant within the intensity range studied. Thus, the recombination rate is completely governed by n_e with $\theta = 1$ and $n_{id} = 1$. Now, in the case of P3HT which is characterized by a more moderate energetic offset and no doping, the model reconstructs precisely the n_{id} experimentally determined. Interestingly, also in a hypothetical solar cell with strongly misaligned (but undoped) PTAA (**Fig.11.3.8B, Appendix 11.3**) the situation is almost identical to the PEDOT:PSS, suggesting a stronger influence of the energetic offset on the n_{id} rather than the doping. One reason is that the large energy offset in combination with interface recombination prevents that holes in the HTL exhibit a quasi-equilibrium with holes in the perovskite, meaning that n_h in the HTL becomes nearly independent of illumination intensity. All the obtained values are reported in **Table 6.1**.

Importantly, in all cases with interface recombination, the minority carrier density increases linearly with illumination intensity, meaning that its density at the contact is governed by a first order recombination process. Yet, the ideality factor is close or equal to 1. Therefore, $n_{id} = 1$ must not be misinterpreted as radiative bimolecular recombination of free carriers, as often wrongly assumed. Lastly, it is worth to note that

the above analysis does not give the correct ideality factor if the electron/hole densities are considered at the “wrong spot” in the device, i.e. at a location where the recombination rate is comparatively small and not limiting the V_{OC} . This is shown in **Fig. 11.3.9 (Appendix 11.3)** for the PTAA device, where the same analysis is done using the carrier densities in the bulk, which results in $n_{id} = 1.8$ as expected for SRH in the bulk of our cells. Notably, the strength of the recombination at the metal contacts does not influence the above discussed recombination picture, as shown in **Fig. 11.3.10 (Appendix 11.3)**.

Table 6.1: Summary of V_{OC} , n_{id} from JV scans, θ and n_{id} calculated from θ for the ideal device, the PTAA device, the PEDOT:PSS device and the PTAA device with an energetic offset.

	V_{oc} [V]	n_{id}	θ	$n_{id}(\theta)$
Ideal device	1.26	1.8	0.55	1.81
PTAA	1.13	1.3	0.77	1.29
P3HT	0.96	1.1	0.93	1.07
PEDOT:PSS	0.87	1	1	1
PTAA (0.5eV offset)	0.75	1	1	1

Consequently, and to some extent counterintuitively, a higher n_{id} may actually correspond to a better perovskite device. These conclusions are summarized in **Fig. 6.5a-b**, where we show the simulated n_{id} values of a perovskite solar cell by reducing first the energetic offset at the HTL interface (E_{maj}), then interface recombination and finally the contribution of bulk SRH over bimolecular recombination. In **Fig.6.5b** experimental data points of devices with different degree of interface recombination and E_{maj} are included. The respective JV characteristics of all devices are presented in **Fig.11.3.11, Appendix 11.3**, while the n_{id} of the LiF passivated cell with a PCE of ~21% is shown in **Fig.11.3.12, Appendix 11.3**. It is evident that a larger n_{id} correspond to larger V_{OC} in the interface limited region, while the trend is opposite in the bulk limited regime. This trend is confirmed experimentally by the series of devices with higher V_{OC} s and higher n_{id} . It is only in the case of optimized interfaces and highly suppressed interface recombination that an n_{id} of 1 would be again desirable, being representative of predominate free carrier recombination and reduced SRH in the bulk. However, we emphasize that we do not exclude that there might be other parameters which could influence this trend in actual devices.^[220] Consistent with our experiments (passivated neat perovskite film, **Fig.6.1a**, in the bulk limited regime in **Fig. 6.5a**, we observe a transition from a bulk SRH dominated to a bimolecular dominated n_{id} when going from low to high intensity. On the contrary, in the interface limited region no interplay between different recombination processes is observed. Interestingly, in the bulk limited regime, the ideality factor as a function of V_{OC} changes faster than in the interfaces limited region when approaching the Shockley Queisser (S.Q.) limit. On the

other hand, especially for V_{OC} s below 1.2V, the variation in n_{id} with respect to the V_{OC} increase is rather small.

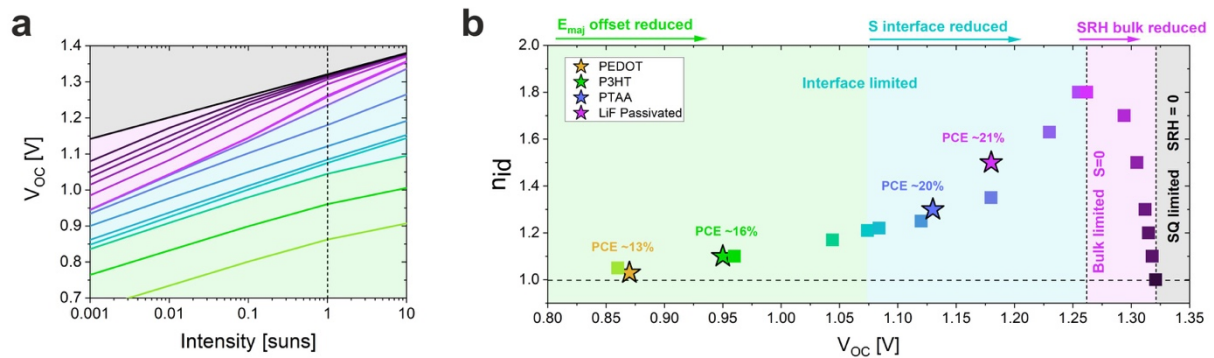


Figure 6.5: Numerically simulated intensity-dependent V_{OC} a) and external ideality factors at 1 sun b) of pin-type perovskite cells as a function of V_{OC} by varying the interface recombination velocity S symmetrically at both interfaces from $1 \cdot 10^5$ to 0 (interface limited region) and subsequently the SRH recombination in the bulk (bulk limited region). The bulk SRH recombination has been reduced by increasing the bulk carrier lifetime from 400 ns to 10 μ s. The black region represents the Shockley-Queisser (S.Q.) limit in the case of bimolecular recombination only. The stars indicate experimental V_{OC} s and n_{id} values for cells characterized by different degree of interface recombination and E_{maj} offsets. The cell with highest V_{OC} implement a interlayer of LiF at the C60 interface in order to reduce the effect of interfacial recombination.^[127]

Chapter 7.

7. High Open Circuit Voltages through Strontium Addition

This chapter is an adapted preprint of the publication:

Caprioglio, P., Zu, F., Wolff, C. M., Prieto, J. A. M., Stolterfoht, M., Koch, N., Unold, T., Rech, B., Albrecht, S., Neher, D., Márquez Prieto, J. A., Stolterfoht, M., Becker, P., Koch, N., Unold, T., Rech, B., Albrecht, S. & Neher, D. High Open Circuit Voltages in pin-Type Perovskite Solar Cells through Strontium Addition. *Sustain. Energy Fuels* **3**, 550–563 (2019)

In this chapter we will move from the fundamental understanding of the physics governing perovskite solar cells, and we will explore the practical optimization of the devices. Despite the earlier date of publication of this work, the findings related to interface recombination in perovskite devices are complementary to the knowledge acquired in **Chapter 4, 5** and **6**. Here we modify the perovskite precursor solution by adding small amount of SrI₂, which segregates and creates a new surface. This new surface is characterized by a strong *n*-doping and larger bandgap, effectively reducing the non-radiative recombination in the neat material and the actual device.

Several works in literature dealt with the reduction and understanding of non-radiative recombination in perovskite solar cell, as detailed in **Chapter 2**. However, a conclusive picture regarding which particular recombination channels is detrimental for the solar cell performance is often missing. Our work has demonstrated, in **Chapter 4**, and thoroughly explored, in **Chapter 5** and **Chapter 6**, that non-radiative recombination at or across the interface between the perovskite absorber and the adjacent transport layer constitutes a major recombination loss.^[101,127] In this chapter we will explore a practical methodology to further reduce these energy losses. In the recent years, different types of strategies, such as surface treatment or passivation, interlayers and compositional engineering have been used to boost the V_{OC} of the perovskite solar cells.^[73,108,114,221] However, most of these approaches require a multistep deposition process, where either the existing perovskite layer is altered through a post-deposition treatment or an additional thin layer is deposited on top. Both approaches are not suitable when aiming at fast production schemes. Alternatively, attempts have been made to increase the performance of perovskite devices by adding suitable components to the perovskite precursor solution.^[44,49,222] Such additives were shown to enrich at grain-boundaries or at the perovskite surface, paving the way for suppressing unwanted non-radiative recombination while avoiding a multistep preparation scheme. One recent example of this strategy is the addition of SrI_2 to the precursor solution of hybrid and inorganic perovskites. It has been shown that Sr^{2+} partially substitute Pb^{2+} in the perovskite lattice,^[45,46] owing to the nearly almost identical ionic radii of both ions ($Sr^{2+} = 132$ pm, $Pb^{2+} = 133$ pm).^[45] Recent results suggested, however, that Sr segregates preferentially at the surface of solution-processed perovskites films, going along with specific changes of the photovoltaic parameters. For example the addition of 1-2 % SrI_2 to the $MAPbI_3$ precursor solution increased the PCE, of an *pin*-type device from 12 % to nearly 15 %, mainly through an increase in J_{SC} and the FF , while the V_{OC} was actually reduced.^[223] The overall improvement in device efficiency, was attributed to an increased carrier lifetime in combination with surface passivation, resulting in an improved charge extraction. More recently Lau *at al.* reported Sr^{2+} insertion into a $CsPbI_3$ perovskite.^[224] Here, addition of Sr at a concentration of 2 % improved all photovoltaic parameters of a *nip*-type solar cell, resulting in a stabilized PCE of nearly 11 %. Based on an improved PL lifetime and predominant Sr surface aggregation, the authors concluded that Sr mainly acts as a surface passivating agent. Furthermore, also in Cl-containing perovskite the presence of Sr has shown positive effects on the performance of actual devices.^[225,226] On the other hand, a more recent paper demonstrated a significant reduction of all photovoltaic parameters of *nip*-type devices when adding Sr to a MAPI precursor solution.^[227]

Here, we apply this approach to efficient *pin* type devices comprising a solution processed quadruple cation perovskite^[43] sandwiched between the hole-transporting polymer PTAA and a C_{60} electron-transporting layer. However, we also know that the efficiency of such devices is largely limited by the perovskite/ C_{60} interface, limiting the V_{OC} . We find that addition of Sr leads to a large reduction of non-radiative recombination loss in the device, with an increase of the V_{OC} by 70 mV, up to a

remarkable value of 1.18 V. A combination of methods, including transient and absolute PL, SIMS, SEM, and UPS/IPES is applied to arrive at a comprehensive picture of the morphology and surface energetics of the neat perovskite layers, with and without Sr. Our study confirms that Sr segregates mostly at the perovskite surface, where it widens the band gap and induces a stronger *n*-type surface band bending. We demonstrate that these modifications limit the accessibility of the surface to photo-generated holes, thereby enhancing the quasi-Fermi level splitting and reducing interface-mediate non-radiative recombination with C₆₀ in the Sr-containing perovskite samples.

Although, also in this case our devices utilize PTAA and C₆₀ as transport layers, this time the perovskite composition slightly differs from the one presented in the previous chapters. For this work, the starting perovskite composition uses a combination of four different cations, namely MA, FA, Cs and Rb.^[40] The final molar composition resulted in the following ratios $(\text{Rb}_{0.05}(\text{Cs}_{0.05}(\text{MA}_{0.17}\text{FA}_{0.83})_{0.95})_{0.95})\text{Pb}(\text{I}_{0.83}\text{Br}_{0.17})_3$. Finally, a small amount of SrI₂ dissolved in DMF:DMSO (4:1) was added in different quantities to yield a Sr/Pb ratio of 0%, 0.05%, 0.1%, 0.3%, 0.5%, 1%, 2%, with the goal to study the effect of the Sr insertion from fairly small to considerably high quantities.

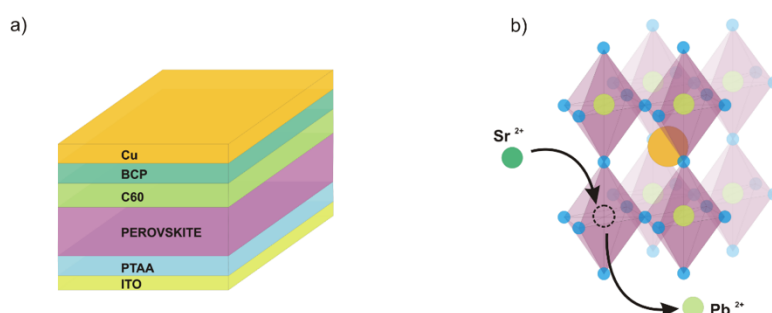


Figure 7.1: a) Solar cell device structure representing the layer stack utilized here, b) ABX₃ perovskite cubic structure with the different species implemented in this study. The figure indicates how the Sr²⁺ can take the place of Pb²⁺ into the perovskite lattice.

Importantly, regardless the presence of Sr, our devices do not show any evidence of hysteresis effect during *J-V* scans (**Fig. 11.4.1A, Appendix 11.4**). Importantly, already a small quantity of Sr (0.05%) affects the photovoltaic performance, especially the V_{OC} , which increases from 1.10 V to 1.12 V. The rather low V_{OC} of the Sr-free device is most likely caused by the poor selectivity of C₆₀ as an electron-extracting contact, as mentioned above. Further increasing the Sr/Pb ratio to 2% in various steps, a consistent increase of V_{OC} from 1.12 V to 1.18 V is found, see **Figure 7.2b**, highlighting an exceptional V_{OC} increase of 70 mV compared to the reference cell. A V_{OC} of 1.18 V, for a perovskite absorber with a band gap of 1.6 eV in a *pin* solar cell architecture is only enabled by a strong minimization of the energy losses. The resulting cells show a power conversion efficiency of 20.3 % for the record device, well exceeding the value of any other Sr containing perovskite reported so far.^[223–226] Higher Sr concentrations (**Fig. 11.4.1B** and **Fig. 11.4.1D, Section 11.4**) did not improve the V_{OC} further, while

causing a significant drop of the FF and J_{SC} . We attribute this to the significant changes of the surface morphology when increasing the amount of Sr as discussed below. For this reason, we refer to a 2% Sr addition as the optimized amount and use this concentration for further comparisons. Adding Sr until 2% does not compromise the J_{SC} , which varies in a non-systematic way around an average value of 22 ± 0.5 mA/cm² (Table 7.1), but we consistently observe a higher J_{SC} for the device with 2% Sr. A conclusive interpretation for this phenomenon is not clear, but we note that the higher J_{SC} of the 2% Sr device is also reflected in the slightly larger external quantum efficiency (EQE_{PV}) (Fig. 11.4.2A, Appendix 11.4). On the other hand, increasing the Sr concentration causes a continuous decrease of the FF . Notably, an opposite effect has been reported when Sr was added to MAPbI₃ in a solution-processed *pin* device, as described above.^[223] Here, the addition of Sr led to a marked increase in J_{SC} and FF , assigned to improved charge extraction while the V_{OC} decreased by 50 meV.^[223] We cannot resolve this discrepancy but we note that our devices differ from those employed in that work substantially (the choice of the perovskite and all charge-transporting layers as well as a different way of perovskite layer preparation). Following a previous study,^[75] we tried to further enhance the V_{OC} by adding a thin (less than 5nm) insulating polystyrene (PS) layer at the interface between perovskite and C₆₀. The resulting solar cell shows an extraordinarily high V_{OC} of nearly 1.23 V due to the significantly reduced interface recombination. This result highlights the V_{OC} potential of well optimized electron selective contact. However, as reported in Fig. 11.4.1C, Appendix 11.4, the inclusion of the ultra-thin insulating PS interlayer led to a significant reduction of the FF by probably limiting the extraction of electrons from the perovskite layer. For a better comparison, a box charts representing all parameters for the most important type of devices analyzed in this work is presented in Fig. 11.4.1D, Appendix 11.4. As our work is mostly concerned with the suppression of interfacial recombination through mixed solution processing, we will not consider this approach further in the work.

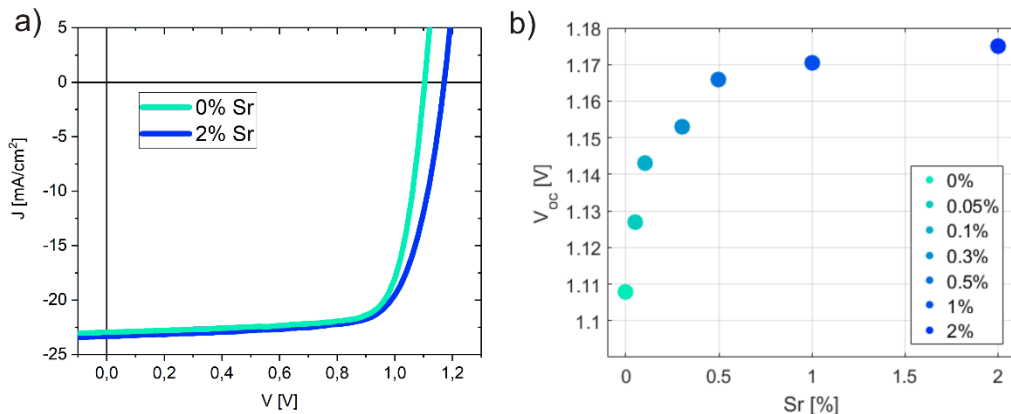


Figure 7.2: a) J - V characteristics in reverse scan (0.1 V/s with voltage step of 0.02V) under simulated AM 1.5G illumination calibrated to 100 mW/cm² of the best devices for the two cases 0% Sr and 2% Sr. b) Averaged V_{OC} values at 100 mW/cm² illumination as a function of Sr content based on 10 cells for each Sr concentration.

Table 7.1: Averaged J-V parameters for devices with different Sr concentrations including the standard errors based on a statistic of 10 cells for each Sr concentration. Values are taken from J-V scans with scan rate of 0.1 V/s and voltage step of 0.02V. The J_{SC} values calculated from the integrated EQE_{PV} spectrum (**Fig. 11.4.2A, Appendix 11.4**) match within a 5% deviation with the J_{SC} measured in J-V scans. As shown in **Fig. 11.4.1, Appendix 11.4** forward and reverse scan gives identical values showing total absence of hysteresis effect. The record parameters are reported in brackets.

Sr [%]	V_{oc} [V]	J_{sc} [mA/cm ²]	FF [%]	PCE [%]
0	1.108 ±0.007 (1.121)	22.0 ±0.6 (22.9)	76.0 ±0.8 (77.6)	19.2 ±0.3 (19.4)
0.05	1.127 ±0.005 (1.133)	21.4 ±0.5 (22.2)	73.0 ±2.0 (75.8)	18.4 ±0.6 (18.9)
0.1	1.145 ±0.002 (1.150)	22.0 ±0.2 (22.2)	73.2 ±0.5 (74.0)	18.8 ±0.1 (19.1)
0.3	1.150 ±0.003 (1.153)	21.4 ±0.3 (21.7)	71.0 ±1.0 (72.6)	18.2 ±0.4 (18.7)
0.5	1.166 ±0.004 (1.169)	21.9 ±0.1 (22.0)	70.9 ±0.2 (71.1)	18.3 ±0.6 (18.7)
1	1.170 ±0.003 (1.174)	21.4 ±0.4 (22.9)	71.0 ±1.0 (72.5)	18.8 ±0.4 (19.2)
2	1.175 ±0.004 (1.180)	22.6 ±0.4 (23.2)	70.0 ±2.0 (74.0)	19.7 ±0.7 (20.3)
5	1.168 ±0.006 (1.178)	15.0±0.5 (16.3)	64.8±2.0 (66.8)	12.3±0.6 (13.1)

Notably, the position and shape of the onset of the EQE_{PV} (**Fig. 11.4.2C, Appendix 11.4**) remain almost unaltered within sample reproducibility on Sr addition in the range up to 2%. A widening of the band gap, which might be assumed as a cause of the V_{OC} increase after composition modification,^{[43],[22],[21]} is not found here. This is also supported by absorption measurements (**Fig. 11.4.2B, Appendix 11.4**) which show no shift in the absorption onset when changing the composition from 0% Sr to 2% Sr. Overall, the data suggest that the addition of SrI₂ to the perovskite precursor solution has no appreciable effect on the bulk energy gap, consistent with what was reported previously,^{[49],[223]} meaning that the observed increase in V_{OC} must be related to reduced recombination at grain boundaries or interfaces.

Time resolved photoluminescence lifetime (TRPL) measurements were applied to investigate the effect of Sr addition on the charge carrier recombination in the bare perovskite material. The TRPL traces for neat perovskite films on glass substrates containing different amounts of Sr, shown in **Fig. 7.3a**, are in accordance with a double exponential decay model:^[228]

$$I_{\text{PL}}(t) = A \cdot e\left(-\frac{t}{\tau_{\text{fast}}}\right) + B \cdot e\left(-\frac{t}{\tau_{\text{slow}}}\right) \quad \text{Eq.7.1}$$

In **Eq.7.1**, the parameters A and B are the relative amplitudes for the fast and slow lifetimes, τ_{fast} and τ_{slow} , respectively.

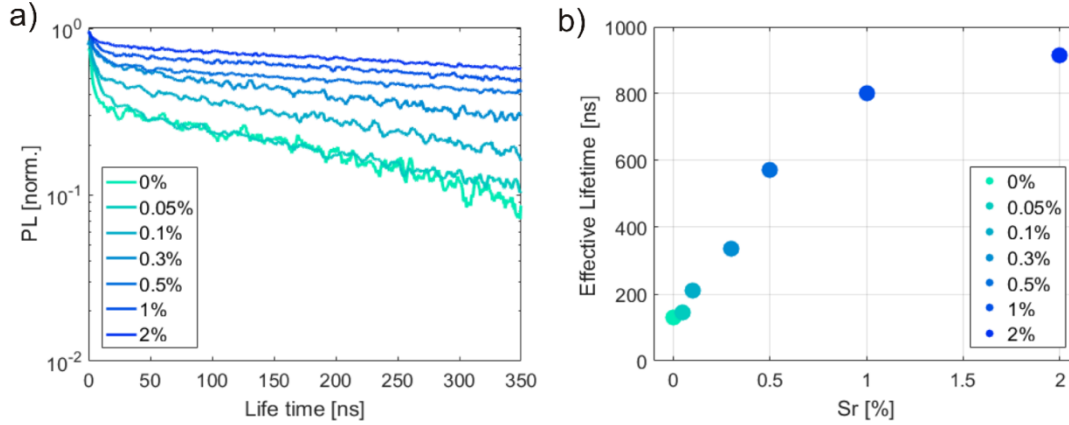


Figure 7.3: a) Time resolved photoluminescence (TRPL) traces of neat perovskite layers for the different Sr concentrations measured in inert atmosphere with fluence of $\sim 30\text{ nJ/cm}^2$ at a wavelength of 470nm, normalized to the initial transient peak. b) Calculated effective life times from fitting of the TRPL traces according to equation 1 and 2.

Commonly, the initial fast decay (below 20 ns) is associated to the capture of charges by trap states and recombination at grain boundaries or at the surface.^[229] An increase of the fast photoluminescence lifetime, indicated by the first initial decay in **Fig. 7.3a**, point out that the addition of Sr either reduces the concentration of such traps acting as a passivating agent, or limits the accessibility of these traps to photogenerated free carriers. At the same time, TRPL traces also show an improvement of the slow (longer than 50 ns) photoluminescence lifetime, suggesting that non-radiative recombination, commonly associated with the slow decay and most likely due to processes happening at the surface,^[230] is considerably attenuated. An effective (amplitude averaged) photoluminescence lifetime τ_{eff} was then calculated according to the following equation^[132]:

$$\tau_{\text{eff}} = \frac{A \cdot \tau_{\text{fast}} + B \cdot \tau_{\text{slow}}}{A + B} \quad \text{Eq.7.2}$$

The effective lifetimes are plotted in **Fig. 7.3b** for the different compositions. The addition of Sr has a significant effect on the PL lifetime. With the addition of 2% Sr an extraordinarily long PL lifetime of almost 1 μs is measured. The positive effect of Sr addition on the PL lifetime found here, is qualitatively in agreement with the enhancement of carrier lifetime after insertion of Sr in MAPbI_3 as deduced from

transient microwave conductivity experiments^[223] or with the increase of the PL lifetime in perovskites of different compositions.^[224,225] Given the fact that the addition of Sr increases both PL lifetime and V_{OC} , but it has basically no effect on the shape and amplitude of the EQE or absorption spectrum, we propose that Sr mainly reduces the strength of non-radiative recombination. In order to quantify this reduction of energy losses in the bare absorber, we measured QFLS by means of the absolute PL intensity measurements. In this specific case, the approach differs from what introduced in **Chapter 2** and **Chapter 3**. Here, we make use of Würfel's generalized Plank's law^[231] describing the non-thermal emission of a semiconductor:

$$I_{PL}(E) = \frac{2\pi E^2 a(E)}{h^3 c^2} \frac{1}{\exp\left(\frac{E - \Delta E_F}{kT}\right) - 1} \quad \text{Eq.7.3}$$

Here, h is Planck's constant, c is the speed of light, E is the photon energy, ΔE_F the QFLS, $a(E)$ is the spectral absorptivity, and k is the Boltzmann constant. Approximating the Bose-Einstein distribution with a Boltzmann distribution ($E - \Delta E_F \gg kT$) and assuming the absorptivity $a(E)=1$ for energies above the band gap, the PL intensity I_{PL} can be expressed as function of E where the QFLS, ΔE_F , can be extrapolated from a fit of $\ln(I_{PL}/E^2)$ above the band gap:^[132]

$$\ln\left(\frac{h^3 c^2 I_{PL}(E)}{2\pi E^2}\right) = \frac{\Delta E_F}{kT} - \frac{E}{kT} \quad \text{Eq.7.4}$$

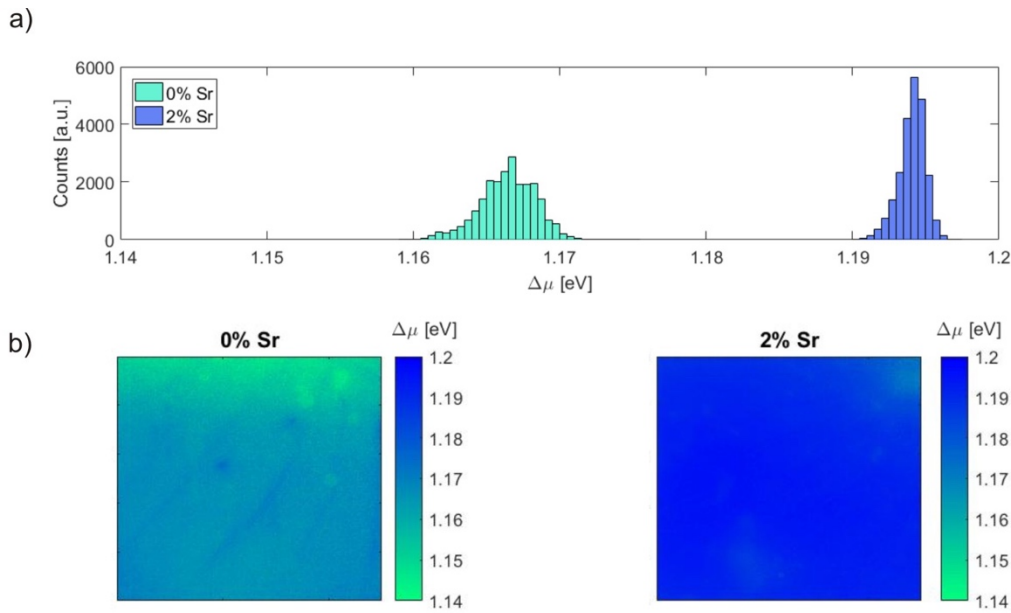


Figure 7.4: a) Histogram of the quasi-Fermi level splitting (QFLS) extrapolated from the PL maps (5 mm²) of a neat perovskite layer with 0% and 2% Sr represented in b). The maps

represent the QFLS distribution on the surface of the bare perovskite film of an area of 5 mm^2 in a range from 1.14 eV to 1.2 eV . The standard deviation of the histograms is considered as the error of the given absolute value.

Fig. 7.4b shows the QFLS maps calculated from the PL intensity mapping using **Eq. 7.4** for two samples of neat perovskite with 0% and 2% Sr. In **Fig. 7.4a** the histograms for the corresponding QFLS distributions are reported. In the case of 2% Sr a high QFLS of $\Delta E_F = 1.194 \pm 0.001 \text{ eV}$ (FWHM = 2.3 meV) was extrapolated from absolute PL mapping, whereas in the case of 0% Sr the quasi Fermi levels splitting was only $\Delta E_F = 1.167 \pm 0.002 \text{ eV}$ (FWHM = 5 meV), indicating that the losses correlated to non-radiative recombination are considerably lower and the maximum achievable V_{OC} higher when Sr is incorporated. This finding is consistent with the observed increase of the PL lifetimes. Also, the QFLS distribution of the Sr-containing device is significantly narrower, indicating that the Sr-addition also reduces the spatial inhomogeneity of recombination pathways across the perovskite film.

A simple method to investigate radiative and non-radiative recombination in a full device is to measure the external electroluminescence efficiency (EQE_{EL}) by applying a forward bias to the solar cell in the dark operating it as a light-emitting diode (LED). **Fig. 7.5** displays EQE_{EL} for the 0% and the 2% samples for a range of applied voltages around the V_{OC} and the corresponding injected dark currents.

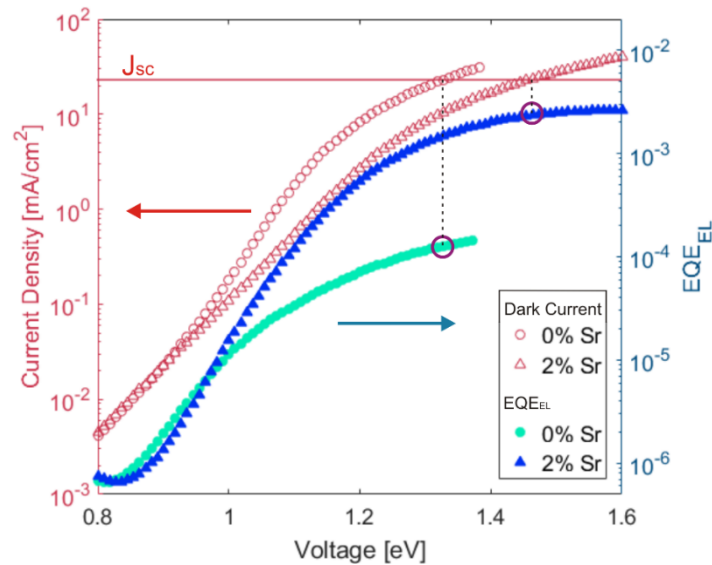


Figure 7.5: The external electroluminescence efficiency EQE_{EL} (right y-axis) and the injected dark current (left y-axis) for complete solar cells without (0% Sr) and with 2% of Sr as a function of the applied voltages. Dashed lines and circles indicate the applied voltage, where the dark injected current is equal to the J_{SC} under simulated AM1.5G illumination.

When Sr is added, the EL efficiency is increased by more than one order of magnitude, reaching a remarkably high EQE_{EL} value of $2.5 \cdot 10^{-3}$ for injection currents approaching J_{SC} under illumination, denoting stronger emissive behavior and reduction of non-radiative recombination also in the complete device structure. A luminescence efficiency of 0.25% is among the best values reported in literature so far.^[75,232] EQE_{EL} values are taken for an injected current density equal to J_{SC} (being a good approximation of the generation current J_G), meaning that the so-determined EQE_{EL} is a good measure for the radiative recombination efficiency at V_{OC} under 1 sun illumination and, therefore, relevant for the calculation of the radiative and non-radiative losses presented here. Following the same approach detailed in **Chapter 2** and already used in the previous chapters, we calculated exceptionally low non-radiative losses of $\Delta V_{\text{OC,non-rad}} = \frac{k_{\text{B}}T}{e} \ln\left(\frac{1}{\text{EQE}_{\text{EL}}}\right) = 0.161 \text{ eV}$ at $T = 300 \text{ K}$ when Sr is present. The radiative V_{OC} limit for this cell is $V_{\text{OC,rad}} = \frac{k_{\text{B}}T}{e} \ln\left(\frac{J_{\text{SC}}}{J_{\text{rad},0}}\right) = 1.337 \text{ eV}$, where $J_{\text{rad},0}$ was calculated as detailed in **Fig. 11.4.3, Appendix 11.4**, and J_G is set equal to J_{SC} . Combining these values results in a predicted $V_{\text{OC}} = V_{\text{OC,rad}} - \Delta V_{\text{OC,non-rad}} = 1.337 - 0.161 = 1.176 \text{ V}$, which is very close to the measured averaged V_{OC} for 2% Sr cells. The perovskite without Sr shows higher non-radiative voltage loss $\Delta V_{\text{OC,non-rad}} = 0.232 \text{ eV}$ with an almost identical radiative limit $V_{\text{OC,rad}} = 1.338 \text{ eV}$, leading to a predicted $V_{\text{OC}} = 1.338 - 0.232 = 1.106 \text{ V}$, again in very good agreement with the measured averaged V_{OC} for 0% Sr cells. The non-radiative voltage losses $\Delta V_{\text{OC,non-rad}}$ of the two samples differ by 70 mV, matching exactly the V_{OC} enhancement measured by J - V scans. The small difference of only 15 meV found between the QFLS and the V_{OC} for the Sr containing sample indicates that the energy losses due to the implementation of the charge transporting layer are successfully minimized.

As noted above, previous work showed that Sr segregates at the perovskite surface.^[223,224] **Fig. 7.6** shows the elemental distributions of several elements of our samples on ITO/glass as measured by secondary ion mass spectrometry (SIMS), utilizing O as primary ion source. According to **Fig. 7.6a** the elements comprising the perovskite, such as Cs, Pb, and Rb, are homogeneously distributed when Sr is not present. On the other hand, the SIMS in **Fig. 7.6b** clearly proves a significant enrichment of Sr at the surface and interface to ITO, with the Sr concentration being considerably lower in the bulk. In both measurements the signal of the negatively charged ions is low due to limitations of the sputtering yield; however, those species have been detected with Cs ions as primary ion source and they have also shown homogeneous distribution (**Fig. 11.4.4d, Section 11.3**). To exclude the possibility of lateral inhomogeneities, we analysed different spots of ca. $250 \times 250 \mu\text{m}^2$ on the surface and from samples of different batches. In all measurements (**Fig. 11.4.4a, 11.4.4b, 11.4.4c, Appendix 11.4**), Sr traces show the same inhomogeneous distribution with a significant enrichment at the surface/interface. Following this picture, when the Sr is added to the precursor solution and the film is formed after spin coating, Sr clearly segregates the surface/interface, whereas the bulk remains almost unaltered. Additional XPS measurements (**Fig. 11.4.5A, Appendix 11.4**) show Sr traces on the

sample surface with the rise of the characteristic Sr 3p peaks, in accordance to the SIMS results. A more detailed XPS surface composition analysis (**Fig. 11.4.5B, Appendix 11.4**) quantitatively shows that the relative atomic Sr concentration compared Pb is 10 times higher than what should be predicted by stoichiometry, in good agreement with the findings by Perez Del Rey et al. ^[223] Detailed analysis of the core-level spectra results in the Sr/Pb molar ratio of 0.21 and the Sr/I molar ratio of 0.07, which are both much higher than the expected stoichiometry. This finding is in good agreement with SIMS traces and it confirms a Sr enriched region at the surface. Moreover, we can exclude a coverage of the surface with non-reacted SrI₂, since the I concentration found at the surface, and consequently its ratio with Sr, should be consistently higher than what found here. In addition, the I/Pb molar ratio, for the sample with Sr, is higher than sample without Sr, which can be possibly ascribed to the fact that Sr can partially replace Pb, leading to a decrease of Pb/I ratio at the surface in the perovskite lattice compared to what predicted by stoichiometry by a full Pb perovskite.

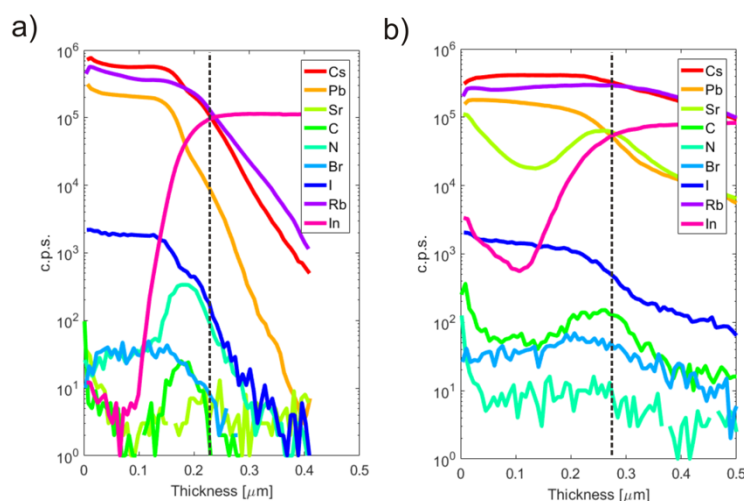


Figure 7.6: Secondary ion mass spectrometry (SIMS) profiles for a specified group of elements as a function of depth for a neat perovskite layer on ITO/glass substrates a) with no Sr added and b) with 2% Sr. Note that in both figures a thickness equal to zero represent the top surface of the perovskite layer, while the rise of the indium signal (highlighted with a black dotted line) indicates that the perovskite layer is almost completely sputtered off and that the ITO substrate becomes exposed. The initial Indium signal for the Sr containing Sr might originate from pin holes or non-uniform film areas substrate and therefore being detected at the beginning of the scan. This agrees with the smeared profile of the signals in the Sr containing sample as an indication of a rougher surface as confirmed in SEM images in **Fig. 11.4.8d**.

Scanning electron microscopy (SEM) confirms a notable change of the surface when Sr is added to the perovskite, as represented in **Fig. 11.4.6A, Appendix 11.4**. Upon Sr addition the surface starts to be characterized by leave-like bright areas. These brighter islands appear to be characterized by different work function after imaging them through energy sensitive SEM in-lens detector. We notice that these features can be resolved exclusively through this in-lens detector and not with an Everhart-Thornley

lateral detector, more topographical sensitive. This excludes the possibility of having a non-conductive material covering the surface, otherwise appearing evidently with area of different brightness due to strong charging effect in both detectors. A comparison between the two different imaging techniques on the same surface spot is presented in **Fig. 11.4.6B, Appendix 11.4**. Features of similar size and shape have been reported previously on the surface of Sr-containing CsPbI₂Br perovskite processed from solution.^[224] The cross section (**Fig. 11.4.6Ad Appendix 11.4**) shows that grains propagate from the top to the bottom even in the presence of the additional features sitting on top of the layer. The results indicate that the top surface of the Sr-containing perovskite contains a material of a different composition spread across the surface area increasing the roughness. A series of images representing the surface after addition of Sr at different concentrations (**Fig. 11.4.6C, and Figure 11.4.6D, Appendix 11.4**) show that the density of these islands on the surface is directly correlated with the concentration of Sr added. In fact, the surface of 5 % Sr perovskite is almost entirely covered with these features, while the paddlestone-type surface topography of the underlying perovskite is barely visible. Given the fact that solar cells made with the 5% perovskite absorber exhibit significantly lower FF and J_{SC} we conclude that these features can potentially have larger bandgap/lower electron conductivity than the underlying Pb-containing perovskite. On the other hand, X-ray diffraction patterns (XRD) (**Fig. 11.4.6E Appendix 11.4**) of a series of sample containing 0%, 2% and 5% Sr show no significant shifts of the reflections assigned to the lead-halide perovskite phase, indicating no major changes in the unit cell volume. However, a new reflection at $\sim 11.6^\circ$ appears in the Sr containing samples suggesting the presence of a new phase, most probably containing Sr. Importantly, the intensity of the perovskite reflections decrease with increasing Sr concentration, potentially indicating that this new phase segregates at the surface of the film and attenuates the X-ray signals coming from the underlying perovskite phase. Additionally, the broadening of the perovskite peaks suggests a reduction in crystal domain size or an increase in microstrain due to a decrease in compositional uniformity upon Sr addition. The results above provide evidence that adding Sr to a quadruple cation perovskite has a significant effect on the perovskite surface, whereas the bulk properties seem to remain fairly unaltered, asking for a detailed investigation of the electronic structure of samples with and without Sr. Photoemission and inverse photoemission spectroscopy (PES and IPES) experiments were performed for solar cell related multilayer stacks comprising ITO, the hole-transporting PTAA, and the active perovskite, to retrieve information on surface work function (WF), ionization energy (IE), electron affinity (EA), as well as position of the valence band maximum (VBM) and the conduction band minimum (CBM) with respect to the Fermi level (E_F).

As shown in **Fig. 7.7a and c**, the valence band and VBM, when Sr is incorporated, are shifted to higher binding energy while the conduction band and CBM move closer to E_F , **Fig. 7.7a and d**. VBM and CBM were evaluated by linear extrapolation of the valence and the conduction band onsets towards the background on a linear intensity scale, respectively, as shown in **Fig. 7.7a**. For the 0% Sr-perovskite we extrapolated the VBM to be at 1.42 eV and the CBM at 0.31 eV relative to the Fermi level, giving a

band gap of 1.73 eV. This value is comparable with the optical band gap of 1.63 eV reported for this type of quadruple cation perovskite^[43]. We note that an overestimation of the band gap (from UPS and IPES) compared to the optical gap can be due to the linear extrapolation,^[163,233] and our results are consistent with examples reported in literature.^[163,233–235] A lower band gap would be expected if the extrapolation was based on logarithmic plots, but due to the uncertainty of cross-section effects and rather large experimental broadening in IPES we refrain from such procedures here. Most importantly, we observe a strong effect on the electronic structure when Sr is incorporated. In particular, the CBM for 2% Sr perovskite locates at the Fermi level, indicating a strongly *n*-type surface. Concomitantly, the VBM is shifted towards higher binding energy, i.e., 1.92 eV (relative to E_F). From these measurements, we deduce that the Sr-enriched perovskite surface features a ca. 190 meV wider band gap compared to the surface of Sr-free perovskite, which is consistent with the smaller electronegativity of Sr compared to Pb. We notice that an increased band gap was predicted by DFT calculations for Pb^{2+} being completely replaced by Sr^{2+} in MAPbI_3 .^[45] Since our samples have a different composition, a quantitative comparison of our results and theory is precluded.

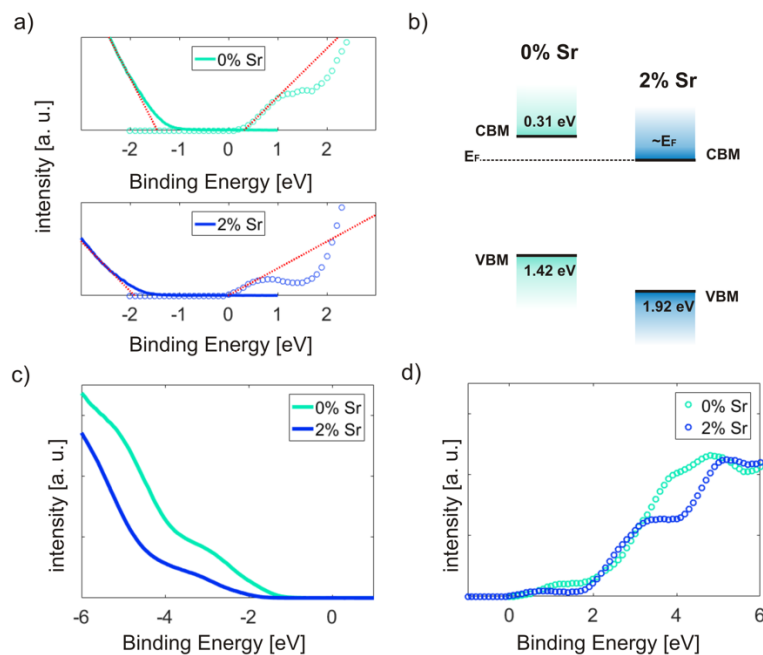


Figure 7.7: UPS and IPES spectra for 0% Sr and 2% Sr containing perovskites. a) Magnified valence and conduction band regions near E_F . The binding energy scale is referenced to E_F , set to zero. b) Energy levels with respect to E_F for 0% and 2% Sr perovskites obtained from UPS and IPES spectra. From this picture, we observe a strong *n*-type character of the perovskite surface, as well as a larger band gap for the case of 2% Sr. Wide range (c) valence and (d) conduction band regions.

The observation that the surface of the two perovskites appear strongly *n*-type in photoemission measurements does not readily imply that the bulk is also strongly *n*-

doped. As the presence of surface states at semiconductor surfaces, which induces surface band bending in electronic equilibrium, is more the rule than the exception,^[236] we need to attend to this issue. In fact, for the prototypical methylammonium lead iodide perovskite the presence of, seemingly ubiquitous, Pb^0 surface states has been evidenced.^[237,238] These donor-type surface states donate electrons to the region close to the surface, leaving behind an accumulation of immobile positive charges at the surface. This gives rise to a surface space charge region with a downward band bending from the (intrinsic) bulk towards the surface in electronic equilibrium (i.e., in dark), termed surface band bending. Even if the density of these Pb^0 -related surface states can often not be directly measured by PES experiments (due to limited sensitivity of the method), their presence is yet manifested by surface downward band bending.^[239] Since it is likely that Pb^0 -related surface states also occur at the surface of our perovskites under study, in the following we provide evidence that while the bulk of our samples does not exhibit pronounced *n*-type character, the surface does due to surface band bending. The observation of a strongly *n*-type surface of the Sr-containing sample raises the question whether the addition of Sr introduces *n*-doping also in the perovskite bulk. Unfortunately, ultraviolet (UV) photoemission is not suited to address this issue due to the short inelastic electron escape depth. On the other hand, the pronounced concurrent increase in PL lifetime and absolute PL yield upon Sr addition as reported above excludes the presence of a high density of doping-induced background charges in the Sr-containing sample, similar to what has been reported by Bolink and coworkers on Sr-doped MAPbI_3 .^[223] To support this claim, we simulated the TRPL decay and PL efficiency of the neat perovskite for varying doping concentration, using realistic parameters for the recombination coefficients (**Fig. 11.4.7A, Appendix 11.4**). According to these simulations, if the increase in PL efficiency is due to doping, we would expect a concurrent reduction of the PL lifetime, confirming previous studies.^[240,241] The pronounced increase of both PL decay times and PL efficiencies, therefore rules out extensive bulk doping in the presence of Sr. An effective lifetime of nearly 1 μs combined with a large QFLS suggests a doping density of less than 10^{15} cm^{-3} , meaning that the perovskite bulk is nearly intrinsic. The low doping density in the bulk combined with the strongly *n*-type surface suggests significant surface band bending to occur. To provide experimental evidence for this effect, surface photovoltage (SPV) measurements were performed on neat perovskite layers with and without Sr being present. This technique determines the shift of the surface electrostatic potential between measurements done in dark and under light illumination, e.g., through Kelvin Probe or UPS (indicated by parallel shifts of work function and valence band). Under illumination, photogenerated carriers are created due to band-to-band (or trap-to-band) transition. These carriers will redistribute under the influence of the space charge field, thereby compensating the local excess of positive charges at the surface. As a result, increasing the illumination intensity the level of surface band bending will gradually decrease until flat band condition is reached, as schematically represented in **Fig. 7.8a**. SPV is a common method to measure the degree of surface band bending of semiconductors,^[236,242,243] including halide perovskites.^[244–246] For example, surface band bending in perovskite has been proven with the same methodology used in our study for bare $\text{MAPbI}_x\text{Cl}_{3-x}$ films. There,

the effects of an n -type surface with downward band bending was clearly demonstrated^[238] and attributed to the presence of donor levels at the perovskite surface, likely consisting of reduced lead (Pb^0).

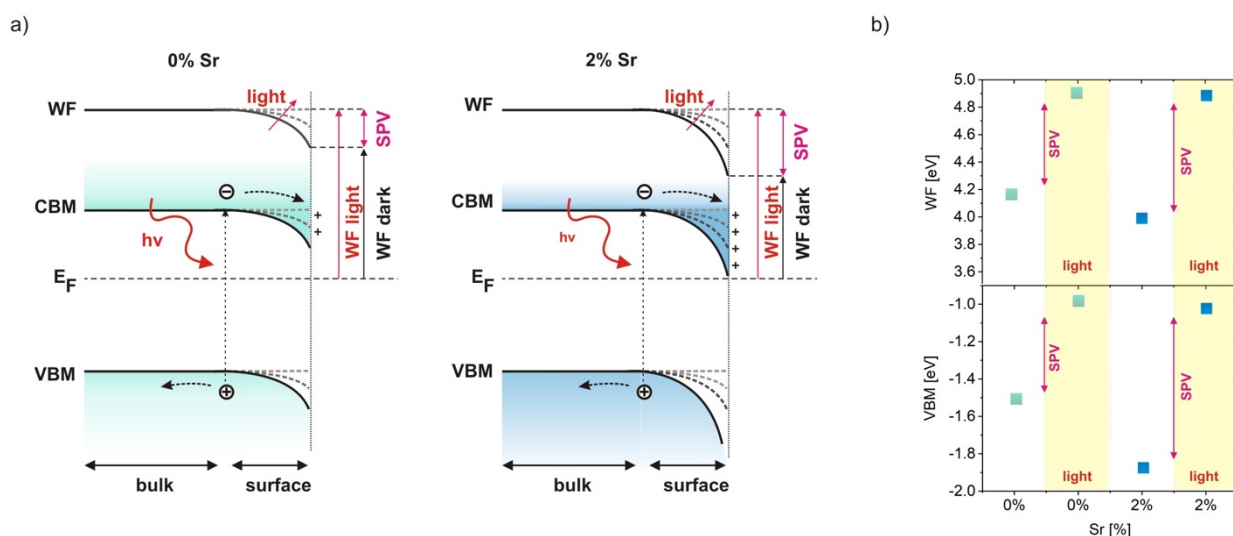


Figure 7.8: a) Schematic representation of the SPV effect of 0% and 2% Sr samples. Dotted lines represent the effect of white light illumination on the vacuum level (VL), conduction band minimum (CBM) and valence band maximum (VBM) in the surface-near region. At sufficiently high illumination conditions, the space charge region is completely screened by photogenerated charges and flat band conditions are established. The positions of the relevant energy levels are depicted with respect to the E_F of the substrate (independent on illumination), and plotted as function of bulk-to-surface distance for different illumination conditions. The bulk and surface energetics in dark are represented by solid lines. Surface energy levels are obtained from measurements of the work function and the valence band onsets in the dark, while the bulk values are obtained from the corresponding measurements under illumination, assuming that flat-band conditions are established as reported in Zu et al.^[238] b) Corresponding WF and VBM values from UPS, measured without and with simultaneous white light illumination for 0% and 2% Sr samples. Both samples display very similar VL and VBM positions under illumination, indicating nearly identical bulk energy levels for 0% and 2% Sr, while surface band bending is significantly more pronounced in the Sr-containing sample due to a much larger SPV effect as indicated with pink arrows.

The effect of white light illumination on the WF and VBM is summarized in **Fig 7.8b** (see **Fig. 11.4.8 Appendix 11.4** for the corresponding UPS spectra). In the case of 0% Sr, the WF increases from 4.17 eV in dark to 4.93 eV under illumination (light intensity sufficient to saturate the shift, i.e., the establishment of flat band conditions), accompanied with the VBM shifting from 1.51 eV to 1.00 eV binding energy. VBM and WF do not shift perfectly in parallel, most likely due to surface inhomogeneities, which affect SPV the VBM and WF in SPV experiments differently, but cannot be differentiated in the area-averaging photoemission experiment. A much stronger SPV effect was observed for 2% Sr samples where WF shifted from 4.00 eV in dark to 4.89 eV under illumination, and the VBM from 1.87 eV to 1.03 eV, respectively. We note

that the SPV was reversible for multiple illumination/dark cycles, thus photochemical reactions and degradation can be excluded. Additionally, in this measurements we notice a reduction in work function due to Sr addition, in agreement with the effects previously reported in literature.^[223] A change of sample work function can have manifold reasons, e.g., due to formation of dipoles at the surface^[233], a change in stoichiometry^[247,248], or it can be indeed associated with a more *n*-type surface.^[249] In conclusion, UPS reveals a much larger degree of surface band bending of the Sr containing perovskite, resulting in a stronger SPV effect compared to the 0% Sr sample, see magenta colored arrows in **Fig 7.8a-b**. At the same time, both perovskites exhibit very similar values of the WF and VBM under illumination, demonstrating that the bulk energy levels (notably the position of E_F in the gap) is almost independent of the Sr content.

Before proposing a model to explain the beneficial effect of adding Sr to a quadruple cation perovskite, we first summarize the key findings from our studies (**Tab. 7.2**). From SIMS and XPS, we find a strong enrichment in Sr at the surface denoted in a Sr/Pb ratio of 0.21 being much higher than the expected 0.02 from a homogeneous Sr addition assumption. In TRPL, we find that Sr addition strongly suppresses the initial fast PL decay, indicating reduced trapping, but also prolongs the long-term decay attributed to non-radiative recombination. In accordance with this, we observe a ca. 30 meV increase in the quasi-Fermi level splitting in the neat perovskite under 1 sun equivalent illumination conditions if 2 % Sr is added. In the complete device, Sr suppresses non-radiative recombination, strongly enhancing the electroluminescence efficiency 25-fold and reducing the non-radiative voltage loss from 230 to 160 meV. On the other hand, very similar results of the absorption, EQE_{PV} , and XRD measurements suggest an only minor effect of Sr addition on the perovskite bulk properties. This is consistent with the outcome of the SPV experiments where upon illumination bands flatten at the same position. Meanwhile, the more pronounced shift of the work function indicates stronger band bending in the Sr-containing samples. In combination, these properties must be the cause of the significant enhancement of V_{OC} by 70 mV.

Table 7.2: Summary of the most relevant photovoltaic and optoelectronic properties determined for 0% Sr and 2% Sr containing perovskite films and/or solar cells. The insertion of Sr results in a consistent improvement of all parameters.

Sr [%]	Sr/Pb	τ_{eff} [ns]	ΔE_F [eV]	EQE_{EL} [%]	$\Delta V_{oc,non-rad}$ [eV]	WF shift. [eV]	VBM shift [eV]	V_{oc} [V]
0	0	180	1.16	0.01	0.23	0.76	0.51	1.11
2	0.21	980	1.19	0.25	0.16	0.89	0.84	1.18

In **Fig. 7.9** we schematically represent two perovskite samples, without and with Sr, combining findings from all previous studies as a summarizing figure. We propose that this specific energetic landscape is responsible for a considerable reduction of surface recombination as indicated in **Fig. 7.9**. Notably, a strong *n*-type character of the surface

goes along with a nearly complete occupation of the electron traps already in the dark, reducing the probability that photo-generated electrons become trapped by these states, fully consistent with the almost complete absence of an initial fast PL decay in the Sr-containing layer. More important, the stronger surface band bending, as measured in SPV when Sr is added, repels holes from the surface, with the benefit of limiting the probability of a captured electron in a surface state to recombine with a hole. The most well-known example of this phenomena is the so-called “back-surface field”^[250] which is an established approach^[250] for suppressing surface recombination in inorganic semiconductors. In addition, the accessibility of the surface for electrons and/or holes may be reduced by the wider band gap of the Sr-containing surface perovskite region, similar to what has been proposed recently for a compositionally engineered perovskite/HTL interface.^[114] Additionally, the Sr induced surface modification and the formation of the islands on the top surface may also act as a passivating agent, reducing the number of interfacial states responsible for trap-assisted recombination. Even though these three effects cannot be disentangled based on the presented set of experiments, we can conclude that these are all possible beneficial effects due to the addition of Sr. Additionally, they all may act in combination together to reduce non-radiative recombination in actual devices by strongly suppressing interface recombination with C₆₀, as proposed in **Fig. 7.9**.

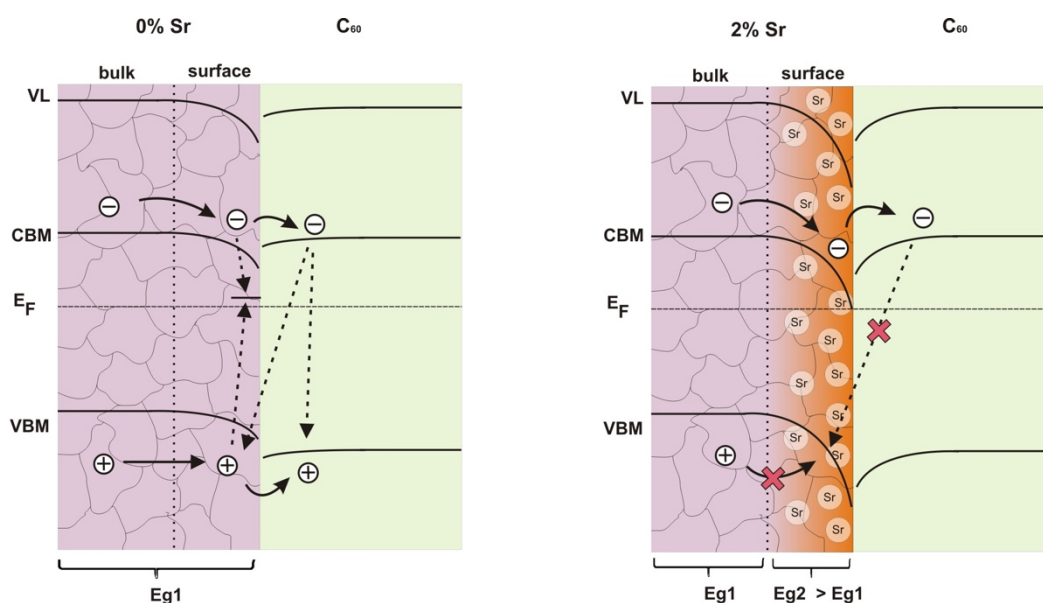


Figure 7.9: Schematic representation of the two perovskite samples with and without Sr addition with respective recombination schemes. From a combination of morphological studies, PES and SPV experiments it is possible to draw a picture where Sr segregates at the perovskite surface inducing a wider band gap and a more pronounced n-type character. On the other hand, optical measurements and SPV suggests that the bulk shows very similar characteristics for both samples. The energy levels in the bulk and at the surface for the 0% Sr and the 2% Sr cases, respectively, are based on values from UPS and IPES (**Fig. 7.7, 7.8, Fig. 11.4.7a-b**), taking into account the surface band bending found from SPV measurements, all with respect to the E_F of the substrate. In the sample without Sr the recombination of charges

can happen at the surface or across the interface with C₆₀. We note that these measurements do not provide a concise interfacial energy level diagram of perovskite/C₆₀ interface, which is drawn only schematically. The Sr enriched surface repels holes from the surface reducing the non-radiative recombination at or across the interface and improve the selectivity of the contact with C₆₀. The lack of trap states in the scheme of the 2% Sr sample illustrates surface passivation or that these traps are permanently occupied.

In order to prove the beneficial effect of Sr in reducing non-radiative recombination at the perovskite/C₆₀ surface, absolute PL efficiencies were measured for perovskite films on glass, without and with 2 % Sr, additionally covered with a 30 nm thick layer of C₆₀ (see **Fig. 11.4.10, Appendix 11.4** for the results). As expected, the measurements reveal a substantial decrease of the PL efficiency in the presence of C₆₀ for both samples. However, when Sr is present the decrease in PL attributed to the presence of C₆₀ is strongly reduced. This confirms our proposal that Sr addition improves the device performance by reducing the strength of the non-radiative recombination specifically at the surface of the absorber and at the interface with C₆₀. However, the modification of the interface morphology and energetics upon Sr addition might induce an extra barrier for extraction of electrons or holes, as extensively discussed for **Fig. 11.4.9, Appendix 11.4**, which may be a main cause for the systematic decrease in *FF*. This will be subject to the work presented in **Chapter 8**.

Chapter 8.

8. Bifunctional Interfaces Through Poly-Ionic Liquid Surface Modification

This chapter is an adapted preprint of the publication:

Caprioglio P., Saul-Cruz D., Caicedo-Dávila S., Zu F., Sutanto A.A., Kegelmann L., Wolff C.M., Perdigón-Toro L., Koch N., Rech B., Grancini G., Abou-Ras D., Nazeeruddin M.K., Stollerfoht M., Albrecht S., Antonietti M., Neher D., *Bi-functional Interfaces by Poly-Ionic Liquid Treatment in Efficient pin and nip Perovskite Solar Cells* (under revision)

In the previous chapter we have seen how specifically addressing the perovskite/C₆₀ we were able to effectively reducing the non-radiative losses and improve the V_{OC} of the device. However, the strong n -doping of the surface was inducing an extraction barrier for electrons with consequent increase of the series resistance and decrease of the FF . Moreover, acting directly on the precursor solution might be beneficial in terms of simplicity for future industrial development but it can increase the complexity of crystallization and reduce the control and reproducibility. In this chapter by using a poly-ionic liquid as interlayer between the perovskite and the C₆₀, we manage to concomitantly decrease the non-radiative losses and to improve the charge extraction. These solar cells exhibit outstanding V_{OC} and FF values of 1.17 V and 83% respectively, resulting in conversion efficiencies up to 21.4%.

In this work, we introduce a novel approach to concomitantly increase the efficiency and the stability of different PSCs by treating the perovskite surface with a poly(ionic-liquid) (PIL). In the past, a large number of studies dealt with the implementation of ionic liquids in perovskite solar cells, either as additives in the perovskite precursor solution to improve the material quality and stability^[251–254] or as contact work-function modifier^[109,255–257] to enhance charge collection. On the other hand, the usage of the polymeric version of this class of material as post treatment of halide perovskites has not been explored yet. Polymer ionic liquids are “liquid”, i.e. their glass transition temperature is below room temperature, and as that, they are ion conductors which form a conformal coating on surfaces by spreading down even to nanometer dimensions. Conceptually, this coating not only protects the surface, but also provides charge stabilization (by other charges) and lowering of interface resistance and impedance. PILs are also known to be extremely versatile due to the interchangeability of the counterion, allowing them to achieve high ionic conductivity, hydrophobicity, thermodynamic and thermal stability, as well as chemical durability.^[258,259] Here, we employ an imidazolium-based PIL with a bis(trifluoromethane)sulfonimide (TFSI) counterion, abbreviated as [Pelm][TFSI], to modify the interface between a triple cation perovskite and a C₆₀-based electron transport layer (ETL). We show that the PIL assembles primarily on the perovskite surface, where it reduces non-radiative losses in the neat material as well as in the complete cell. Detailed microscopic studies reveal the presents of extended areas where the PIL acts as blocking layer between perovskite and C₆₀, preventing interfacial non-radiative recombination and thus, increasing the V_{OC} of the device. On the neighboring areas, the modified interface promotes the extraction of charges and provides a more ideal energy alignment between the layers, resulting in extraordinary high FF values. Additionally, the hydrophobic nature of the PIL counterions and the passivating behavior of the PIL improves the stability of the device under maximum power point tracking and long-term shelf storage. Finally, we demonstrate the beneficial effect of the PIL in *nip* cells where the treatment modifies the interface between the perovskite and a Spiro-OMeTAD-based hole transport layer (HTL), increasing the FF and enhancing the reproducibility. Our work focuses primarily on our standard device structure, as already detailed in the previous chapters. This time the perovskite absorber has the composition (Cs_{0.05}(MA_{0.17}FA_{0.83})_{0.95})Pb(I_{0.83}Br_{0.17})₃, with an optical bandgap of 1.62 eV.^[22] The PIL is introduced between the perovskite and the C₆₀ layer, as depicted in **Fig. 8.1a** by spin coating a highly diluted solution (0.5 mg/ml in acetonitrile:isopropanol (1:4)) on top of the perovskite. After that, the device is completed by depositing C₆₀, BCP and Cu by thermal evaporation, see **Fig.8.1a**. The positive effect of the PIL treatment on power conversion efficiency is exemplified in the current-voltage (J - V) characteristics in **Fig. 8.1b**, where a parallel improvement of the V_{OC} and the FF is observed. Notably, the treated cells do not present any significant hysteresis behaviour, **Fig. 11.5.1A (Appendix 11.5)**. The increase of the V_{OC} , reaching values up to 1.17 V, suggests that the presence of the PIL reduces the non-radiative recombination of charges at the interface between the perovskite and the C₆₀.^[127] Moreover, the FF increases to outstanding values of nearly 83%, indicating that the PIL improves the charge

extraction and reduces the transport resistance.^[260] The average FF values averaged over a large number of devices plotted in **Fig. 8.1c** increases from below 77% for the reference cells to nearly 81% for the PIL containing ones. **Fig. 8.1c** also denotes a large improvement of the reproducibility of the device performance of the PIL-containing devices, which results also in a smaller spread of the J_{SC} values. The combination of the improved V_{OC} and FF results in an efficiency enhancement from an averaged PCE of 19% for the reference cells to an average PCE of nearly 21%, again with a narrower distribution. The best device, **Fig. 11.5.1B (Appendix 11.5)** reaches a PCE of 21.4%, which is among the best ever reported for *pin*-type PSCs.^[178,261] We note that the introduction of the PIL treatment does not affect the EQE_{PV} nor the absorption, **Fig. 11.5.2A-B (Appendix 11.5)**, thus not influencing the bandgap of the perovskite absorber. To disprove that the improvement comes from just one of the two species of the PIL, in **Fig. 11.5.1C (Appendix 11.5)**, we compare cells with imidazolium-based PILs using different counterions, namely [Pelm][Br] and [Pelm][PF₆]. Interestingly, [Pelm][Br] limits the performance of the device, whereas [Pelm][PF₆] gives identical results to the [Pelm][TFSI]. This finding suggests superior effects of fluoride containing hydrophobic anions over (hydrophilic) halides as counterions, consistent with earlier results^[254], but may also imply that the improvement of the [Pelm][TFSI] does not come from only one of the two constituents.

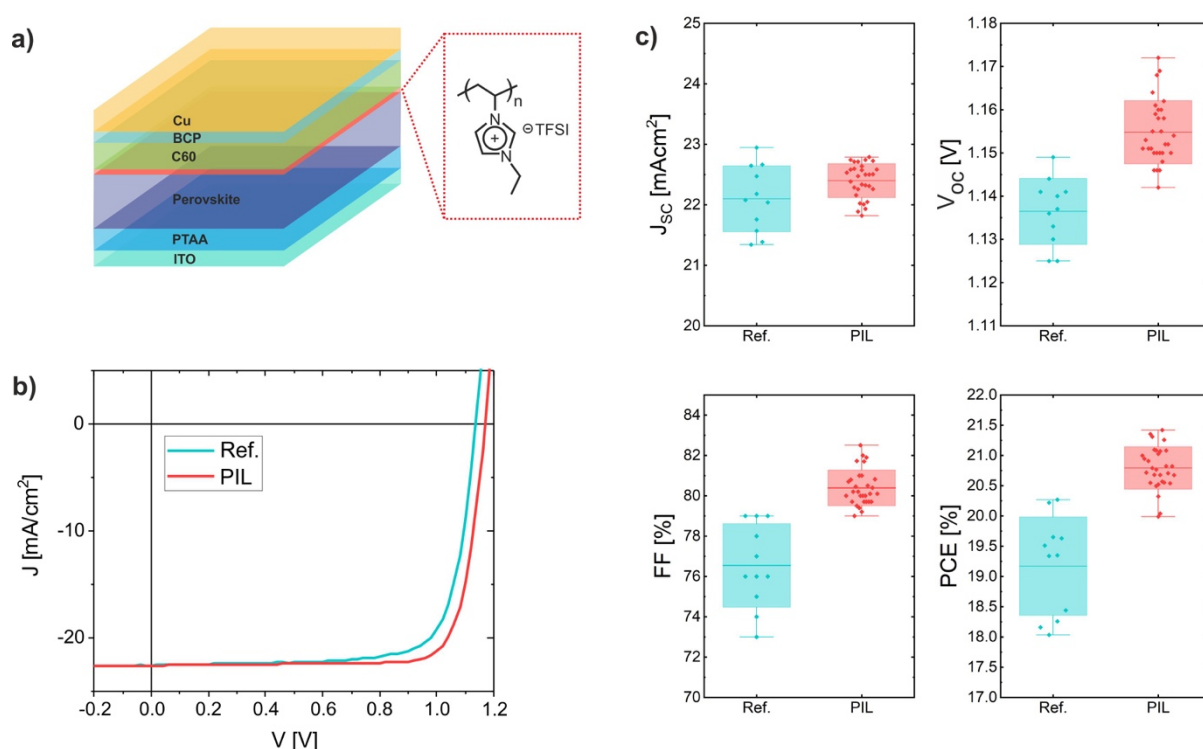


Figure 8.1: a) *Pin*-type device layer structure with highlighted chemical structure of the poly(ionic-liquid) (PIL) layer inserted between the perovskite and the C₆₀. b) Typical current-voltage characteristic for a reference untreated cell and for a PIL-modified cell in reverse scan at 0.025 V/s (hysteresis shown in **Fig. 11.5.1A, Appendix 11.5**). c) Device parameter statistics for the reference cells and the PIL containing cells; the boxes indicate the standard deviation.

In **Fig. 11.5.3A (Appendix 11.5)**, top surface scanning electron microscopy (SEM) images show that after spin coating the PIL, the typical cobblestone perovskite surface exhibits island-like features, which we assign to polymer aggregates. In **Fig. 11.5.4 (Appendix 11.5)**, X-ray diffraction (XRD) measurements indicate that the PIL surface treatment does not influence the crystal structure of the perovskite, nor additional phases were detected. However, contact angle measurements revealed that the PIL treatment induces an enhanced robustness of the perovskite surface in contact with water, as expected from the hydrophobic character of [Pelm][TFSI],^[262] **Fig. 11.5.5 (Appendix 11.5)**. Energy-dispersive X-ray (EDX) elemental-distribution maps acquired on the surface of the PIL treated sample (**Fig. 8.2b-c**) confirm that these islands are composed of a carbon-rich material, presumably mostly the polymer [Pelm]. On the other hand, the O signal, not detectable in the reference sample, is attributed to the TFSI counter-ion (a more detailed discussion can be found in **Appendix 11.5.6**, and its spatial distribution indicates that the mobile TFSI diffuses over the perovskite surface. Additionally, EDX maps and line-scans of the cross-section of the PIL-treated sample in **Fig. 8.2g** exhibit higher concentrations of C and O on the surface of the film, indicating that both, the polymer and the counter-ion, do not diffuse into the perovskite layer. Notably, the reference sample does not present any O at the perovskite surface. As detailed in **Fig. 11.5.6A (Appendix 11.5)**, the O and C on the top surface appear to be anticorrelated, meaning that the PIL-modified surface features areas rich in the positively-charged polymer, surrounded by regions covered predominately by the TFSI anion. In **Fig. 8.2d-f**, comparative imaging of the surface with cathodoluminescence (CL) reveals a homogeneous increase in radiative efficiency upon surface treatment. The enhanced luminescence is visible both in the areas enriched by the TFSI counterion (**Fig. 8.2e**) and in the areas where the polyimidazole aggregates are detected (**Fig. 8.2f**). Here, small spots of enhanced luminescence originated by the perovskite underneath are visible through the pores of the covering non-emitting polymer islands (**Fig. 11.5.6B, Appendix 11.5**). Interestingly, in **Fig. 8.2e** the surface features small spots of increased luminescence, which are not present in CL maps of the neat perovskite. This suggests that trap passivation is more efficient at specific locations, which are uncorrelated with the morphology, as visible when the SEM and CL images are superimposed, **Fig. 11.5.6C (Appendix 11.5)**. Generally, this scenario indicates that both species contained in the [Pelm][TFSI] can effectively passivate surface defects preventing the non-radiative recombination of charges. Possibly, commonly reported perovskite defects such as uncoordinated I, antisite PbI_3 as well as MA^+ or FA^+ vacancies can be passivated by the imidazolium groups.^[61,254,263] Simultaneously, N and S can act as Lewis base and passivate I vacancies, uncoordinated Pb^{2+} , or metallic Pb clusters.^[71,263–265]

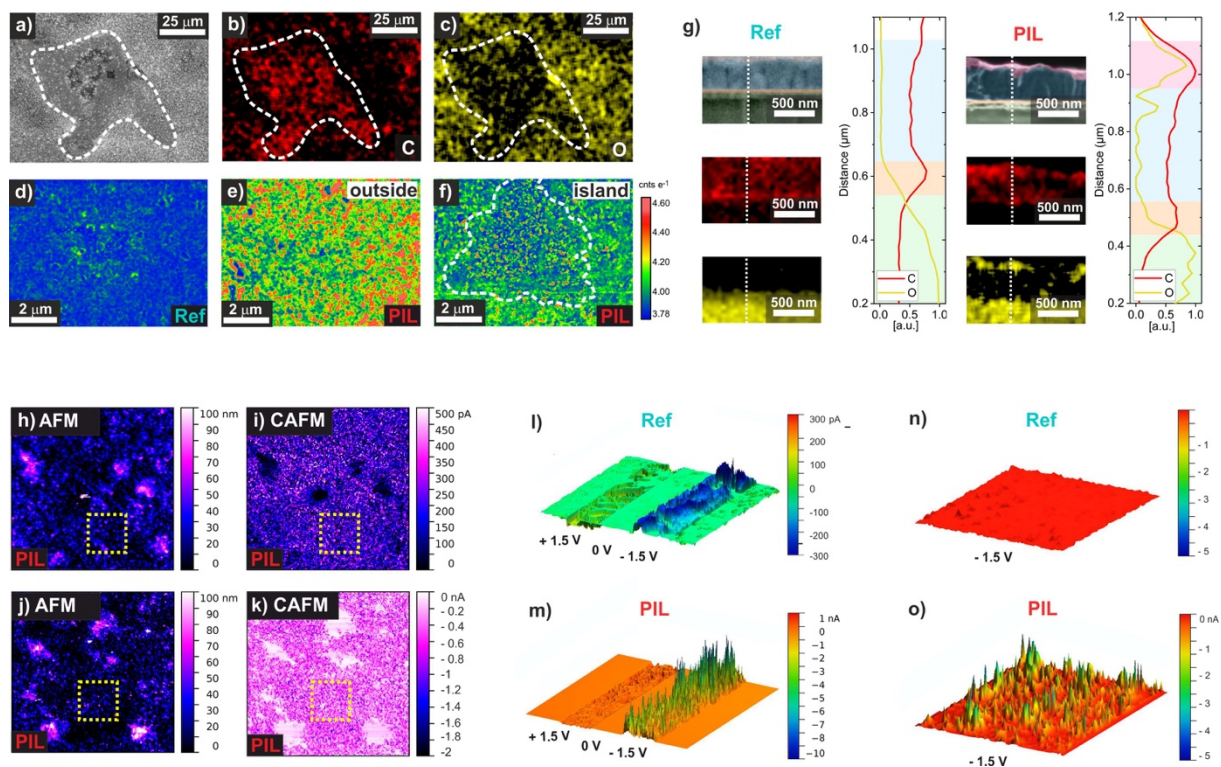


Figure 8.2: a) SEM image showing a typical polymer-rich island on the surface of the perovskite (dashed contours). Corresponding EDX elemental-distribution maps for b) carbon and c) oxygen showing the enhancement and depletion of the signal on the island region, respectively. CL map of d) untreated perovskite film, e) PIL-treated film outside the polymer island and f) PIL-treated film on top of a polymer island. Notably, in f), luminescent spots are visible from the emitting perovskite beneath the non-emitting polymer island. g) SEM and EDX cross-section images for reference and PIL treated perovskite films with corresponding EDX line scans. For both samples, the C signal appears to be enhanced on the ITO/PTAA/perovskite interface, due to the PTAA. The O signal is concentrated on the glass region in both samples while the PIL-treated sample shows in addition the O signal at the surface indicating the presence of the TFSI molecules in that region. AFM topography images ($40 \times 40 \mu\text{m}^2$) of reference and PIL-treated perovskite h) and j) show the presence of the polymer island, with heights between 50-100 nm. The corresponding CAFM images i) and k) reveal that the polymeric island presents a strong insulating character, reducing drastically the current signal when both a positive i) and a negative k) bias is applied. The dotted yellow lines indicate exemplary areas scanned in l)-o). l) 3D CAFM images ($3 \times 3 \mu\text{m}^2$) of the untreated perovskite layer. The image represents a scan while applying different voltages from -1.5 V to 1.5 V in step-like fashion. m) 3D CAFM images ($9 \times 9 \mu\text{m}^2$) of a perovskite layer treated with PIL. The image represents a scan with the same conditions of l). n) and o) shows 3D representations of two areas of $3 \times 3 \mu\text{m}^2$ with the same current scale to directly compare the reference perovskite and the PIL treated film upon applying a bias of -1.5V.

Atomic force microscopy (AFM) and conductive AFM (CAFM) analyses provide microscopic information on the correlation between surface topography and conductive properties (instrument configuration depicted in **Fig. 11.5.7A Appendix 11.5**). From large area surface scans, we observe that the reference sample exhibits a rather

smooth topography and low uniform conductivity (**Fig. 11.5.7B, Appendix 11.5**). In contrast, the thick polymeric islands in the PIL treated surface, with a height of roughly 100 nm (**Fig. 11.5.7C, Appendix 11.5**), are highly insulating, as presented in **Fig. 8.2h-k**. Interestingly, the areas outside the islands show enhanced conductivity compared to the reference perovskite. To investigate this finding further, in **Fig. 8.2l-o** we performed CAFM measurements on these areas with higher spatial resolution, as indicated by the yellow lines in **Fig. 8.2h-k**. Here, the voltage (applied to the tip) is swept from positive to negative bias during the vertical scan in a step-like fashion. Surprisingly, while the reference samples exhibit low current signal (pA range), which is symmetric for positive and negative bias, the PIL treated surface demonstrates a tremendously increased current, approaching values of ~ 10 nA. Notably, the current enhancement is larger when the tip is biased negatively, namely electron injection at the top surface is more efficient compared to hole injection from the tip. Thereby, the improved electron transfer is in line with the higher FF of the PIL-treated device as the collection at the transport layer is facilitated. Interestingly, when CAFM images of the two samples are directly compared on an area of $3 \times 3 \mu\text{m}^2$ in the same current range, **Fig. 8.2c-d**, it is evident that the PIL treated surface features inhomogeneously distributed highly conductive points, which create isolated spikes in the current signal, reminiscent of the CL luminescence pattern. Also in this case, these spikes do not correlate with the surface topography, suggesting that a certain degree of surface modification is present on an atomic level and is not detectable by AFM or SEM. As proposed for other types of ionic liquids, the conductivity can be enhanced due to defect passivation of the surface.^[266] In agreement with this, conductivity measurements, presented in **Fig. 11.5.8 (Appendix 11.5)** show that the PIL treated perovskite shows a 3 fold improvement in lateral conductivity and lower contact resistance compared to the reference perovskite. We will show that this property is not related to a higher net doping density in the perovskite layer. Consistently with this picture, the dark J - V characteristic of a series of actual devices, **Fig. 11.5.9 (Appendix 11.5)**, shows that the PIL treated samples present lower leakage current in the low voltage region, indicating the presence of higher shunt resistance and a more ideal contact, also potentially increasing the FF . The X-ray photoemission spectroscopy (XPS) survey spectrum of the PIL treated perovskite presents all the expected core level peaks of the characteristic elements present in both the neat perovskite and the neat PIL (**Fig. 11.5.10A, Appendix 11.5**). Moreover, high-resolution XPS measurements, presented in **Fig. 8.3a**, show that the deposition of the PIL on top of the perovskite surface induces a shift in all core levels of the perovskite elements towards lower binding energies by about 0.2 eV compared to the reference sample. Notably, in **Fig. 8.3b** the valence band spectra confirm the shift of the valence band maximum (VBM) closer to the Fermi level for the PIL treated perovskite. This result suggests that the PIL reduces the n -type character of the surface compared to the reference perovskite. It is reasonable to assume that the passivating behaviour can eliminate defects or impurities at the very surface, potentially responsible for the n -type character.^[238] Surprisingly, the upwards shift in the VBM towards the Fermi level does not translate into a corresponding increase of the work function (WF). Such a scenario is only possible if the PIL, additionally to the reduction of the n -doping at the surface,

creates a surface dipole pointing towards the vacuum. This phenomenon is associated to the nature of the polyionic liquids, where the arrangement of the two ions induces a Maxwell-Wagner-Sillars type interfacial polarization.^[267,268] Next, to understand the impact of the PIL on the energetic alignment with respect to the C₆₀ ETL, UPS measurements were performed on samples with 20 nm of C₆₀ deposited on top, **Fig. 8.3d**. The resulting interfacial energy diagram is depicted in **Fig. 8.3c**. It is evident that the PIL-treated perovskite film exhibits a better alignment of the perovskite conduction band edge with the lowest unoccupied molecular orbital (LUMO) of the C₆₀ layer, promoting charge extraction by eliminating the small extraction barrier found for the reference sample. Additionally, the surface dipole introduces a downwards shift of the highest occupied molecular orbital (HOMO) of the C₆₀ with respect to the VBM of the PIL-treated perovskite, improving the contact selectivity. Overall, we observe that the application of the PIL besides passivating the surface traps also provides a better energy alignment, beneficial in terms of increased *FF* due to better charge extraction.

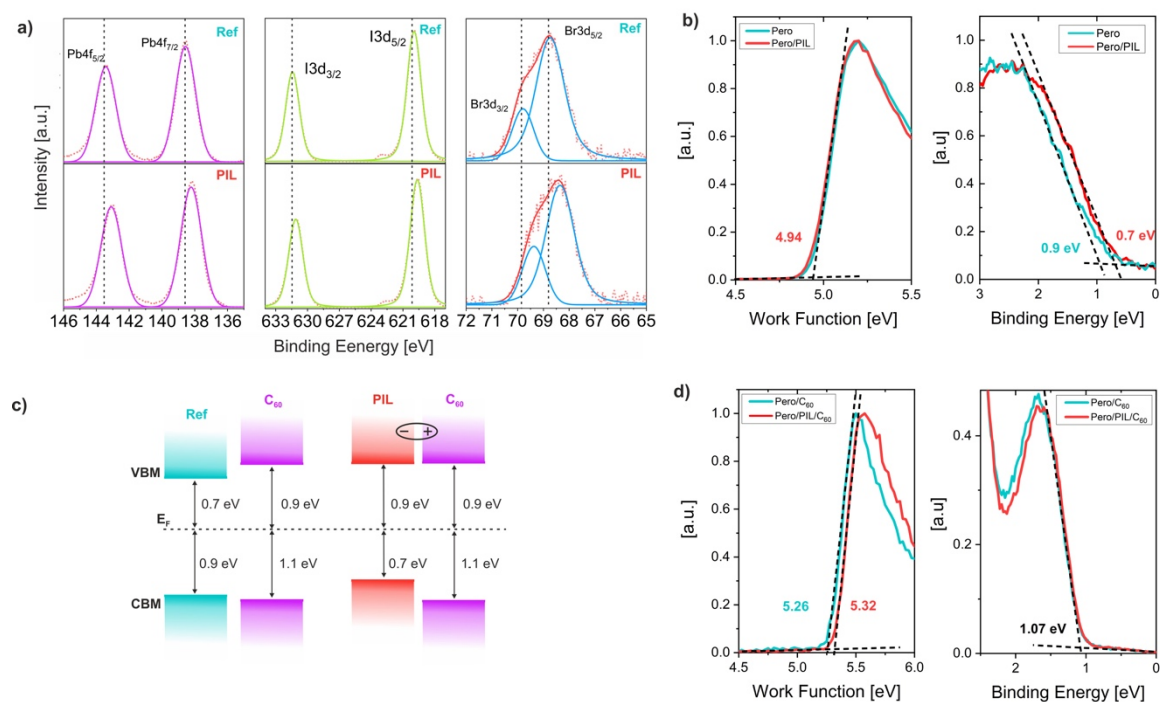


Figure 8.3: a) High resolution XPS spectra of perovskite films with and without PIL treatment for characteristic perovskite elements to highlight the core level shifts. b) Ultraviolet photoelectron spectroscopy (UPS) results for work function and valence bands (probed by X-ray) of the reference and PIL treated neat perovskite and c) with C₆₀ films on top of the perovskite layer with and w/ PIL treatment. d) Interfacial energy levels of the perovskites/C₆₀ interfaces as obtained from the photoemission spectroscopy data shown in panel (b) and (d). Note, all perovskite films were deposited on top of ITO/PTAA substrates and UPS as employed here probes only the surface energetics of the studied sample

The experimental results collected so far reveal that the PIL treatment enhances the transfer of charges across the neat perovskite surface while also improving the energy alignment at the perovskite/C₆₀ junction, both being beneficial for a high *FF* of the PIL-containing devices. Next, we address the increased V_{OC} of PIL treated samples. As shown in **Fig. 8.4a-b**, the analysis of the photoluminescence of the neat films and the complete cells reveals a significant reduction of non-radiative recombination in the PIL-treated samples. We find that the photoluminescence quantum yield (PLQY) of the bare material increases from 1.2% for the reference sample to 7.2% for the PIL treated one. Following the approach presented in **Chapter 2** and **Chapter 3**, by combining the information from PLQY measurements and the EQE_{PV} spectra allows to calculate the QFLS in the absorber, and relate this to the thermodynamic radiative limit for these cells (**Section 11.5.11**). The latter is found to be ~ 1.32 eV for both samples. The QFLS in the neat material essentially corresponds to the maximum achievable V_{OC} for a given perovskite and illumination condition. We find that the QFLS increases from ~ 1.20 eV to ~ 1.26 eV for the PIL-treated perovskite, indicating that the non-radiative losses in the neat material are reduced from 120 meV to 60 meV. This substantial reduction in non-radiative recombination is qualitatively consistent with the increase in CL emission, where the passivation of the PIL is visualized on the surface. Moreover, in full devices, the PLQY of the treated sample increases from 0.1% to nearly 0.5%, increasing the QFLS from 1.14 eV to 1.18 eV, in good agreement with the measured V_{OC} of the cells (1.14 V and 1.17 V, respectively). Consequently, the total non-radiative losses in the complete device are reduced from 180 meV to 140 meV. Consistently, the electroluminescence efficiency (EQE_{EL}) presented in **Fig. 11.5.12 (Appendix 11.5)** exhibits a more than a two-fold increase for the PIL treated device. These results highlight the beneficial effects of the newly-formed perovskite/PIL/C₆₀ junction, where interfacial non-radiative recombination is reduced, allowing for higher QFLS and V_{OC} . In particular, the insulating polymer islands act as a blocking layer, spatially separating the holes in the perovskite from the electrons on C₆₀ and decreasing the possibility for non-radiative recombination of charges across this interface. In agreement with this picture, the photoluminescence decays (TRPL) in **Fig. 8.4c** show that the neat perovskite and the perovskite covered with C₆₀ exhibit longer decays when they are treated with PIL. By fitting the decay with a double exponential model and extracting the lifetime from the slower component characteristic for SRH recombination,^[127] upon PIL treatment the lifetimes increase from 400 ns to 900 ns for the neat material and from 60 ns to 110 ns for perovskite/C₆₀ junction. Interestingly, this reduction in interfacial non-radiative recombination does not translate in a change in ideality factor, which is found to be 1.35 for both samples (**Fig. 11.5.13, Appendix 11.5**).

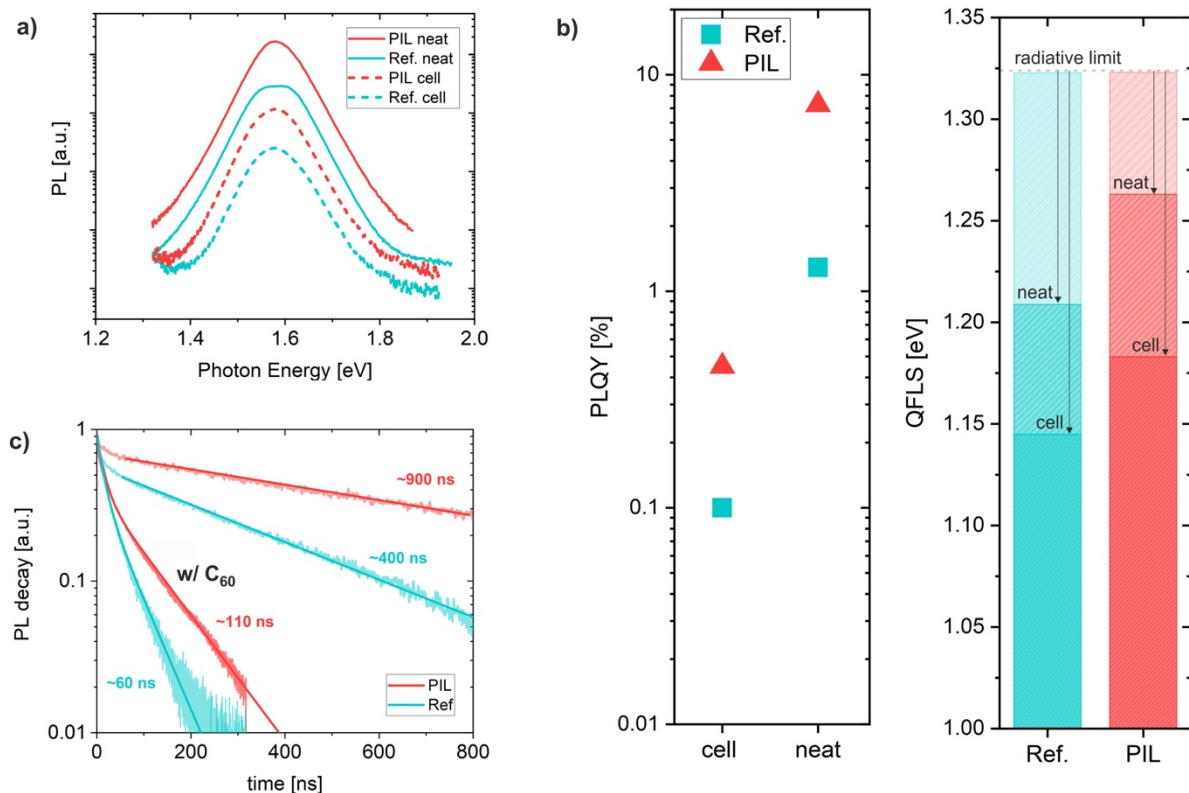


Figure 8.4: a) Photoluminescence spectra of the neat perovskite and complete cells for the reference and the PIL-treated samples. b) Photoluminescence quantum yield measured on the neat material and the complete device stack with the respective calculated quasi-Fermi level splitting. The calculated radiative limit is shown to highlight the energy losses with respect to the theoretical thermodynamic limit. c) Normalized TRPL decays of the reference and the PIL-treated perovskite, with and without C₆₀ deposited on top. In both cases the PIL-treated samples show longer lifetimes denoting an effective reduction of non-radiative recombination.

Remarkably, introducing the PIL in the device stack does not only improve of the material quality and the device performance, but also the stability of the devices. We find that non-encapsulated device comprising the PIL exhibit significantly increased stability under maximum power point (MPP) tracking in inert atmosphere as compared with the reference cell. Notably, the PIL treated cell retains 90% of its initial efficiency after more than 90 h at 50° C, as presented in **Fig. 8.5c**. Moreover, PIL treated non-encapsulated devices stored under inert atmosphere and exposed to indoor light can fully retain their PCE of ~21% during 10 months of shelf storage, as exemplarily shown in **Fig. 8.5a** and **8.b**. A larger set of devices aged for up to 15 months is presented in **Fig. 8.5d**, demonstrating that the PIL-treated devices exhibit a longer shelf life compared to the reference devices, which degrade significantly over time. The improved stability may originate from two main factors. On one hand, the new hydrophobic surface induced by the PIL treatment helps to prevent the penetration of water and moisture, which leads to degradation of the perovskite material. On the other hand, the PIL layer improves the stability of the perovskite from a structural point of

view. As proposed in previous studies, the presence of surface defects and trapped charges can accelerate moisture, oxygen- and light-induced degradation.^[269,270] Additionally, in presence of surface defects, light exposure can trigger the migration of iodine species from bulk to the surface leading to an intrinsic degradation of perovskite material.⁴⁹ In presence of an effective surface passivation, these effects can be mitigated, leading to increased intrinsic stability as previously observed.^[271,272]

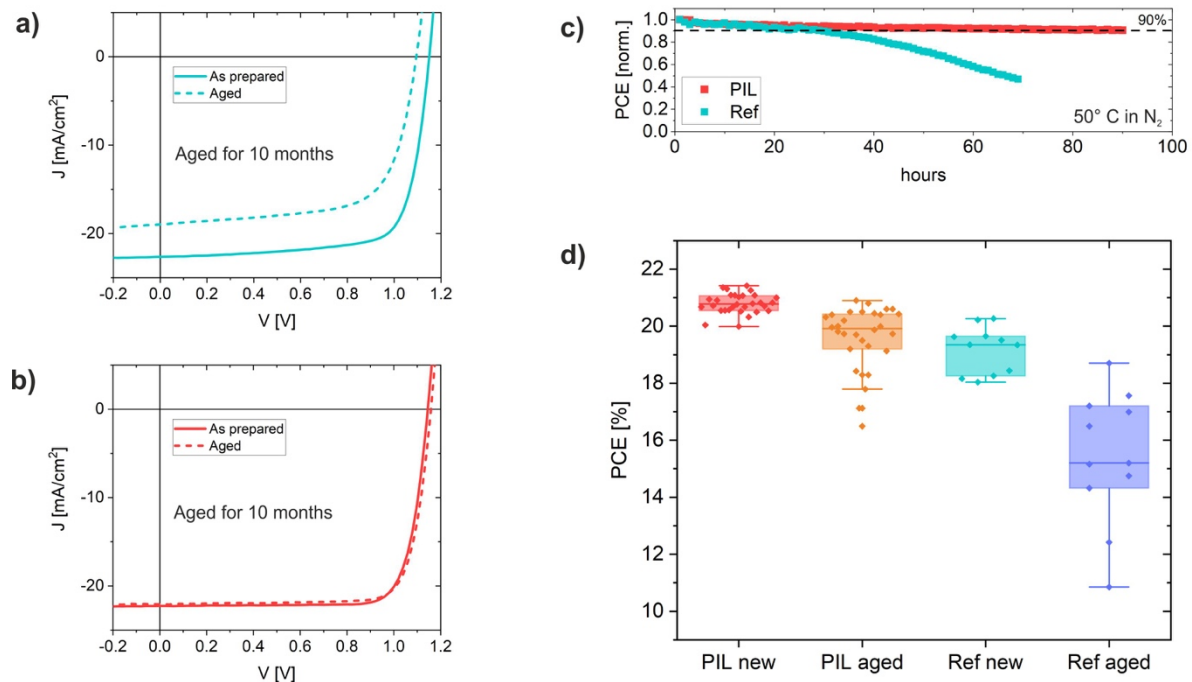


Figure 8.5: a) and b) JV scans of as-prepared and 10 months aged reference and PIL treated devices. The samples were stored under N_2 atmosphere, non-encapsulated and exposed to indoor room light conditions. c) Maximum Power Point (MPP) tracking at 1 sun illumination conditions under N_2 atmosphere at 50°C for non-encapsulated devices with and without PIL. While the PCE of the reference device drops below 90% after roughly 20 h, the PIL device retains 90% of its efficiency even after 90h at MPP. d) Statistics of the PCE of the as-prepared (new) and aged (old) pin devices with and without PIL treatment. The aging time varies from 6 to 15 months, during which the samples were stored in nitrogen under room light.

Finally, as a proof of concept, to corroborate the generality of this surface treatment, we expand our study to *nip* devices utilizing a lower bandgap perovskite (**Fig. S11.5.14, Appendix 11.5**). As in the *pin*-type cells, the PIL is deposited on top of the perovskite surface, but for this device structure being in contact with the Spiro-OMeTAD-based HTL. Surprisingly, also in this case, the introduction of the PIL at the perovskite/HTL interface results in an increased FF , from 70.19 ± 4 to 74.99 ± 1.4 , and in enhanced reproducibility of the final devices. As for *pin* cells, the effective passivation of the perovskite surface upon PIL treatment results in a more ideal contact with the transport layers. However, in *nip* devices, the beneficial effects of the reduced interface

recombination are less visible in terms of V_{OC} increase, only 20 mV, possibly due to the significant non-radiative recombination occurring at the perovskite/ETL interface, as reported recently.^[128] Overall, these results highlight the versatility of this approach and open the door for this class of material to be explored in different device architectures and different perovskite compositions in the future.

Chapter 9.

9. Microscopic emission properties and optical reciprocity failure in MA-free large bandgap halide-segregated perovskites

This chapter is an adapted preprint of the publication:

Caprioglio P., Caicedo-Dávila S., Yang C.J., Rech B., Ballif C., Abou-Ras D., Stolterfoht M., Albrecht S., Jeangros Q., Neher D., *Microscopic emission properties and optical reciprocity failure in MA-free large bandgap halide-segregated perovskites* (submitted)

After investigating the role of non-radiative processes of the energy losses in perovskite solar cells, focusing on the interfaces, here we move the study on the neat material. Particularly, we investigate effect of the halide segregation in large bandgap perovskites to the radiative efficiency of the material. By coupling the PLQY studies with a detailed SEM and CL microscopy analysis, we find that small low bandgap segregated domains are able to efficiently funnel and radiatively recombine the charges photogenerated in the high bandgap domains. We will show how this phenomenon has important implication for the detailed balance principle and Shockley-Queisser theory described in **Chapter 2**.

As introduced in **Chapter 2**, one peculiarity of these materials is the ability of optimizing the spectral range of photo-response by tuning the optical band gap (E_G) through compositional engineering. Within the classic ABX_3 structure, different types of halogen anions, commonly I, Br and Cl, can be accommodated on the X crystallographic site at a low energy and, rather homogeneously,^[273] intermixed with highly tolerant ratios. For example, increasing the amount of Br present in the crystal structure induces an enlarging of the optical E_G . In principle, in a $MAPb(I_{1-x}Br_x)_3$ system, by changing the halogen ratio, an E_G range of 1.57–2.27 eV could be potentially achieved and the respective V_{OC} in the solar cell device tuned accordingly.^[28] This is of particular interest for using this absorber in multijunction tandem devices, either Si-perovskite or perovskite-perovskite, where an accurate selection of the E_g is mandatory to ensure that the sub-cells are current-matched and produce the highest voltage. However, the practical tunability of the E_G is limited by the intrinsic material instability under illumination when a certain Br concentration is surpassed. A frequent problem, widely observed in literature^[34–41], is the phase segregation of the originally intermixed perovskite composition into I- and Br-rich domains, possibly due to a gradient in photo-generated charge carriers across the absorber thickness resulting in strain.^[274] Commonly, this effect is strongly visible in the photoluminescence (PL) spectra, where the initial emission peak of the mixed phase shifts towards lower energies upon light exposure. This, unequivocally indicates the formation of small E_G emitting domains, rich in I.^[38] Practically, this phenomenon sets the limit to the amount of Br that can be mixed into a I-based perovskite while maintaining full phase purity.^[275] Many studies interpreted this phenomenon as a complete demixing of the initial phase, facilitated by the “soft” ionic nature of the perovskite crystal lattice and the large mobility of ions, reducing the E_G range practically achievable.^[27,38,276] However, more recent works pointed out the spectral differences in the emission and absorption of phase-separated perovskites, suggesting only a partial demixing of the total volume of the initial phase.^[37,277] A model largely proposed consists of a semiconductor where the low E_G phase covers only a small fraction of the total volume (e.g. 1 %) and where photoexcited carrier efficiently funnel from large E_G domains into small E_G domains, where they recombine radiatively.^[34,38] Additionally, in accordance with this model, the emission from the I-rich domains is found to be more efficient than the one from the original mixed phase.^[278] Regarding the performance of high bandgap perovskite solar cells, it has been reported that the V_{OC} saturates at the same Br concentration were photoluminescence spectroscopy indicates the onset of halide segregation.^[275] This led to the conclusion that phase segregation is the main cause of the inability in achieving a high V_{OC} in solar cells by increasing the perovskite E_g using more Br.^[34,35,41,275] This picture was, however, challenged in a recent work by Mahesh et al. in which they rationalized and highlighted the negligible impact of the formations of the I rich domains on the V_{OC} loss.^[39] In particular, this work points out that the V_{OC} of the phase segregated mixed halide perovskites is limited by the very low external radiative efficiency of the large E_G phase. It was concluded that the low E_G I-rich domains contribute only little to the V_{OC} loss and are, therefore, not responsible for the observed V_{OC} pinning.

In this work, we quantify the impact of photo-induced phase segregation on the photoluminescence quantum yield (PLQY) of absorbers with different Br contents. We find that increasing the Br content speeds up the phase segregation and increases the PLQY of the resulting segregated phase, reaching extraordinary values up to 25%. Interestingly, and as previously reported,^[277] the absorption onset of phase segregated samples appears to be unaltered. Excitation spectra and PDS results show that the phase segregation occurs only in a small percentage of the overall material volume (less than 1%). Secondary electron microscopy (SEM) and cathodoluminescence (CL) mapping shows the presence of spot-like dispersed small domains emitting at lower energies, preferentially located at the grain boundaries and at the surface of the material. Moreover, by studying the recombination mechanisms in the different domains via intensity dependent PLQY measurements, we decouple the mechanisms behind the emission at the different energies. The resulting picture shows that emission from the large E_G domains is by band-to-band recombination, competing with charge trapping and first order non-radiative recombination. On the other hand, the emission from the small E_G domains occurs mostly via efficient trapping of carriers from the neighboring large E_G regions (charge funneling). These conclusions have strong implication in the estimation the QFLS and the non-radiative losses in the system. Specifically, we will show that the detailed balance principle used in Shockley-Queisser theory is not fulfilled in these systems. Moreover, the low energy emitting domains exhibit local PLQY values exceeding 100% for the actual number of absorbed photons, which could open doors for the usage of this unusual material properties in LEDs or lasers applications.

In this work, we perform PLQY measurements on perovskite films featuring Cs and FA cations on the A site, Pb on the B site and varying ratios of I and Br on the X site. These layers were processed using the hybrid method reported in previous works.^[184,279] In short, a 180 nm-thick $\text{PbI}_2:\text{CsBr}$ template is thermally evaporated (at an evaporation rate of 1 Å/s for PbI_2 , 0.1 Å/s for CsBr), before spin coating a $\text{FAI}:\text{FABr}$ solution (in ethanol) and annealing the stack at 150 °C in air to crystallise the perovskite absorber. The bandgap is varied by tuning the $\text{FAI}:\text{FABr}$ molar ratio in the solution (1:0, 1:2 and 0:1, labelled here as low, medium and high Br content), resulting in films with a nominal composition of $\text{Cs}_{0.18}\text{FA}_{0.82}\text{Pb}(\text{I}_{1-x}\text{Br}_x)_3$, with x ranging from ~ 0.06 to ~ 0.33 . The excitation is provided by a 445 nm laser at 1 sun equivalent photon flux density and the PL spectra are recorded every 10 s in order to monitor the variation in the shape and position of the emission peak over time under continuous light exposure. Importantly, in this part of the study, the PLQY is calculated as the ratio of the total absorbed photons to the total emission flux, not distinguishing between the different emission and absorption contributions.^[128,207] As expected, the sample with lower Br content ($x \sim 0.06$), **Fig. 9.1a**, does not exhibit any evident phase segregation and the peak position remains unaltered under prolonged illumination. The PLQY of the sample decreases over time, going from a value of 0.6% to 0.3%, where it saturates, **Fig. 9.1d**. Notably, even exciting this composition at higher illumination intensities (3 and 5 suns equivalent) does not trigger any phase segregation (**Fig.11.6.1, Appendix 11.6**). On the other hand, the samples with medium ($x \sim 0.24$) and high ($x \sim 0.33$) Br content are

prone to severe phase segregation, **Fig. 9.1b-c**. Already the medium Br sample shows a significant shift of the PL peak from 1.68 eV to 1.59 eV after ~ 800 s of constant illumination. This process is largely accelerated in the high Br samples, with the PL maximum moving from 1.78 eV to 1.57 eV within less than ~ 400 s. Interestingly, for these two types of sample, the PLQY increases upon phase segregation, going from 1% to 4.5% for the medium Br content and, more drastically, to 24% for the high Br content perovskite, **Fig. 9.1e-f**. Despite the much lower PLQY, the original emission peak is still observable in the sample with medium Br, with a constant peak position at 1.68 eV, but it is significantly reduced in the case of high Br concentration, even at complete phase segregation.

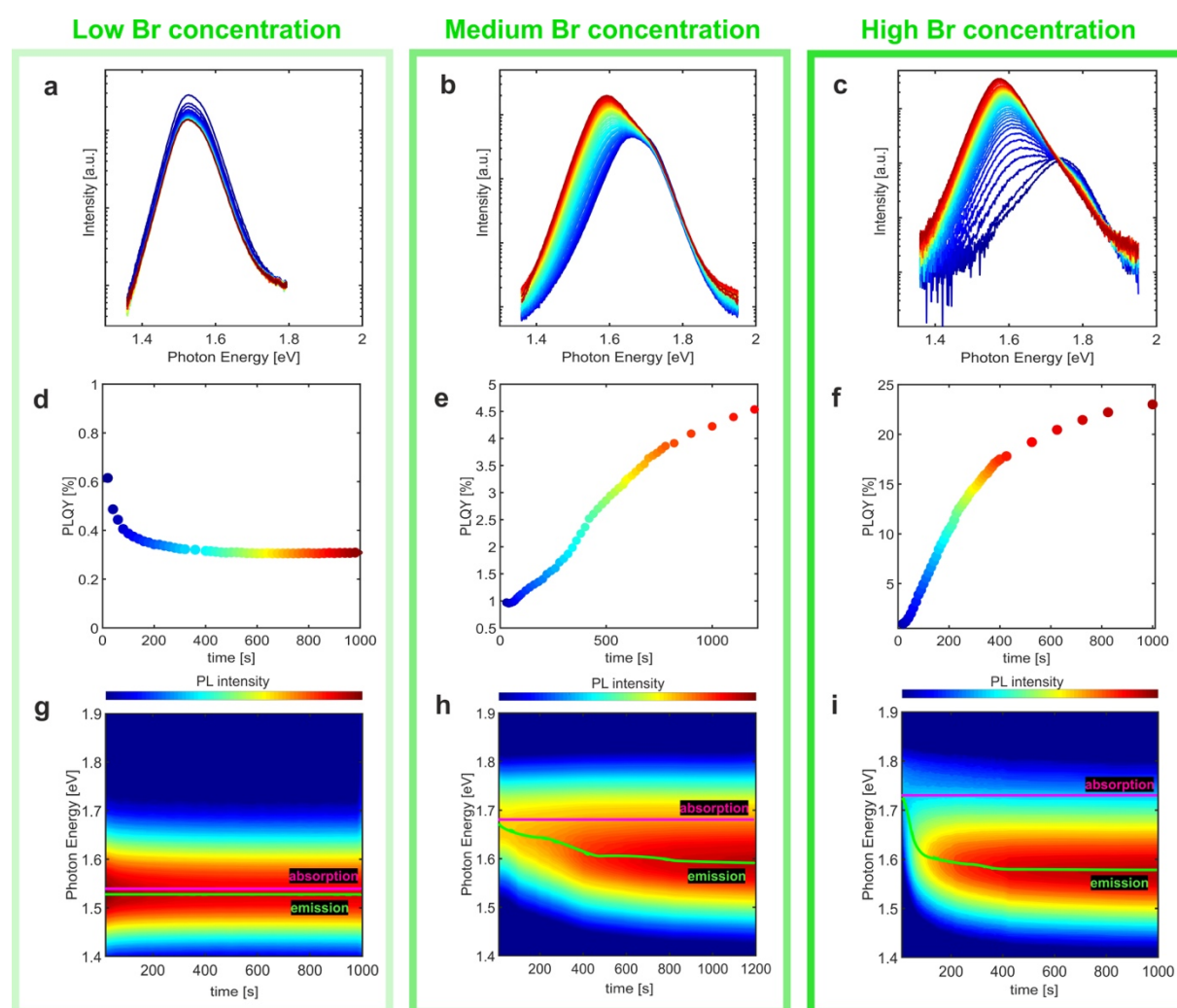


Figure 9.1: Series of photoluminescence spectra for samples with low a), medium b) and high c) Br content recorded every 10 s under constant illumination at 445 nm at 1 sun equivalent. Change of the PLQY over time under light exposure for low d), medium e) and high f) Br content samples. Evolution of the PL peaks presented in a), b) and c) over time under constant illumination in relation to the absorption onset of the same sample for low g), medium h) and high i) Br content samples.

In line with this, the absorption spectra from UV-VIS measurements (**Fig. 11.6.2, Appendix 11.6**) show no change of the absorption onset upon phase segregation for any of the composition studied here, as summarized in **Fig. 9.1h-i**. This suggests that only a fraction of the material undergoes a change in composition, as previously proposed, and that the low E_G domains cover only a small volume.^[39,277] Given the extremely high PLQY values observed for these samples, the low energy emissive volume must efficiently collect the photo-generated carriers from the surrounding volume of the mixed phase. Confirming this argument, excitation spectra performed on a fully phase segregated high Br content sample show no detectable absorption at ~ 1.55 eV contributing to the emission recorded at 1.55 eV (**Fig. 11.6.3, Appendix 11.6**). Essentially, no detectable contribution in absorption at low energy is responsible for the emission at the very same energy. In line with this, given the low absorption at the emission energy of the I-rich domains, the PLQY of the low E_G emission is not affected by photon recycling. In absence of this phenomenon and interference effects, the achievable PLQY is given by $PLQY = \frac{1}{2n^2} IQE$ per exit face, where n is the refractive index of the absorber at the wavelength of emission and IQY is the internal quantum efficiency of PL. With $n \cong 1.8$, $PLQY \cong 0.16 \cdot IQE$. Our finding of PLQY being 25 % for the highly halide-segregated sample, therefore, points to nearly unity IQY from the phase-separated region, with the total PLQY being possibly enhanced by light emission from the high bandgap phase and improved outcoupling due to bulk and surface heterogeneities.^[280] The findings require a better understanding of the structural properties of the phase segregation phenomenon at a microscopic level. Therefore, two of the halide-segregated films are investigated via correlative high-resolution cathodoluminescence (CL) mapping and scanning electron microscopy (SEM). By filtering out the emission of one of the two contributions of the total emission, 700 nm and 800 nm respectively, we are able to map the origin of the emission at the two wavelengths. The results for the medium Br content are presented in **Fig. 11.6.4, Appendix 11.6**. Grain boundaries (GBs) are mapped and highlighted (blue contour lines) using a segmentation algorithm, as detailed in SI (**Fig. 11.6.5, Appendix 11.6**), to facilitate the correlation between the emissive spots and the underlying grains structure. In **Fig. 9.2a** the phase segregated high Br content sample presented in **Fig. 9.1c** exhibits rather homogeneously distributed emission at 700 nm (in green). On the other hand, the emission at 800 nm originates from small phase segregated domains (in red), presented in **Fig. 9.2b**, largely spread on the surface in a spot-like fashion. Clearly, only a small fraction ($\sim 1\%$) of the overall surface show emission at low energies, characteristic of the phase segregated I-rich domains. Similar conclusions have been previously reported mostly from macroscopic measurements technique (CIT), although a few reports aimed for a better detailed microscopic picture for different compositions.^[37,278,281,282]

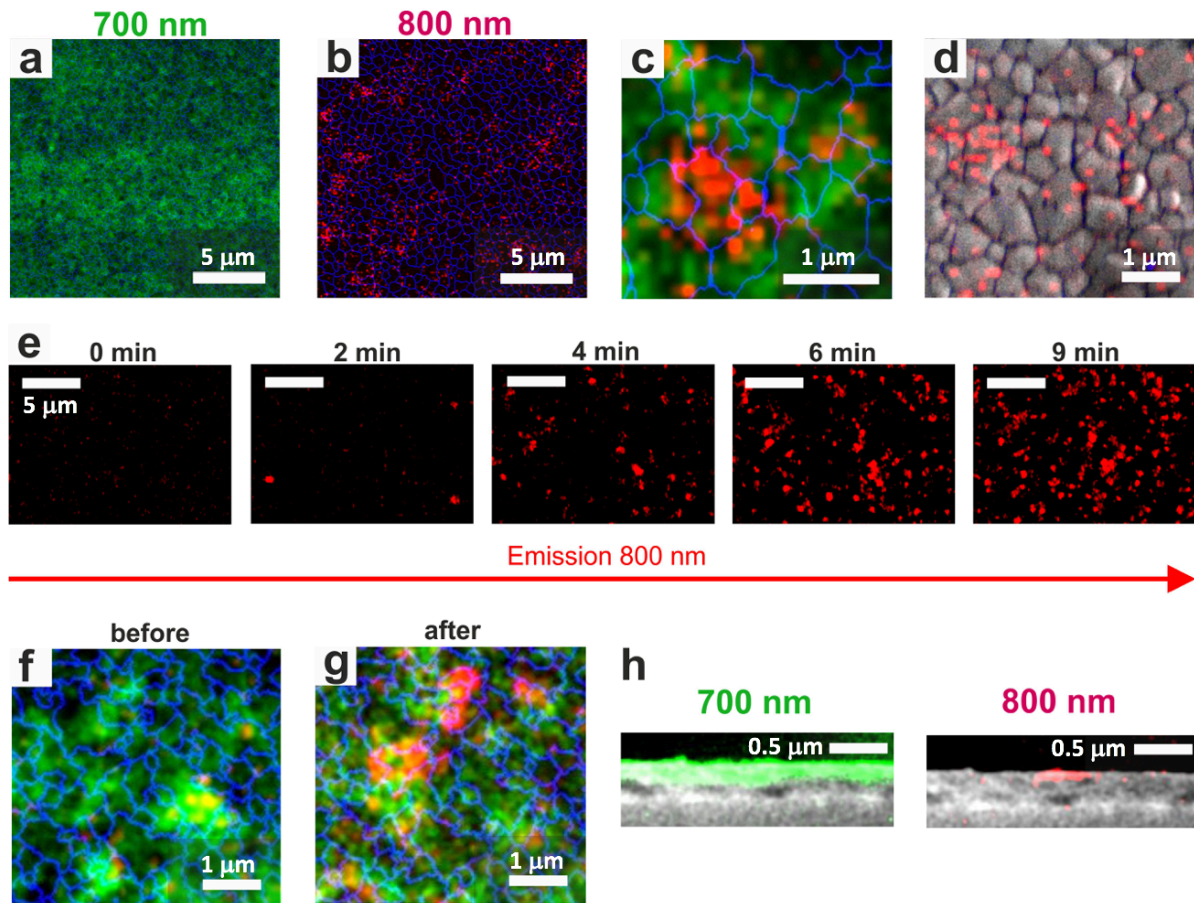


Figure 9.2: a) Top surface CL intensity map for the emission at 700 nm of the fully phase segregated high Br content sample presented in **Fig. 9.1c**. b) Top surface CL intensity map for the emission at 800 nm of the same sample in a). c) High magnification CL intensity of the sample in a) overlaying the emission at 700 nm and 800 nm. The blue contour lines in a), b) and c) reconstruct the grain boundaries from the SEM image, as detailed in SI. d) Superposition of SEM and CL intensity map for the emission at 800 nm of the sample in a). e) Series of different time frames from the video recording of the CL intensity at 800nm during the phase segregation of a high Br content sample. The series goes from a pristine non-segregated sample at $t = 0$ min to a full segregation at $t = 9$ min. f) and g) Overlay of the CL intensity at 700 nm and 800 nm for a sample before and after phase segregation. h) SEM cross section images of a fully segregated high Br content sample overlaying the emission at 700 nm and 800 nm.

In order to get detailed insights of the correlation of the microstructure with the spatial distribution of emission, we acquired CL maps at higher magnification, **Fig. 9.2c-d**. The results show that the small 800 nm emitting clusters are preferentially located at GBs or isolated at small grains. It is important to point out that the emission is not distributed along the GBs, but stems from isolated emitting points. In order to track the dynamics of formation of these domains, fresh non-segregated films were constantly irradiated by the electron beam, while monitoring their CL signal and recording the emission at 800 nm, presented in **Fig. 9.2e**. We find that the electron beam irradiation induces the phase segregation in similar time scales as the 445 nm irradiation, in agreement with previous reports.^[67] The series of images show how, during phase

segregation, small isolated spots emitting at 800 nm start to appear scattered on the surface of sample. The density of these domains increases with time until reaching a saturation after roughly 9 minutes. In **Fig. 9.2f-g** we compare the emission at 700 nm and 800 nm of the same sample shown in e) before and after segregation, respectively. The initial CL map, **Fig. 9.2f**, shows how the 700 nm emission is distributed over the whole film, although with non-uniform intensity. After phase segregation, the 800 nm isolated emitting clusters are present on the surface, while the 700 nm luminescence is still distributed across the entire surface. For the majority of the cases, the 800 nm emission appears in spots which were characterized by a low-intensity 700 nm emission, in the as-deposited state, suggesting that a high density of defects helps nucleating the low E_g phase, as highlighted in **Fig.11.6.6, Appendix 11.6**. Defects, notably halide vacancies, act as diffusion pathways and likely accelerate halide migration in these regions,^[274,276]. Additionally, in **Fig. 9.3h**, the cross-section CL-SEM imaging of the film allows to locate the 800 nm emitting clusters confined to the surface, in contrast with the 700 nm emission, which is evenly distributed throughout the bulk of the film, in agreement with previous studies.^[274]

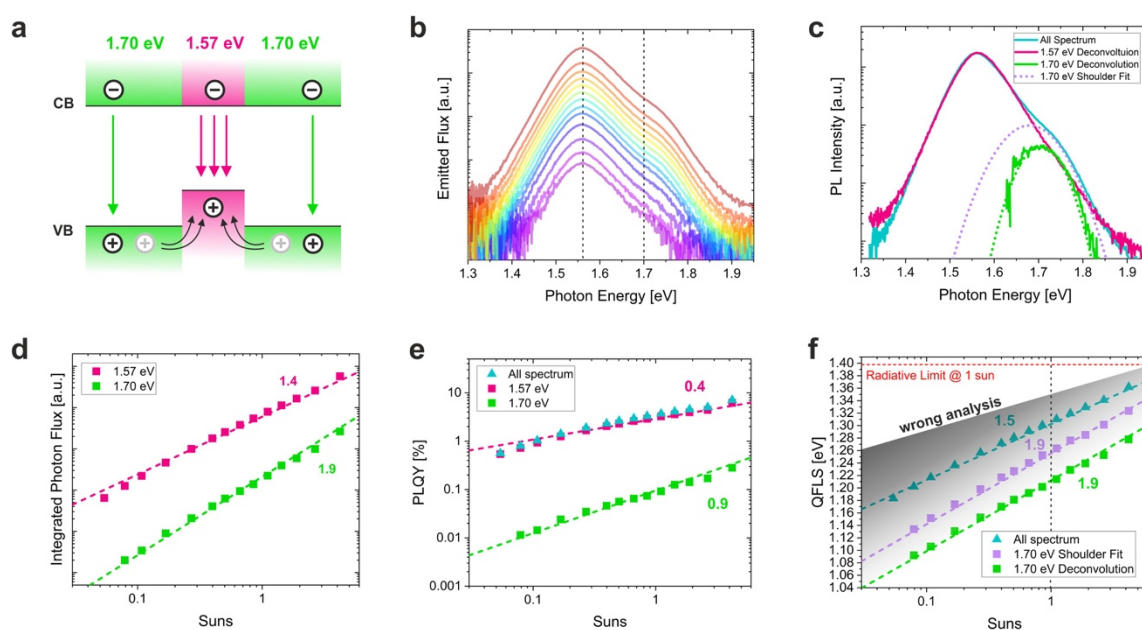


Figure 9.3: a) Schematic representation of hole trapping and the radiative emission processes from the different domains. b) Intensity dependent PL spectra of a fully segregated high Br content sample. c) Example of different deconvolution methods for the components at 1.57 eV and 1.70 eV. d) Integrated photon flux for the single emission contributions with respect to the intensity. The numbers indicate the slope of the respective fit. e) PLQY intensity dependence of the single contributions calculated from the integrated emission in d). f) QFLS calculated with different methods namely, full spectrum integration (turquoise dots), Gaussian shoulder fit at 1.70 eV (pink dots) or spectra deconvolution by subtraction of the fully segregated high Br spectrum (green dots). The shades indicate moving from the wrong analysis towards the correct one. Here, also the S.Q. radiative limit for a bandgap of 1.70 eV under 1 sun equivalent conditions is plotted.

Next, we turn to the mechanisms determining the emission properties of the halide-segregated layers. It has been shown that replacing I by Br in Pb-based perovskites causes a significant increase of the ionization energy while the electron affinity remains rather unaffected.^[283–285] The I-rich phase is, therefore, expected to act primarily as a hole trap, with subsequent (radiative) recombination of the trapped hole with a free electron, as schematically represented in **Fig. 9.3a**. Given this situation, the emission from this phase must be treated in the framework of the Shockley-Read-Hall theory, compared to the classic band-to-band recombination in the mixed phase. As an important consequence, the two emission contributions will obey a different dependence on the illumination intensity. To this end, we recorded the PL spectra of a fully phase-separated Br-rich sample over a wide range of excitation intensities. For this measurement, we chose a sample with a slightly smaller Br-content than the one in **Fig. 9.1c**, in order to still display emission from the mixed high bandgap phase. For all excitation intensities the spectra are comprised of a peak at 1.57 eV and a broad and well-distinguishable shoulder at ca. 1.7 eV, as indicated in **Fig. 9.3b**. In order to deconvolute the contribution at different emission, we follow two different approaches. In the first case, we refer to the spectrum of the halide-segregated sample in **Fig. 9.1c**, as reference for the emission from the pure I-rich phase. This spectrum is then subtracted from the spectrum containing both contributions, effectively decoupling the emissions from high energies domains. An example for a spectral decomposition based on this assumption is shown in **Fig. 9.3c** (see the Supporting Information for details). From here, we integrate the photon flux of the two components as function of illumination intensity, as presented in **Fig. 9.3d**. In the second approach, we assume that emission from the low E_G phase (at 1.57 eV) is weak at ~ 1.7 eV, and the two contributions are deconvoluted by fitting the spectrum with two Gaussians functions (see **Fig. 11.6.7 Appendix 11.6** for the deconvolution and the results). As expected and visible in **Fig. 9.3c**, the latter approach yields a more intense emission from the Br-rich phase, but both analyses give the same strict power-law dependences of the emitted photon flux on the illumination intensity $\phi \propto I^k$, with $k = 1.4$ and 1.9 for the low bandgap and high bandgap emission, respectively (see **Fig. 9.3f**, as discussed below). This insures us that the following analysis of the data is not severely affected by the choice of the reference spectrum. The integrated photon flux of the high bandgap emission depends nearly quadratically on the illumination intensity $\phi_{1.70} \propto I^2$. Such behaviour is characteristic for photon generation by the radiative bimolecular recombination of free electrons and holes, competing with a dominant non-radiative first-order recombination process (see also the **Appendix 11.6**). Related to this, the PLQY of the high energy emitting component in **Fig. 9.3c** is nearly linear in intensity. Note that the exact functional dependence of $\phi_{1.70}$ and PLQY on I depends on the details of the trap-assisted recombination pathway (see Supporting Information). On the other hand, the k value of the low energy emission is smaller ($\phi_{1.57} \propto I^{1.4}$) and suggests a radiative process involving the recombination of trapped charges. Simple models describing the exclusive radiative recombination of trapped carriers with free carriers predict a k -values of unity and a constant PLQY. The fact that $\phi_{1.57}$ increases via a higher slope suggests, also here, the presence of a parallel competing non-

radiative recombination pathway. Unfortunately, given that there is no easily detectable absorption from the I-rich phase, it is difficult to selectively excite these domains directly and investigate these processes separately. Notably, a less efficient trapping of holes would also lead to higher slopes, as expected from the lower PLQY values compared to the sample in **Fig. 9.1c**. The finding that the two emission components exhibit different dependences on excitation intensity comes with important consequences for the interpretation of the emission properties of such halide-segregated samples in term of their QFLS and their V_{OC} potential, as described in **Chapter 2**. As pointed out there, for all grey bodies being in thermal equilibrium with its environment, detailed balance requires that the photon flux by the thermal emission from this body is equal to the flux of photons absorbed from the black body radiation of the same temperature at any photon energy interval : $\phi_{em}^0(E_\gamma) = a(E_\gamma)\phi_{BB}^0(E_\gamma)$, where $a(E_\gamma)$ is the absorption of the sample at the given photon energy E_γ . While $\phi_{BB}^0(E_\gamma)$ is not measurable at realistic sample temperatures, Wüffel has shown that the non-thermal emission spectrum $\phi_{em}(E_\gamma)$ of the same body e.g. excited though photoexcitation or in electroluminescence, has the same shape:^[133]

$$\phi_{em}(E_\gamma) = \phi_{em}^0(E_\gamma)\exp\left(\frac{QFLS}{k_B T}\right) \quad Eq.9.1$$

Note that the derivation of **Eq. 9.1** relies on a number of assumptions, the most important being that the emission involves the recombination of equilibrated electron and hole populations, with the population probability of all contributing states described by the same quasi-Fermi levels for electrons in the conduction and valance band, $E_{F,C}$ and $E_{F,V}$, respectively. This allows to determine the $QFLS = E_{F,C} - E_{F,V}$ from the measurements of the photon emission flux at any photon energy (or energy interval), provided that the corresponding value of ϕ_{em}^0 is known.

$$QFLS = k_B T \ln\left(\frac{\phi_{em}}{\phi_{em}^0}\right) \quad Eq.9.2a$$

Also, considering that ϕ_{em} is related to the absorbed excitation flux ϕ_{abs} through $\phi_{em} = PLQY \cdot \phi_{abs}$, a popular approach to calculate the QFLS from emission experiments is based on the relation:

$$QFLS = k_B T \ln\left(\frac{\phi_{abs}}{\phi_{em}^0} PLQY\right) \quad Eq.9.2b$$

The problem in applying this concept to such halide-segregated perovskite films lies in the fact that the population of free states and traps is described by different quasi-Fermi levels.^[126] For example, if the recombination of trapped charges is faster than

trap-reoccupation and thermal release, the trapped charges are no more in equilibrium with the free carrier population. Consequently, the emission spectrum of the body under optical or electrical driving conditions is different from the spectrum of the thermal emission. Therefore, the optical reciprocity does not apply anymore to non-thermal emission spectra, meaning that the spectral shape of $\phi_{em}(E_\gamma)$ is different from the spectrum predicted from $a(E_\gamma)\phi_{BB}^0(E_\gamma)$ in such halide-segregated systems, This is clearly visible in **Fig. 9.4a-b**, when we apply the reciprocity relation to the emission from a high Br content sample before and after segregation, and compare the results to the corresponding excitation spectra. Before the sample segregates, the absorption predicted (calculated) from the PL emission matches quite well with the excitation spectrum. On the other hand, the absorption profiles calculated from the emission of the halide-segregated sample is strongly red-shifted to the excitation spectrum, demonstrating the failure of the optical reciprocity for the emission and absorption of this sample under the given measurement conditions. For the same reason, the analysis of the emission properties of such Br-rich samples with **Eq. 9.2a** or **9.2b** is prone to errors if not done properly. Indeed, the QFLS in mixed perovskite phase is related only to the absorption and emission of the high energy photon flux via **Eq. 9.2a**. The emission from trapped charges in the low energy states must be omitted from the QFLS contribution for the same reason. To highlight this, we calculated the bulk QFLS as a function of excitation intensity with either neglecting or including the strong low energy component to the totally emitted photon flux. The result is shown in **Fig. 9.3f**. Erroneously applying **Eq. 9.2b** to the total PLQY yields a QFLS of more than 1.3 eV at 1 sun. On the other hand, deducing the QFLS the correct way, by considering only the high energy emission, gives much smaller values, between 1.21 eV and 1.25 eV, depending on the decomposition approaches. Notably, here the ideality factor is almost exactly 2, consistent with photon emission from charges which undergo exclusively first-order non-radiative recombination, consistently with the large amount of non-radiative losses. This is different from the analysis taking into account the PLQY of the whole spectrum, which besides overestimating the QFLS potential of the mixed phase, also yields a too small ideality factor of only 1.5. We remember here that since in the absorption of photons and the emission due to radiative recombination occurs at different energies, the detailed balanced principle of Kirchhoff's law can not be applied.^[121]As a consequence, the photoluminescence or electroluminescence quantum efficiencies obtained from the whole segregated spectrum cannot be used to calculate the QFLS and the V_{OC} losses of a material as proposed by Rau,^[138] and commonly valid for other perovskite systems.^[122,127,130,146,286,287] To be more specific, the incongruence between absorption and emission implies that the dark radiative current $J_{0,rad}$, calculated from the black-body radiation and the absorption onset of the EQE_{PV} , cannot be used in relation to the PL (EL) emission associated to a different E_G as presented in **Fig. 9.4c** and visible in the following equation

$$QFLS_{E_G^1} = k_B T \cdot \ln \left(PLQY_{E_G^1} \cdot \frac{J_{SC E_G^1}}{J_{0,rad E_G^1}} \right) \quad Eq.9.3$$

Here the $PLQY_{E_G^1}$, $J_{SC_{E_G^1}}$ and $J_{0,rad_{E_G^1}}$ are associated to the same band gap E_G^1 . However, in the case of the emission from the low energy domains, we would have a $J_{0,rad_{E_G^2}}$ and $J_{SC_{E_G^2}}$ associated to a different bandgap (mixed phase) compared to the emission $PLQY_{E_G^1}$. This violates the main assumption for the applicability of this relation, as explained above explained.

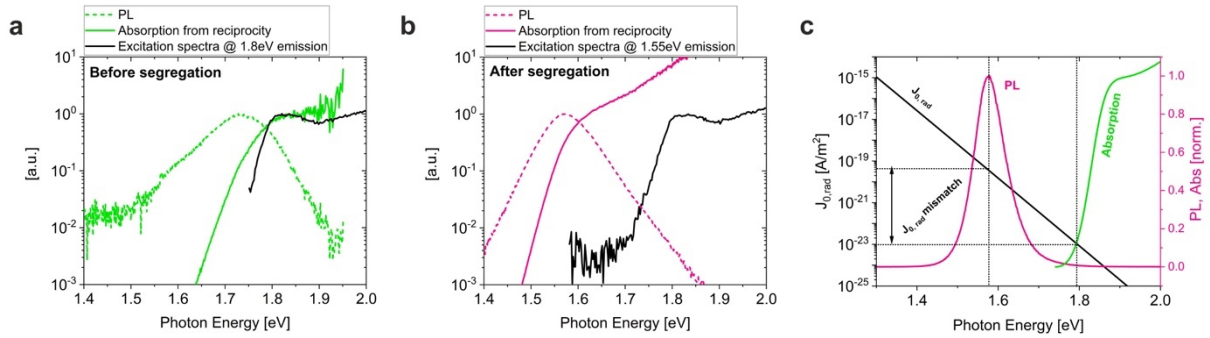


Figure 9.4: Comparison of reciprocity relation before a) and after b) phase segregation of a high Br content. Here the absorption spectra calculated from the PL emission through optical reciprocity is compared to the absorption onset obtained from the excitation spectra. c) Highlighted mismatch between emission and absorption of a fully segregated high-Br content sample. The $J_{0,rad}$ calculated using Shockley-Queisser theory assuming a step-function absorption profile at each energy is plotted to highlight the different values associated to different energy of absorption and emission.

Overall, this analysis confirms the high degree of non-radiative losses in the mixed phase and correlates well with the usually poor V_{OC} values obtained in the respective solar cell devices. Thereby, this approach highlights the detrimental poor radiative efficiency of the mixed phase, rather than the apparent bandgap shift, as main cause of the low performance of these types of devices, compared to what theoretically achievable for the given bandgap. To conclude the picture, the radiative ideality factors, that are calculated from the slope of the QFLS (1.7 eV) versus the emission flux of the two different emissive components (**Fig. 11.6.8, Appendix 11.6**), yield a value of ~ 1 for the 1.7 eV component, as expected from second-order recombination, but higher slopes of ~ 1.35 for the 1.57 eV components. This is closer to 1.5 (full derivation in **Appendix 11.6.9**), which would indicate radiation from 1st order trap-to-band processes. In line with this and as a consequence, the effective trapping of the surrounding charges can effectively limit the radiation from the neighboring large E_G phase. Indeed, as presented in **Fig. 9.5a** for a high Br content sample, the emission at high energies decreases concomitantly with the emission at low energies becoming more and more efficient. Considering that the negligible overall change in absorption cannot justify the decrease of the emission at high energies, this directly translate in a lower QFLS in the high E_G domains and apparent higher non-radiative losses. Consequently, the charge trapping in the low energy domains, will always reduce the

bulk QFLS of the mixed phase, irrespective of whether these trapped charges recombine radiatively or non-radiatively. Therefore, this could be a major V_{OC} limitation in wide-gap Br rich cells.

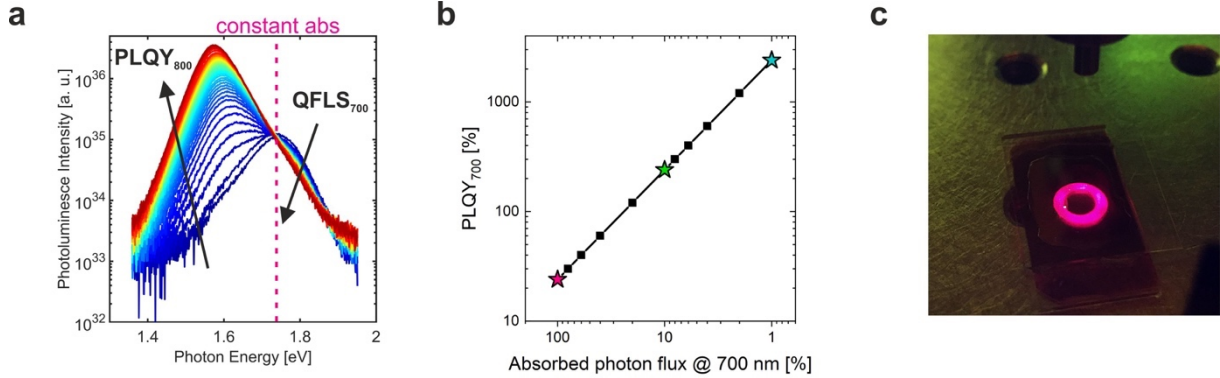


Figure 9.5: a) Light exposure time dependent segregation for a high Br content sample which highlighted the concomitant decrease in QFLS at high energies and increase of emission at low energies. b) The PLQY as a function of the fraction of the absorbed photons from the low energy emissive states. c) PL emission of the phase segregated high Br content samples illuminated with a 445nm laser at 1 sun equivalent, outcoupled from an optical fiber (circular shape).

Lastly, in terms of PLQY, the low energy domains are capable of yielding astonishingly high PL quantum efficiencies exceeding 100% for the actual number of photons that these regions absorb. We can simply express total PLQY_{tot} as follow

$$PLQY_{tot} = \frac{\phi_{em}^{tot}}{\phi_{abs}^{tot}} = \frac{\phi_{em}^{800}}{\phi_{abs}^{700}} \quad Eq.9.4$$

where ϕ_{em}^{tot} is the total emitted photon flux and the ϕ_{abs}^{tot} the total absorbed photon flux. Here, ϕ_{abs}^{tot} can be approximated as the emission at 800 nm ϕ_{em}^{800} and ϕ_{abs}^{tot} approximated as the absorption at 700 nm ϕ_{abs}^{700} . Then we can calculate a local PLQY_{local} for the emission at 800 nm, which can be approximated as the total emission at 800 nm divided by the number of photons absorbed by these low E_G domains as shown in **Fig. 9.5b**. For example. assuming that these low E_G regions absorb 1% of the total number of absorbed photons, the local PLQY is calculated as follows:

$$PLQY_{local} = \frac{\phi_{em}^{800}}{\phi_{abs}^{800}} = \frac{\phi_{em}^{800}}{0.01 \cdot \phi_{abs}^{700}} \quad Eq.9.5$$

Consequently, as these domains are capable of achieving a PLQY_{total} of ~ 20%, the local quantum efficiency reaches values of 2000%. We acknowledge that such values

are possible only in the frame of this specific definition and no material with a real PLQY large than unity can exist. However, here the argument is used to highlight the efficiency of the charge funneling and re-emission process. As such, this mechanism can potentially open doors for the usage of this material property for future application, such as highly efficient LEDs or lasers.

10.

10. Discussion and Conclusions

In conclusion, in this thesis work we studied the details of non-radiative recombination in perovskite solar cells in relation to the device efficiency, and in particular to the V_{OC} . The use of photoluminescence quantum yield measurements on the neat material, single interfaces and complete devices, allowed us to draw a comprehensive picture of the role of the CTLs with respect to the overall recombination mechanisms of the device. In **Chapter 4**, by comparing the non-radiative losses calculated via PLQY at the single interfaces, we found that all commonly used transport layers, although indispensable in perovskite solar cells, introduce a significant degree of interface recombination at their interfaces with the perovskite absorber, with the consequence increase of the energy losses in the system. With this, an important step forward in understanding of the physics ruling the energy losses in perovskite solar cells has been achieved. Our findings challenge the general picture where the detrimental recombination centers are located at the grain boundaries or, generally, in the perovskite absorber, as early reports pointed out.^[101,141] As a consequence, we demonstrated that in order to approach the high V_{OC} s potentially achievable by the perovskite absorber, the interfaces need to be properly addressed and optimized. This again disputes the general interpretation in many studies in literature, where decreasing the trap density in the perovskite absorber is automatically believed to translate in a larger V_{OC} in the solar cell device.^[108,142] Moreover, these findings highlighted the selectivity of the transport layer and its alignment with the perovskite bands as decisive parameters in controlling the strength of interfacial recombination. In addition, in the case of strong interface recombination and energy misalignment, the equality between QFLS and V_{OC} is not fulfilled anymore. In **Chapter 5**, studying the relation between these two quantities at different illumination conditions, allowed us to calculate the associated internal and external ideality factors. With this, we managed to decouple the external recombination processes influencing the V_{OC} of the cell to the internal ones, influencing the QFLS in perovskite absorber. These results showed that, in many systems, the V_{OC} can be influenced by additional recombination processes at the interfaces which do not strongly influence the QFLS. Therefore, the V_{OC} cannot be used alone to draw ultimate conclusion regarding the nature of recombination processes happening in the perovskite material. This is an important conclusion which has strong implications on the applicability of several methods which relies on the V_{OC} as representative parameter for the recombination taking place in the absorber, such as TPV and, more commonly, the V_{OC} vs. intensity.^[141,181,211,288] Thereby, we propose that the parallel monitoring of the QFLS and the V_{OC} is essential in order to have a full picture of the different recombination mechanisms ruling the device performance. Moreover, these additional recombination processes at the transport layer interfaces are found to be responsible for the V_{OC} saturation, commonly observed at high illumination condition. Importantly, by safely excluding a possible temperature effect as being responsible for this phenomenon, as recently proposed,^[198] we clarified an important under-debate topic in literature. However, although the relation between external and internal recombination processes has been clarified, the origin of the ideality factor value still remained poorly understood. To shed light on this matter, in **Chapter 6**, by performing intensity dependent PLQY measurements on the neat

material, single interfaces and full devices, we studied the effect of the single interfaces on the ideality factor. The results allowed us to conclude that the stronger recombination channel, in this case at the interfaces, completely dictates the ideality factor of the complete cell. Importantly, at the present, most of the studies in literature associated the ideality factor to bulk recombination properties, often neglecting the role of the interfaces.^[141,288] Furthermore, considering only interface recombination, we proposed a recombination model able to rationalize the ideality factors values of perovskite solar cells utilizing different transport layers. Notably, our model allowed us to explain the ideality factor values between 1 and 2, commonly observed in perovskite solar cells and often poorly understood. Also in this case, the common explanation for this values usually relies on to mixed contribution of first and second order recombination processes,^[139,211] which here we disproof for several reasons. Mainly, the competition of two different recombination orders would result in a carrier density dependent value of the ideality factor, in other words, the slope of the $V_{OC}(I)$ would be increasing or decreasing with the carrier density in the device. On the contrary, for the devices and the carrier density regimes investigated here, the $V_{OC}(I)$ dependence obeys one defined and constant power law, ruling out a competition between first and second order recombination processes. Instead, there is only one mechanism dominating recombination, in this case interface recombination. In line with this, we concluded that interface recombination alone can lower the ideality factor towards unity. Importantly, in these systems, this value does not represent the desirable pure bimolecular recombination, as commonly assumed. As a consequence, counterintuitively, in devices limited by interface recombination a larger ideality factor can correspond to less non-radiative recombination and higher V_{OC} s. The conclusions of **Chapter 4**, **5** and **6**, allowed us to delineated a clearer picture of the relevant recombination processes currently limiting the performance per perovskite solar cell device, often unclear in literature. A such, the acquired device physics knowledge is directly translated in different approaches for device optimization, presented in **Chapter 7** and **8**. Firstly, in **Chapter 7**, we managed to effectively decrease the strength of non-radiative recombination at the perovskite/ C_{60} interface by inducing a strong *n*-type surface by adding a small amount of Sr into the perovskite precursors. A combination of structural and energetic characterization, highlighted how the Sr can segregate at the perovskite surface creating a strong downward band-bending, which effectively repels holes from the surface and the ETL interface. As a consequence, the rate of interface recombination is effectively slowed down. The resulting devices showed V_{OC} up to 1.18 V, which was further improved to nearly 1.23 V with the implementation of an additional PS layer. These important conclusions rely on the combination of different sophisticated experimental techniques and simulations, which require a delicate interpretation, e.g. surface doping not to be misinterpreted with bulk doping, which would result in a completely different outcome. Although at the time of this publication several other works reported Sr as additive for halide perovskites,^[45,223,226] in our work, we aim to provide a mechanistic insight on the working mechanism of this approach. Importantly, the beneficial effects of an *n*-type surface in *p-i-n* type devices opened doors to possible future strategies for device optimizations, as confirmed by another important coeval publication.^[289] Although the

V_{OC} of these devices experienced a significant improvement, the FF appeared to suffer from these modifications, with the consequence of limiting the boost in efficiencies. To answer to this problem, in **Chapter 8**, we fabricated devices implementing a novel combination of materials by postprocessing a PIL interlayer between the perovskite and the ETL. These devices experienced a concomitant improvement of the FF and the V_{OC} , reaching outstanding values of 83% and 1.17 V respectively, ultimately increasing the efficiency up to more than 21.4%. We found that this polymeric layer can effectively passivate the perovskite surface and reduce the contact area with the ETL, effectively reducing non-radiative recombination in the neat material and in the complete cell. At the same time, the charge extraction is improved by the better energy alignment at the PIL modified perovskite/ C_{60} interface, increasing the FF . Furthermore, long (>500h) MPP tracking measurements on these devices highlighted that the PIL is able effectively improve V_{OC} , FF and stability all at once. Importantly, common transport layer approaches rely on surface passivation or the implementation of a large bandgap material at the surface as a main working mechanisms.^[61] In our case, the PIL layer is capable of inducing a bi-functionality of the surface where at the same time carrier recombination is reduced but charge extraction is enhanced. Importantly, as the best of our knowledge, this is the first report of the combination of PIL with halide perovskite in solar cell devices. As such, these findings open doors for a new class of materials to be further implemented and studied in combination with perovskite solar cells. **Chapter 7** and **8** corroborated and complemented the understanding reached in **Chapter 4**, **5** and **6** regarding the detrimental aspects that need to be addressed in perovskite solar cells in order to push their efficiencies close the theoretical limit. Lastly, in **Chapter 9**, we moved to the study of the recombination processes in halide-segregated large bandgap perovskite systems. Here, we investigated the effect of the phase segregation on the radiative efficiency of these materials. By coupling the PLQY studies with correlative SEM and CL microscopy imaging, we revealed how small segregated low energy domains can act as efficient radiative recombination centers (PLQY > 20%) for the photogenerated carriers in the large energy domains, which still occupy most of the volume of the material. As such, we managed to visualize that the phase segregation effectively take place only in a small fraction (1%) of the overall volume of the sample. As a consequence, we showed how this phenomenon has strong implication on the reciprocity between absorption and emission, largely used to estimate the energy losses of solar cells from PL or EL efficiencies. Importantly, the failure of the optical reciprocity between absorption and emission does not allow the apply the Shockly-Queisser theory and Rau's reciprocity on such halide-segregated systems. However, we propose an alternative approach to correctly estimate the radiative potential and the QFLS in these systems. Our results highlighted a large degree of non-radiative losses in the large energy domains, most probably caused by the efficient charge trapping happening in the low energy domains, possibly responsible for the small V_{OC} compared to the nominal bandgap, commonly observed in solar cell device featuring these absorbers. This findings challenge the general understanding that the appearance of the new low energy phase automatically sets the V_{OC} of the device to the corresponding low bandgap.^[35,275] Our conclusions are in

line with a recent important publication,^[39] where the V_{OC} losses in this large bandgap systems are related to the poor radiative efficiency of the original mixed phase. In conclusion, this thesis work provides a thorough understanding of the recombination processes taking place in different perovskite systems and their detrimental effects in perovskite solar cells and materials. As such, the research contained in this work aims to provide a guidance for future development and optimization of perovskite materials in devices. Furthermore, by corroborating our fundamental understanding with practical strategies and new methodologies for device optimization and material improvement, we aim to provide a solid base for the future follow up studies.

As outlook, our studies thoroughly investigated the importance and impact of interface recombination on the energy losses of perovskite solar cells, however, a more detailed picture of these recombination processes is not fully achieved. In particular, as we explained in **Chapter 2**, interface recombination comprises the sum of several different possible charge recombination pathways, which are currently not resolved. As such, transient techniques, such a ns- and fs-TAS, have to be carefully applied in order to disentangle these different contributions and to achieve a more complete understanding. In line with this, at the present, a rigorous reconstruction of the energy alignment between the various layers implemented in perovskite solar cells is still missing, due to the problematic reconstruction of the energy levels of the buried interfaces. As presented throughout this thesis work, the details of the interface energetics will have a strong influence on the overall recombination processes in the device and on the interpretation of the ideality factors, as well as on the general interpretation of the energy losses. Moreover, a better understanding of this aspect sets the basis for future device improvement strategies. On this note, a better control of the degree of n -doping to be induced at the top surface of p - i - n devices could results in an effective strategy to reduce the strength of surface and interface recombination. Additionally, the combination of multiple approaches could be investigated. For example, given that PILs are vast class of materials, the molecular composition of the PIL can be varied over a wide range, aiming at establishing design rules for the improvement of device performance. Related to this, given the early stages of this approach, there is a large space for further characterization and understanding on the local interaction between these materials and the surface of the perovskites. As such, different perovskite compositions could be explored as well, such large bandgap perovskites or MA-free compositions. On this note, although we demonstrated that halide segregation is not direct cause for the low V_{OC} observed this large bandgap systems, a better control of this phenomenon is essential in order to safely and successfully implement such compositions in tandem devices.

List of Publications

1. Stolterfoht, M., Wolff, C. M., Amir, Y., Paulke, A., Perdigón-Toro, L., Caprioglio, P. & Neher, D. Approaching the fill factor Shockley–Queisser limit in stable, dopant-free triple cation perovskite solar cells. *Energy Environ. Sci.* 10, 1530–1539 (2017).
2. Caprioglio, P., Zu, F., Wolff, C. M., Prieto, J. A. M., Stolterfoht, M., Koch, N., Unold, T., Rech, B., Albrecht, S., Neher, D., Márquez Prieto, J. A., Stolterfoht, M., Becker, P., Koch, N., Unold, T., Rech, B., Albrecht, S. & Neher, D. High Open Circuit Voltages in pin-Type Perovskite Solar Cells through Strontium Addition. *Sustain. Energy Fuels* 3, 550–563 (2019).
3. Stolterfoht, M., Caprioglio, P., Wolff, C. M., Márquez, J. A., Nordmann, J., Zhang, S., Rothhart, D., Hörmann, U., Redinger, A., Kegelmann, L., Albrecht, S., Kirchartz, T., Saliba, M., Unold, T., Neher, D., Márquez, J. A., Nordmann, J., Zhang, S., Rothhardt, D., Hö, U., Amir, Y., Redinger, A., Kegelmann, L., Zu, F., Albrecht, S., Koch, N., Kirchartz, T., Saliba, M., Unold, T. & Neher, D. The impact of energy alignment and interfacial recombination on the open-circuit voltage of perovskite solar cells. *Energy Environ. Sci.* 10, 6, 1530-1539 (2019).
4. Caprioglio, P., Stolterfoht, M., Wolff, C. M., Unold, T., Rech, B., Albrecht, S. & Neher, D. On the Relation between the Open-Circuit Voltage and Quasi-Fermi Level Splitting in Efficient Perovskite Solar Cells. *Adv. Energy Mater.* 9, 1901631 (2019).
5. Würfel, U., Perdigón-Toro, L., Kurpiers, J., Wolff, C. M., Caprioglio, P., Rech, J. J., Zhu, J., Zhan, X., You, W., Shoaee, S., Neher, D. & Stolterfoht, M. Recombination between Photogenerated and Electrode-Induced Charges Dominates the Fill Factor Losses in Optimized Organic Solar Cells. *J. Phys. Chem. Lett.* 10, 3473–3480 (2019).
6. Zhang, S., Hosseini, S. M., Gunder, R., Petsiuk, A., Caprioglio, P., Wolff, C. M., Shoaee, S., Meredith, P., Schorr, S., Unold, T., Burn, P. L., Neher, D. & Stolterfoht, M. The Role of Bulk and Interface Recombination in High-Efficiency Low-Dimensional Perovskite Solar Cells. *Adv. Mater.* 31, 30, 1901090 (2019).
7. Trimby, P., Bewick, A., Abou-Ras, D., Caprioglio, P., Neher, D. & Otter, L. The Analysis of Sensitive Materials Using EBSD: The Importance of Beam Conditions and Detector Sensitivity. *Microsc. Microanal.* 25, 2394–2395 (2019).
8. Wolff, C. M., Caprioglio, P., Stolterfoht, M. & Neher, D. Nonradiative Recombination in Perovskite Solar Cells: The Role of Interfaces. *Adv. Mater.* 31, 1902762 (2019).
9. Stolterfoht, M., Le Corre, V. M., Feuerstein, M., Caprioglio, P., Koster, L. J. A. & Neher, D. Voltage-Dependent Photoluminescence and How It Correlates with the Fill Factor and Open-Circuit Voltage in Perovskite Solar Cells. *ACS Energy Lett.* 4, 2887–2892 (2019).
10. Pisoni, S., Stolterfoht, M., Löckinger, J., Moser, T., Jiang, Y., Caprioglio, P., Neher, D., Buecheler, S. & Tiwari, A. N. On the origin of open-circuit voltage losses in flexible n-i-p perovskite solar cells On the origin of open-circuit voltage losses in flexible n-i-p perovskite solar cells. *Sci. Technol. Adv. Mater.* 20, 1, 786–795 (2019).

11. Wolff, C. M., Canil, L., Rehermann, C., Ngoc Linh, N., Zu, F., Ralairisoa, M., Caprioglio, P., Fiedler, L., Stolterfoht, M., Kogikoski, S., Bald, I., Koch, N., Unger, E. L., Dittrich, T., Abate, A. & Neher, D. Perfluorinated Self-Assembled Monolayers Enhance the Stability and Efficiency of Inverted Perovskite Solar Cells. *ACS Nano ACS Nano* 14, 2, 1445-1456 (2020).
12. García-Benito, I., Quarti, C., Quelo, V. I. E., Hofstetter, Y. J., Becker-Koch, D., Caprioglio, P., Neher, D., Orlandi, S., Cavazzini, M., Pozzi, G., Even, J., Nazeeruddin, M. K., Vaynzof, Y. & Grancini, G. Fluorination of Organic Spacer Impacts on the Structural and Optical Response of 2D Perovskites. *Front. Chem.* 7, 946 (2020).
13. Stolterfoht, M., Grischek, M., Caprioglio, P., Wolff, C. M., Gutierrez-Partida, E., Peña-Camargo, F., Rothhardt, D., Zhang, S., Raoufi, M., Wolansky, J., Abdi-Jalebi, M., Stranks, S. D., Albrecht, S., Kirchartz, T. & Neher, D. How To Quantify the Efficiency Potential of Neat Perovskite Films: Perovskite Semiconductors with an Implied Efficiency Exceeding 28%. *Adv. Mater.* 32, 17, 2000080 (2020).
14. Caprioglio, P., Wolff, C. M., Sandberg, O. J., Armin, A., Rech, B., Albrecht, S., Neher, D., Stolterfoht, M. On the Origin of the Ideality Factor in Perovskite Solar Cells. Accepted in *Adv. Energy Mater.* (2020)
15. Schulze P. S. C., Bett A.J., Bivour M., Caprioglio P., Gerspacher F.M., Kabaklı Ö. Ş., Richter A., Stolterfoht M., Zhang Q., Neher D., Hermle M., Hillebrecht H., Glunz S.W, Goldschmidt J.C., 25.1% high-efficient monolithic perovskite silicon tandem solar cell with a high band gap perovskite absorber. Accepted in *Solar RRL* (2020)

Under revision:

16. Caprioglio P., Saul-Cruz D., Caicedo-Dávila S., Zu F., Sutanto A.A., Kegelmann L., Wolff C.M., Perdigón-Toro L., Koch N., Rech B., Grancini G., Abou-Ras D., Nazeeruddin M.K., Stolterfoht M., Albrecht S., Antonietti M., Neher D., *Bi-functional Interfaces by Poly-Ionic Liquid Treatment in Efficient pin and nip Perovskite Solar Cells* (under revision)
17. Caprioglio P., Caicedo-Dávila S., Yang C.J., Rech B., Ballif C., Abou-Ras D., Stolterfoht M., Albrecht S., Jeangros Q., Neher D., *Microscopic emission properties and optical reciprocity failure in MA-free large bandgap halide-segregated perovskites* (submitted)
18. Diekmann, J., Caprioglio, P., Rothhardt, D., Arvind, M., Unold, T., Kirchartz, T., Neher, D. & Stolterfoht, M. *Pathways towards 30% efficient perovskite solar cells.* (2019). <http://arxiv.org/abs/1910.07422> (under revision)

19. Wang Q., Smith J.A., Skroblin D., Steele J.A., Wolff C.M., Caprioglio P., Stolterfoht M., Köbler H., Li M., Turren-Cruz S.H., Gollwitzer C., Neher D., Abate A., *Managing Phase Purities and Crystal Orientation for High Performance and Photo-Stable Caesium Lead Halide Perovskite Solar Cells* (under revision)

20. Wang Q., Zu F., Caprioglio P., Wolff M.W., Stolterfoht M., Li M., Turren-Cruz S.H., Koch N., Neher D., Abate A. *Large Conduction Band Energy Offset is Critical for Extracting Electron from Inorganic Perovskite in Efficient Solar Cells* (under revision)

11.

11. Supporting Material

11.1 Appendix 1

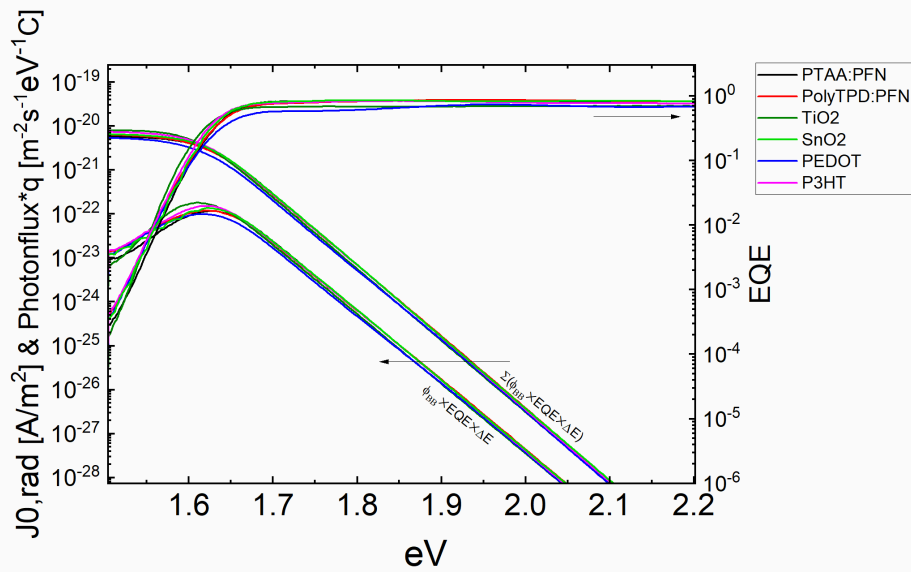


Figure 11.1.1: External Quantum Efficiency (EQE) spectra, the product of the black body (ϕ_{BB}) spectrum and the EQE, and the integral of $\phi_{BB} * EQE$. The graphs shows that $J_{0,rad}$ is very similar for all system ($6.5 \pm 1 \times 10^{-21} \text{A/m}^2$) independent of the bottom charge transport layer. This also suggests that the optoelectronic quality of the perovskite layer is not significantly altered due to the different HTL underneath.

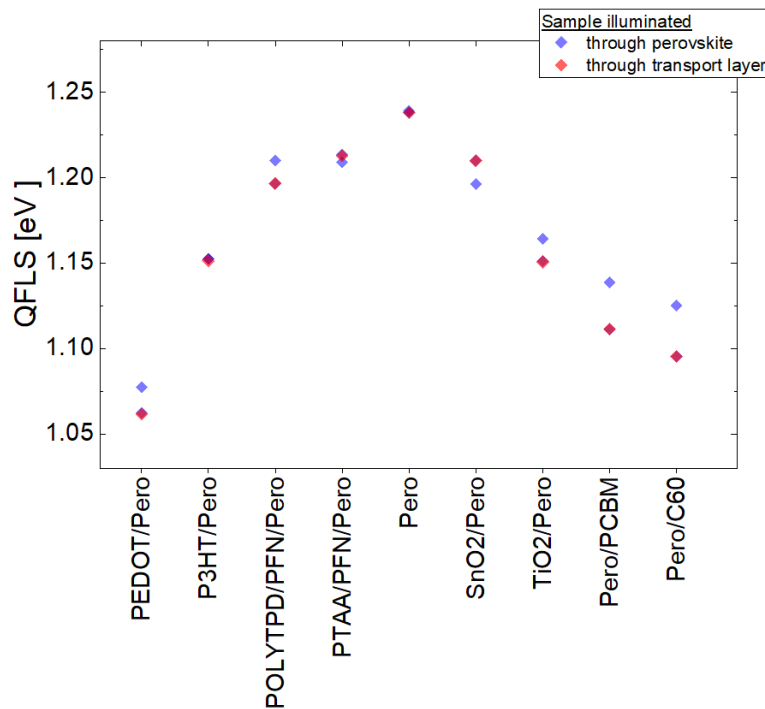


Figure 11.1.2: Quasi-Fermi level splitting of various perovskite films illuminated through the perovskite (blue circles) or the charge transport layer (red symbols) using a 445 nm CW laser. In case of the neat perovskite film, the red symbol corresponds to a measurement through the

bottom glass substrate. We note that the 445 nm laser is absorbed within a narrow window in the perovskite layer (<150 nm penetration depth) according to optical transfer matrix simulations which are also shown in **Fig. 11.1.12**. The graph shows that illuminating through the electron transport layers (ETLs) C₆₀, PCBM causes a significantly lower QFLS (up to 30 meV) compared to illumination through the perovskite, which is attributed to substantial parasitic absorption in the ETL at this wavelength. A smaller difference in the QFLS depending on the illumination side was observed for the other transport layers.

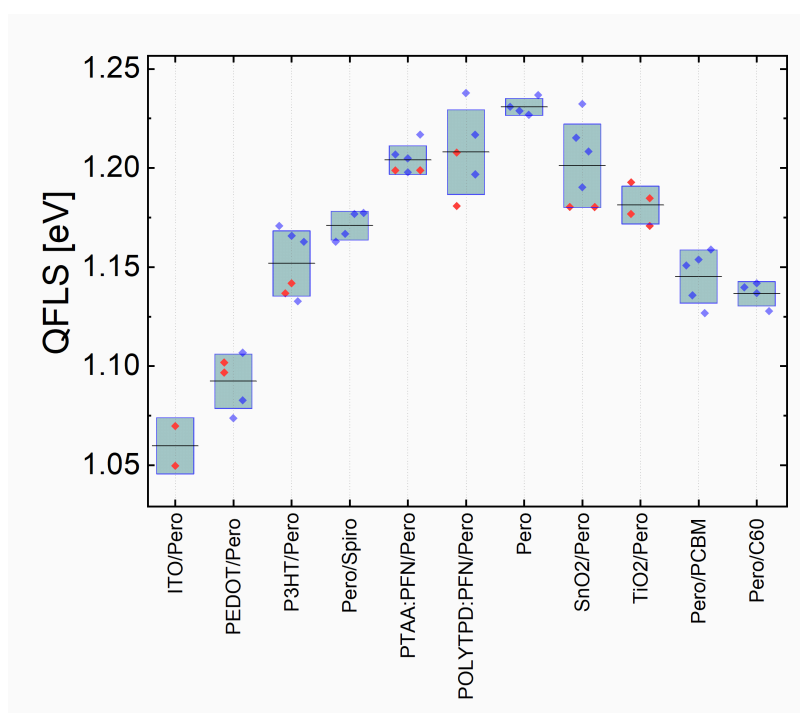


Figure 11.1.3: The obtained quasi-Fermi level splitting of perovskite films including the studied hole and electron transporting materials and the neat absorber layer. Each data point corresponds to a different sample film. For each film an area of 1 cm² was illuminated and the average QFLS plotted. We also studied films on glass and glass/ITO substrates (glass/FTO in case of TiO₂) which are more relevant for actual devices. The values obtained on glass/ITO (glass/FTO) are plotted in red (films on glass in blue). We note small differences between these two substrates indicating small losses between the HTL and the metal electrode in some cases. The lines show the mean values and the boxes the standard deviations.

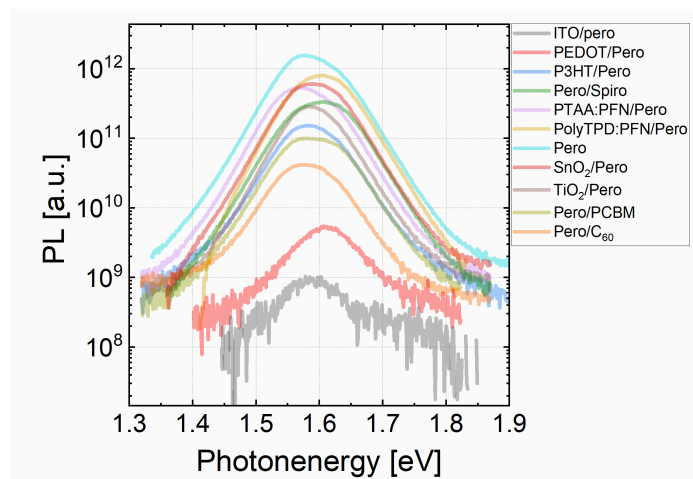


Figure 11.1.4: Representative PL spectra of the bare perovskite film and perovskite films with different electron and hole transport layers.

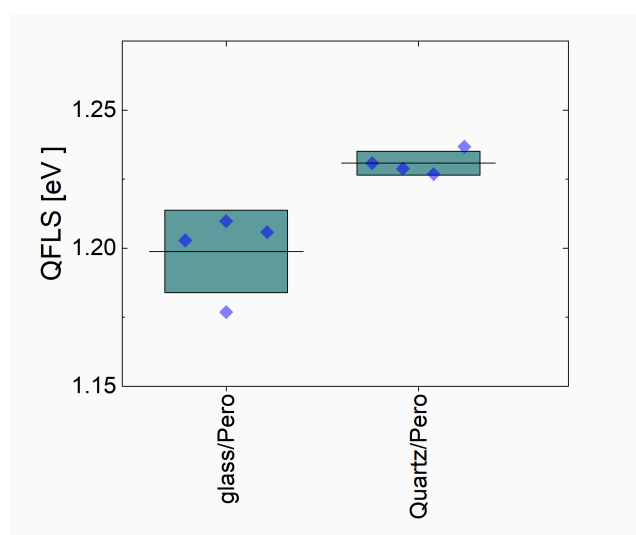


Figure 11.1.5: The QFLS of triple cation perovskite films on glass and fused silica shows that the latter substrate causes less non-radiative recombination losses, which indicates some recombination is occurring at the glass/perovskite interface. The lines show the mean values and the boxes the standard deviations.

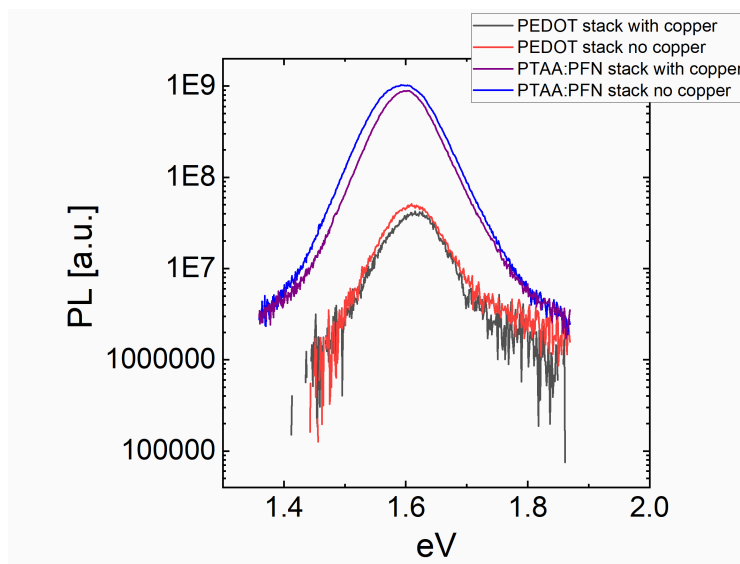


Figure 11.1.6: The PL emitted from glass/ITO/PEDOT/pero/ C_{60} and glass/ITO/PTAA/PFN/pero/ C_{60} stacks with and without the copper electrode. No significant difference in the emission is observed in the presence of copper which is attributed to the fact that all samples are placed on a reflective sample holder in the Ulbricht sphere where the PL experiment was performed. Thus, emission that is emitted to the bottom sample holder is likely reflected back, similar to light that is emitted to the copper electrode which might explain the small impact of the copper electrode.

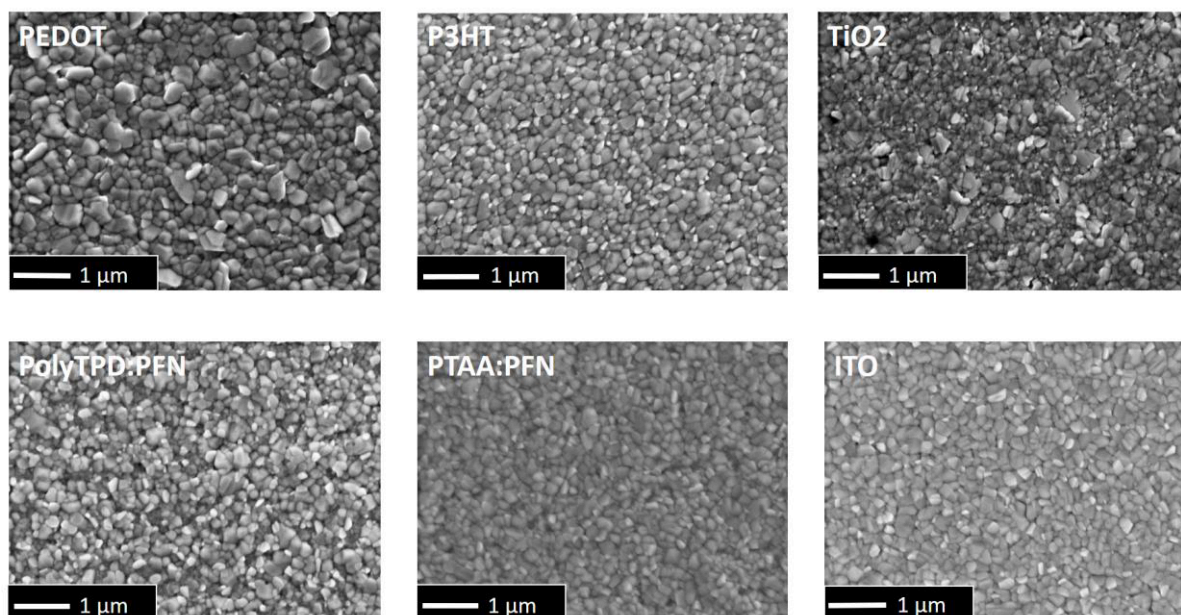


Figure 11.1.7: Scanning electron microscopy (SEM) top sectional images of perovskite films fabricated on different underlying charge transport layers reveal differences in the perovskite morphology. Remarkably, are the substantially larger grains on PEDOT hole transport layers (despite their low radiative efficiency) and the broad distribution of different grain sizes on TiO_2 films. Relatively small grains are observed on PolyTPD:PFN, ITO, P3HT and PTAA:PFN bottoms layers. Overall, no clear correlation between the perovskite morphology and the photovoltaic performance can be deduced from these SEM results.

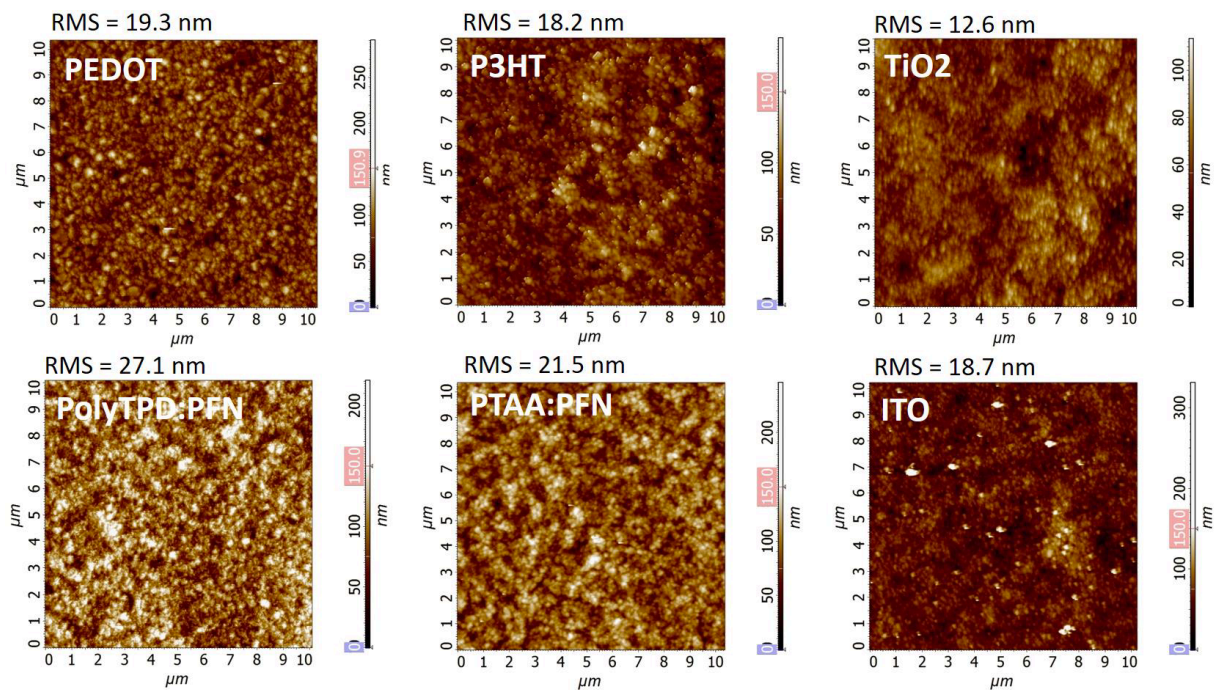


Figure 11.1.8: Atomic Force Microscopy (AFM) top sectional measurements on perovskite films fabricated on different underlying charge transport layers reveal differences in the root mean square roughness (RMS) for each layer. Interestingly, the most efficient films in terms of photoluminescence exhibit a slightly rougher surface compared to the others, while films on TiO₂ were the smoothest.

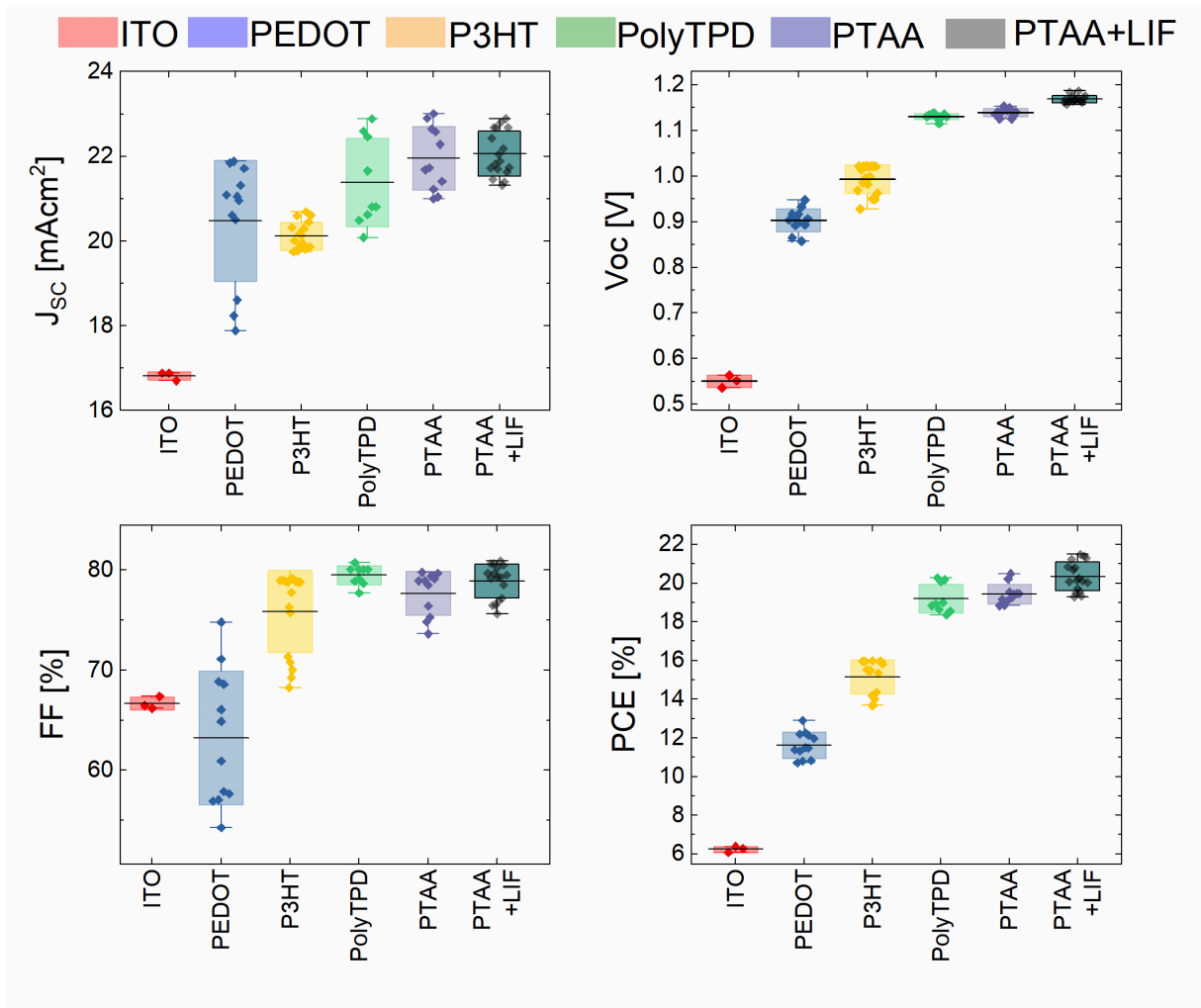


Figure 11.1.9: Device statistics of 6 mm²-size perovskite solar cells (with standard configuration ITO/HTL/perovskite/C₆₀/BCP/Cu) showing the impact of the hole transport layer on the solar cell parameters. The average V_{oc} values are plotted in Fig. 4.2. The cells plotted on the right in each panel were fabricated using an additional LiF layer (~1 nm) between the perovskite and C₆₀ which allowed efficiencies above 20%. The lines show the mean values and the boxes the standard deviations.

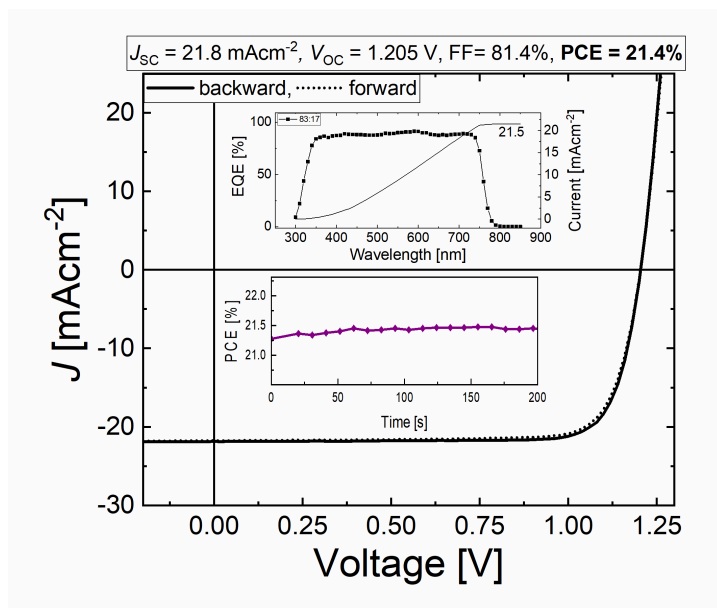


Figure 11.1.10: JV-characteristics of one of our most efficient cells fabricated at low temperatures (100 °C) using the standard $\text{Cs}_{0.05}(\text{FA}_{0.83}\text{MA}_{0.17})_{0.95}\text{PbI}_{0.83}\text{Br}_{0.17}$ triple cation perovskite absorber with a bandgap of approximately 1.6 eV, with PTAA/PFN and LiF/C₆₀ as hole- and electron selective CTLs. The inset shows the stabilized efficiency evolution of the cell and the external quantum efficiency spectrum. The integrated product of the EQE and the solar spectrum (21.5 mAcm⁻²) closely matches the measured short-circuit current density under the solar simulator (21.8 mAcm⁻²).

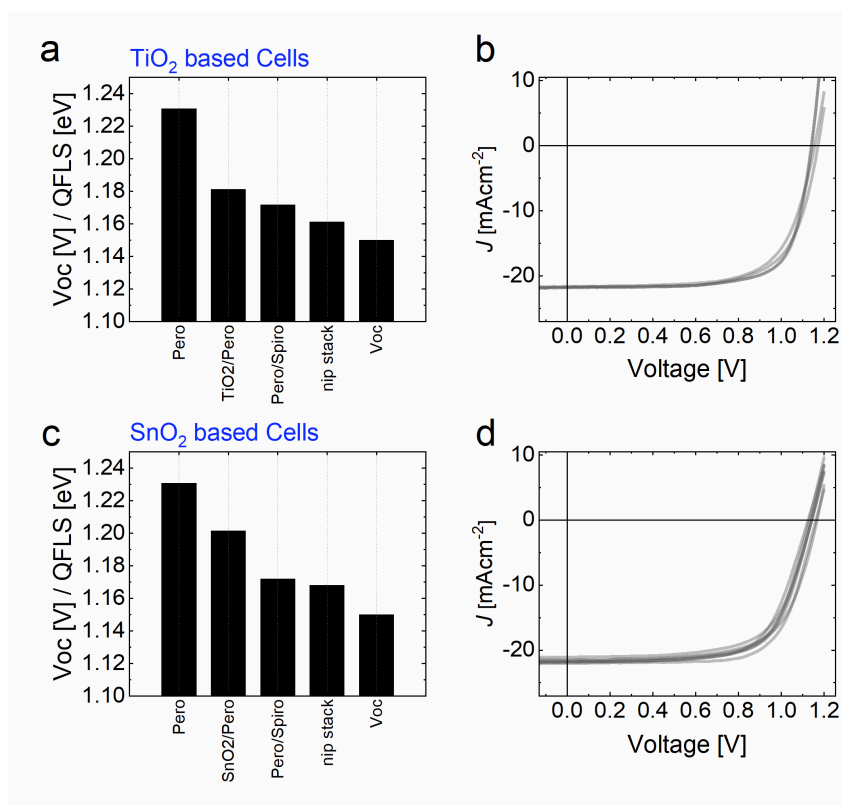


Figure 11.1.11: Quasi-Fermi level splitting of the individual perovskite/transport layer films as well as the average device V_{oc} of nip cells based on (a, b) TiO_2 and (c, d) SnO_2 confirming that

substantial interfacial non radiative recombination losses lower the QFLS of the perovskite (1.23 eV) to 1.16-1.17 eV in the stack. For both cell types, the non-radiative recombination losses at the perovskite/spiroOMeTAD junction appear to limit the QFLS of the complete stack. For TiO₂ cells, 2 substrates with 4 pixels (30 mm²) in total were fabricated of which the JV-curves are shown in panel (b) with efficiencies of around 19%. For SnO₂ cells, 2 substrates with 12 pixels in total (16 mm²) were fabricated of which the JV-curves are shown in panel (d) with efficiencies up to 18% (max).

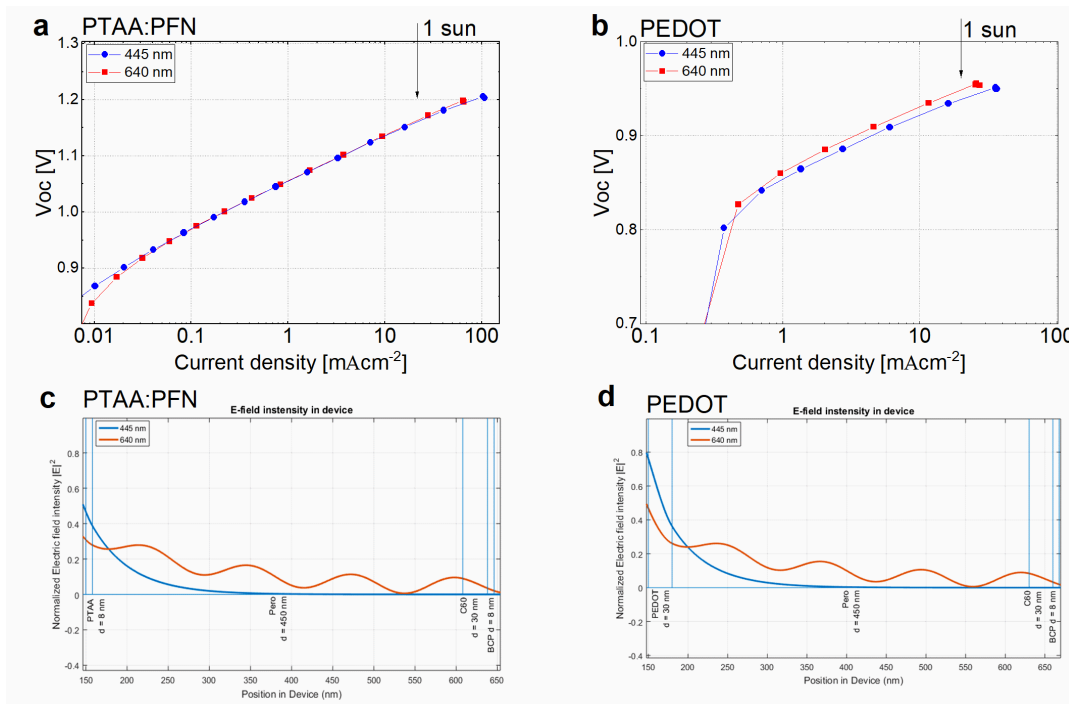


Figure 11.1.12: V_{oc} vs. short-circuit current for two different laser wavelengths (445 nm and 638 nm) on pin type devices with (a) PTAA:PFN and (b) PEDOT as hole transport layer, while C60 was used as electron transport layer in both cases. The graph demonstrates that the V_{oc} is essentially independent on the initial carrier generation profile over several orders of magnitude in laser intensity (or short-circuit current). (c) and (d) show the corresponding E-field intensity in the two devices which was simulated based on optical transfer matrix simulations using an open source code developed by McGehee et al. which was adapted from ref.2,3

Parameter	Symbol	Value	Unit
Majority carrier band offset between perovskite and C ₆₀ *	$\Delta E_{\text{maj,c}}$	0	eV
Majority carrier band offset between perovskite and PTAA*	$\Delta E_{\text{maj,v}}$	0	eV
Majority carrier band offset between perovskite and PEDOT*	$\Delta E_{\text{maj,v}}$	0.5	eV
lifetime in perovskite*	τ_{pero}	1000	ns
lifetime in PTAA	τ_p	1	ns
lifetime in C ₆₀	τ_n	1	ns
Ionized acceptors in PTAA*	$N_{\text{A,p}}^-$	1x10 ⁵	cm ⁻³
Ionized donors in C ₆₀ *	$N_{\text{D,n}}^+$	1x10 ⁵	cm ⁻³
Intrinsic carrier density in perovskite	N_i	1x10 ¹⁰	cm ⁻³
Minority carrier recombination velocity from perovskite to PTAA*	S_n	200	cm/s
Minority carrier recombination velocity from perovskite to PEDOT*	S_n	200	cm/s
Majority carrier recombination velocity from perovskite to PEDOT*	\bar{S}_p	1x10 ⁷	cm/s
Minority carrier recombination velocity from perovskite to C ₆₀ *	S_p	1000	cm/s
Thickness of PTAA*	d_{PTAA}	10	nm
Thickness of perovskite*	d_{pero}	400	nm
Thickness of C ₆₀ *	d_{C60}	30	nm
Offset between metal and PTAA*	$\Delta E_{\text{F,metal-p}}$	0.2	eV
Offset between metal and C ₆₀ *	$\Delta E_{\text{F,metal-n}}$	0.2	eV
Device built-in voltage*	V_{BI}	1.2	V
Electron affinity PTAA*	$E_{\text{A,PTAA}}$	2.7	eV
Bandgap PTAA*	$E_{\text{G,PTAA}}$	2.8	eV
Workfunction PEDOT*	E_{PEDOT}	5.0	eV
Bandgap perovskite	$E_{\text{G,pero}}$	1.6	eV
Electron affinity perovskite*	$E_{\text{A,pero}}$	3.9	eV
Bandgap perovskite	$E_{\text{G,pero}}$	1.6	eV
Electron affinity C ₆₀ *	$E_{\text{A,C60}}$	4.2	eV
Bandgap C ₆₀ *	$E_{\text{G,C60}}$	1.8	eV
Electron mobility in C ₆₀ *	$\mu_{\text{n,PTAA}}$	1x10 ⁻²	cm ² /V s
Hole mobility in PTAA*	$\mu_{\text{p,PTAA}}$	1x10 ⁻⁴	cm ² /V s
Electron mobility in perovskite*	$\mu_{\text{n,pero}}$	10	cm ² /V s
Hole mobility in perovskite*	$\mu_{\text{p,pero}}$	10	cm ² /V s
relative dielectric constant PTAA	ϵ_{PTAA}	3.5	
relative dielectric constant perovskite*	ϵ_{pero}	22	

relative dielectric constant ϵ_{C60}	ϵ_{C60}	4.2	
Effective electron density of states in HTL	$N_{C/V,PTAA}$	1×10^{20}	cm^{-3}
Effective electron density of states in C_{60}	$N_{C/V,C60}$	1×10^{20}	cm^{-3}
Effective electron density of states in perovskite	$N_{C/V,pero}$	3.1×10^{18}	cm^{-3}

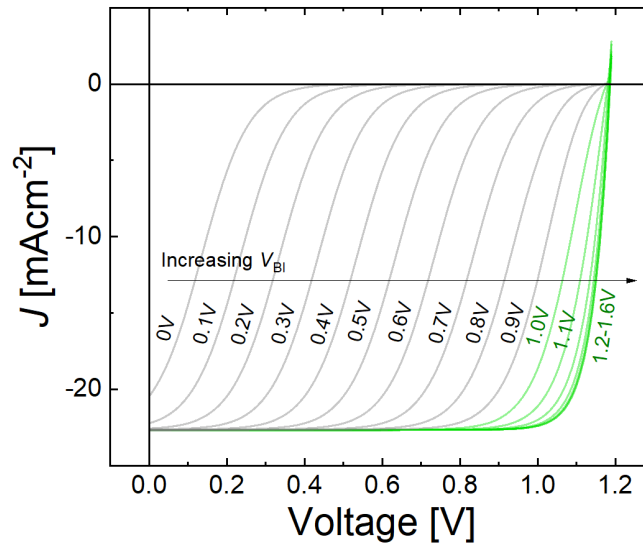


Figure 11.1.13: Simulated J/V -curves for different built-in voltages (V_{Bi}) across the device. The V_{Bi} is given by the workfunction difference of the electrodes and is limited by the perovskite bandgap of 1.6 eV. The V_{Bi} was varied by equally reducing the energetic offsets between and the perovskite valence/conduction bands and the workfunctions of the metals at the bottom and top contact, respectively. The results suggest that a considerable V_{Bi} of $\sim 1V$ is required in order to efficiently extract the charges and reproduce experimental JV curves.

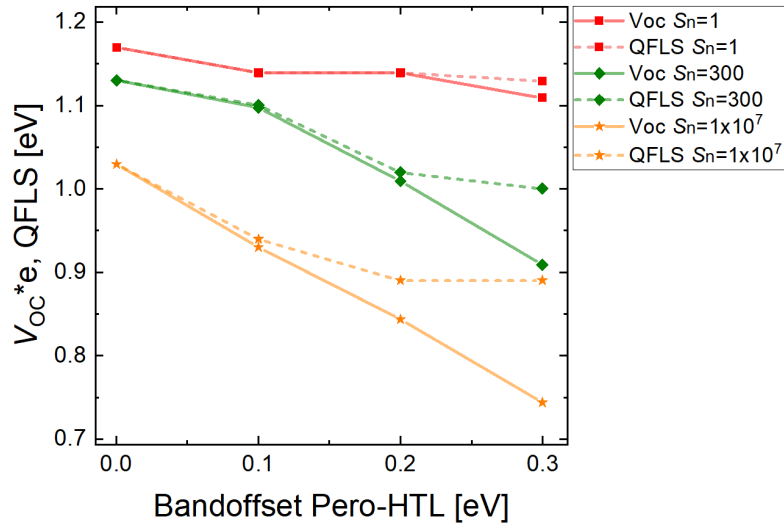


Figure 11.1.14: Device simulations of V_{oc} and average quasi-Fermi level splitting (QFLS) on PTAA/perovskite/C60 stacks for different interface recombination velocities of electrons at the HTL/perovskite interface (S_n) to reveal the origin of a mismatched QFLS and device V_{oc} . The simulations predict such a mismatch in case of a majority carrier band offset (E_{maj}) between the perovskite valence band and the highest occupied molecular orbital of PTAA if the interface recombination velocities are above 1 cm/s. Notably, based on these simulations we expect no QFLS-mismatch in absence of a band offset regardless of the interface recombination velocity. The simulated V_{oc} for the most realistic scenario with $S_n = 300$ cm/s (green curve) at the HTL/perovskite interface shows that that even small majority carrier band offsets larger than >0.1 eV are already inconsistent with the experimentally measured V_{oc} 's of ~ 1.14 V in the PTAA/PFN/perovskite/C60 device. We also note that for low interface recombination velocities $S_n \sim 1$ cm/s, the simulated QFLS and V_{oc} are limited by the interface recombination velocity S_p at the perovskite/ETL interface which was set to 1000 cm/s for these simulations. Voltages above 1.26 V can be achieved in the limit of negligible recombination at both interfaces (< 1 cm/s).

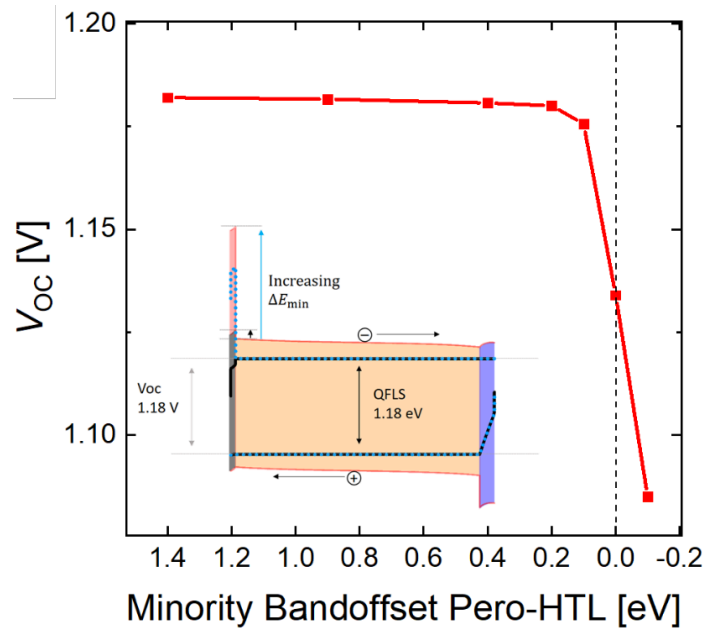


Figure 11.15: Simulated open-circuit voltage versus minority carrier band offset (E_{min}) demonstrating that even smallest ΔE_{min} values of only 0.1 eV are in principle sufficient to prevent substantial charge recombination at the wrong interfaces. The primary reason for this result is that rapid recombination at the HTL/perovskite junction (which was set here to 200 cm/s) prevents minority carriers from entering the wrong CTL. The inset illustrates the energy bands for two device simulations where ΔE_{min} was increased from -0.1 eV to 1.4 eV demonstrating the nearly identical QFLS in the bulk (QFLS and energy bands are superimposed). The simulated electron and hole quasi-Fermi levels are shown by black lines and blue dots for ΔE_{min} energy offsets of 0.1 eV and 1.4 eV, respectively. Also shown are the conduction and valence bands in red, the device V_{OC} and average quasi-Fermi level splitting (QFLS). We acknowledge that these simulations represent an ideal scenario where we only varied the position of the LUMO level of the HTL, however in reality such small minority carrier offsets would likely influence other critical parameters such as the accessible defect density for minority carriers which could, for example, cause much higher recombination velocities (S). Thus, while we can say that even small energetic offsets are sufficient to prevent minority carriers from entering the wrong contact, we cannot exclude that in reality such small offsets would cause much larger recombination losses by affecting other important parameters.

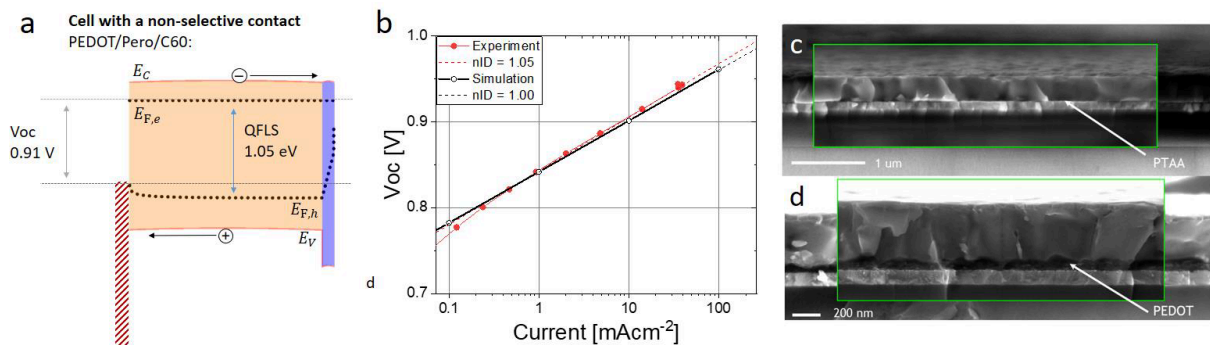


Figure 11.1.16: (a) The simulated quasi-Fermi level splitting (QFLS, black dotted lines) of a PEDOT:PSS/perovskite/C60 stack shows a bending of the hole QFL towards the p-interface. The simulations can well reproduce the experimentally observed QFLS- V_{OC} mismatch of ~ 150 meV. The perovskite absorber layer and C60 are represented by their unoccupied states in orange and blue, respectively. Occupied states are drawn for PEDOT:PSS in striped red. (b) The drift diffusion simulations can also closely predict the experimentally obtained ideality factor (n_{ID}) of the perovskite cell with PEDOT:PSS as HTL. (c) Cross sectional scanning electron microscopy (SEM) images of a PTAA:PFN/perovskite and (d) PEDOT:PSS/perovskite film reveal a quite rough PEDOT:PSS layer. Therefore, a morphological problem cannot be excluded at the p-interface in case of PEDOT:PSS despite the good match between the simulations and the experimental data (V_{OC} , QFLS and n_{ID}).

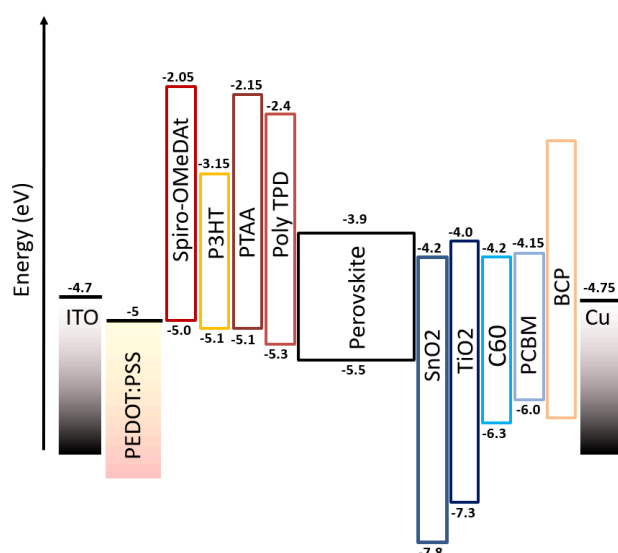


Figure 11.1.17. The ionization potentials (IPs) of the materials shown in the main text measured with photoelectron yield spectroscopy in air. The optical bandgaps were estimated from Tauc plots based on UV-Vis measurements. The IPs of C₆₀, TiO₂, and SnO₂ were outside the measurement range of the spectrometer (< -6.5 eV), therefore IPs previously determined from ultraviolet photon electron spectroscopy are plotted ref.5 It is important to note that the plotted energy levels are only relevant for each film in isolation and by no means represent the true energetics in the complete solar cell stack where junctions form and the vacuum level is not constant across all interfaces.

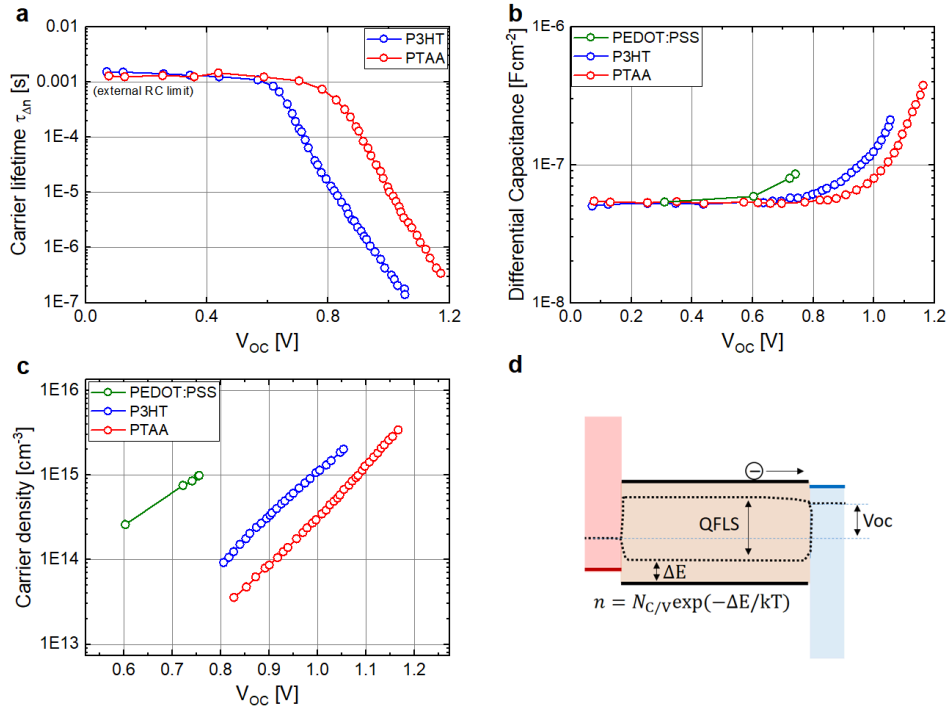


Figure 11.1.18: (a) Transient Photovoltage (TPV) experiments on pin-type triple cation perovskite solar cells based on P3HT and PTAA. Lifetimes of the excess charge carriers are plotted as a function of the steady-state V_{OC} in the devices. The shorter lifetime at a given V_{OC} is consistent with the increased interfacial recombination in the P3HT cell as compared to PTAA cell. (b) To further prove the observed mismatch between the QFLS and the V_{OC} in case of PEDOT:PSS and P3HT containing devices, we performed differential charging capacitance measurements $\text{CDC} = \Delta Q / \Delta V$, where the differential charge (ΔQ) was obtained from transient photocurrent (TPC) extraction and the differential voltage (ΔV) from TPV upon a small laser perturbation.^{6,7} The graph clearly displays two regions, where at low V_{OC} s the capacitance is given by the geometric capacitance while the sudden rise of the differential capacitance at higher V_{OC} s is caused by the accumulation of charge in the active layer (chemical capacitance). (c) The carrier density as obtained from the integration of the voltage dependent chemical capacitance in (b) shows that, for a given V_{OC} , the charge density in the device is substantially larger for the PEDOT:PSS cell than for the P3HT cell and the PTAA cell. This suggests that there is a substantial mismatch between the internal QFLS and the external V_{OC} . (d) A schematic illustration showing why a mismatch between the QFLS and the V_{OC} leads to more charge in the device than expected from the device V_{OC} .

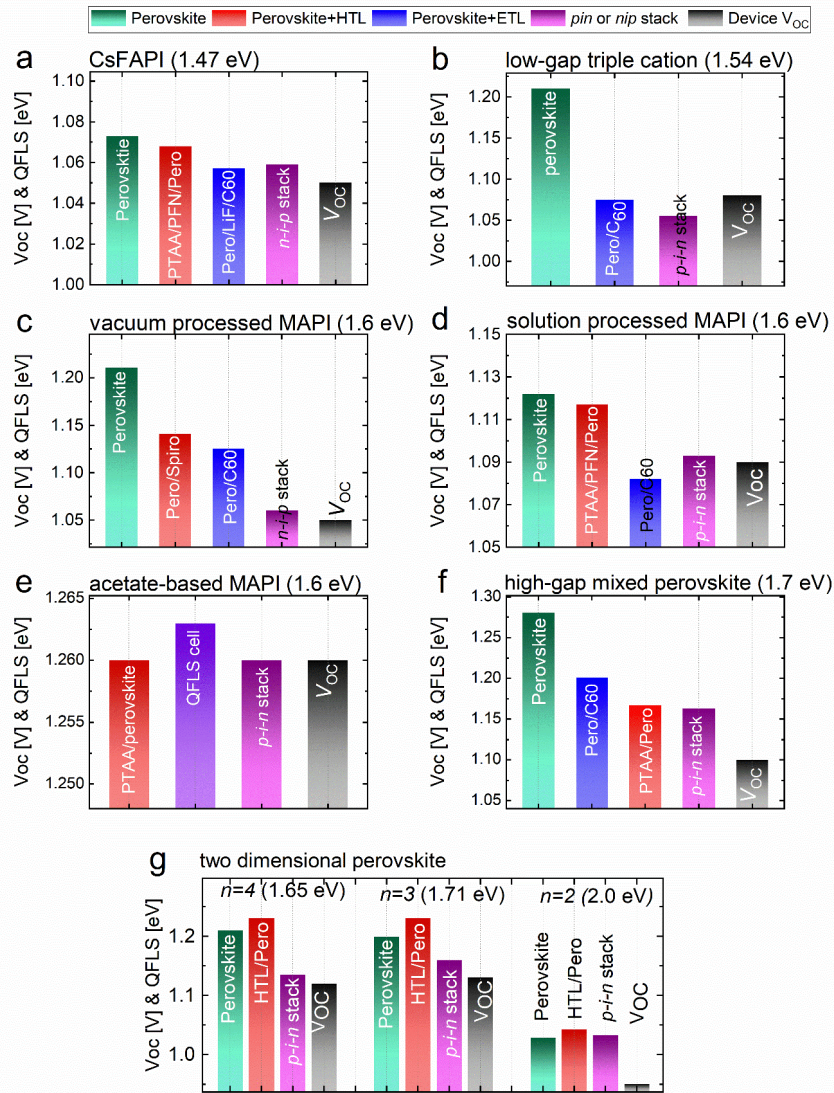


Figure 11.1.19: Quasi-Fermi level splitting (QFLS) of different perovskite systems with and without attached transport layers, *n-i-p* and *p-i-n* stacks and corresponding device V_{oc} . The different perovskite systems include (a) methyl ammonium and bromide-free Cs_{0.05}FA_{0.95}PbI₃ with power conversion efficiencies of up to 20%, (b) low-gap triple cation perovskite Cs_{0.05}(FA_{0.95}MA_{0.05})_{0.95}Pb(I_{0.95}Br_{0.05})₃ as used in today's record *n-i-p* cells,⁸ (c) hybrid vacuum/solution processed MAPI⁹ which is relevant for application on textured substrates for Si/perovskite tandem applications,¹⁰ (d) a simple one-step solution processed MAPI, (e) Pb-acetate based MAPI with exceptional V_{oc} s of 1.26 V (published in ref.11), (f) high-gap mixed perovskite Cs_{0.15}FA_{0.85}Pb(I_{0.75}Br_{0.25})₃ with optimal bandgap for monolithic Si/perovskite tandem cells,¹² (g) and two-dimensional perovskite solar cells²³ based on BA₂MA_n-1PbI_{3n+1} ($n=2-4$) (published in ref.13). In most systems the absorber layer allows to reach substantially higher open-circuit voltages than achieved in the cells, but not in all systems. For example, in lowgap CsFAPI and our solution processed MAPI, the V_{oc} of the cell is close (20 – 30 meV) to the QFLS of the perovskite. Substantial V_{oc} improvements through interfacial optimizations seem however feasible for low-gap triple cation perovskite (b), hybrid vacuum processed perovskite (c), high-gap mixed perovskite (f) and 2D perovskite (g). In the high-bandgap perovskite system (f), we observe again a considerable mismatch

between the QFLS of the pin-stack and the V_{OC} (~120 mV). As discussed in this paper, such a mismatch can be explained by an energetic misalignment between the perovskite and the transport layers. This highlights the difficulties in increasing the perovskite bandgap while maintaining the energy level alignment and demonstrates the relevance of the findings for other perovskite systems. In the 2D systems, the application of the HTL was found to passivate the bottom surface while the perovskite/C60 is limiting also here the V_{OC} of the final cells.

11.2 Appendix 2

Radiative losses

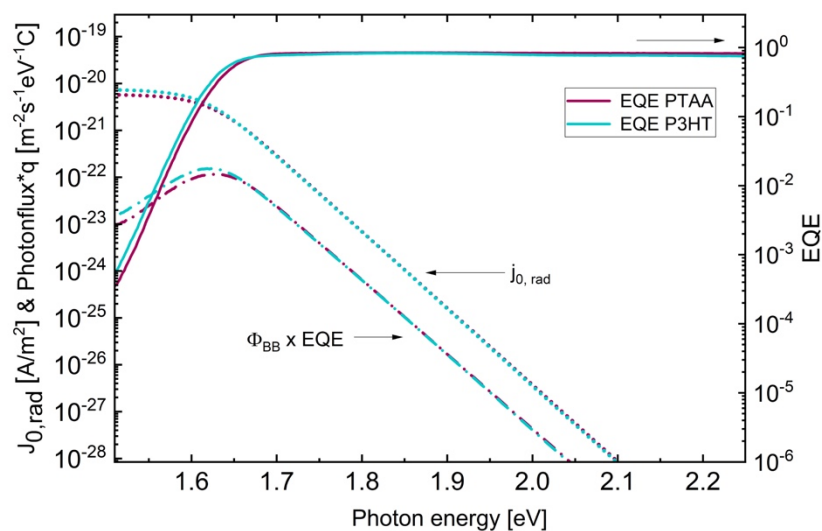


Figure 11.2.1: EQE_{PV} onset of two perovskite solar using PTAA and P3HT as HTL and their emitted spectral photon flux calculated when the device is in equilibrium with the black-body (BB) radiation of the surroundings at 300K according to equation S1.

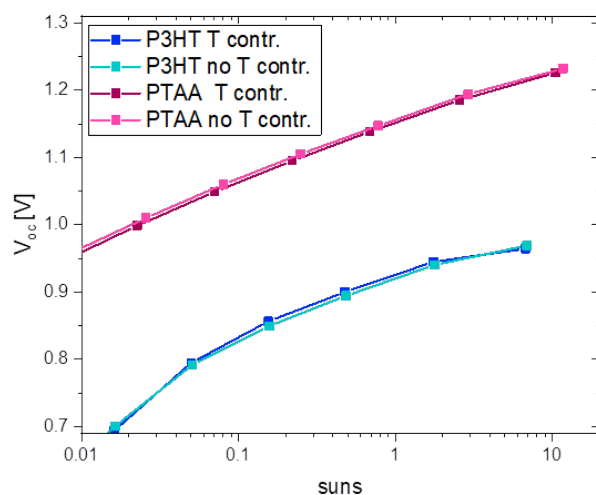


Figure 11.2.2A: Effects of the temperature controller on the V_{OC} (I) measurement for two perovskite solar cells using PTAA and P3HT as HTL. The curves show no detectable effects whether a temperature controller is used to keep the cell at a constant temperature of 300K.

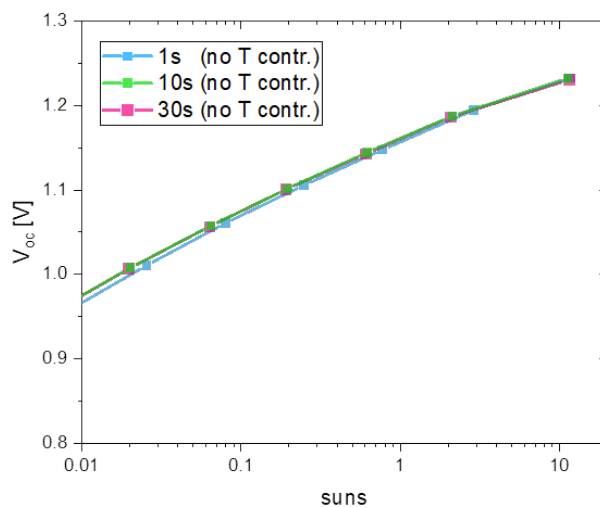


Figure 11.2.2B: Effects of the illumination time on the V_{OC} (I) measurement for a typical perovskite solar cell in the absence of a temperature controller. The curves show no detectable differences depending on the illumination time before the V_{OC} is recorded.

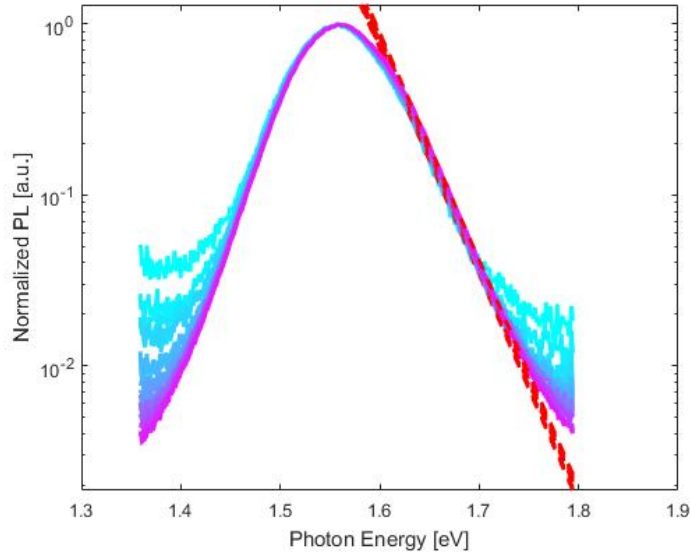


Figure 11.2.2C: Normalized PL spectra of 23 spectra with different illumination intensities varying from 0.1 suns (light blue) to roughly 10 suns (purple).

All spectra are fitted at the high energy shoulder (red dashed lines) in order to extract the local temperature during the emission of the photoluminescence radiation^[133] following the approach presented in ^[132,137]

$$\ln \left[\frac{I_{\text{PL}}(E)h^3c^2}{2\pi E^2} \right] = -\frac{1}{kT}E + \frac{\mu}{kT} \quad (\text{Eq.11.2.4}).$$

Being aware of the possible mismatch in the absolute values of T obtained from this method ^[73], we limit our discussion merely to the ΔT , which is of our main interest. Notably, for the 23 spectra fitted we obtain a non-progressive $\Delta T = 2$ K, which indicates that the temperature does not increase locally within the intensity regime experimentally investigated. This highlights the negligible effects of the temperature on the QFLS and the V_{OC} until 10 suns.

Drift-diffusions simulations

Table 11.2.1: SCAPS Simulation parameters used for simulating both the simulations models.

Parameter	Symbol	Value	Unit
Majority carrier band offset between perovskite and C ₆₀	$\Delta E_{\text{maj,c}}$	0	eV
Majority carrier band offset between perovskite and PTAA	$\Delta E_{\text{maj,v}}$	0	eV
Majority carrier band offset between perovskite and P3HT	$\Delta E_{\text{maj,v}}$	0.2	eV
Lifetime in perovskite	τ_{pero}	1000	ns
Lifetime in PTAA	τ_p	1	ns
Lifetime in P3HT	τ_p	1	ns

Ionized acceptors in PTAA	$N_{A,p}^-$	1×10^5	cm^{-3}
Ionized acceptors in P3HT	$N_{A,p}^-$	1×10^5	cm^{-3}
Ionized donors in C ₆₀	$N_{D,n}^+$	1×10^5	cm^{-3}
Intrinsic carrier density in perovskite	N_i	1×10^{10}	cm^{-3}
Minority carrier recombination velocity from perovskite to PTAA	S_1	100	cm/s
Minority carrier recombination velocity from perovskite to P3HT	S_2	1000	cm/s
Additional minority carrier recombination velocity from perovskite to HTL	S_3	3×10^5	cm/s
Offset between S ₁ and perovskite CB	$\Delta E_{\text{min},S}$	0.1	eV
Offset between S ₂ and perovskite CB	$\Delta E_{\text{min},S}$	0.03	eV
Minority carrier recombination velocity from perovskite to C ₆₀	S_4	1000	cm/s
Thickness of HTL	d_{PTAA}	10	nm
Thickness of perovskite	d_{pero}	400	nm
Thickness of C ₆₀	d_{C60}	30	nm
Offset between metal and PTAA	$\Delta E_{\text{F,metal-p}}$	0.25	eV
Offset between metal and P3HT	$\Delta E_{\text{F,metal-p}}$	0.1	eV
Offset between metal and C ₆₀	$\Delta E_{\text{F,metal-n}}$	0.1	eV
Device built-in voltage	V_{BI}	1.25	V
Electron affinity PTAA	$E_{A,\text{PTAA}}$	2.5	eV
Bandgap PTAA	$E_{G,\text{PTAA}}$	3	eV
Electron affinity P3HT	$E_{A,\text{PTAA}}$	3.3	eV
Bandgap P3HT	$E_{G,\text{PTAA}}$	2	eV
Electron affinity perovskite	$E_{A,\text{pero}}$	3.9	eV
Bandgap perovskite	$E_{G,\text{pero}}$	1.6	eV
Electron affinity C ₆₀	$E_{A,\text{C60}}$	3.9	eV
Bandgap C ₆₀	$E_{G,\text{C60}}$	2	eV
Electron mobility in C ₆₀	$\mu_{n,\text{PTAA}}$	1×10^{-2}	cm^2/Vs
Hole mobility in PTAA	$\mu_{p,\text{PTAA}}$	1×10^{-5}	cm^2/Vs
Hole mobility in P3HT	$\mu_{p,\text{PTAA}}$	1×10^{-4}	cm^2/Vs
Electron mobility in perovskite	$\mu_{n,\text{pero}}$	10	cm^2/Vs
Hole mobility in perovskite	$\mu_{p,\text{pero}}$	10	cm^2/Vs
relative dielectric constant HTL	ϵ_{PTAA}	3.5	
relative dielectric constant perovskite	ϵ_{pero}	22	
relative dielectric constant C ₆₀	ϵ_{C60}	4.2	
Effective electron density of states in HTL	$N_{\text{C/V,PTAA}}$	1×10^{20}	cm^{-3}
Effective electron density of states in C ₆₀	$N_{\text{C/V,C60}}$	1×10^{20}	cm^{-3}
Effective electron density of states in perovskite	$N_{\text{C/V,pero}}$	3.1×10^{18}	cm^{-3}

Additional traps states

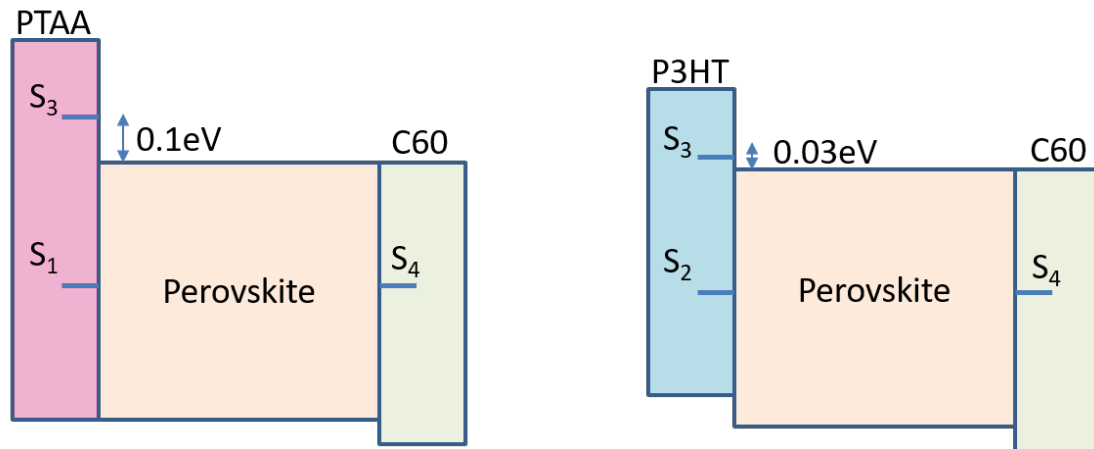


Figure 11.2.3A: Schematic representation of the simulation model for two different perovskite solar cells using PTAA and P3HT as HTL. The surface recombination velocities has been set to be as realistic as possible to experimental values obtained in our previous work.^[127] Namely, $S_1=100$ cm/s, $S_3=1000$ cm/s and $S_4=1000$ cm/s. For the P3HT case an energetic offset of 0.2eV between the HOMO of P3HT and the VBM of the perovskite has been introduced. In this simulation model an additional interfacial trap has been added between the perovskite and the HTL ($S_3=3 \times 10^5$ cm/s). The position of this trap has been varied from PTAA to P3HT in order to obtain a realistic match between the simulation results and the experiments. As this trap is above the CB of the perovskite, it starts to be accessible only at high carrier concentrations, thus leading to an intensity dependent recombination. The closer this trap is to the CB the sooner its effects on the V_{OC} bending start to manifests.

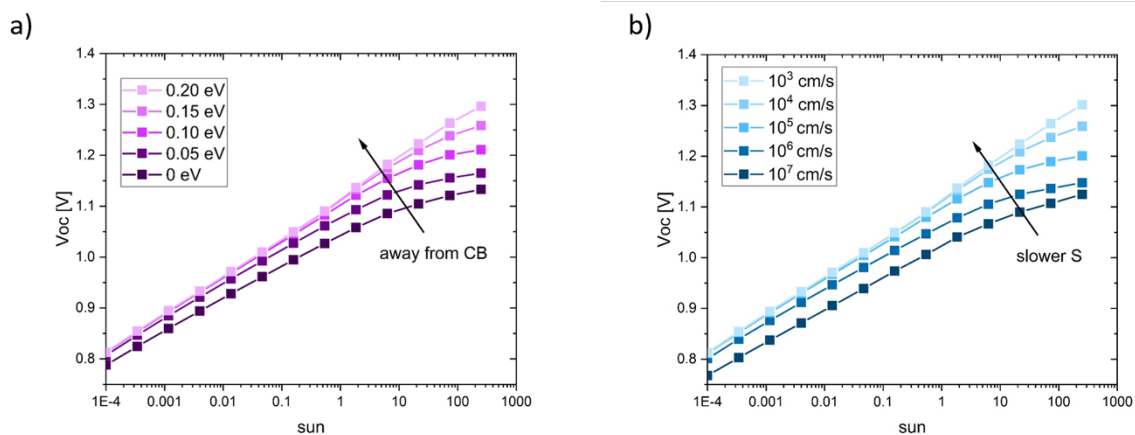


Figure 11.2.3B: Simulation results for the $V_{OC}(I)$ varying the position of the trap states above the perovskite conduction band a) and the recombination velocity associated to those trap states b). In both cases increasing the effectiveness of this new recombination path induce a more prominent V_{OC} saturation. Interestingly, when the trap states became too easily or hardly accessible for the minority carriers, even at lower carrier density, the intensity dependent behaviour is reduced.

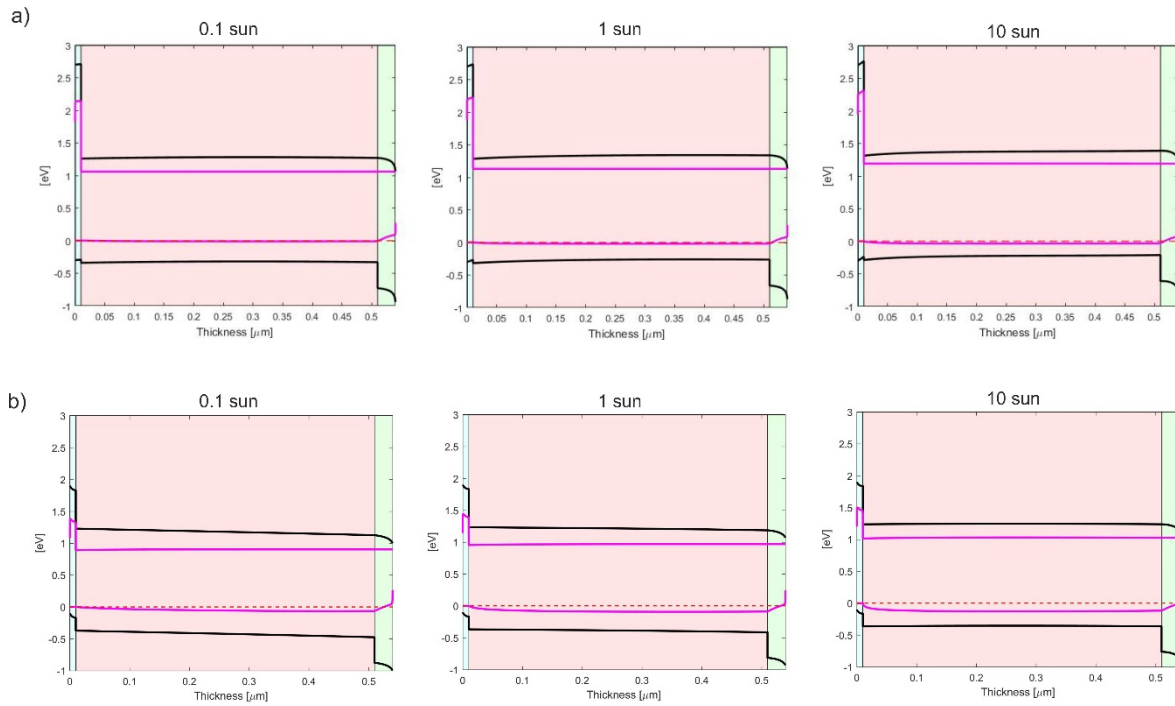


Figure 11.2.3C: Simulated energy band diagram at V_{OC} for different illumination condition for the two different perovskite solar cell using a) PTAA and b) P3HT as HTL. The left side characterized by light turquoise background represents the HTL, the central one (purple background) the perovskite and the right side (green background) the C_{60} . The respective energy levels for each layer are represented by full black lines, whereas the pink lines indicate the QFLS and the dashed red line the V_{OC} (which is defined by the QFLS at the electrodes).

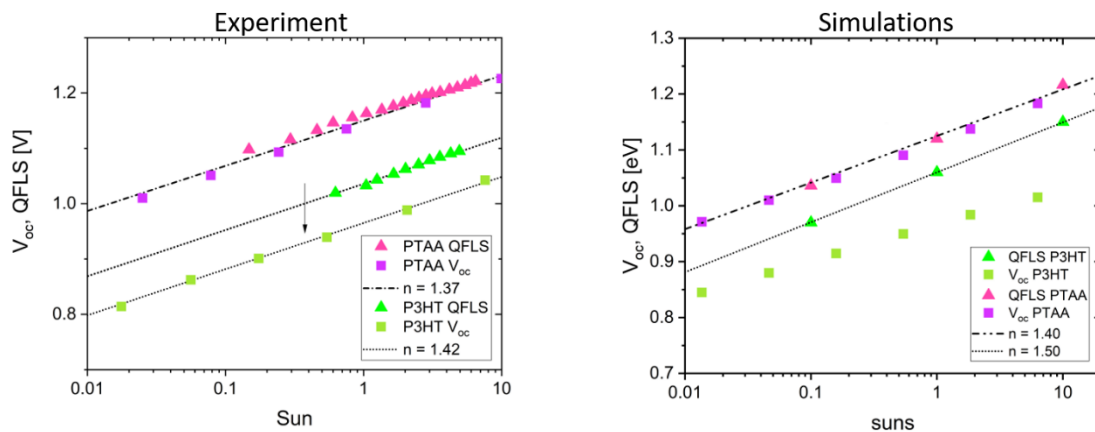


Figure 11.2.3D: Comparison between experimental results and simulations in the case of $QFLS(I)$ and $V_{OC}(I)$. In this case, the V_{OC} saturation has been removed experimentally by increasing the thickness of the transport layer and in the simulation by removing the additional intensity dependent recombination channel. Both PTAA and P3HT simulation matches nicely the experimental data. For the PTAA when not additional recombination channel is present $QFLS$ and V_{OC} matches perfectly, presenting a mildly larger ideality factor. In the case of P3HT, due to energetic offset, even when no additional intensity dependent recombination is present the $QFLS$ - V_{OC} mismatch is still present. We note that in the case of this simulation the

$V_{OC}(I)$ present a slope non identical to the $QFLS(I)$, which is not observed experimentally in the intensity regime studied.

Unselectivity of the HTL

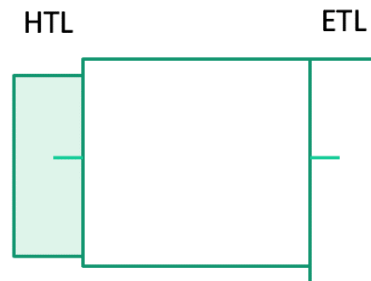


Figure 11.2.4A: Schematic representation of simulation model implementing the completed unselectivity of the HTL, which lead to the V_{OC} saturation. In this case the HOMO of the HTL has been varied in order represent a simplified picture where the minority carriers can access the HTL which loses its selectivity. Consequently, the electrons in the HTL can recombine with the majority carriers within the HTL and/or at the metal contacts depending on the recombination lifetime in the HTL.

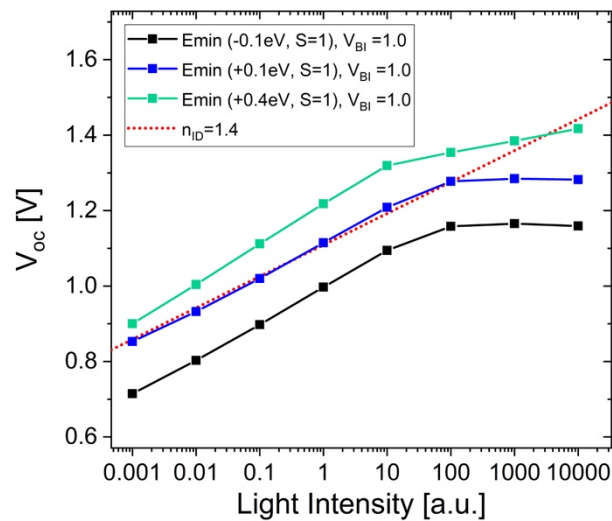


Figure 11.2.4B: Simulation results corresponding to the simulation model implementing the completed unselectivity of the HTL. The results show how as soon as the HTL starts to become unselective (minority carrier bandoffset <0 eV), the saturation of the V_{OC} starts to appear of high illumination intensities. However, given that we implemented an unselective HTL, the simulated V_{OC} is lower than the experimental results across the whole intensity range. Notably, in this scenario, the built-in field start to play an important role in determining the V_{OC} of the resulting cell.

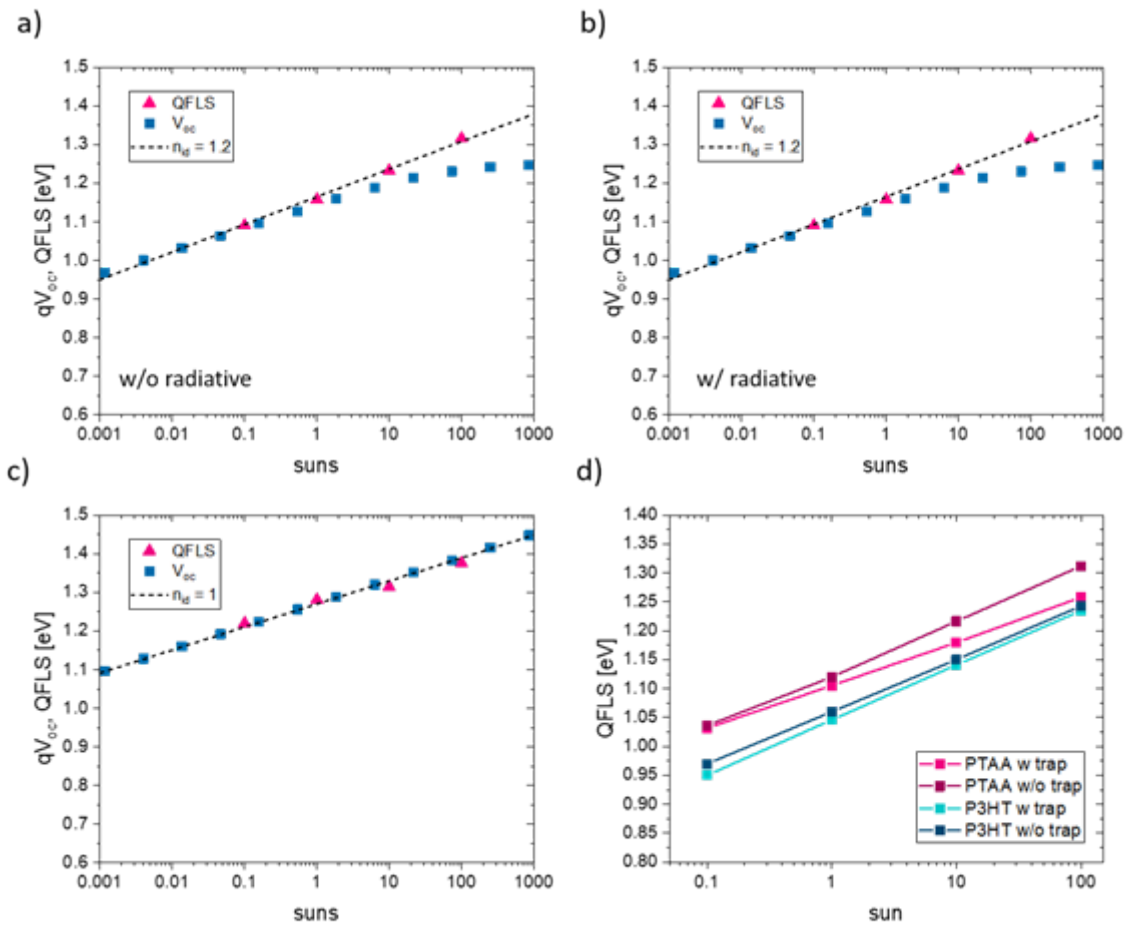


Figure 11.2.5: Simulation of the prototypical perovskite solar cell including only intensity dependent recombination channel at the HTL/perovskite interface a), including intensity dependent recombination channel at the HTL/perovskite interface and radiative recombination in the perovskite layer b) and including only radiative recombination in the perovskite layer c). Effects of the addition of the intensity dependent recombination channel on the QFLS in the bulk d).

11.3 Appendix 3

Current-Voltage Characteristic

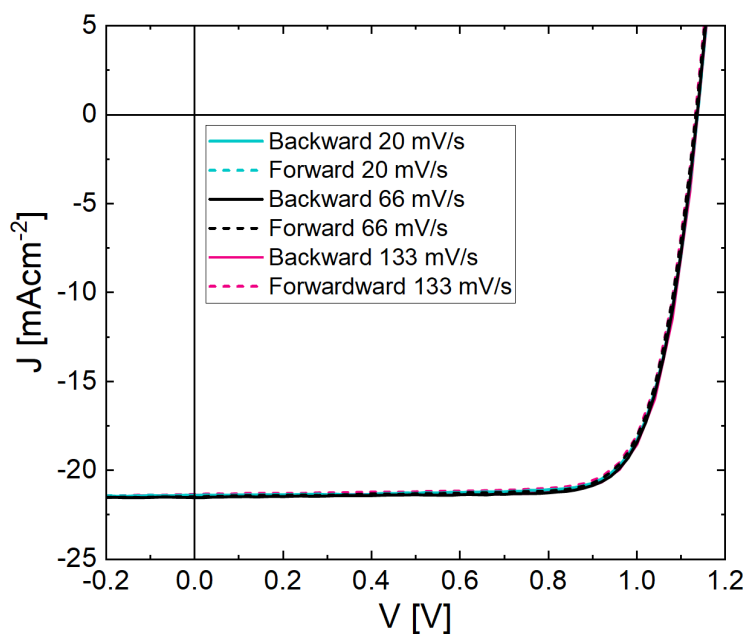


Figure 11.3.1: Forward and reverse J-V characteristic at different scan rates of a perovskite solar cells utilizing PTAA as HTL. The almost complete absence of hysteresis denotes a minimal impact of ion movement in this particular cell architecture.

Illumination Exposure Time Effects

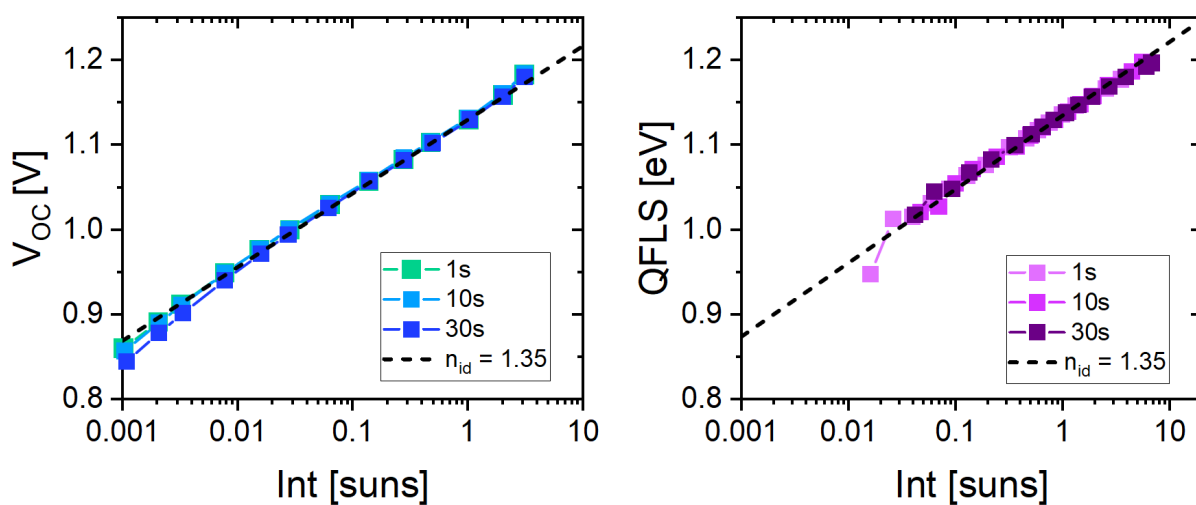


Figure 11.3.2: Illumination exposure time effects on intensity dependent V_{OC} and QFLS measurements on a PTAA device. The exposure time is varied from 1s to 30s at each point measured. The results show no influence on the intensity dependent measurements nor on the ideality factors extracted.

Radiative losses

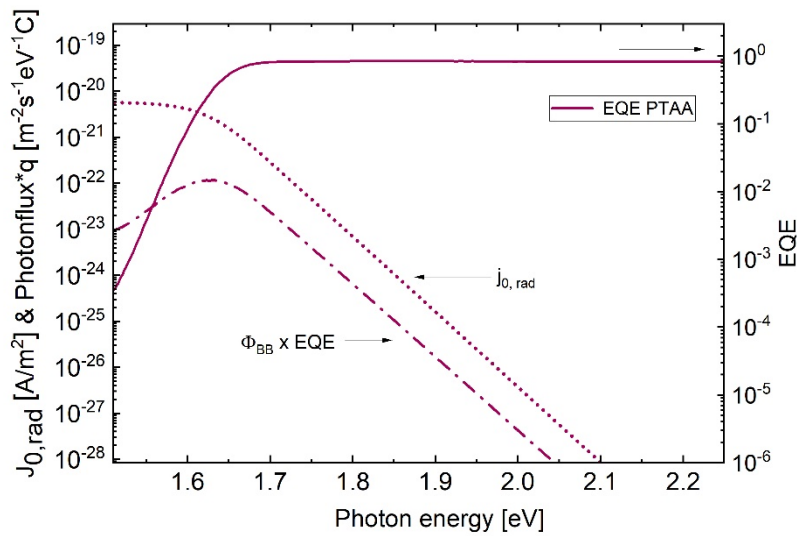


Figure 11.3.3: EQE_{PV} onset of two perovskite solar using PTAA as HTL and their emitted spectral photon flux calculated when the device is in equilibrium with the black-body (BB) radiation of the surroundings at 300K according to equation S1.

Passivation Effects

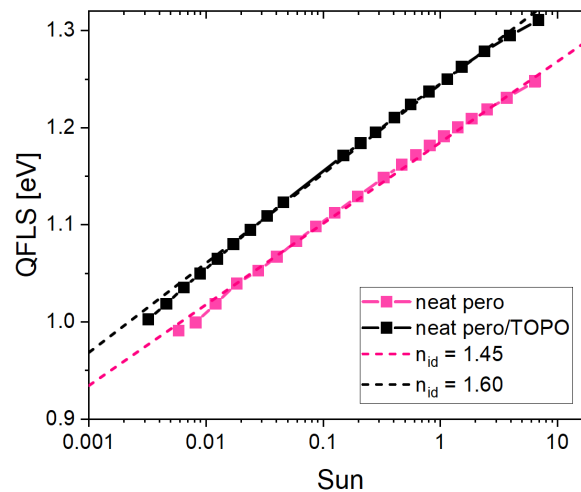


Figure 11.3.4: QFLS(I) of neat perovskite with and without TOPO passivation. As expected

by the reduction of surface recombination the overall QFLS values increase and the ideality factor is close to 2, given the stronger influence of bulk SRH recombination.

11.3.5 Relation between ideality factor and photoluminescence internal quantum efficiency

Assuming equal densities of electrons and holes, $n_e \propto n_h \propto n$, the carrier density n is related to the quasi-Fermi level splitting ΔE_F in the absorber by

$$n = n_i e^{\left(\frac{\Delta E_F}{2k_B T}\right)} \quad \text{Eq.11.3.1}$$

where n_i is intrinsic carrier density, k_B the Boltzmann constant and T the temperature. Here for simplicity we introduce the variables Δ and β

$$n^2 = n_i^2 e^{\left(\frac{\Delta E_F}{k_B T}\right)} = n_i^2 e^{(\beta \Delta)} \quad \text{with} \quad \Delta = \Delta E_F \quad \text{and} \quad \beta = \frac{1}{k_B T} \quad \text{Eq.11.3.2}$$

If recombination is only by a non-radiative 1st order process and a radiative 2nd order process, the total recombination current J_R and the dark recombination current $J_{R,0}$ are defined in the following

$$J_R = ed(k_1 n + k_2^* n^2) = edR \quad \text{Eq.11.3.3}$$

$$\text{and} \quad J_{R,0} = edR_0 \quad \text{Eq.11.3.4}$$

where e is the elementary charge, d is the layer thickness, k_1 is the first order recombination coefficient and k_2 the effective (external) second order recombination coefficient, R the total recombination rate and R_0 the dark recombination rate. Compared to the intrinsic radiative second order recombination coefficient k_2 , k_2^* is reduced via internal reabsorption of photons according to $k_2^* = (1 - p_r)k_2$, where p_r is the probability of reabsorption of photons in the absorber.^[123,149] In absence of parasitic absorption, p_r is related to the escape probability p_{esc} via $(1 - p_r) = p_{esc}$, resulting in $k_2^* = p_{esc}k_2$

Alternatively, we can express the total recombination current by a modified diode equation

$$J = J_0 e^{\left(\frac{\Delta E_F}{n_{id} k_B T}\right)} = J_0 e^{(\alpha \beta \Delta)} \quad \text{with } \alpha = \frac{1}{n_{id}} \quad \text{Eq.11.3.5}$$

where n_{id} is the ideality factor. This can be rewritten as

$$\ln\left(\frac{J_R}{J_{R,0}}\right) = \ln\left(\frac{R}{R_0}\right) = \alpha \beta \Delta \quad \text{Eq.11.3.6}$$

From this, it follows that

$$\frac{d \ln\left(\frac{R}{R_0}\right)}{d \Delta} = \alpha \beta = \frac{1}{n_{id} k_B T} \quad \text{Eq.11.3.7}$$

Eq 7 can be rewritten as

$$\frac{d \ln\left(\frac{R}{R_0}\right)}{d \Delta} = \frac{R_0}{R} \frac{1}{R_0} \frac{dR}{d\Delta} = \frac{1}{R} \frac{dR}{d\Delta} = \alpha \beta \quad \text{Eq.11.3.8}$$

We now combine Eq. 11.2.1, 11.2.3 and 11.2.5 to show that

$$\frac{dR}{d\Delta} = \frac{\beta}{2} k_1 n + \beta k_2^* n^2 = \frac{\beta}{2} (k_1 n + 2k_2^* n^2) \quad \text{Eq.11.3.9}$$

This leads to

$$\frac{1}{R} \frac{dR}{d\Delta} = \frac{\beta}{2} \frac{k_1 n + 2k_2^* n^2}{k_1 n + k_2^* n^2} = \frac{\beta}{2} \left(1 + \frac{k_2^* n^2}{k_1 n + k_2^* n^2}\right) = \alpha \beta \quad \text{Eq.11.3.10}$$

Finally, in absence of parasitic absorption^[290]

$$\frac{k_2^* n^2}{k_1 n + k_2^* n^2} = \text{PLQY} \quad \text{Eq.11.3.11}$$

where PLQY is the (external) quantum efficiency of photoluminescence, also the external emission efficiency.

Then, with $\alpha = \frac{1}{n_{id}}$:

$$n_{id} = \frac{2}{1 + PLQY} \quad \left\{ \begin{array}{l} 2 \quad \text{for } PLQY = 0 \\ 1.76 \quad \text{for } PLQY = 0.18 \\ 1 \quad \text{for } PLQY = 1 \end{array} \right. \quad \text{Eq. 11.3.12}$$

11.3.6 Simulations

Using transient PL measurements, we obtained an interfacial recombination velocity of $S=2000$ cm/s at the perovskite/C₆₀ interface, $S=200$ cm/s at the PTAA/PFN/perovskite interface and a bulk lifetime of approximately 500 ns in the absorber layer.

Table 11.3.1: SCAPS Simulation parameters used for simulating both the simulations models.

Parameter	Symbol	Value	Unit
Majority carrier band offset between perovskite and C ₆₀	$\Delta E_{maj,c}$	0	eV
Majority carrier band offset between perovskite and PTAA	$\Delta E_{maj,v}$	0	eV
Majority carrier band offset between perovskite and P3HT	$\Delta E_{maj,v}$	0.2	eV
Majority carrier band offset between perovskite and PEDOT:PSS	$\Delta E_{maj,v}$	0.4	eV
Lifetime in perovskite	τ_{pero}	500	ns
Lifetime in passivated perovskite	$\tau_{pero\ TOPO}$	1000	ns
Radiative recombination in perovskite	k_2	6×10^{11}	cm ³ /s
Lifetime in PTAA	τ_p	1	ns
Lifetime in PEDOT:PSS	τ_p	1	ns
Lifetime in C ₆₀	τ_n	1	ns
Ionized acceptors in PTAA	$N_{A,p}^-$	0	cm ⁻³
Ionized acceptors in P3HT	$N_{A,p}^-$	0	cm ⁻³
Ionized acceptors in PEDOT:PSS	$N_{A,p}^-$	1×10^{18}	cm ⁻³
Ionized donors in C ₆₀	$N_{D,n}^+$	0	cm ⁻³
Intrinsic carrier density in perovskite	N_i	1×10^{13}	cm ⁻³
Minority carrier recombination velocity from perovskite to PTAA	S_1	200	cm/s
Minority carrier recombination velocity from perovskite to PEDOT:PSS	S_2	200	cm/s
Minority carrier recombination velocity from perovskite to C ₆₀	S_4	2000	cm/s
Thickness of HTL	d_{PTAA}	10	nm
Thickness of perovskite	d_{pero}	400	nm
Thickness of C ₆₀	d_{C60}	30	nm
Offset between metal and PTAA	$\Delta E_{F,metal-p}$	0.2	eV

Offset between metal and P3HT	$\Delta E_{F,metal-p}$	0.2	eV
Offset between metal and PEDOT:PSS	$\Delta E_{F,metal-p}$	0.2	eV
Offset between metal and C ₆₀	$\Delta E_{F,metal-n}$	0.2	eV
Device built-in voltage	V_{BI}	1.2	V
Electron affinity PTAA	$E_{A,PTAA}$	2.5	eV
Bandgap PTAA	$E_{G,PTAA}$	3	eV
Electron affinity PEDOT:PSS	$E_{A,PEDOT}$	2.15	eV
Bandgap PEDOT:PSS	$E_{G,PEDOT}$	3	eV
Electron affinity perovskite	$E_{A,pero}$	3.9	eV
Bandgap perovskite	$E_{G,pero}$	1.6	eV
Electron affinity C ₆₀	$E_{A,C60}$	3.9	eV
Bandgap C ₆₀	$E_{G,C60}$	1.8	eV
Electron mobility in C ₆₀	$\mu_{n,C60}$	1×10^{-2}	cm ² /Vs
Hole mobility in PTAA	$\mu_{p,PTAA}$	1.5×10^{-4}	cm ² /Vs
Electron mobility in perovskite	$\mu_{n,pero}$	1	cm ² /Vs
Hole mobility in perovskite	$\mu_{p,pero}$	1	cm ² /Vs
relative dielectric constant HTL	ϵ_{PTAA}	3.5	
relative dielectric constant perovskite	ϵ_{pero}	22	
relative dielectric constant C ₆₀	ϵ_{C60}	5	
Effective electron density of states in HTL	$N_{C/V,HTL}$	1×10^{20}	cm ⁻³
Effective electron density of states in C ₆₀	$N_{C/V,C60}$	1×10^{20}	cm ⁻³
Effective electron density of states in perovskite	$N_{C/V,pero}$	3.1×10^{18}	cm ⁻³

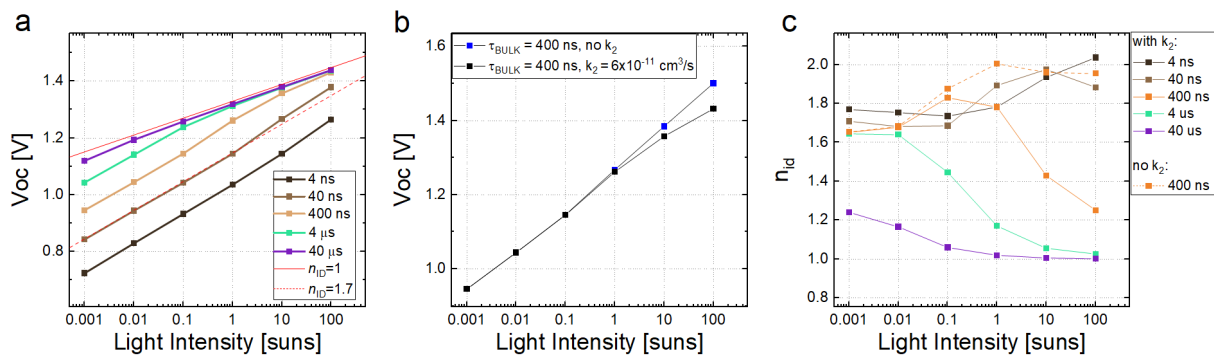


Figure 11.3.7. a) Numerically simulated intensity dependent open-circuit voltages (V_{OC}) in the bulk-only considering only the SRH lifetime and the bimolecular recombination rate constant (k_2) which was set to $6 \times 10^{-11} \text{ cm}^3 \text{ s}^{-1}$.^[215] The graph shows that bimolecular recombination dominates at lifetimes of 4 μ s or above under 1 sun conditions. For lower lifetimes, the ideality factor is approximately 1.8 at 1 sun which corresponds to dominant SRH recombination in the bulk. **b)** Numerically simulated intensity dependent V_{OC} in the bulk-only with and without k_2 . In

absence of k_2 and intensities above 0.1 suns, the ideality factor in the bulk reaches a value of 2 due to pure SRH recombination. **c)** The incremental ideality factors obtained in (a) and (b) as a function of intensity.

11.3.8 Ideality Factor from Shockley-Read-Hall Recombination

The classic Shockley-Read-Hall (SRH) recombination describes the recombination of free charges with impurity states. In the model the recombination rate is expressed with respect to the impurity density N_I , the electron and holes densities, n_e and n_h , their capture cross sections, C_e and C_h , and their de-trapping rates, β_e and β_h .

$$R = \frac{C_e C_h (n_e n_h - n_i^2)}{[C_e n_e + \beta_e] + [C_h n_h + \beta_h]} \cdot N_I \quad \text{Eq.11.3.13}$$

In the case of an intrinsic semiconductor, with negligible de-trapping rates (i.e. assuming mid-gap trap states), *Eq.1* can be approximated to

$$R = \frac{C_e C_h (n_e n_h)}{[C_e n_e] + [C_h n_h]} \cdot N_I \quad \text{Eq.11.3.14}$$

If we are in a situation where at the recombination site $n_e = n_h$ and $C_e = C_h$, the recombination rate can be expressed as

$$R = \frac{C_e^2 n_e^2}{2[C_e n_e]} \cdot N_I = \frac{C_e n_e}{2} \cdot N_I \propto n_e \quad \text{Eq.11.3.15}$$

In the interest of this discussion, we express the carrier density in terms of the intrinsic dark Fermi level of an undoped absorber layer

$$E_F^0 = \frac{E_C + E_V}{2} + \frac{1}{2} k_B T \ln \left(\frac{N_V}{N_C} \right)$$

$$n_e = N_C e^{\left(\frac{E_C - E_{F,e}}{k_B T} \right)} = n_e^0 e^{\left(\frac{E_{F,e} - E_F^0}{k_B T} \right)} \quad \text{Eq.11.3.16}$$

We rewrite now the rate in *Eq.3* expressing n_e in relation to the total QFLS

$$R \propto n_e \propto n_e^0 e^{\left(\frac{E_{F,e} - E_F^0}{k_B T}\right)} \propto e^{\left(\frac{\Delta E_{F,e}}{k_B T}\right)} \propto e^{\left(\frac{0.5 QFLS}{k_B T}\right)} \propto e^{\left(\frac{QFLS}{2k_B T}\right)} \quad \text{Eq.11.3.17}$$

$$\propto e^{\left(\frac{QFLS}{n_{id} k_B T}\right)}$$

In such a scenario, given that $n_e = n_h$, the splitting of the Fermi level is symmetric and the n_{id} results exactly equal to 2.

If we are now in a situation where $C_e = C_h$ but $n_e \neq n_h$ at the recombination site, the recombination rate will be governed by the minority carriers. For example, with unbalanced carrier densities $n_e \ll n_h$, the recombination rate is governed by the minority carrier n_e and it can be rewritten as

$$R = \frac{C_e C_h (n_e n_h)}{[C_h n_h]} \cdot N_I = C_e n_e \cdot N_I \propto n_e \quad \text{Eq.11.3.18}$$

We rewrite now *Eq.6* expressing n_h in relation to the total QFLS

$$R \propto n_e \propto n_e^0 e^{\left(\frac{E_{F,e} - E_F^0}{k_B T}\right)} \quad \text{Eq.11.3.19}$$

In this situation, given the unbalanced carrier densities, $(E_{F,e} - E_F^0) \neq \frac{1}{2} QFLS$, which implies an asymmetric splitting of the Fermi level, namely $(E_{F,e} - E_F^0) \neq (E_F^0 - E_{F,h})$. Therefore, $(E_{F,e} - E_F^0)$ has to be expressed more generally in terms of its share of the total *QFLS*.

$$R \propto n_e \propto n_e^0 e^{\left(\frac{E_{F,e} - E_F^0}{k_B T}\right)} \propto e^{\left(\frac{\Delta E_{F,e}}{k_B T}\right)} \propto e^{\left(\frac{\theta QFLS}{k_B T}\right)} \propto e^{\left(\frac{QFLS}{n_{id} k_B T}\right)} \quad \text{Eq.11.3.20}$$

In this case then $n_{id} = \frac{1}{\theta}$ and its value is dictated by the asymmetry of the splitting of the Fermi level. In an extreme case, where the whole *QFLS* is defined by the minority carriers, $\theta = 1$ and therefore, $n_{id} = 1$ even for first order monomolecular processes.

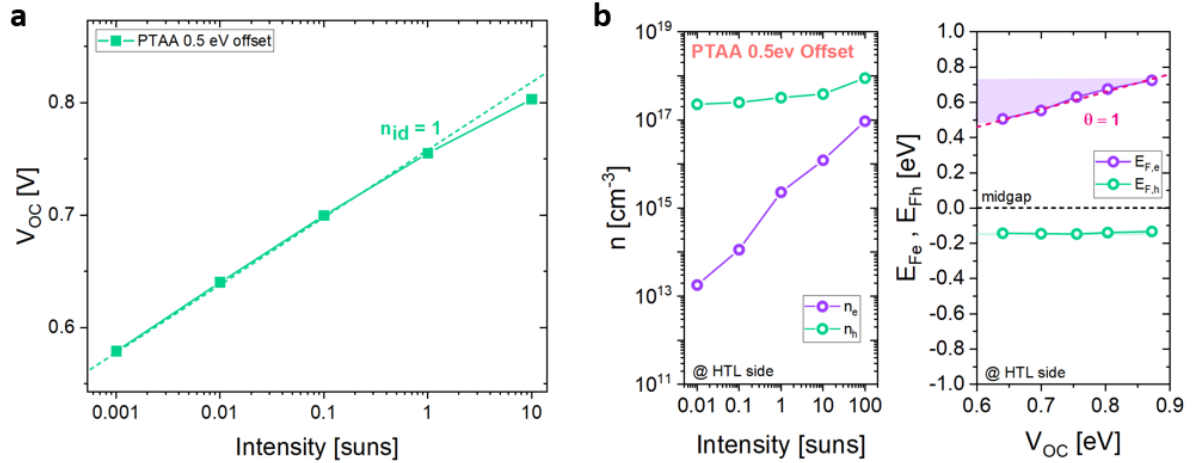


Figure 11.3.8: Hypothetical PTAA cell simulated with the standard settings but misaligned energy levels at the HTL-interface ($E_{maj}=0.5$ eV). a) V_{OC} vs. I plot with corresponding $n_{id} = 1$. b) The left panel shows the electron and hole densities as a function of the light intensity. The right panel shows electron and hole quasi-Fermi levels at the site of predominant recombination, plotted against the respective V_{OC} of the cell. The series shows how in devices with a large majority carrier energy level offset and faster interface recombination, the majority carrier density in the TL is essentially pinned while the minority carrier density increases linearly with the intensity. This scenario results in an asymmetry of the splitting quasi-Fermi levels.

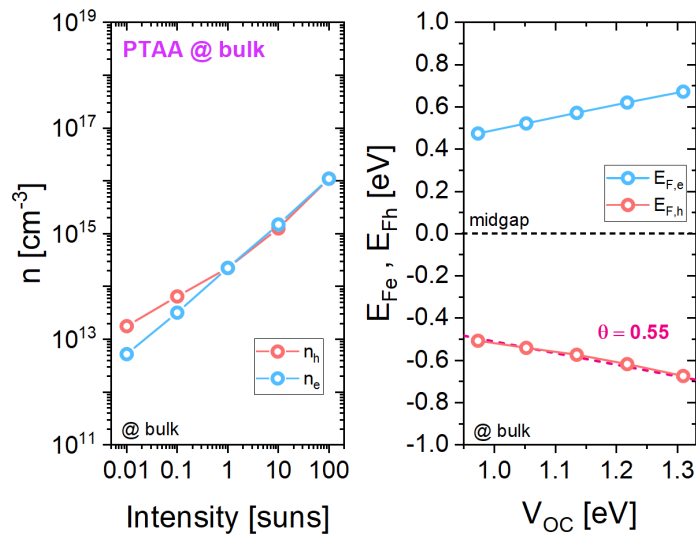


Figure 11.3.9: The left panel shows the electron and hole densities with respect to the light intensity in the bulk for a PTAA cell. The right panel shows the electron and hole quasi-Fermi levels in the bulk plotted against the respective V_{OC} of the cell. Here $\theta = 0.55$ which corresponds to $n_{id} = 1.8$, as expected from SRH recombination in the bulk. However, since here bulk recombination is not the limiting recombination process, but interface recombination is, this n_{id} value does not determine the n_{id} obtained from the V_{OC} (I) analysis.

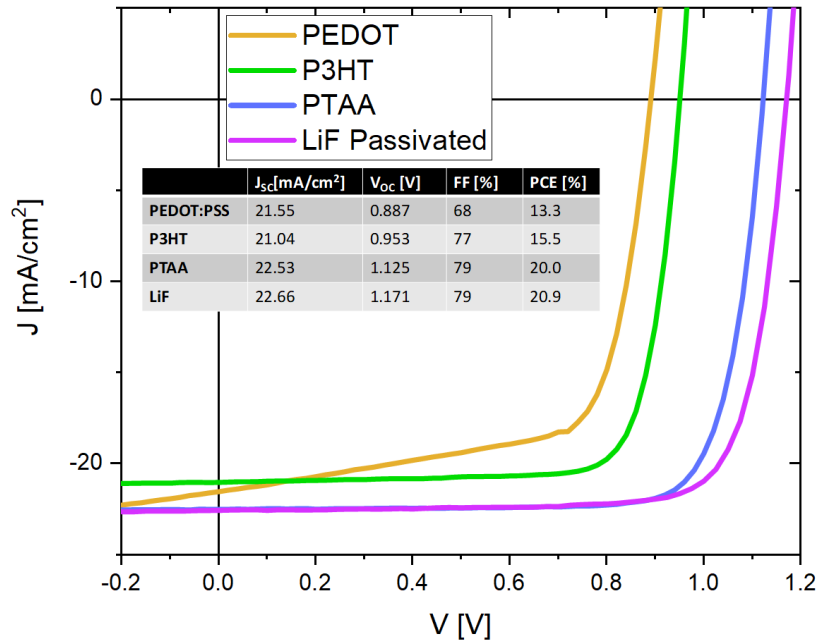


Figure 11.3.10: JV characteristic for perovskite solar cells utilizing PEDOT:PSS, P3HT and PTAA as HTL. Additionally, a PTAA with perovskite/C60 interface passivated with LiF is presented^[127].

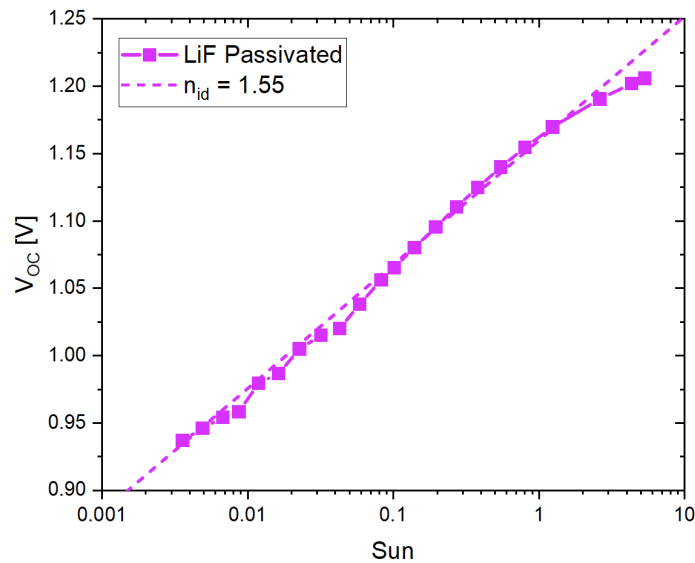


Figure 11.3.11: V_{OC} vs. intensity for a PTAA perovskite solar cell where a LiF interlayer has been deposited between the perovskite and the C60 ETL. As previously reported, this modification allow for reduced interfacial recombination at this limiting interface. Consequently, both the V_{OC} and the n_{id} increase.

11.4 Appendix 4

Current density – voltage characteristic

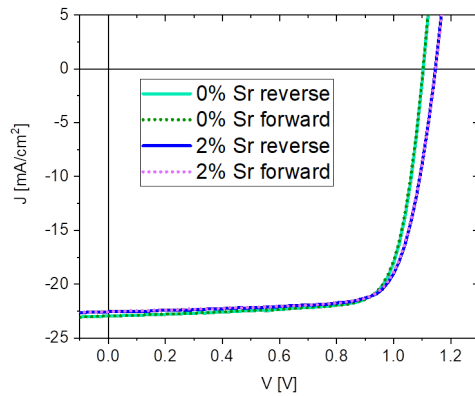


Figure 11.4.1A: J-V characteristic showing both forward and reverse scan at 0.1V/s with a voltage step of 0.02 V for two samples containing 0% and 2% Sr respectively. Both samples show complete absence of any hysteresis effect.

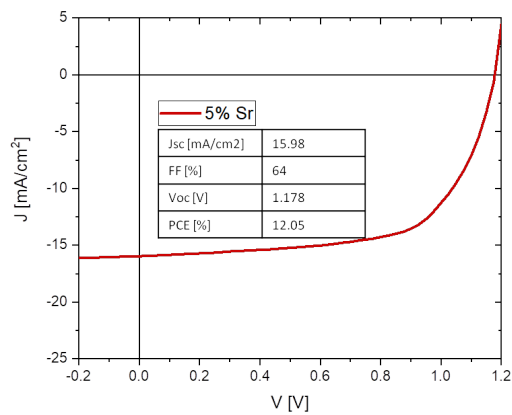


Figure 11.4.1B: J-V characteristic showing a reverse scan at 0.1V/s with a voltage step of 0.02 V for a sample containing 5% Sr. The curve shows how a higher Sr concentration has negative effects on both J_{SC} and FF without any appreciable improvement of the V_{OC} .

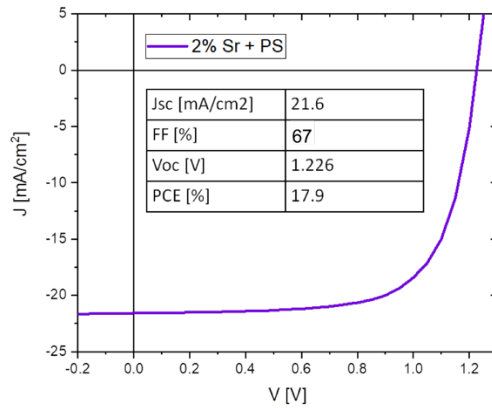


Figure 11.4.1C: J-V characteristic showing a reverse scan at 0.1V/s with a voltage step of 0.02 V for a sample containing 2% Sr with additional ultra-thin (less than 5nm) polystyrene layer deposited between perovskite and C₆₀ following the experimental procedure described in Wolff et al.^[75] The resulting solar cell show an extraordinarily high V_{OC} of 1.215V. Unfortunately, the presence of this insulating PS layer led to a considerable reduction of the FF, probably by limiting the extraction of charges via tunneling^[75]

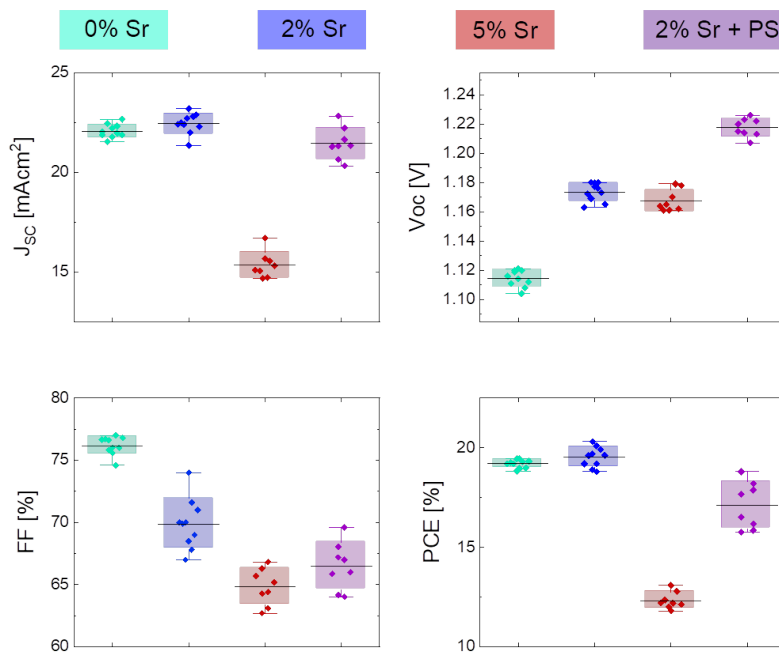


Figure 11.4.1D: Box chart for the most relevant type of devices, 0% Sr, 2% Sr, 5% Sr and 2%Sr + PS. From the picture trends are more evident: it is clear that upon Sr addition the V_{OC} is improved whereas the FF decreases. We can identify a ratio of 2% Sr as the optimum concentration considering the strong decrease in performances observed with a 5% Sr ratio, without showing any further improvement in V_{OC}. On the contrary, the addition of a polystyrene layer onto a 2% Sr increase considerably further the V_{OC} reaching a record value of 1.226 V. However, it is also clear of this has a negative effect on the FF and the overall PCE

unfortunately is not improved. For this reason we refer to this additional increase in V_{OC} as a proof of concept for the suppression of recombination at the interface with C_{60} .

EQE and Absorption Measurement

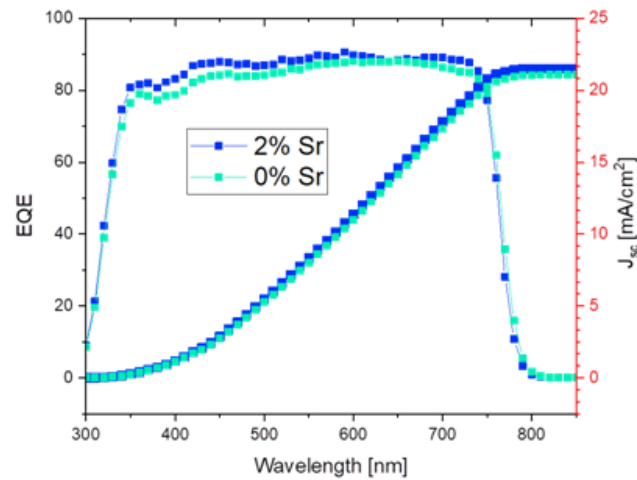


Figure 11.4.2A: External Quantum Efficiency including the integrated current for 0% and 2% Sr cells. We acknowledge that for the 2% Sr cell the integrated current of 21.5 mA/cm² represents approximately a 4% relative mismatch compared to the J_{SC} of 22.4 mA/cm² as obtained from the JV scan of the corresponding solar cell. A similar mismatch has been systematically found for the 0% Sr cell.

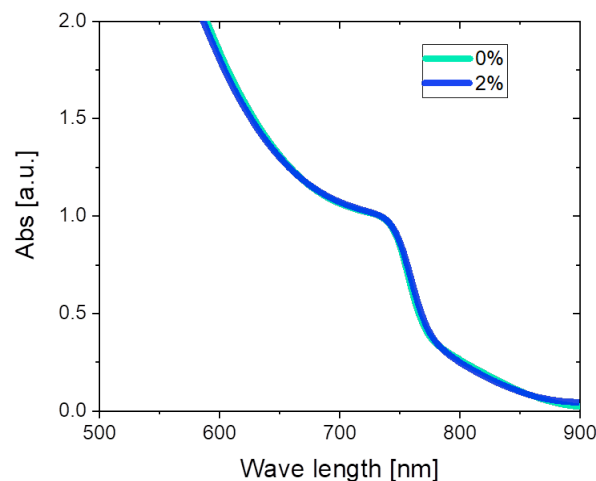


Figure 11.4.2B: Absorption measurement of two perovskite film with same thickness (400nm) with 0% and 2% Sr respectively, deposited on glass.

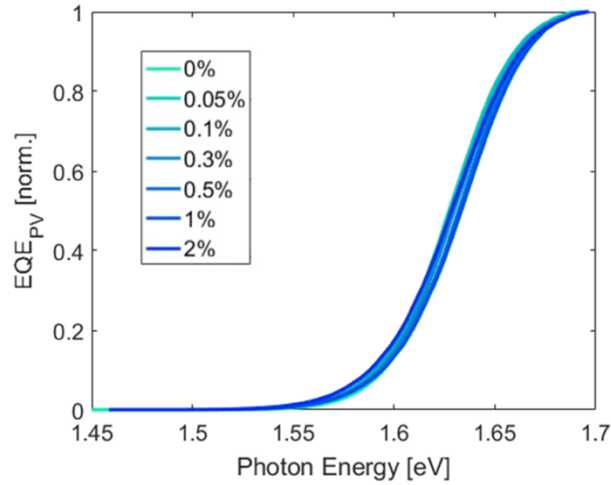


Figure 11.4.2C: EQE_{PV} onset as function of photon energy for all different Sr concentrations, normalized to 1.7 eV.

Radiative losses

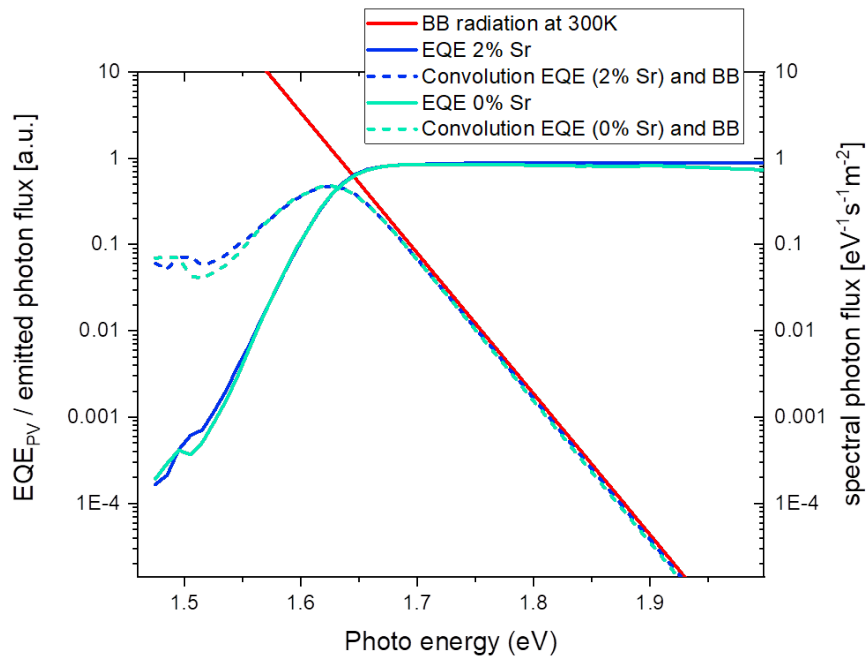


Figure 11.4.3: EQE_{PV} onset of two perovskite solar cell containing 0% and 2% Sr respectively and their emitted spectral photon flux calculated when the device is in equilibrium with the black-body (BB) radiation of the surroundings at 300K according to equation S1.

SIMS (Secondary Ion Mass Spectroscopy)

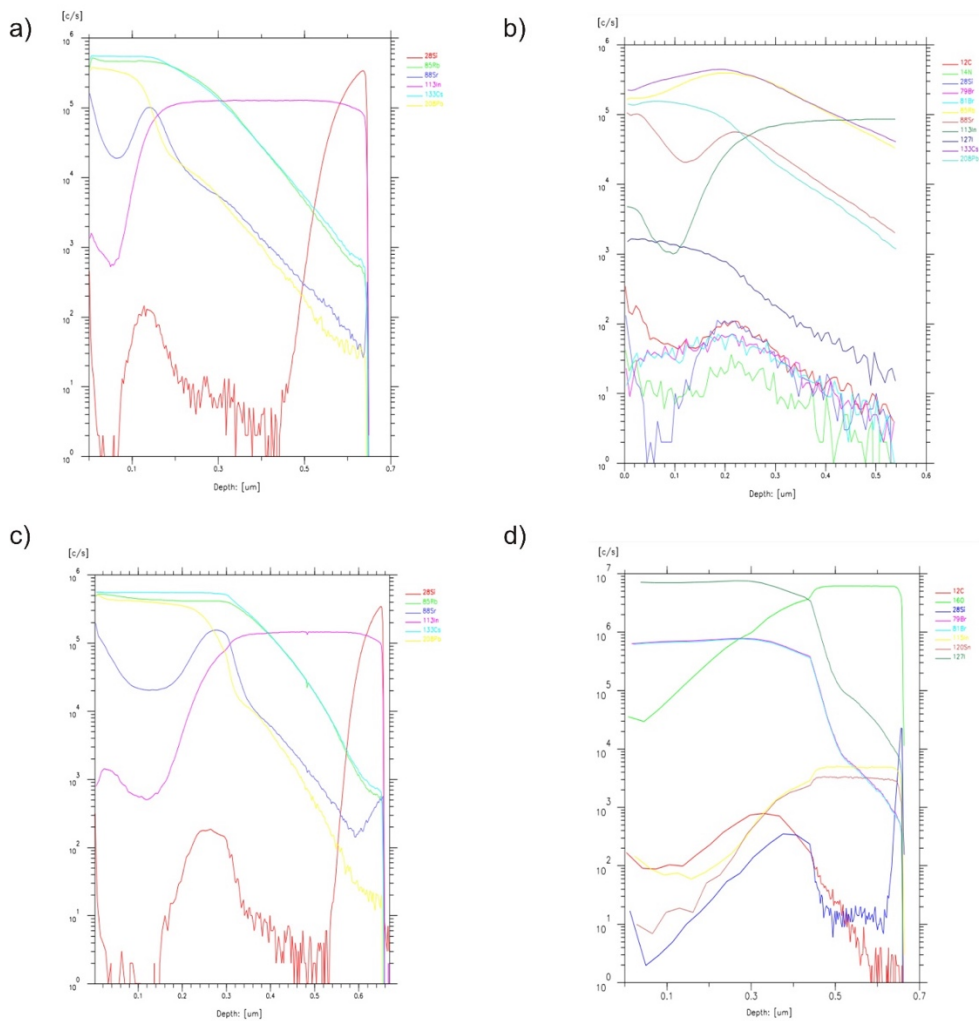


Figure 11.4.4: a) and b) SIMS (Secondary Ion Mass Spectroscopy) depth profile of two different spots on the surface of the same perovskite sample containing 2% Sr. c) SIMS depth profile of the different perovskite sample containing 2% Sr. All measurements here are performed using O ions. d) SIMS depth profile using Cs ions in order to detect the distribution of Br and I across the perovskite layer

XPS (X-Ray Photoelectron Spectroscopy)

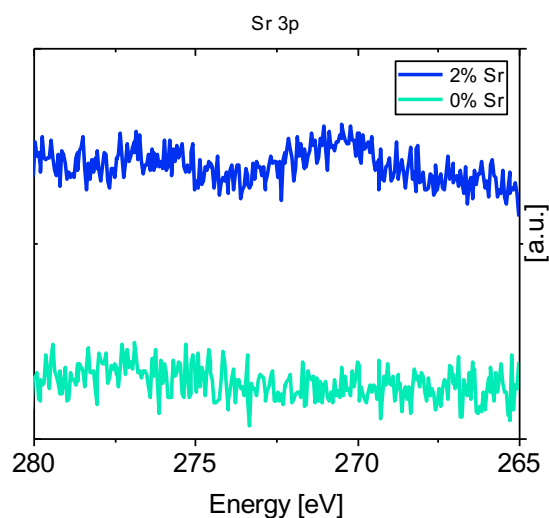


Figure 11.4.5A: XPS measurements of the surface of two perovskite layers containing 0% and 2% Sr respectively.

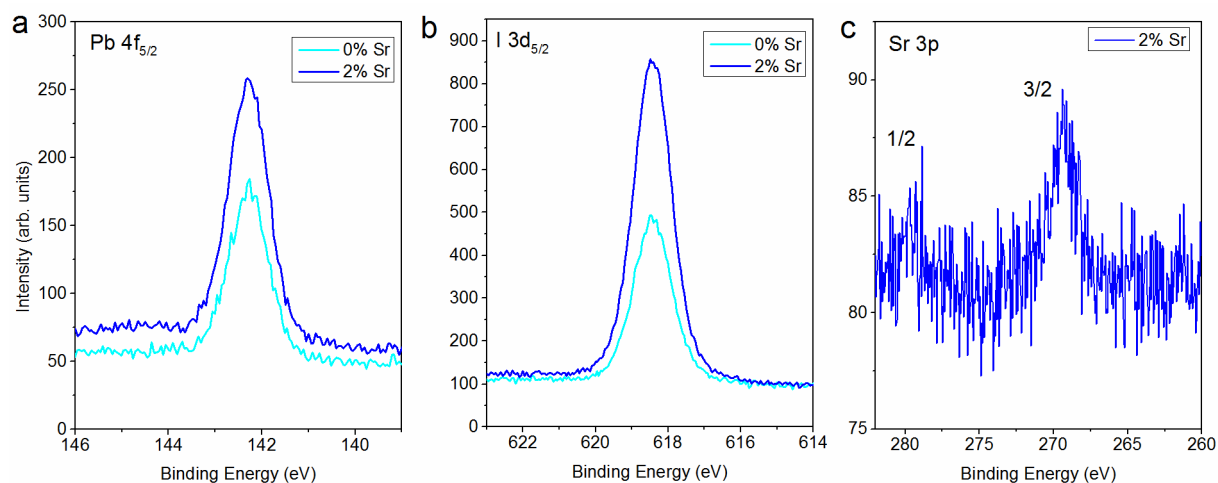


Figure 11.4.5B: XPS core-level spectra of (a) Pb 4f, (b) I 3d and (c) Sr 3p on two mixed perovskite films without and with 2% Sr incorporation.

In order to investigate quantitatively the surface composition of the perovskite films, XPS measurements employing monochromated Al K α radiation were performed on the samples without and with Sr incorporation. As shown in Figure S5, clearly, we observed relatively large amount of Sr on the perovskite surface with 2% Sr. Detailed analysis of the core-level spectra results in the Sr/Pb molar ratio of 0.21 and the Sr/I

molar ratio of 0.07, which are both much higher than the expected stoichiometry from an homogenous Pb substitution through the whole volume. This proves strong enrichment of Sr on the perovskite surface, in good agreement with the findings by Perez Del Rey et al.^[223]. Moreover, if the surface would be covered with unreacted SrI₂ the I concentration found at the surface, and consequently its ratio with Sr, should be consistently higher than what found here. In addition, the I/Pb molar ratio (2.49 by stoichiometry) is estimated to be 2.78 for the sample with Sr, in contrast to 2.13 for the sample without Sr, which can be possibly ascribed to the fact that Sr partially replace Pb, leading to a decrease of Pb/I ratio at the surface in the crystal lattice.

SEM (Scanning Electron Microscopy)

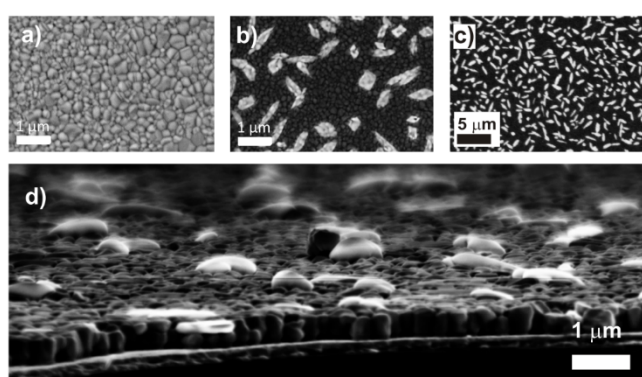


Figure 11.4.6A: Energy sensitive SEM in-lens detector top view images of perovskite films with a) 0% Sr and b) 2% Sr. c) shows a zoomed-out view of the same sample as in b). Image d) displays SEM in-lens detector images of a tilted sample containing 2% of Sr to visualize the cross section.

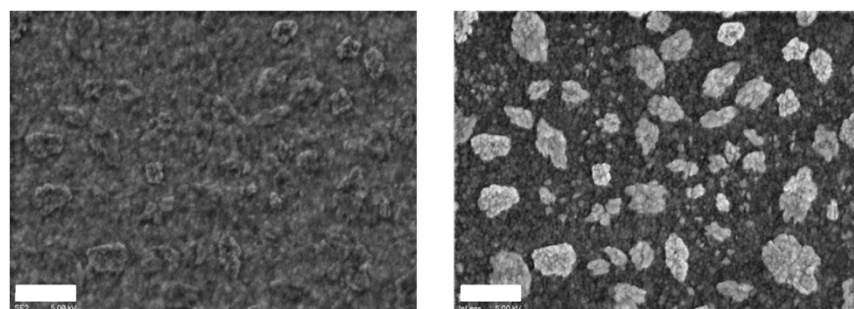


Figure 11.4.6B: Comparison between Everhart-Thornley detector (left) and In-Lens detector (right) imaging of a 2% Sr sample. The images show that the brighter feature on the top surface can be imaged only through the energy sensitive In-Lens detector whereas with the more topographic sensitive detectors those are barely visible. The comparison shows how from a more topography sensitive imaging it is possible to barely distinguish these features only by a light shadowing effect due to the different height compared to the rest of the layer, but no change in brightness is observed, excluding the presence of non-conductive material. Scale bar here is 1 μm.

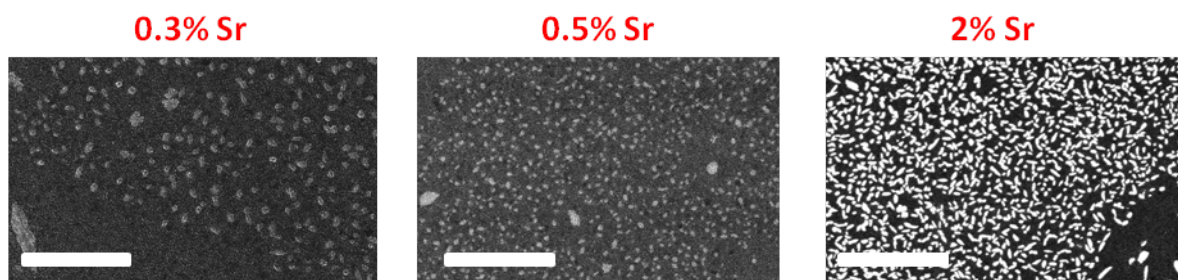


Figure 11.3.6C: Top SEM images of 0.3%, 0.5% and 2% Sr samples. The series of images indicates that increasing the Sr concentration the density of the brighter feature on top increase. Scale bar here is 10 μm .

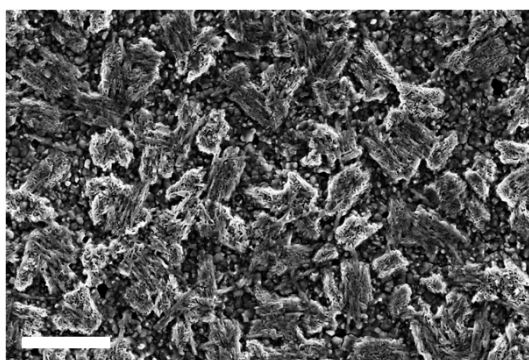


Figure 11.4.6D: Top SEM images of a 5% Sr sample. The image indicates that increasing the Sr concentration the density of the brighter feature on top increase. As expected, in this case the surface is almost entirely covered with feature of a different nature from the underlying perovskite typical paddlestones. This, consistently with the reduced PCE, indicates that in this case amount of Sr added is probably too much and that the elevated concentration of this features, beneficial in the case of 2%, now could substantially limits the performance of the resulting solar cell. Scale bar here is 2 μm .

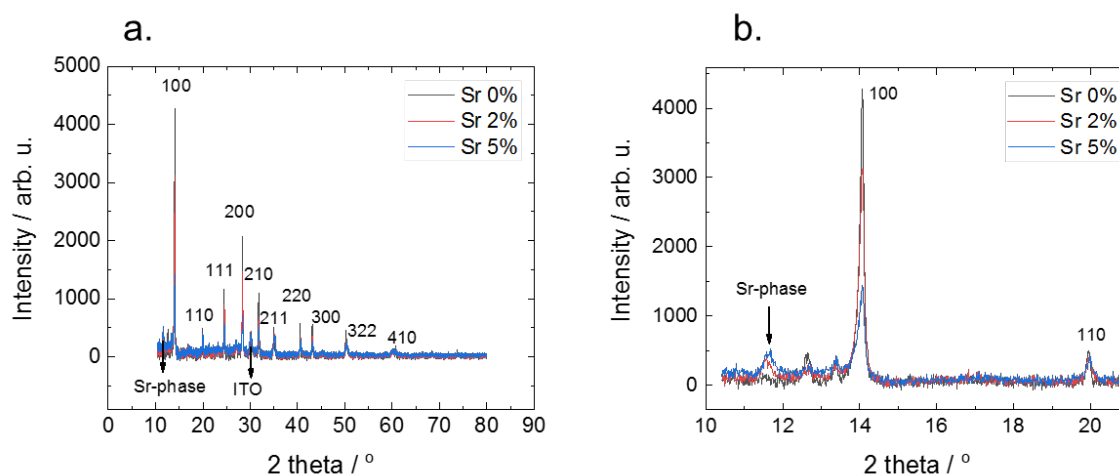


Figure 11.4.6E: a) X-ray diffraction patterns for samples containing 0%, 2% and 5% Sr respectively. The patterns show the typical perovskite distinctive peaks for all three samples (space group $Pm-3m$). No significant shifts are observed in the reflections of the perovskite phase indicating no major changes in the unit cell volume. b) Magnification of X-ray diffraction

patterns for samples containing 0%, 2% and 5% Sr respectively. Concomitantly with the presence of Sr in the films, at $\sim 11.6^\circ$ a new reflection not identified in the 0% Sr sample appears. Since this is the only new reflection appearing, the exact identification of the crystal structure and the chemical nature of this phase is rather difficult, particularly taking into account the chemical complexity of the films. More importantly, the intensity of the perovskite reflections decrease as the new phase appears. This potentially indicates that the new phase segregates towards the surface of the film attenuating the X-ray signals coming from the underlying perovskite phase. We additionally note that the broadening of the peaks increase as the Sr content increases in the sample. This might be caused by an increase in microstrain and/or reduction of the domain size. An increase of microstrain might be caused by an increase of point or planar defect concentration or a decrease of the compositional uniformity of the domains.

11.4. 7 Recombination Dynamic Simulations

In this simulation the recombination of charges has been simulated using the following rate equation

$$\frac{dn}{dt} = -(k_1 n + k_2 (n_0 + n) \cdot n + k_3 n^3) \quad \text{Eq.11.4.1}$$

where n is the initial photogenerated carrier density, n_0 is the background carrier concentration due to doping, and k_1 , k_2 and k_3 are the monomolecular, bimolecular and Auger recombination coefficient, respectively. The simulations were carried out in MATLAB R2017b, running an iterative code with the given constants and equations. To obtain the steady state carrier concentration we assumed $G = 4 * 10^{21} \text{ cm}^{-3} \text{ s}^{-1}$ and let the time run for ~ 10 ms until steady state conditions were assured.

Fig. 11.4.7A displays the result of simulations where the background carrier concentration n_0 was varied. For the pulsed simulation we assumed $n_{t=0} = 1 * 10^{14} \text{ cm}^{-3}$ at $t = 0$ and no further generation thereafter. In this case we simulated the recombination dynamic varying the doping concentration n_0 from $n_0 = 1 * 10^{14} \text{ cm}^{-3}$ to $n_0 = 1 * 10^{18} \text{ cm}^{-3}$, whereas the recombination constants fixed at $k_1 = 4 * 10^6 \text{ s}^{-1}$, $k_2 = 1 * 10^{-10} \text{ s}^{-1}$ and $k_3 = 1.8 * 10^{-28} \text{ s}^{-1}$, being those realistic values and similarly already reported in literature^[123,291]. The PL efficiencies at a carrier concentration equivalent to 1 sun has been simulated using

$$\text{PL} = k_2 \cdot (n + n_0) \cdot n \quad \text{Eq.11.3.2}$$

And

$$\text{PLQY} = \frac{k_2 \cdot (n + n_0) \cdot n}{(k_1 n + k_2 (n_0 + n) \cdot n + k_3 n^3)} \quad \text{Eq.11.3.3}$$

The simulations show that increasing the background density due to doping provides additional centres for radiative recombination (we assumed exclusively radiative second order recombination), with the effect of increasing the radiative efficiency but at the same time enhancing the speed of the recombination of photogenerated charges, resulting in faster PL decays. Clearly, a very different situation is found in our study when increasing the Sr concentration, where we observe a parallel increase of the PL life times and PL efficiencies.

To explain the experimental results, a second set of simulations where performed where the PL decay rate and absolute PL efficiency was simulated for different k_1 in absence of doping. In this case simulation shows how the reduction of k_1 has positive effects on both PL decays and efficiencies.

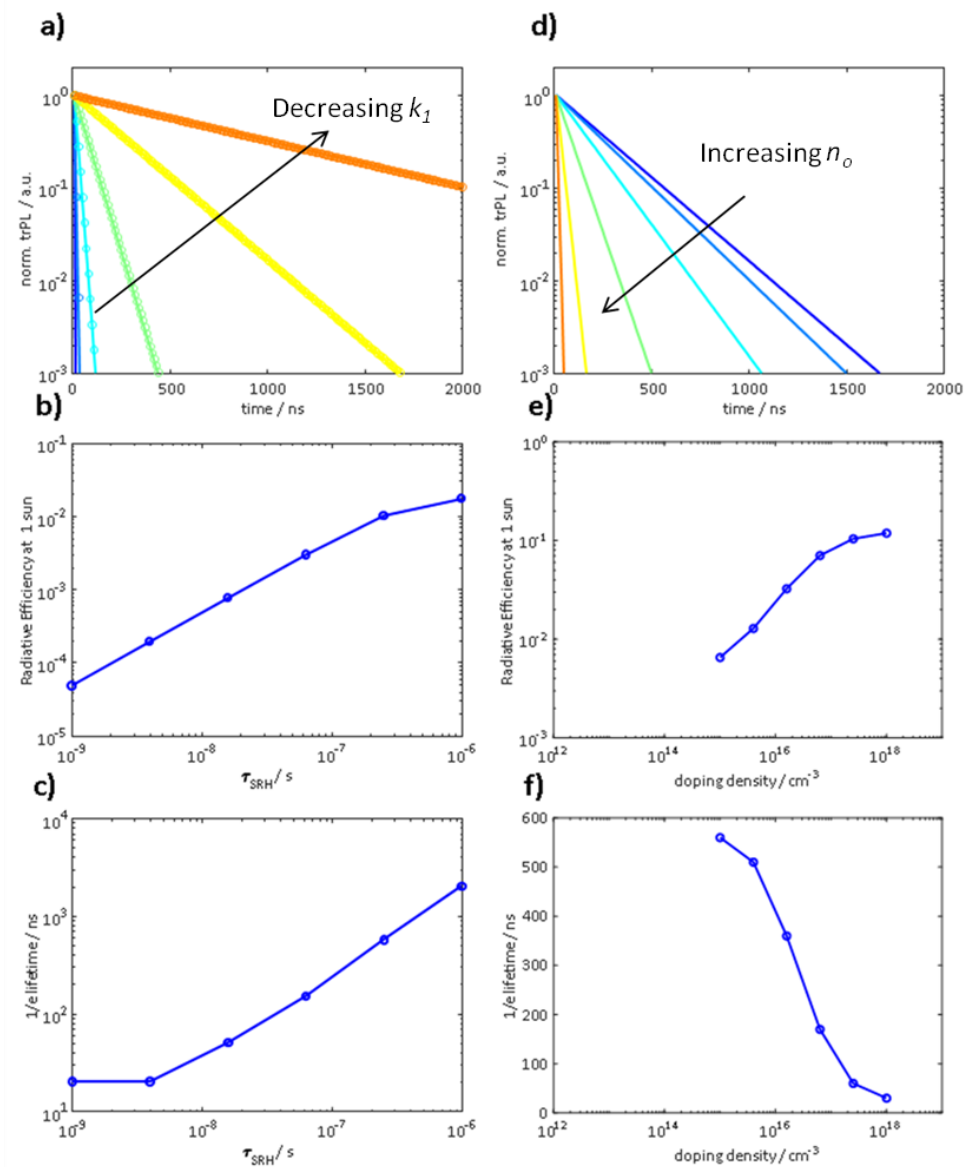


Figure 11.4.7A: Simulations of photoluminescence decays at low intensities ($n_{t=0} = 10^{14} cm^{-3}$), a) and d), radiative efficiencies (PLQY), b) and e), and $1/e$ PL decay, c) and f). On the left side,

a), b) and c), the simulations present the results for reducing the monomolecular rate constant k_1 from 10^9 and 10^6 s^{-1} and plotted against the SRH life times $\tau_{SRH} = 1/k_1$. On the right side, d), e) and f), we increase the background doping concentration from 10^{15} to 10^{18} cm^{-3} , using a fixed $k_1 = 4 * 10^6$ s^{-1} .

Surface Photovoltage Effect (measured by UPS)

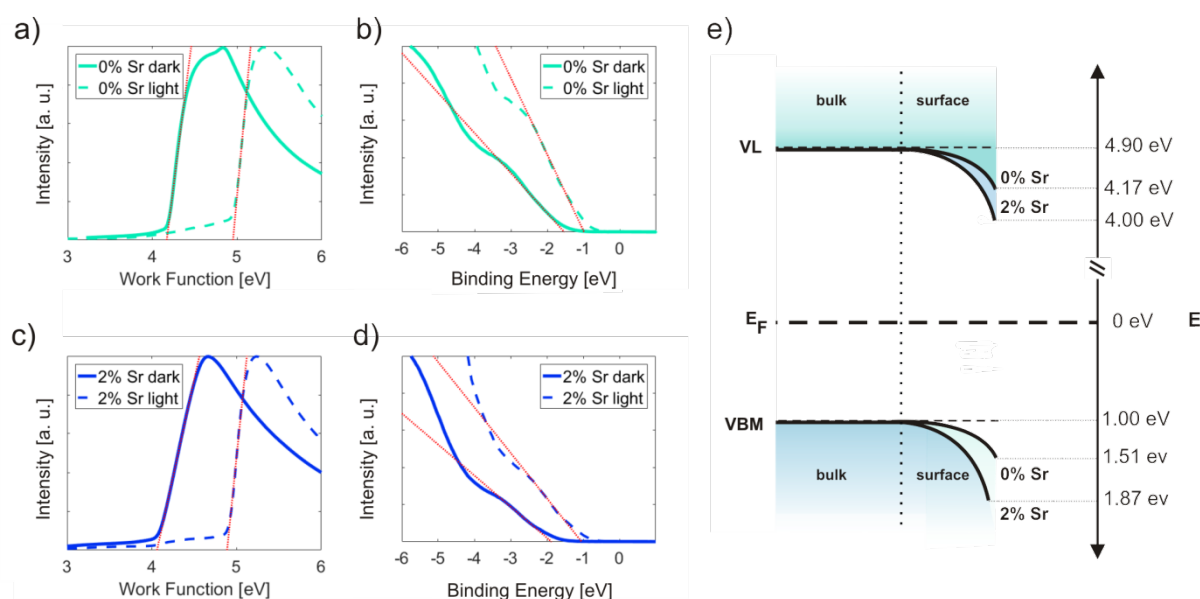


Figure S11.4.8: Effect of visible light illumination on the work function and valence band for 0% Sr and 2% Sr containing samples. a) and c) work function measured under dark and illumination conditions. b) and d) valence band regions measured under dark and illumination conditions. e) schematic representation of the surface band bending for 0% and 2% Sr-perovskites in the dark and under illumination. Vacuum level (VL) and valence band maximum (VBM) positions are given with respect to the Fermi level of the substrate (E_F).

Photoemission Spectroscopy

While we refrained from measurements of intermediate C_{60} coverage to minimize eventual sample changes due to prolonged illumination with UV light, we can yet draw a realistic picture of the energy level alignment based on prior art, as follows. Since the electron affinity of C_{60} is in the range of 4.0 eV [292] to 4.9 eV (our measurements, **Fig. 11.4.9A**), contact with a substrate of comparable work function will result in Fermi level pinning, i.e., electron transfer from the substrate to the acceptor C_{60} and thus partial filling of its LUMO manifold [293]. In our case the substrate is the perovskite film, and the electron transfer to the molecular layer will result in reduced downward surface band bending within the perovskite [294]. The accumulated electron density with the C_{60}

layer promotes charge carrier diffusion away from the interface, i.e., upward energy level bending within the acceptor layer occurs [293,295], in full analogy to band bending in conventional semiconductors. Note that the amount of energy level bending, as well as final work function and Fermi level position within the energy gap of the acceptor depend on the amount of transferred charge and details of the actual density of states distribution [295], which can be notably influenced by structural disorder. In addition, we stress that the Fermi level position of a 20 nm thick C_{60} layer is still determined by the substrate and does not represent the intrinsic position, as the Debye length of C_{60} was reported to be several 100 nm [296]. Consequently, there are three components that contribute to the work function of the 20 nm C_{60} layer, i.e., reduced downward surface band bending within the perovskite, an interface dipole due to the transferred charge, and upward energy level bending within the C_{60} film. Attending to the two specific examples examined here, we first observe that the work function of 0% Sr perovskites was consistently 0.15 eV (or more) higher than that of 2% Sr samples, and thus a larger amount of electron transfer to the C_{60} layer when Sr is incorporated into the perovskite. This implies stronger energy level bending within the C_{60} and indeed justifies the observation of higher work function, as well as wider energy spacing between Fermi level and LUMO for the $C_{60}/2\%$ Sr perovskite interface, compare to the Sr-free one.

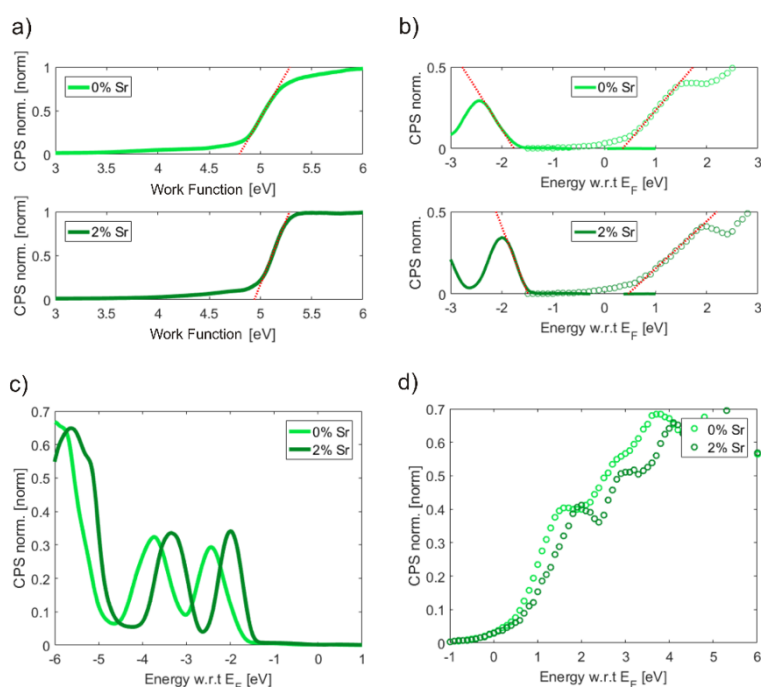


Figure 11.4.9A: UPS and IPES data of 20nm layer C_{60} deposited on two different ITO/PTAA/perovskite samples, containing 0% and 2% Sr respectively. a) Secondary electron cut-off regions. b) Magnified valence and conduction band region near E_F . c) Wide range of valence band structure obtained from UPS and d) conduction band structure obtained from IPES.

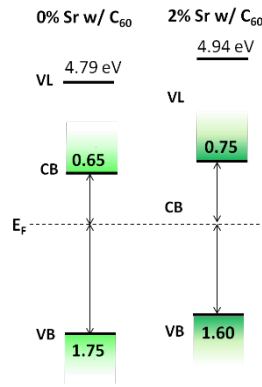


Figure 11.4.9B: Valance band maximum, conduction band minimum and work function energy scheme using values extrapolated from UPS/IPES (**Fig. 11.4.9A**) for two layers of 20nm C₆₀ deposited on two different PTAA/perovskite samples, containing 0% and 2% Sr respectively.

Photoluminescence Quantum Yield at Perovskite/C60 interface.

To study the importance of non-radiative recombination at the perovskite/C₆₀ interface, different samples with and w/o a 30 nm thick C₆₀ layer were subject to absolute PL measurements. This new set of measurements has been performed using a 445nm CW laser (adjusted ad 1 sun condition intensity) exciting our sample through an optical fiber connected to an integrating sphere. The PL spectra have been recorded with a Silicon CCD camera (Andor), calibrated with a Xe lamp of know spectral irradiance. The spectral photon density has been obtained from the corrected detector signal and the photon numbers of the excitation and emission obtained from numerical integration carried out in MATLAB R2017b. The PLQY values in **Fig. 11.4.10** confirm how indeed the presence of C₆₀ drastically reduces the PL efficiency compared to the neat perovskite layer. The measurements also show that this reduction is significantly smaller for the Sr-containing perovskite, meaning that non-radiative recombination at this “unfavourable” interface has been reduced. This finding is perfectly in agreement with the increase in V_{OC} observed in the device and the recombination scheme proposed for the Sr-containing samples, where the selectivity of the contact is improved due to the present of a larger bandgap and strong downward band bending, which limits the accessibility of holes to this interface. We acknowledge that the PL values measured for this new set of experiments during resubmission period are overall slightly lower than what we should expect from the high V_{OC} of our devices, most probably due to the present unfavourable conditions of our gloveboxes which has affected sample preparation during resubmission period (most probably caused by the exceptionally elevated temperature and high degree of humidity recorded during this period of the year in Germany). However, the trend our results is solid and clear for multiple sets of samples.

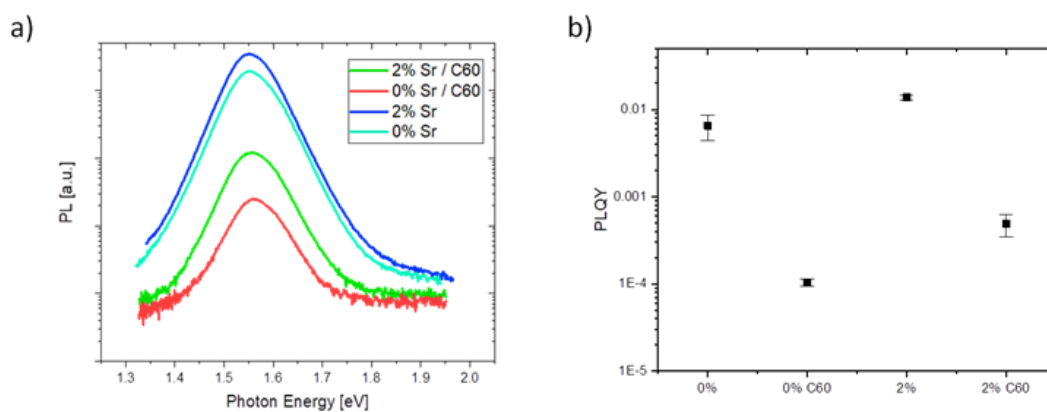


Figure 11.4.10: a) Photoluminescence Quantum Yield (PLQY) measurements for a neat 0% and 2% Sr sample and covered with 30nm of C₆₀. Averaged PLQY values, b), for the corresponding set of samples. Statistics here is calculated over 4 films for each type of sample.

11.5 Appendix 5

Additional J-V

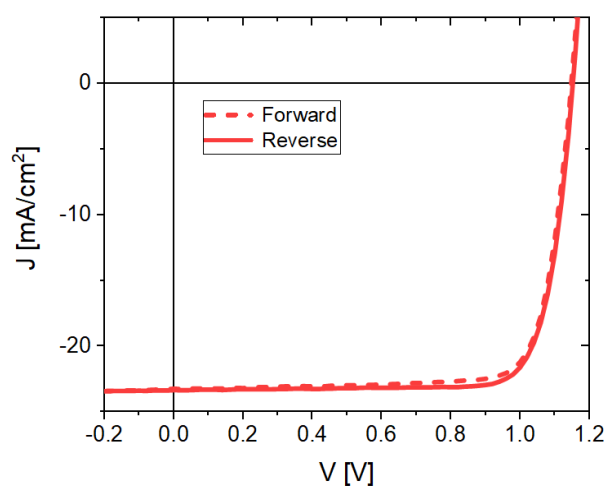


Figure 11.5.1A: Forward and reverse J-V scans (0.02 V/s with a voltage step of 0.02 V) for a PIL treated solar cell. The scans denote a negligible hysteresis behaviour in the presence of the PIL layer.

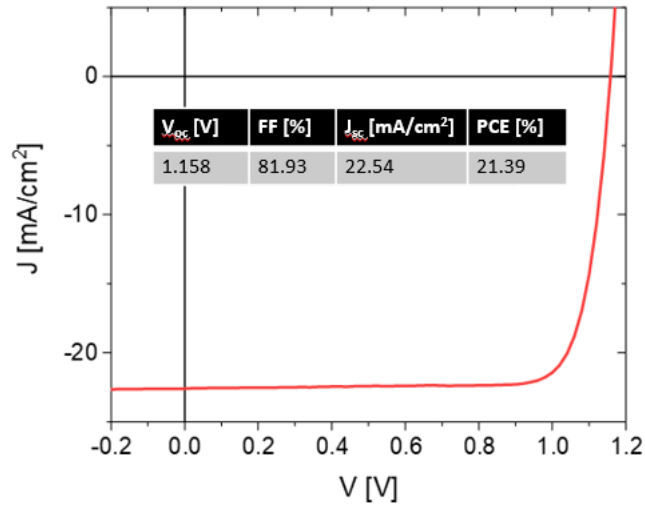


Figure 11.5.1B: Reverse J-V scans (0.02 V/s with a voltage step of 0.02V) for the champion PIL treated solar cell measured with a mask.

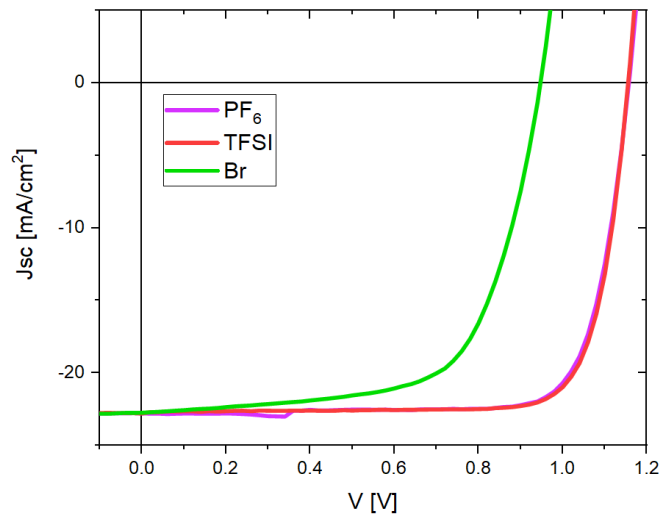


Fig. 11.5.1C: J-V scans of perovskite solar cells treated with different PILs: [Pelm][TFSI], [Pelm][Br] and [Pelm][PF₆]. While the TFSI and PF₆ version demonstrate a very similar performance, the Br version decreases the efficiency significantly.

EQE_{PV} - Absorption

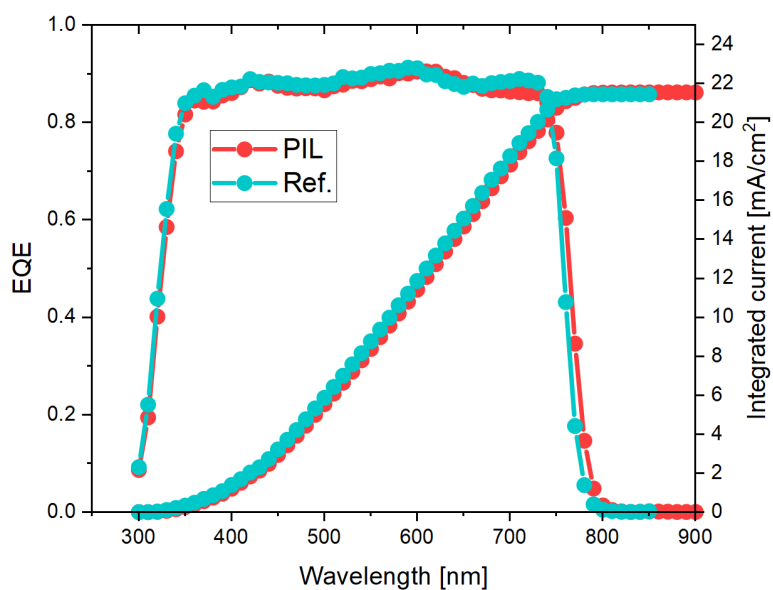


Figure 11.5.2A: External Quantum Efficiency including the integrated current for reference and PIL treated cells.

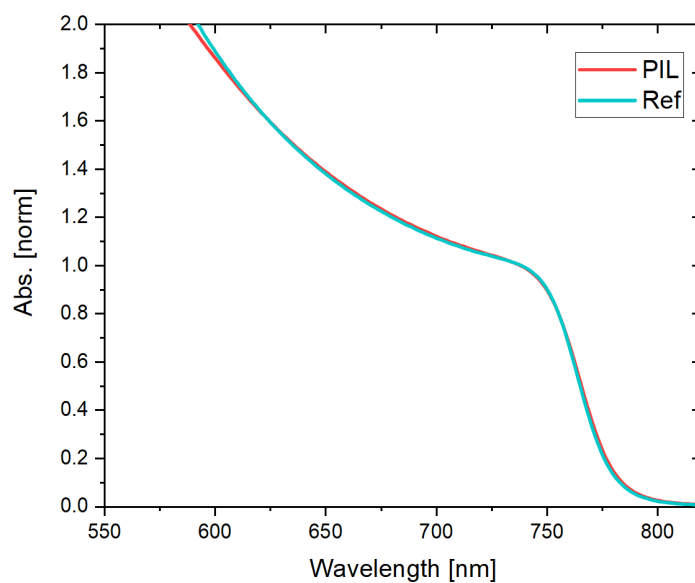


Figure 11.5.2B: Absorbance of the reference and PIL treated perovskite films.

Scanning Electron Microscopy

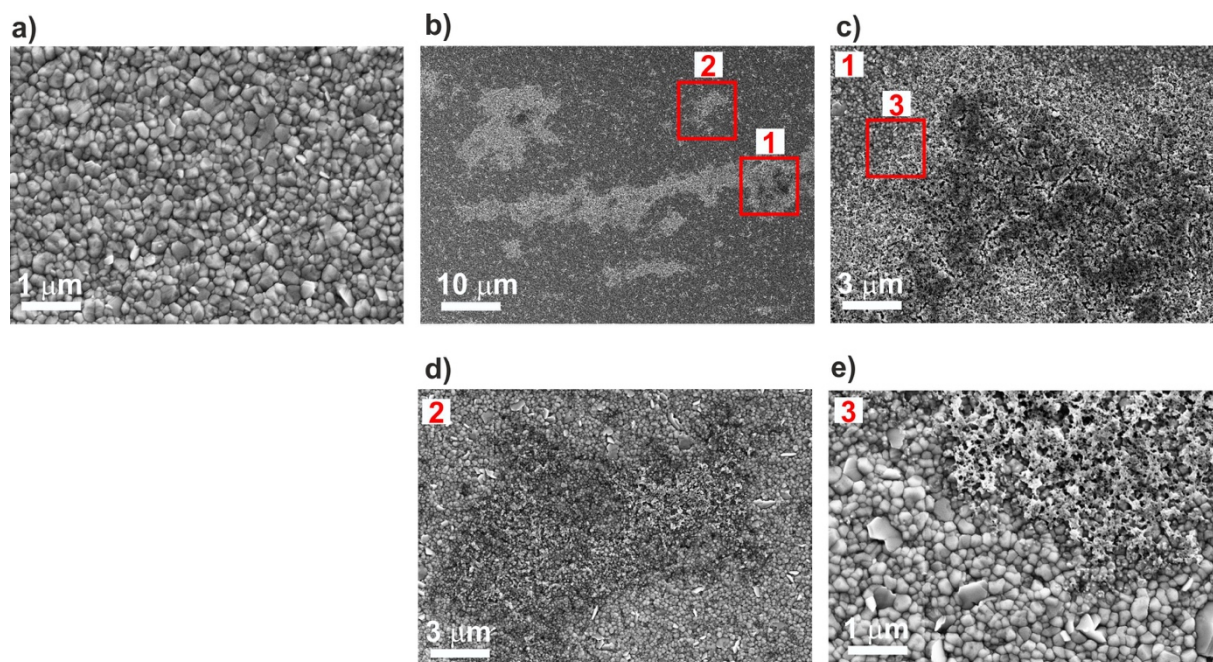


Figure 11.5.3A: Scanning electron microscopy images of the top surface of the reference perovskite a) and of the PIL treated surface b)-e). In b) the polymer patches spreads around the surface after spin coating. In c) and d) the central spot of this polymer island is magnified and the porous nature of the material is observed. In e) we can identify the border between the underlying perovskite and the polymer, it is evident that the polymer attaches to the perovskite top layer without penetrating in it.

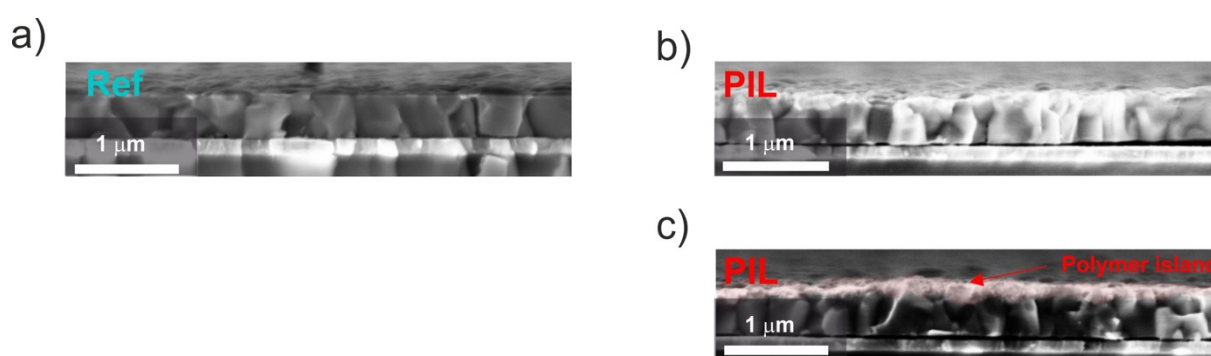


Figure 11.5.3B: Cross section SEM images of a reference a) and PIL treated perovskite films b)-c) deposited on ITO/PTAA. In b) the cross section image of the PIL treated perovskite sample is representing an area where there are no polymer highlands present at the surface. In c) the cross represent an area where the perovskite is covered by a polymer island. Both images do not show any sign of alteration of the bulk structure compared to the reference perovskite nor penetration of the PIL in the bulk.

X-Ray Diffraction

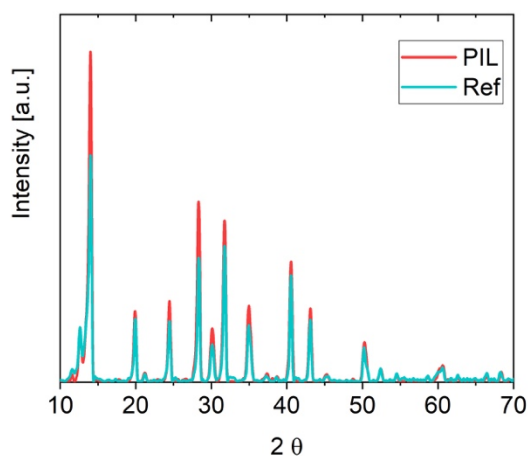


Figure 11.5.4: X-ray diffraction for the neat perovskite reference and the PIL treated one. We notice that the PIL treatment do not induce a significant change in the crystallinity of the sample nor induce the appearing of a secondary phase. We note that the slightly lower intensity in the peaks of the reference sample can be simply attributed to a difference in the crystal orientation.

Contact Angle

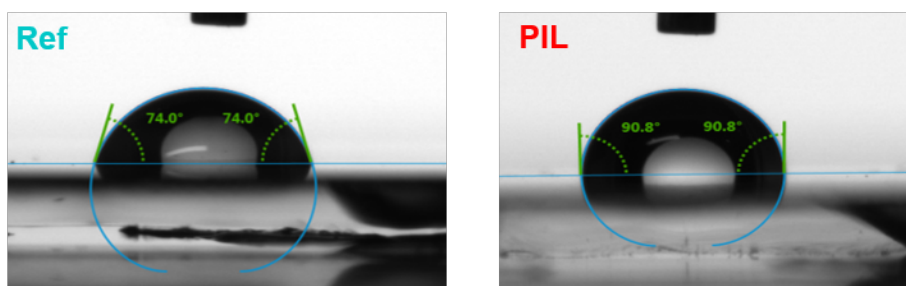


Figure 11.5.5: Contact angle measurements using water for a neat reference and a PIL treated perovskite. We note that for the PIL treated sample the contact angle with water is larger, denoting a stronger hydrophobicity of the surface. The effect is expected due to the deposition of a hydrophobic material (PIL) on top of the perovskite surface.

Additional EDX

Given the low signal of S and the covering of the F signal from the I, much highly concerted, we addressed the O signal as characteristic of the TFSI counterion. Naturally, we checked the reliability of the signal by comparing the treated and neat

perovskite in order to verify that the O was coming exclusively from the TFSI and not from the environment, as shown in **Fig. 8.3**.

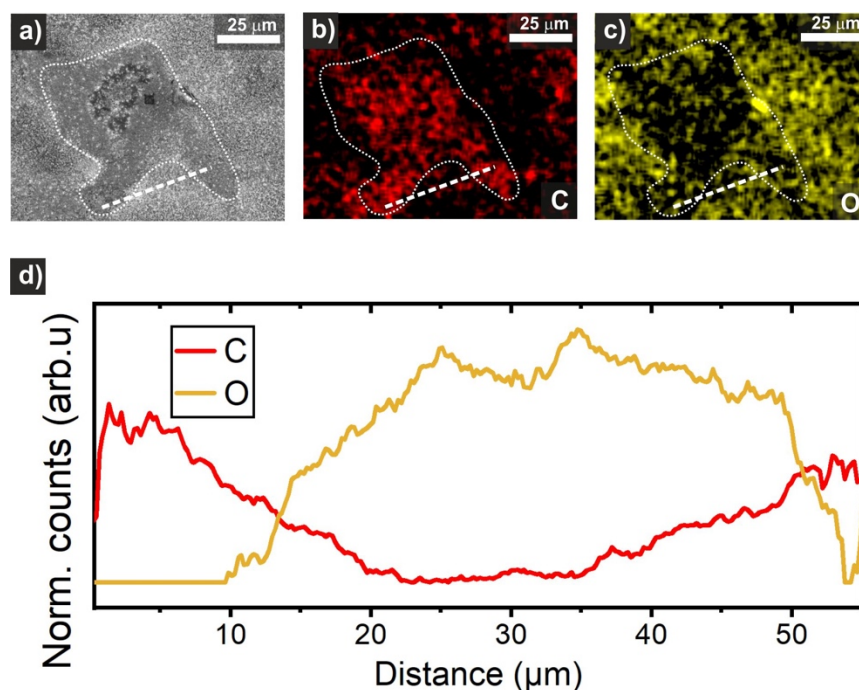


Figure 11.5.6A: SEM a) and EDX b)-c) top surface of a PIL treated perovskite. The line scan of the C and O contraction is indicated by the thick white dotted lines and the concentration profile plotted in d). It is clearly visible the anticorrelation between C and O signal at the top surface.

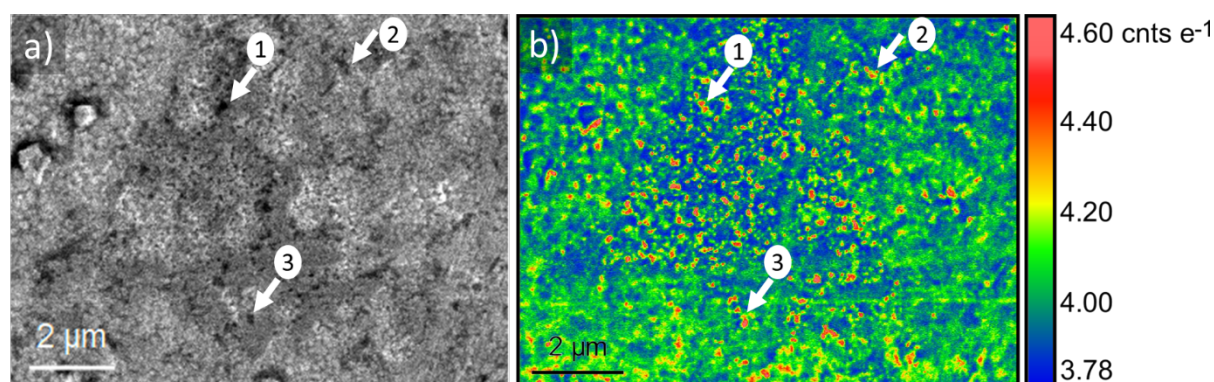


Figure 11.5.6B: SEM image (a) and corresponding CL map (b) of an area of the PIL-treated perovskite film covered by a polymer island. Note that the apparent high CL-intensity spots on the polymer island correspond to pores, which indicate that the enhanced luminescence stems from the underlying passivated perovskite, as shown with arrows for the points 1, 2 and 3. The uncovered perovskite still exhibits luminescence enhancement.

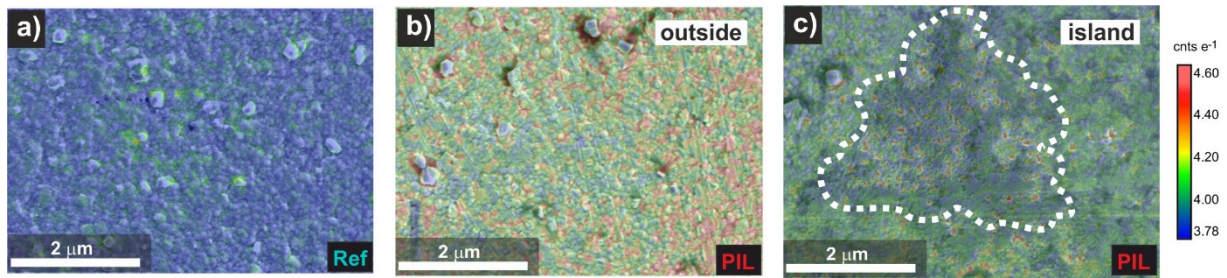


Figure 11.5.6C: Superposition of SEM and CL images of the top surface of a untreated perovskite a), a PIL treated perovskite outside the polymeric islands b) and PIL treated perovskite on a polymeric island. Notably, where the reference samples present a certain degree of correlation between topography and CL emission, in the PIL samples the enhanced luminescence seems to be not correlated with the topography. Particularly, the high luminescence passivated spots are invisible on the bare SEM image.

Additional AFM / C-AFM

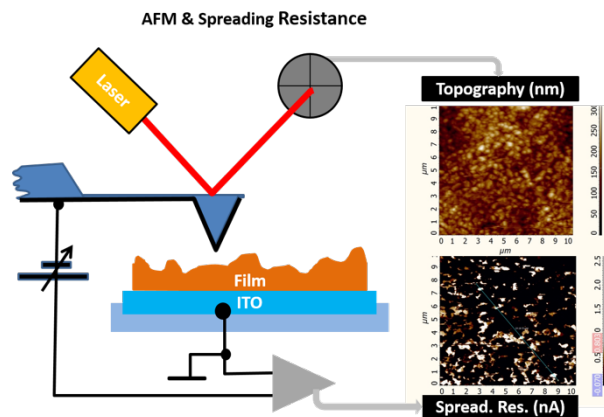


Figure 11.5.7A: Schematic representation of the CAFM setup, where a positive or negative bias is applied to the perovskite substrate in contact with the platinum coated tip.

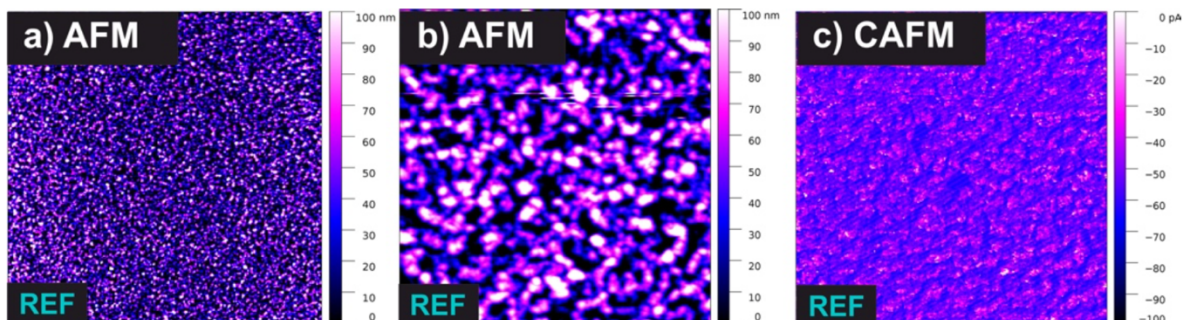


Figure 11.5.7B: AFM and CAFM images of the neat reference perovskite and PIL treated one. In a)-c) the reference sample is presented. We notice that the top surface presents a rather homogeneous topography on large scale a) of 50x50 μm . In b) and c) AFM and CAFM is directly compared (10x10 μm). The CAFM image shows a homogeneous low current response for the whole surface scanned.

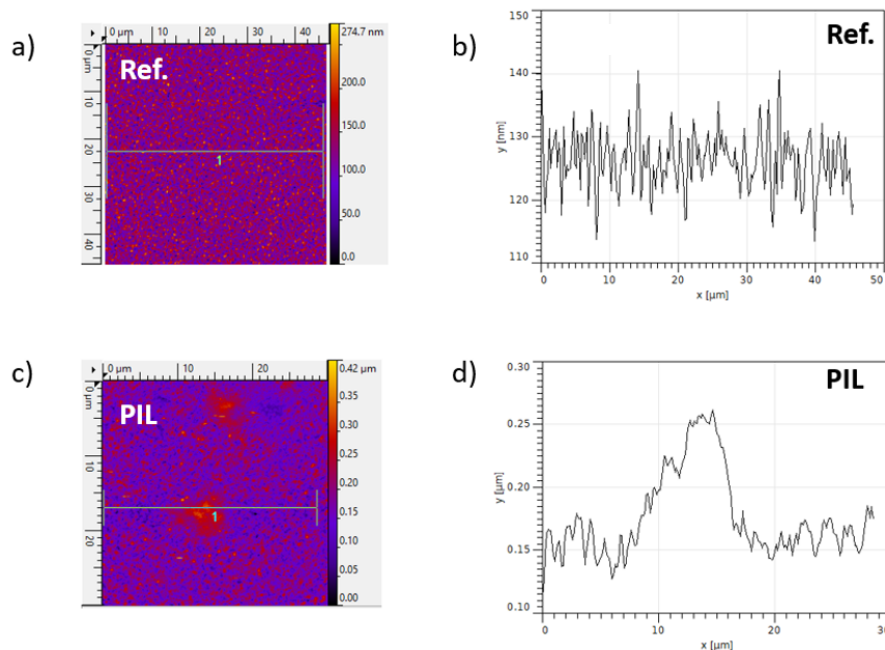
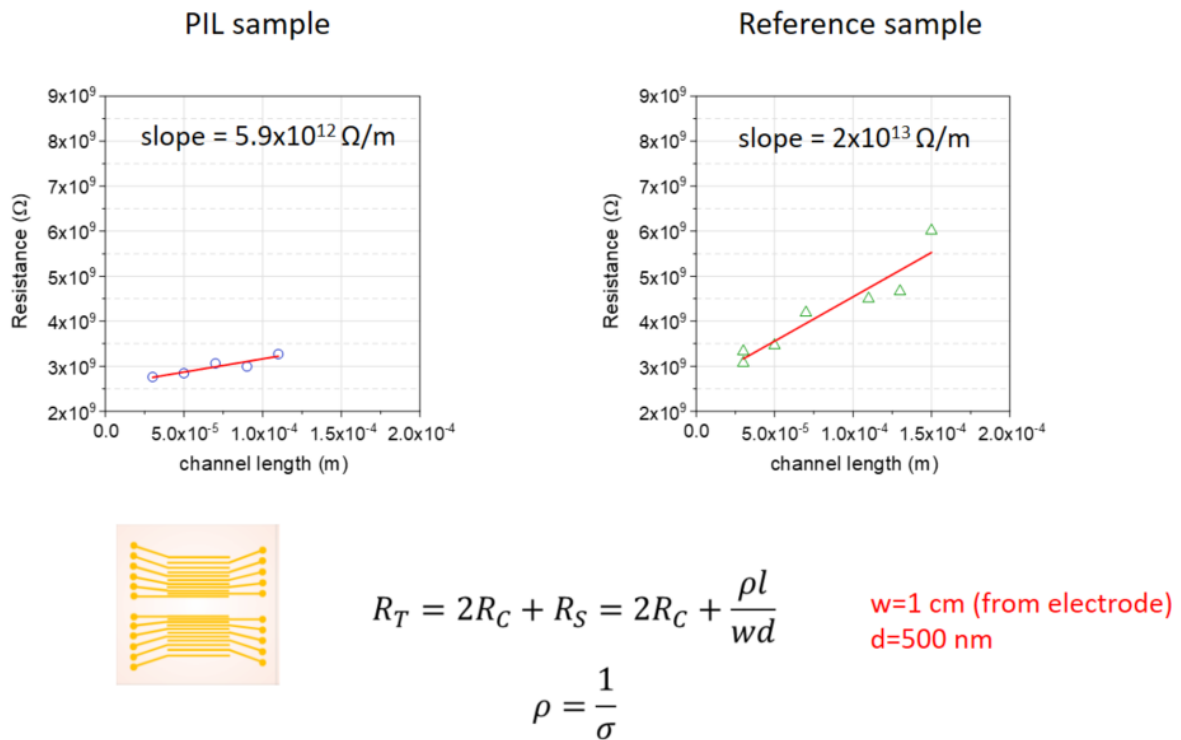


Figure S11.5.7C: Topography AFM images of the neat reference perovskite a) and PIL treated one c) with the respective height line scan b) and d). The line scan shows a rather homogenous surface for the reference samples whereas for the PIL treated one, the top island is roughly 100 nm high.

11.5.8 Conductivity



Sample	Conductivity [S/cm]
PIL	$3.6 \times 10^{-7} \pm 0.8 \times 10^{-7}$
Ref	$1.0 \times 10^{-7} \pm 0.2 \times 10^{-7}$

1

Dark Currents

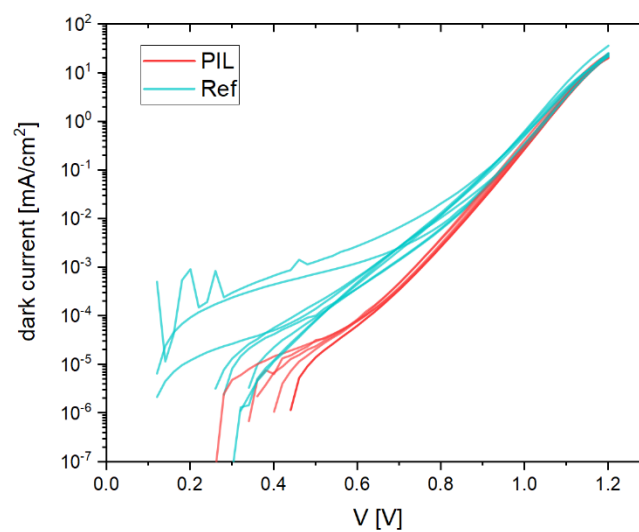


Figure 11.5.9: Dark J-V characteristic of the series of devices with and without PIL treatment. For the PIL treated devices the dark J-V show lower leakage currents in the low voltage range compared to the reference samples, suggesting the presence of a better contact.

Photoelectron Spectroscopy

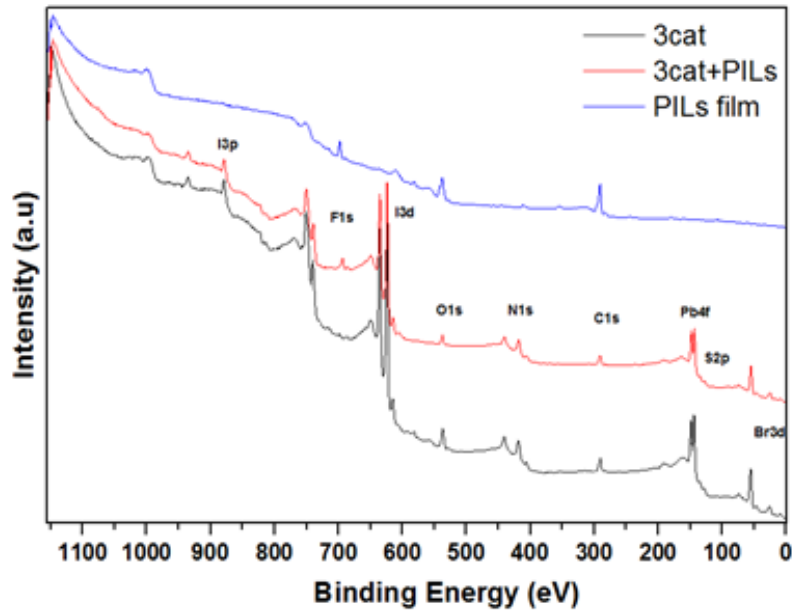


Figure 11.5.10A: XPS survey for 3 cat-perovskite, after [Pelm][TFSI] implementation and [Pelm][TFSI] bare thin film. The scans show the characteristic core levels of the elements present in our halide perovskite: I3p, I3d, N1s, C1s, Pb4f, and Br3d. Additionally, on the PIL treated surface, the emerging peaks at 688 eV and 165 eV corresponds to F1s and S2p, indicating the polymer adhesion on perovskite surface.

Radiative Limit and quasi-Fermi level splitting

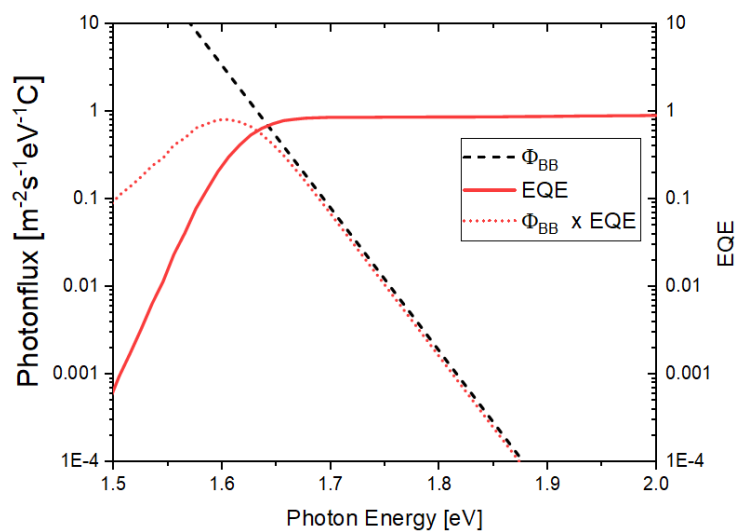


Figure 11.5.11: EQE_{PV} onset of the PIL treated device. The plotted emitted spectral photon flux of the device is calculated when the device is in equilibrium with the black-body (ϕ_{BB}) radiation of the surroundings at 300K.

Additional Optoelectronic Characterization

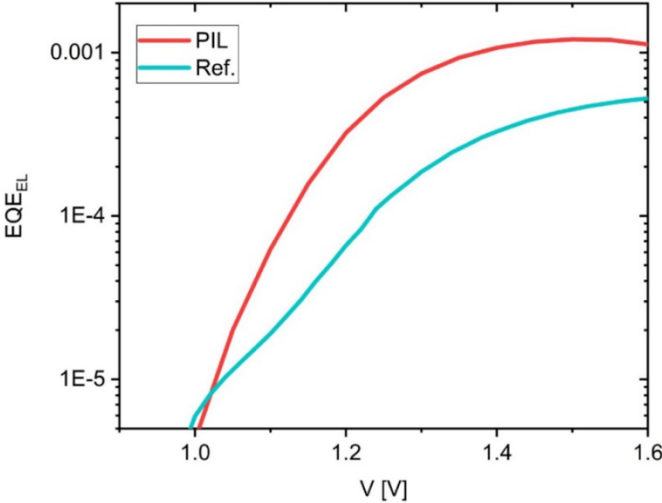


Figure 11.5.12: Electroluminescence quantum yield for reference and PIL treated cells.

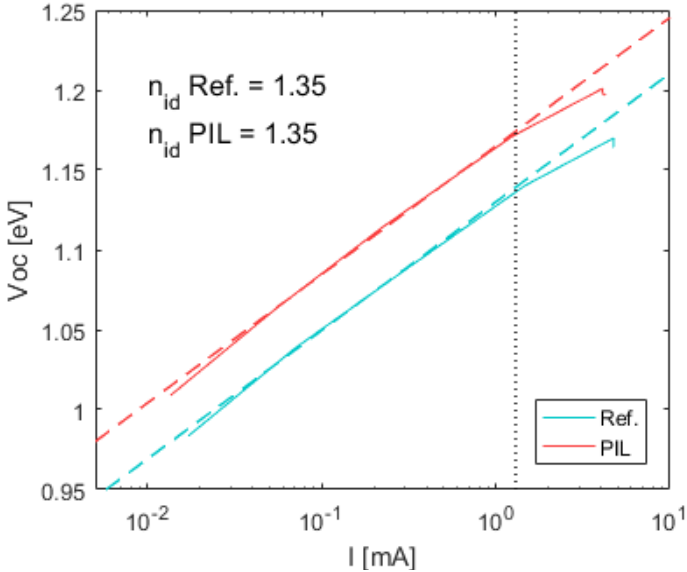


Figure 11.5.13: Ideality factor calculated from the illumination intensity dependence of the V_{OC} .

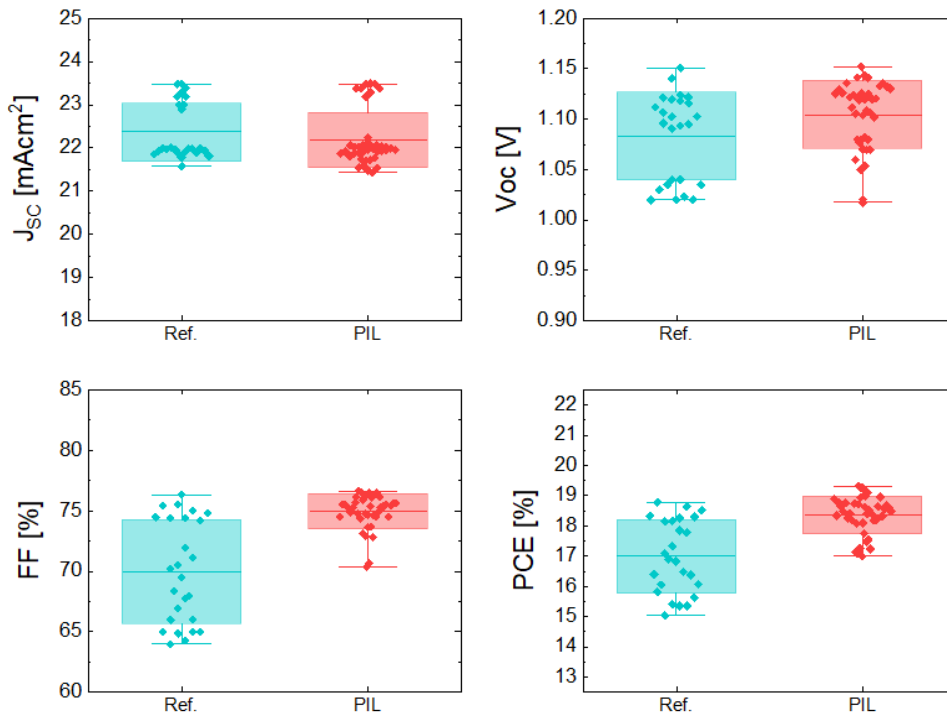


Fig. 11.5.14: Statistic of nip devices comparing reference cells with PIL treated ones. The cells reported in the statistic utilize both mesoporous TiO_2 and planar SnO_2 as ETL. The interface modified with the PIL is in contact with the doped Spiro in both type of cells.

11.6 Appendix 6

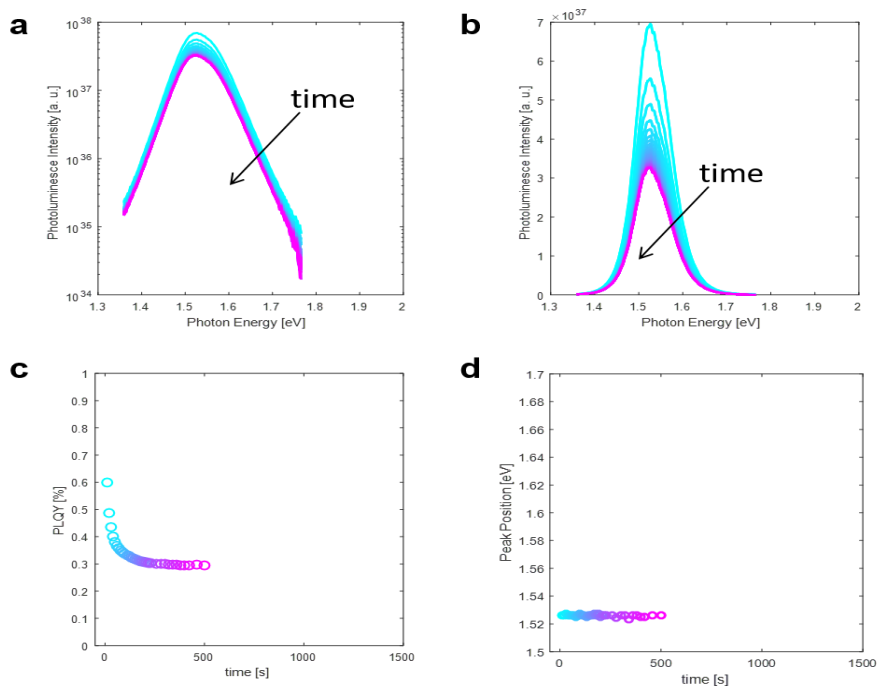


Figure 11.6.1: Time dependent PLQY under constant illumination at 445nm at 3 suns equivalent of intensity for a low Br content sample at. a) and b) PL spectra under constant

illumination. c) Variation of the PLQY over light exposure time. d) Variation of the peak position under the illumination time of the experiment.

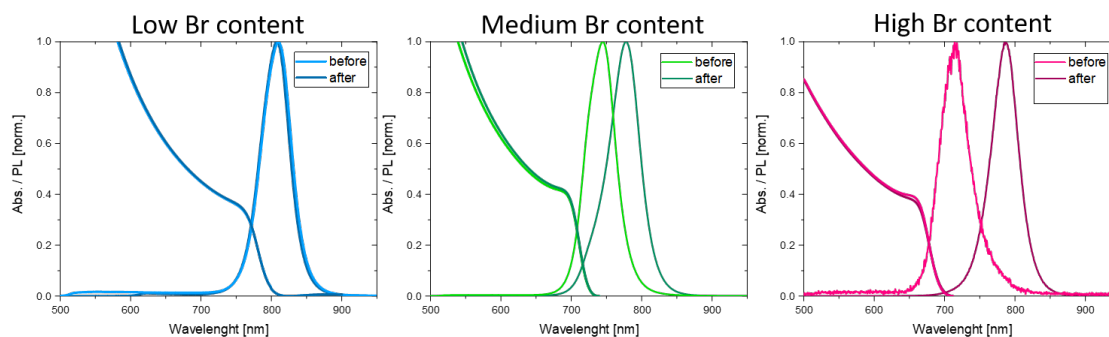


Figure 11.6.2: Relation between UV-VIS-NIR absorption and PL emission before and after phase segregation for a series of samples with different Br content.

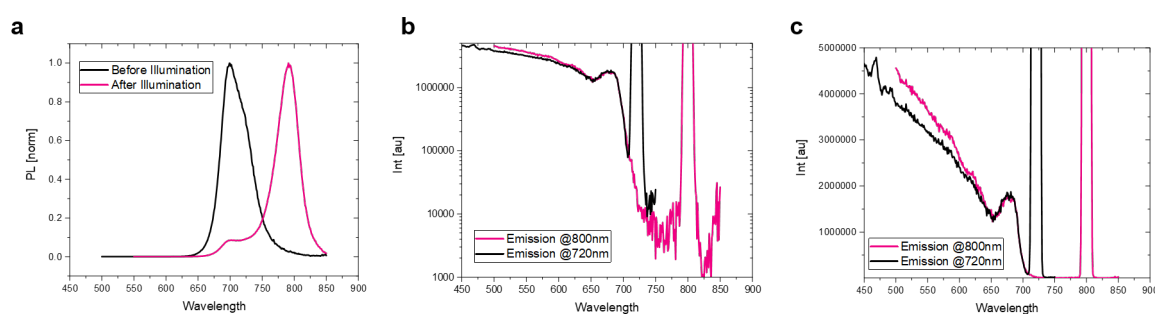


Figure 11.6.3: a) PL before and after phase segregation of a high Br content sample. b) and c) excitation spectra by detecting the emission at 720nm and 800nm after the phase segregation.

The excitation spectra measurement is performed by setting the detector to a specific wavelength and then exciting the samples with a monochromatic light over a wide range of wavelength. As soon as light is absorbed and a PL at the wavelength specified at detector is recorded the intensity of the signal increases. The emission at 720nm follow the bandgap profile, when photons are absorbed and the PL at 720 nm appear the signal increase following the band edge of the material. On the other hand, the emission at 800nm is indeed detected during the measurement scan but the signal increases exclusively when photons are absorbed at roughly 700nm, which is the bandgap of the mixed phase. This is a direct indication that the emission at 800nm is mostly due to absorption of carrier in the high energy domains at 700nm.

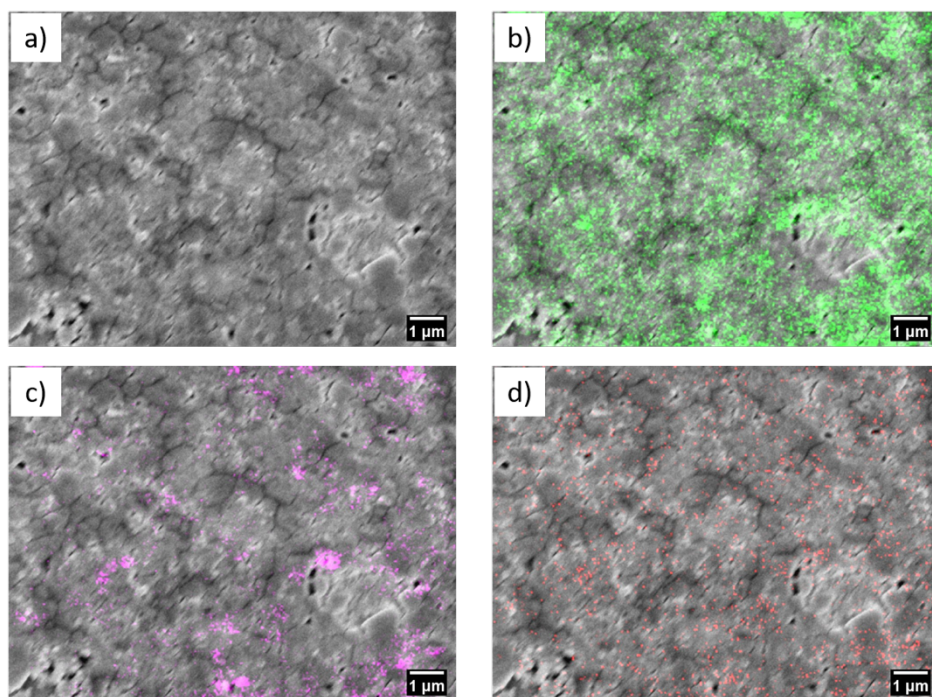


Figure 11.6.4: a) SEM image of the perovskite film with medium Br content after phase separation. The quality of the film surface does not allow the identification of the microstructure. CL distribution maps, superimposed on the SEM image are also shown for luminescence with center wavelengths b) 700 nm, c) 750 nm and d) 800 nm.

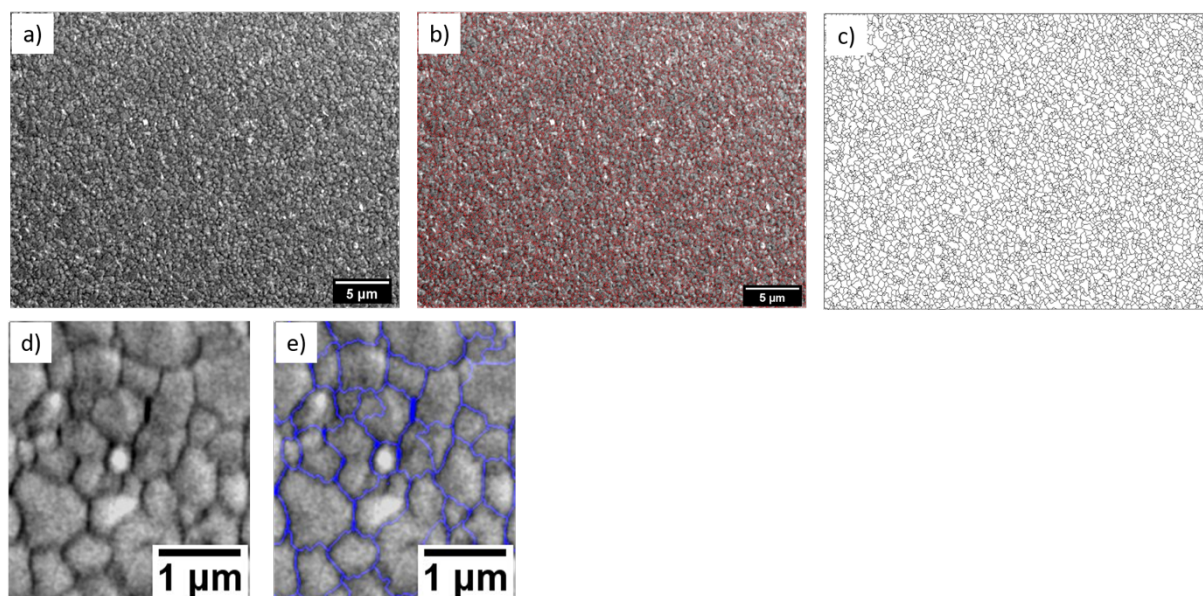


Figure 11.6.5: a) and d) Surface SEM image of the perovskite film with high Br concentration after light-induced phase separation, and b) and e) identification of the approximate microstructure on the SEM image. c) Mask of showing the GBs on the surface

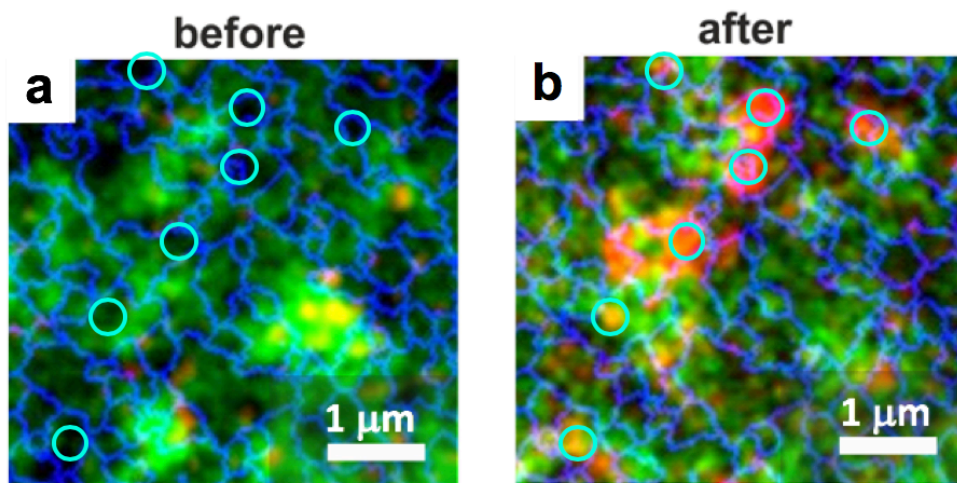


Figure 11.1.6: Comparison of the location of the 800nm emissive spots in CL mapping before and after the segregation of a high Br content sample.

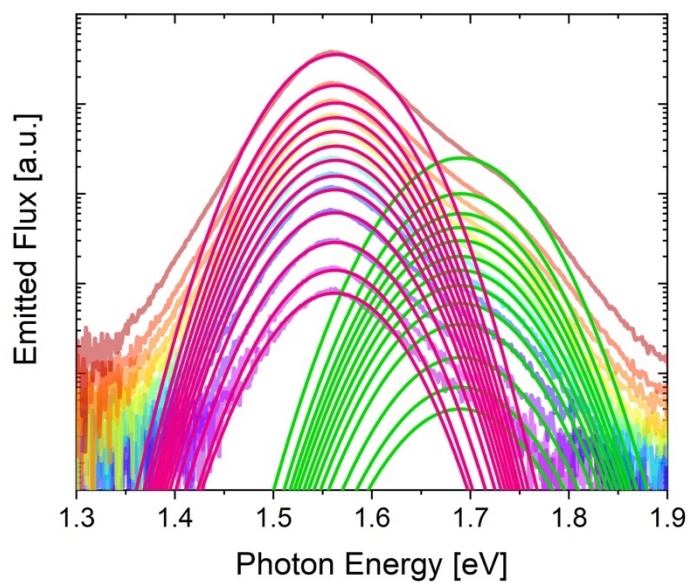


Figure 11.6.7: Gaussian fitting of the two emission components in the intensity dependent PL spectra.

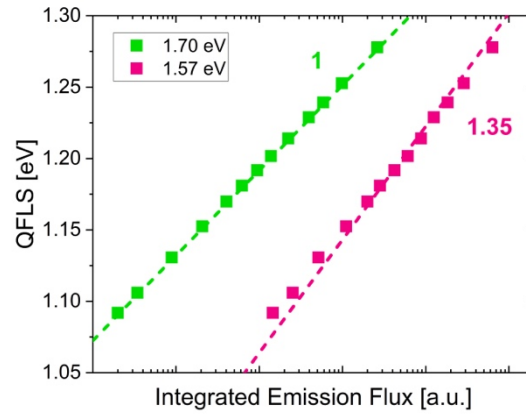


Figure 11.6.8: Radiative ideality factor from QFLS vs. emission flux. Here the QFLS is the one calculated for the large E_G domains, whereas the emission flux is characteristic of the single domains.

11.6.9 Luminance ideality factor

Consider emission from band-to-band and recombination from the recombination of trapped electrons with free holes

Photon flux from band-to-band:

$$\phi_{bb} = edk_2n_en_h \quad \text{Eq.11.6.1}$$

Photon flux from trap to band:

$$\phi_{tb} = edk_7n_7n_h \quad \text{Eq.11.6.2}$$

Here, e is the elementary charge, d is the thickness of the active layer, n_e and n_h is the density of free electrons and holes, respectively, k_2 is the coefficient for radiative band-to-band recombination, k_7 the coefficient for the radiative recombination for a trapped electron with a free hole.

Since

$$n_en_h = n_i^2 e^{\left(\frac{\Delta E_F}{k_B T}\right)} \quad \text{Eq.11.6.3}$$

$$\phi_{bb} = k_2 n_i^2 e^{\left(\frac{\Delta E_F}{k_B T}\right)} \quad \text{Eq.11.6.4}$$

Therefore, the luminance ideality factor of band to band recombination is 1

Now we consider an electron trap. According to fundamental rate considerations, the density of trapped electrons is:

$$n_T = \frac{C_e n_e + \beta_h}{[C_e n_e + \beta_e] + [C_h n_h + \beta_h]} N_T \quad \text{Eq.11.6.5}$$

If we consider a trap near the CB and far away from the VB, detrapping of holes is highly inefficient, so $\beta_h \cong 0$ Then,

$$n_T = \frac{C_e n_e}{[C_e n_e + \beta_e + C_h n_h]} N_T \quad \text{Eq.11.6.6}$$

Also, for a realistic trap depth of 0.4 eV, electron detrapping is slower than trapping, so $C_e n_e \gg \beta_e$. Finally, electron trapping will reduce the density of free electrons, so $n_e < n_h$. Then

$$n_T = \frac{C_e n_e}{C_h n_h} N_T \quad \text{Eq.11.6.7}$$

We simplify this to,

$$n_T = M_T \frac{n_e}{n_h} \quad \text{Eq.11.6.8}$$

where $M_T = \frac{C_e}{C_h} N_T$ is an effective trap density.

In the following, we assume that there are two types of electron traps. One is radiative, and all recombination of trapped electrons with holes goes along with the emission of light. The second is non-radiative with no significant photon emission upon trap-assisted recombination. If these traps are occupied independently:

$$n_{Tr} = \frac{C_{er}}{C_{hr}} N_{Tr} \frac{n_e}{n_h} = M_{Tr} \frac{n_e}{n_h} \quad \text{Eq.11.6.9}$$

And

$$n_{Tnr} = \frac{C_{enr}}{C_{hnr}} N_{Tnr} \frac{n_e}{n_h} = M_{Tnr} \frac{n_e}{n_h} \quad \text{Eq.11.6.10}$$

where the subscript r and nr refers to the trapped electrons density and effective trap density of the respective trap-type.

Since only the radiative trap emits light, the photon flux is

$$\phi_{tb} = edk_r n_{Tr} n_h = edM_{Tr} n_e \quad \text{Eq.11.6.11}$$

Therefore, this photon flux is strictly proportional to the electron density.

We now need to consider the density of free and trapped charges in relation to the QFLS in the high bandgap bulk phase? Here, we consider charge neutrality:

$$n_e + n_{Tr} + n_{Trn} = n_e + n_T = n_h \quad \text{Eq.11.6.12}$$

where $n_T = n_{Tr} + n_{Trn}$ is the total density of trapped electrons. For efficient trapping, $n_e < n_T$. Then, with the above equation for trap occupation:

$$n_T = (M_{Tr} + M_{Trn}) \frac{n_e}{n_h} = (M_T) \frac{n_e}{n_h} = n_h \quad \text{Eq.11.6.13}$$

Here, $M_{Tr} + M_{Trn} = M_T$

Therefore,

$$n_e M_T = n_h^2 = \frac{(n_e n_h)^2}{n_e^2} \quad \text{Eq.11.6.14}$$

$$\Rightarrow n_e^3 = \frac{1}{M_T} (n_e n_h)^2$$

$$\Rightarrow n_e = \left(\frac{1}{M_T} \right)^{\frac{1}{3}} (n_e n_h)^{\frac{2}{3}}$$

$$\Rightarrow n_e = \left(\frac{1}{M_T} \right)^{\frac{1}{3}} (n_i)^{\frac{4}{3}} \exp\left(\frac{2 \Delta E_F}{3 k_B T}\right)$$

Therefore, since

$$\phi_{tb} = edk_r n_{Tr} n_h = edk_r M_{Tr} n_e = edk_r (M_T n_i^2)^{2/3} \exp\left(\frac{\Delta E_F}{1.5 k_B T}\right) \quad \text{Eq.11.6.15}$$

So, the luminance ideality factor for the trap to band recombination is exactly 1.5.

Notably, this results also holds if the non-radiative trap is more efficient in removing electrons from the CB as long as trapping on both types of traps occurs independently. However, the presents of the presence of the non-radiative trap may drastically reduce the free charge density and with that the QFLS at a given illumination intensity and with that the PLQY

Dependence of the photon flux to the incident intensity.

We consider that steady state recombination of electrons is dominated by their rate of trapping. This is justified in case of deep traps, where detrapping is faster than trapping. Therefore, in the electron recombination rate (which is equal to the hole recombination rate) is

$$G = G_e = G_h = R_e = (C_{er}N_{Tr} + C_{enr}N_{Tnr})n_e \quad \text{Eq.11.6.16}$$

This gives:

$$n_e = \frac{G_e}{C_{er}N_{Tr} + C_{enr}N_{Tnr}} \propto G \quad \text{Eq.11.6.17}$$

Given that $\phi_{tb} = edk_r n_{Tr} n_h = edk_r M_{Tr} n_e$

$$\phi_{tb} = edk_r \frac{M_{Tr}}{C_{er}N_{Tr} + C_{enr}N_{Tnr}} G_e \quad \text{Eq.11.6.18}$$

The radiative photon flux is strictly linear in generation rate and illumination intensity.

To determine the photon flux due to band-to-band recombination, we need to know the hole density. With $(M_T) \frac{n_e}{n_h} = n_h$, we arrive at

$$n_h = (M_T)^{\frac{1}{2}} (n_e)^{\frac{1}{2}} = \left(\frac{M_T}{C_{er}N_{Tr} + C_{enr}N_{Tnr}} \right)^{\frac{1}{2}} (G)^{\frac{1}{2}} \quad \text{Eq.11.6.19}$$

And, finally,

$$\begin{aligned} \phi_{bb} &= edk_2 n_e n_h = edk_2 (M_T)^{\frac{1}{2}} (n_e)^{\frac{3}{2}} \\ &= (M_T)^{\frac{1}{2}} \left(\frac{1}{C_{er}N_{Tr} + C_{enr}N_{Tnr}} \right)^{\frac{3}{2}} (G)^{\frac{3}{2}} \end{aligned} \quad \text{Eq.11.6.20}$$

meaning that the photon flux due to band-to-band recombination is proportional to the illumination intensity to the power of 1.5

Finally, with

$$n_e n_h = n_i^2 e^{\left(\frac{\Delta E_F}{k_B T} \right)} \quad \text{Eq.11.6.21}$$

We get

$$e^{\left(\frac{\Delta E_F}{k_B T}\right)} \propto n_e n_h \propto (G)^{\frac{3}{2}} \quad \text{Eq.11.6.22}$$

And

$$J_R = J_G \propto G \propto \left(e^{\left(\frac{\Delta E_F}{k_B T}\right)} \right)^{\frac{2}{3}} = e^{\left(\frac{\Delta E_F}{1.5 k_B T}\right)} \quad \text{Eq.11.6.23}$$

Meaning that the recombination ideality factor is 1.5.

12.

12. Materials and Methods

12.1 Experimental Details Chapter 4

Absolute Photoluminescence Measurements: Excitation for the PL imaging measurements was performed with a 445 nm CW laser (Insaneware) through an optical fibre into an integrating sphere. The intensity of the laser was adjusted to a 1 sun equivalent intensity by illuminating a 1 cm²-size perovskite solar cell under short-circuit and matching the current density to the J_{SC} under the sun simulator (22.0 mA/cm² at 100 mWcm⁻², or 1.375×10^{21} photons m⁻²s⁻¹). A second optical fiber was used from the output of the integrating sphere to an Andor SR393i-B spectrometer equipped with a silicon CCD camera (DU420A-BR-DD, iDus). The system was calibrated by using a calibrated halogen lamp with specified spectral irradiance, which was shone into to integrating sphere. A spectral correction factor was established to match the spectral output of the detector to the calibrated spectral irradiance of the lamp. The spectral photon density was obtained from the corrected detector signal (spectral irradiance) by division through the photon energy (hf), and the photon numbers of the excitation and emission obtained from numerical integration using Matlab. In a last step, three fluorescent test samples with high specified PLQY (~70%) supplied from Hamamatsu Photonics where measured where the specified value could be accurately reproduced within a small relative error of less than 5%. **Measurement conditions:** All films and cells were prepared fresh and immediately encapsulated in a glovebox after preparation with the exception of films and cells with spiro-OMeTAD which require oxygen doping for enabling sufficient transport capability in the device (non-oxygen treated spiro-OMeTAD cells exhibited FFs below 20 % with negligible photovoltaic performance). Thus, films and cells with spiro-OMeTAD were treated in atmosphere overnight at 25% relative humidity, and subsequently encapsulated before the PL measurements. The PL of the samples was readily recorded after mounting the sample after an exposure between 10-20 s to the laser light. Thus, the PLQY is obtained on timescales relevant to the V_{OC} measurements on the cells. We note that all absolute PL measurements were performed on films with the same HTL, ETL and perovskite thicknesses as used in the operational solar cells. The absorption of the samples was considered in the PLQY calculation and was approximately 85% for cells illuminated through the top encapsulation glass, and ~93% through the bottom glass.

Electroluminescence: Absolute EL was measured with a calibrated Si photodetector (Newport) connected to a Keithley 485 pico Ampere meter. The detector (with an active area of ~2 cm²) was placed directly in front of the device (< 0.5 cm) and the total photon flux was evaluated considering the emission spectrum of the solar cell and the external quantum efficiency of the detector (around 86 % in the relevant spectral regime). A slight underestimation of the EQE_{EL} ($\approx 1.25 \times$) cannot be excluded at present as some photons from the solar cells may escaped to the side and were not detected. A forward bias was applied to the cell using a Keithley 2400 source-meter and the injected current was monitored. Measurements were conducted with a home written LabVIEW routine. Typically, the voltage was increased in steps of 20 mV and the current stabilized for

typical 1s at each step. No relevant changes in the EQE_{EL} were observed for different stabilization times.

Device Fabrication: Pre-patterned $2.5 \times 2.5 \text{ cm}^2$ $15 \text{ } \Omega/\text{sq}$. ITO (Automatic Research, Germany), glass or fused silica substrates were cleaned with acetone, 3% Hellmanex solution, DI-water and *iso*-propanol, by sonication for 10min in each solution. After a microwave plasma treatment (4 min., 200W), the samples were transferred to an N_2 -filled glovebox (except PEDOT:PSS which was spincoated in air) where different CTLs were spincoated from solution.

Bottom selective contacts: (HTLs or ETLs): PEDOT:PSS (Heraeus Celivious 4083) was spincoated at 2000 r.p.m for 40s (acceleration 2000 r.p.m/s) and subsequently annealed at $150 \text{ }^\circ\text{C}$ for 15 minutes; P3HT (Sigma Aldrich, Mn~27 000) was spincoated from a 3 mg/mL DCB solution at 3000 r.p.m for 30s (acceleration 3000 r.p.m/s) and subsequently annealed $100 \text{ }^\circ\text{C}$ for 10 minutes. P3HT films were also oxygen plasma treated for 5 s to ensure sufficient wetting of the perovskite as discussed in a previous work.^[171] PolyTPD (Ossila) was spincoated from a 1.5 mg/mL DCB solution at 6000 r.p.m for 30 s (acceleration 2000 r.p.m/s) and subsequently annealed $100 \text{ }^\circ\text{C}$ for 10 minutes. PTAA (Sigma Aldrich) was spincoated was spincoated from a 1.5 mg/mL Toluene solution at 6000 r.p.m for 30 s (acceleration 2000 r.p.m/s) and subsequently annealed $100 \text{ }^\circ\text{C}$ for 10 minutes. For PTAA and PolyTPD coated samples, a $60 \text{ } \mu\text{L}$ solution of PFN-P2 (0.5 mg/mL in methanol) was added onto the spinning substrate at 5000 rpm for 20 s resulting in a film with a thickness below the detection limit of our AFM ($< 5 \text{ nm}$). For compact/mesoporous TiO_2 samples, first a nippon Sheet Glass $10 \text{ } \Omega/\text{sq}$ was cleaned by sonication in 2% Hellmanex water solution for 30 minutes. After rinsing with deionised water and ethanol, the substrates were further cleaned with UV ozone treatment for 15 min. Then, 30 nm TiO_2 compact layer was deposited on FTO via spray pyrolysis at 450°C from a precursor solution of titanium diisopropoxide bis(acetylacetonate) in anhydrous ethanol. After the spraying, the substrates were left at 450°C for 45 min and left to cool down to room temperature. Then, a mesoporous TiO_2 layer was deposited by spin coating for 20 s at 4000 rpm with a ramp of 2000 rpm s⁻¹, using 30 nm particle paste (Dyesol 30 NR-D) diluted in ethanol to achieve 150-200 nm thick layer. After the spin coating, the substrates were immediately dried at 100°C for 10 min and then sintered again at 450°C for 30 min under dry air flow. Before processing the perovskite layer TiO_2 coated films were microwave plasma treatment (4 min., 200W). Compact SnO_2 films were fabricated by using a Tin(IV) oxide nanoparticle dispersion diluted 1:7 vol. with DI-H₂O and filtered through $0.45 \text{ } \mu\text{m}$ PVDF filter prior to spin coating on the substrate at 2000 rpm (acceleration 2000 r.p.m/s) for 30 s. After 20 minutes of annealing at $150 \text{ }^\circ\text{C}$, the spin coating procedure was repeated and the samples were annealed again for 30 more minutes. Before processing the perovskite layer TiO_2 coated films were microwave plasma treatment (4 min., 200W).

Perovskite Layer: The triple cation perovskite solution was prepared by mixing two 1.3 M FAPbI₃ and MAPbBr₃ perovskite solutions in DMF:DMSO (4:1) in a ratio of 83:17 which we call “MAFA” solution. The 1.3 M FAPbI₃ solution was thereby prepared by dissolving FAI (722 mg) and PbI₂ (2130 mg) in 2.8 mL DMF and 0.7 mL DMSO (note there is a 10% excess of PbI₂). The 1.3 M MAPbBr₃ solution was made by dissolving MABr (470 mg) and PbBr₂ (1696 mg) in 2.8 mL DMF and 0.7 mL DMSO (note there is a 10% excess of PbBr₂). Lastly, 40 μL of a 1.2M CsI solution in DMSO (389 mg CsI in 1 mL DMSO) was mixed with 960 μL of the MAFA solution resulting in a final perovskite stoichiometry of (CsPbI₃)_{0.05}[(FAPbI₃)_{0.83}(MAPbBr₃)_{0.17}]_{0.95} in solution. The perovskite film was deposited by spin-coating at 4000 r.p.m (acceleration 1300 rpm/s) for 35 seconds; 10 Seconds after the start of the spinning process, the spinning substrate was washed with 300 μL EA for approximately 1 second (the anti-solvent was placed in the centre of the film). The perovskite film was then annealed at 100 °C for 1 hr on a preheated hotplate.

Top selective contacts: (HTLs or ETLs): SpiroOMeDAT was spincoated from a *spiro-OMeTAD* (Merck) solution in chlorobenzene (70 mM) at 4000 rpm for 20 s (acceleration 4000 rpm/s). Spiro-OMeTAD was doped with bis(trifluoromethylsulfonyl)imide lithium salt (Li-TFSI, Sigma-Aldrich), tris(2-(1H-pyrazol-1-yl)-4-tert-butylpyridine)-cobalt(III) tris(bis(trifluoromethylsulfonyl)imide) (FK209, Dynamo) and 4-tert-Butylpyridine (tBP, Sigma-Aldrich). The molar ratio of additives for spiro-OMeTAD was: 0.5, 0.03 and 3.3 for Li-TFSI, FK209 and tBP respectively. PC₆₁BM (Solenne BV) was spincoated from a 30 mg/mL DCB solution at 6000 rpm (acceleration 2000 r.p.m/s) for 30 s and the resulting Perovskite/PCBM film further annealed at 100 °C for 30 minutes. For C₆₀ (Creaphys) and LiF ETLs, the perovskite films were transferred to an evaporation chamber where 30 nm of C₆₀ (1 nm of LiF) were deposited at 0.1 Å/s (0.03 Å/s) under vacuum ($p = 10^{-7}$ mbar).

Metal contacts: *pin*-type devices were completed by transferring the samples to an evaporation chamber where 8 nm BCP (Sigma-Aldrich) at 0.2 Å/s and 100 nm copper (Sigma-Aldrich) at 0.6 Å/s were deposited under vacuum ($p = 10^{-7}$ mbar). *nip*-type devices were completed by transferring the samples to an evaporation chamber where 100 nm gold (0.7 Å/s) were deposited under vacuum ($p = 10^{-7}$ mbar). *nip*-cells were oxygen doped overnight at 20% relative humidity prior to device and PL measurements.

Current density-voltage characteristics: *JV*-curves were obtained in a 2-wire source-sense configuration with a Keithley 2400. An Oriel class AAA Xenon lamp-based sun simulator was used for illumination providing approximately 100 mW cm⁻² of AM1.5G irradiation and the intensity was monitored simultaneously with a Si photodiode. The exact illumination intensity was used for efficiency calculations, and the simulator was calibrated with a KG5 filtered silicon solar cell (certified by Fraunhofer ISE). The temperature of the cell was fixed to 25 °C and a voltage ramp of

67 mV/s was used. A spectral mismatch calculation was performed based on the spectral irradiance of the solar simulator, the EQE of the reference silicon solar cell and 3 typical EQEs of our cells. This resulted in 3 mismatch factors of $M = 0.9949$, 0.9996 and 0.9976 . Given the very small deviation from unity the measured J_{SC} was not corrected by the factor $1/M$. All EQEs presented in this work were measured by ISE-Fraunhofer.

Scanning Electron Spectroscopy: SEM images were acquired with a Zeiss Ultra Plus SEM.

Photoemission Spectroscopy Measurements: Photoemission experiments were performed at an ultrahigh vacuum (UHV) system consisting of sample preparation and analysis chambers (both at base pressure: 1×10^{-10} mbar) as well as a load lock (base pressure: 1×10^{-6} mbar). All of the samples were transferred to the UHV chamber using a transfer rod under rough vacuum (1×10^{-3} mbar). Ultraviolet photoemission spectroscopy (UPS) was performed using a helium discharge lamp (21.22 eV) with a filter to reduce the photoflux and to block visible light from the source hitting the sample. All spectra were recorded at room temperature and normal emission using a hemispherical Specs Phoibos 100 analyzer, and the overall energy resolution was 140 meV.

Transient Photocurrent (TPC)/Photovoltage (TPV) and differential charging: Photovoltage transients were recorded with an oscilloscope (Agilent 81150A) at different external load resistance (R_{Load}) of $1 \text{ M}\Omega$ (TPV) and $50 \text{ }\Omega$ (transient photocurrent). A constant background illumination was provided by a white LED which was continuously increased ranging from 10^{-3} equivalent suns to approximately 3 suns. Each measured data point corresponds to a different illumination intensity. A Q-switched neodymium-doped yttrium aluminium garnet (Nd:YAG) laser (NT242, EKSPLA)) with a pulse length of 5 ns, a repetition rate of 10 Hz and excitation wavelength of 532 nm was used to generate the charge carriers, while neutral optical density (OD) filters were used to attenuate the power output. The laser fluence was kept low to ensure a small perturbation on top of the constant background current (generating a maximum voltage deflection of 20 mV at $1 \text{ M}\Omega$ without background illumination). In order to obtain the carrier lifetime (τ) from TPV, the photovoltage was fitted with a mono-exponential decay at each laser fluence. τ plotted versus the obtained V_{OC} at the given intensity. At low intensities, the effects of external circuit are visible with an RC -time of ~ 1 ms. The differential capacitance was obtained by integrating the TPV signals to obtain ΔQ , while the ΔV was obtained from the maximum photovoltage of the TPV transients at each intensity. The differential capacitance is obtained from $C_{DC} = \Delta Q / \Delta V$ and plotted versus the V_{OC} . The geometrical capacitance (C_{geo}) is visible at low intensities or V_{OC} s and accumulated charge in the active layer at higher V_{OC} s. The accumulated charge carrier density in the bulk is obtained by

integrating $n_{\text{bulk}} = \frac{1}{eAd} \int_0^V (C_{\text{DC}} - C_{\text{geo}}) dV$ and also plotted versus the V_{OC} at each intensity.

12.2 Experimental Details Chapter 5

Device Preparation: Patterned indium-doped tin oxide (ITO, Lumtec, 15 ohm sqr^{-1}) was washed with acetone, Hellmanex III, DI-water and isopropanol. After microwave plasma treatment (3 min at 200 W) poly[bis(4-phenyl)(2,4,6-trimethylphenyl)amine] (PTAA, Sigma-Aldrich, Mn = 7000–10000, PDI = 2–2.2) in a concentration of 1,5 mg/ml was spin-coated at 6000 rpm for 30 seconds and immediately annealed for 10 minutes at 100° C. After that, a 60 μL solution of PFN-P2 (0.5 mg/mL in methanol) was added onto the spinning substrate at 5000 rpm for 20 s resulting in a film with a thickness below the detection limit of our AFM (< 5 nm). In the case of P3HT as HTL: (Sigma Aldrich, Mn~27 000) was spincoated from a 3 mg/mL DCB solution at 3000 r.p.m for 30s (acceleration 3000 r.p.m/s) and subsequently annealed 100 °C for 10 minutes. P3HT films were also oxygen plasma treated for 5 s to ensure sufficient wetting of the perovskite as discussed in a previous work.^[171] When thicker HTL's has been prepared we used PTAA and P3HT solution with higher concentration, 10mg/ml and 15mg/ml respectively, and spincoated at slower rpm, 1500rpm. The perovskite layer was formed by spin coating a DMF:DMSO solution (4 :1 volume) at 4500 rpm for 35 seconds. After 10 seconds of spin coating, 500 mL of diethyl ether (antisolvent) was dripped on top of the spinning substrate. After spin coating samples were annealed at 100° C for 1 h. Afterwards, samples were transferred to an evaporation chamber and C_{60} (30 nm), BCP (8 nm) and copper (100 nm) were deposited under vacuum ($p = 10^{-7}$ mbar). The active area was 6 mm^2 defined as the overlap of ITO and the top electrode.

Current Density–Voltage Characteristics and EQE_{PV} : J-V curves were measured under N_2 on a Keithley 2400 system in a 2-wire configuration with a scan speed of 0.1V/s and voltage step of 0.02V. One sun illumination at approximately 100 mWcm^{-2} of AM1.5G irradiation was provided by a Oriel class ABA sun simulator. The real illumination intensity was monitored during the measurement using a Si photodiode and the exact illumination intensity was used for efficiency calculations. The sun simulator was calibrated with a KG5 filtered silicon solar cell (certified by Fraunhofer ISE). The AM1.5G short-circuit current of devices matched the integrated product of the EQE spectrum within 5-10% error. The latter was recorded using a home build set-up utilizing a Philips Projection Lamp (Type7724 12 V 100 W) in front of a monochromator (Oriel Cornerstone 74100) and the light was mechanically chopped at 70 Hz. The photo-generated current was measured using a lock-in-amplifier (EG&G Princeton Applied Research Model 5302, integration times 300 ms) and evaluated after calibrating the lamp spectrum with an UV-enhanced Si photodetector (calibrated at Newport).

Absolute Photoluminescence: Excitation for the PL measurements was performed with a 445 nm CW laser (Insaneware) through an optical fibre into an integrating sphere. The intensity of the laser was adjusted to a 1 sun equivalent intensity by illuminating a 1 cm²-size perovskite solar cell under short-circuit and matching the current density to the J_{SC} under the sun simulator (22.0 mA/cm² at 100 mWcm⁻², or 1.375x10²¹ photons m⁻²s⁻¹). A second optical fiber was used from the output of the integrating sphere to an Andor SR393i-B spectrometer equipped with a silicon CCD camera (DU420A-BR-DD, iDus). The system was calibrated by using a calibrated halogen lamp with specified spectral irradiance, which was shone into to integrating sphere. A spectral correction factor was established to match the spectral output of the detector to the calibrated spectral irradiance of the lamp. The spectral photon density was obtained from the corrected detector signal (spectral irradiance) by division through the photon energy (hf), and the photon numbers of the excitation and emission obtained from numerical integration using Matlab. In a last step, three fluorescent test samples with high specified PLQY (~70%) supplied from Hamamatsu Photonics were measured where the specified value could be accurately reproduced within a small relative error of less than 5%. **Measurement conditions:** All PL measurements have been performed on complete cells, prepared fresh and immediately encapsulated in a glovebox under N₂ atmosphere. The PL of the samples was readily recorded after mounting the sample and after an exposure of 1 s at each laser intensity, after that the incident laser was blocked by a shutter and the next intensity adjusted while the sample was kept in dark conditions avoiding any effects induced by constant illumination. The cell was illuminated from the bottom glass, on the glass/ITO side. We note that all absolute PL measurements were performed on films with the same HTL, ETL and perovskite thicknesses as used in the operational solar cells.

Intensity dependent V_{OC} : Intensity dependent V_{OC} measurements were performed illuminating the respective solar cell exactly at the same illumination condition and exposure time (1 s) as during the PL measurements in order to have the same experimental condition for the two measurements. After each measurement the incident light was blocked with a shutter and the next light intensity adjusted. The corresponding V_{OC} was monitored with Keithley 2400 system in a 2-wire configuration.

12.3 Experimental Details Chapter 6

Device Preparation: Patterned indium-doped tin oxide (ITO, Lumtec, 15 ohm sqr.⁻¹) was washed with acetone, Hellmanex III, DI-water and isopropanol. After microwave plasma treatment (3 min at 200 W) poly[bis(4-phenyl)(2,4,6-trimethylphenyl)amine] (PTAA, Sigma-Aldrich, Mn = 7000–10000, PDI = 2–2.2) in a concentration of 1,5 mg/ml was spin-coated at 6000 rpm for 30 seconds and immediately annealed for 10 minutes at 100° C. After that, a 60 µL solution of PFN-P2 (0.5 mg/mL in methanol) was added

onto the spinning substrate at 5000 rpm for 20 s resulting in a film with a thickness below the detection limit of our AFM (< 5 nm). In the case of PEDOT:PSS as HTL: (Heraeus Celvius 4083) was spincoated at 2000 r.p.m for 40s (acceleration 2000 r.p.m/s) and subsequently annealed at 150 °C for 15 minutes. The perovskite layer was formed by spin coating a DMF:DMSO solution (4 :1 volume) at 4500 rpm for 35 seconds. After 10 seconds of spin coating, 500 mL of diethyl ether (antisolvent) was dripped on top of the spinning substrate. After spin coating samples were annealed at 100° C for 1 h. Afterwards, samples were transferred to an evaporation chamber and C₆₀ (30 nm), BCP (8 nm) and copper (100 nm) were deposited under vacuum ($p = 10^{-7}$ mbar). The active area was 6 mm² defined as the overlap of ITO and the top electrode.

Current Density–Voltage Characteristics and EQE_{PV}: J-V curves were measured under N₂ on a Keithley 2400 system in a 2-wire configuration with a scan speed of 0.1V/s and voltage step of 0.02V. One sun illumination at approximately 100mWcm⁻² of AM1.5G irradiation was provided by a Oriel class ABA sun simulator. The real illumination intensity was monitored during the measurement using a Si photodiode and the exact illumination intensity was used for efficiency calculations. The sun simulator was calibrated with a KG5 filtered silicon solar cell (certified by Fraunhofer ISE). The AM1.5G short-circuit current of devices matched the integrated product of the EQE spectrum within 5-10% error. The latter was recorded using a home build set-up utilizing a Philips Projection Lamp (Type7724 12 V 100 W) in front of a monochromator (Oriel Cornerstone 74100) and the light was mechanically chopped at 70 Hz. The photo-generated current was measured using a lock-in-amplifier (EG&G Princeton Applied Research Model 5302, integration times 300 ms) and evaluated after calibrating the lamp spectrum with an UV-enhanced Si photodetector (calibrated at Newport).

Absolute Photoluminescence: Excitation for the PL measurements was performed with a 445 nm CW laser (Insaneware) through an optical fibre into an integrating sphere. The intensity of the laser was adjusted to a 1 sun equivalent intensity by illuminating a 1 cm²-size perovskite solar cell under short-circuit and matching the current density to the J_{SC} under the sun simulator (22.0 mA/cm² at 100 mWcm⁻², or 1.375x10²¹ photons m⁻²s⁻¹). A second optical fiber was used from the output of the integrating sphere to an Andor SR393i-B spectrometer equipped with a silicon CCD camera (DU420A-BR-DD, iDus). The system was calibrated by using a calibrated halogen lamp with specified spectral irradiance, which was shone into to integrating sphere. A spectral correction factor was established to match the spectral output of the detector to the calibrated spectral irradiance of the lamp. The spectral photon density was obtained from the corrected detector signal (spectral irradiance) by division through the photon energy (hf), and the photon numbers of the excitation and emission obtained from numerical integration using Matlab. In a last step, three fluorescent test samples with high specified PLQY (~70%) supplied from Hamamatsu Photonics where

measured where the specified value could be accurately reproduced within a small relative error of less than 5%. **Measurement conditions:** All PL measurements have been performed on complete cells, prepared fresh and immediately encapsulated in a glovebox under N₂ atmosphere. The PL of the samples was readily recorded after mounting the sample and after an exposure of 1 s at each laser intensity, after that the incident laser was blocked by a shutter and the next intensity adjusted while the sample was kept in dark conditions avoiding any effects induced by constant illumination. The cell was illuminated from the bottom glass, on the glass/ITO side. We note that all absolute PL measurements were performed on films with the same HTL, ETL and perovskite thicknesses as used in the operational solar cells.

Intensity dependent V_{OC} : Intensity dependent V_{OC} measurements were performed illuminating the respective solar cell at exactly the same illumination condition and exposure time (1 s) as during the PL measurements in order to have the same experimental condition for the two measurements. To this end a mechanical shutter was used to illuminate the sample for 1 second for each given intensity. The corresponding V_{OC} was monitored with Keithley 2400 system in a 2-wire configuration.

12.4 Experimental Details Chapter 7

Device Preparation

Patterned indium-doped tin oxide (ITO, Lumtec, 15 ohm sq.⁻¹) was washed with acetone, Hellmanex III, DI-water and isopropanol. After microwave plasma treatment (3 min at 200 W) poly[bis(4-phenyl)(2,4,6-trimethylphenyl)amine] (PTAA, Sigma-Aldrich, Mn = 7000–10000, PDI = 2–2.2) in a concentration of 1,5 mg/ml was spin-coated at 6000 rpm for 30 seconds and immediately annealed for 10 minutes at 100° C. The perovskite layer was formed by spin coating a DMF:DMSO solution (4 :1 volume) at 4500 rpm for 35 seconds. After 10 seconds of spin coating, 500 mL of diethyl ether (antisolvent) was dripped on top of the spinning substrate. After spin coating samples were annealed at 100° C for 1 h. Afterwards, samples were transferred to an evaporation chamber and C₆₀ (30 nm), BCP (8 nm) and copper (100 nm) were deposited under vacuum ($p = 10^{-7}$ mbar). The active area was 6 mm² defined as the overlap of ITO and the top electrode.

Current Density–Voltage Characteristics and EQE_{PV}

J-V curves were measured under N₂ on a Keithley 2400 system in a 2-wire configuration with a scan speed of 0.1V/s and voltage step of 0.02V. One sun illumination at approximately 100mWcm⁻² of AM1.5G irradiation was provided by a Oriel class ABA sun simulator. The real illumination intensity was monitored during the measurement using a Si photodiode and the exact illumination intensity was used for efficiency calculations. The sun simulator was calibrated with a KG5 filtered silicon

solar cell (certified by Fraunhofer ISE). The AM1.5G short-circuit current of devices matched the integrated product of the EQE spectrum within 5-10% error. The latter was recorded using a home build set-up utilizing a Philips Projection Lamp (Type7724 12 V 100 W) in front of a monochromator (Oriel Cornerstone 74100) and the light was mechanically chopped at 70 Hz. The photo-generated current was measured using a lock-in-amplifier (EG&G Princeton Applied Research Model 5302, integration times 300 ms) and evaluated after calibrating the lamp spectrum with an UV-enhanced Si photodetector (calibrated at Newport).

Photoluminescence and Electroluminescence

Time-resolved PL data was acquired with a TCSPC system (Berger & Lahr) after excitation with a pulse-picked and frequency-doubled output from a mode-locked Ti:sapphire oscillator (Coherent Chameleon) with nominal pulse durations ~ 100 fs and fluence of ~ 30 nJ/cm² at a wavelength of 470 nm. Hyperspectral Absolute Photoluminescence Imaging was performed by excitation with two 450 nm LEDs equipped with diffuser lenses. The intensity of the LEDs was adjusted to ~ 1 sun by illuminating a contacted perovskite solar cell (short circuit) and matching the current density to the short circuit current measured in the JV sun simulator (The measured short circuit current density of the solar cell under this illumination was 22.2 mA/cm²). The photoluminescence image detection was performed with a CCD camera (Allied Vision) coupled with a liquid crystal tuneable filter. The system was calibrated to absolute photon numbers in two steps in a similar way to the process described by Delemare et al.^[297] For this purpose an IR laser diode and a spectrally calibrated halogen lamp was coupled to an integrating sphere. The pixel resolution of the images corresponds to about 10 μ m in diameter. Sets of images from 650 nm to 1100 nm with 5 nm step size were recorded. All absolute PL measurements were performed on films with the same thicknesses as used in the operational solar cells. The EL spectra were acquired using an Andor SR393i-B spectrometer equipped with a silicon detector DU420A-BR-DD (iDus). The response of this setup was measured with a calibrated lamp (Oriel 63355). The cells were kept under forward bias with a Keithley 2400 at an applied current $J_{inj} \approx J_{SC}$, stabilized for 20 seconds before recording a spectrum. Absolute EL was measured with a calibrated Si photodetector (Newport) attached to a Keithley 485 pA meter. The photodetector was placed directly in front of the device pixel, then a forward bias was applied with a Keithley 2400 source-meter and the resulting photon flux was calculated considering the EL spectrum of the solar cell and the spectral response of the Si photodiode. Injected current and photodetector response were monitored with a home written LebVIEW routine varying the voltage and stabilising for 20 seconds after every voltage step (dV typically 0.02V).

Morphological Characterization

SIMS measurements were performed using a Cameca IMS4f instrument, using O²⁺ and Cs⁺ as primary sputtering ions within an energy range of 5-15 keV. The scanned area on the sample surface was 250x250 μ m². SEM images were acquired with a Zeiss

Ultra Plus SEM. Images has been acquired through the use of Secondary Electron in-lens detector. The structural characterization was performed with a PANalytical X'Pert MPD Pro X-ray diffractometer in Bragg-Brentano configuration using a Cu K- α radiation source ($\lambda=0.15406$ nm) with a step size of 0.013° . The measurements were performed in N₂ atmosphere.

Photoemission and Inverse Photoemission Spectroscopy Measurements:

Photoemission experiments were performed at an UHV system consisting of sample preparation and analysis chambers (both at base pressure of 1×10^{-10} mbar), as well as a load-lock (base pressure of 1×10^{-6} mbar). All the samples were transferred to the UHV chamber using a transfer rod under rough vacuum (1×10^{-3} mbar). UPS was performed using helium discharge lamp (21.22 eV) with a filter to reduce the photo flux and to block visible light from the source to hit the sample. XPS was performed using Al K α radiation (1486.7 eV) generated from a twin anode X-ray source. All spectra were recorded at room temperature and normal emission using a hemispherical SPECSPhoibos 100 analyzer. All perovskite layers were deposited on a ITO / PTAA stack in order to be as much close as possible to real device conditions. The resolution and energy calibration of the PES and IPES were determined by measuring the Fermi edge of a clean Au (111) single crystal. The overall energy resolution was 140 meV and 1.2 eV for UPS and XPS, respectively. The IPES measurements were performed in the isochromat mode using a low-energy electron gun with a BaO cathode and a band pass filter of 9.5 eV (SrF₂ + NaCl). All presented PES and IPES spectra are given in binding energy (BE) referenced to the Fermi level. The overall energy resolution for IPES was 0.74 eV. The UPS spectra of thin films under consecutive on-off illumination circles were conducted using a white halogen lamp at 150 mW/cm^2 (daylight rendering spectrum). The same experimental conditions and setup presented in the work of Zu et al. [238] has been used for our set of measurements. C60 molecules were purchased from *Novaled*, and were used as received and thermally evaporated from resistively heated quartz crucibles. The nominal deposited thickness was monitored by a quartz crystal microbalance.

12.5 Experimental Details Chapter 8

pin Device Preparation: Patterned indium-doped tin oxide (ITO, Lumtec, 15 ohm sq. ⁻¹) was washed with acetone, Hellmanex III, DI-water and isopropanol. After microwave plasma treatment (3 min at 200 W) poly[bis(4-phenyl)(2,4,6-trimethylphenyl)amine] (PTAA, Sigma-Aldrich, Mn = 7000–10000, PDI = 2–2.2) in a concentration of 1,5 mg/ml was spin-coated at 6000 rpm for 30 seconds and immediately annealed for 10 minutes at 100° C. The PTAA was additionally treated by dynamically spin coating a diluted solution (0.5mg/mL in Methanol) of poly[(9,9-bis(30- ((N,N-dimethyl)-N-ethylammonium)-propyl)-2,7-fluorene)- alt-2,7-(9,9-dioctylfluorene)] dibromide (PFN-P2). The perovskite layer was formed by spin coating a DMF:DMSO solution (4 :1

volume) at 4500 rpm for 35 seconds. After 10 seconds of spin coating, 300 mL of Ethylacetate (antisolvent) was dripped on top of the spinning substrate. The perovskite is annealed for 2 minutes at 100°. The PIL is then spincoated on the perovskite, by spin coating a highly diluted solution (0.5 mg/ml in acetonitrile:isopropanol (1:4)). Specifically, 70 μ l are spincoated at 6000 rpm (3 s acceleration step) for 35 s. After deposition of the PIL the samples were annealed at 100° C for 1 h. Afterwards, samples were transferred to an evaporation chamber and C₆₀ (30 nm), BCP (8 nm) and copper (100 nm) were deposited under vacuum ($p = 10^{-7}$ mbar). The active area was 6 mm² defined as the overlap of ITO and the top electrode.

nip Device Preparation: EPFL: FTO-coated glass (Nippon sheet glass) was chemically etched with zinc powder and HCl solution, followed by sonically cleaning using Hellmanex, water, acetone, and 2-propanol. A 30 nm thick compact TiO₂ layer was deposited by spray pyrolysis of a titanium diisopropoxide bis(acetylacetonate) solution (Sigma-Aldrich) diluted in 2-propanol (1:15 v/v) at 450 °C. A 100 nm thick mesoporous TiO₂ layer was spin coated from a solution of TiO₂ paste (GreatCellSolar, 30NR-D) in ethanol (1:8 w/v) at 5000 rpm for 20 s followed by heating at 125 °C for 10 min and sintering at 500 °C for 20 min. A thin layer of passivating tin oxide of \approx 20 nm was spin-coated by using tin (IV) chloride (Acros) solution (12 μ L diluted in 988 μ L water) at 3000 rpm for 30 s, followed by annealing at 100 °C for 10 min and 190 °C for 1 h. The prepared substrates were treated with UV-ozone for 15 min before perovskite deposition. A 1.3M [(FAPbI₃)_{0.87}(MAPbBr₃)_{0.13}]_{0.92}(CsPbI₃)_{0.08} perovskite solution with excess PbI₂ (PbI₂:FAI = 1.05:1) was prepared by mixing FAI (GreatCellSolar), MABr (GreatCellSolar), CsI (ABCR), PbI₂ (TCI), and PbBr₂ (TCI) in DMF and DMSO (0.78:0.22 v/v). The prepared perovskite precursor was then spin-coated on the prepared at 2000 rpm for 12 s and 5000 rpm for 30 s. Chlorobenzene was added as an anti-solvent at 15 s before the end of spin coating process. The perovskite film was heated for 1h. After cooling down to the room temperature, the PIL layer was deposited on top of the perovskite layer at 6000 rpm for 30s, then the film was subsequently annealed at 100 °C for 60 min. Spiro OMeTAD was used as the hole-transporting materials (HTM). The HTM layer was prepared by dissolving 78.2 mg spiro-OMeTAD (Borun Chemical) in 1 mL chlorobenzene doped with 31.28 μ L of 4-tert-butylpyridine (Sigma-Aldrich), 18.57 μ L of Li-bis (trifluoromethanesulphonyl) imide (Aldrich) from the stock solution (196 mg in 379 μ L acetonitrile), 13.69 μ L of FK 209 Co(III) TFSI (GreatCellSolar) from the stock solution (99 mg in 263 μ L acetonitrile). The doped spiro-OMeTAD solution was then deposited by spin-coating at 4000 rpm for 30 s. Finally, a 70 nm-thick gold counter electrode was thermally evaporated on top of HTM layer.

HZB: Planar *n-i-p* type perovskite solar cells were prepared as a layer stack of glass/ITO/SnO₂/Cs_{0.05}((CH(NH₂)₂)_{0.83}(CH₃NH₃)_{0.17})_{0.95}Pb(I_{0.83}Br_{0.17})₃/HTM/Au. Patterned ITO coated glass substrates ($R = 15 \Omega/\text{sq.}$, Automatic Research) were cleaned for 15 min each with detergent, acetone and isopropanol in an ultrasonic bath

and subsequently treated for 15 min in a UV/O₃ cleaner. 22.5 mg/mL SnCl₂·2H₂O was dissolved in ethanol and stirred at room temperature overnight prior to spin coating 60 µl of the solution at 1500 rpm for 30 s. In a second step, another 60 µl of the SnCl₂ solution were dispersed on the substrate and rotated at 2500 rpm for 30 s before annealing at 180°C for one hour. After another UV/O₃ cleaning for 15 minutes, a KNO₃ solution (2.5 mg/ml in DI-H₂O) was spin-coated onto the SnO₂ layer at 4000 rpm and annealed at 120°C for 10 minutes. Further layers were deposited in a N₂ filled glovebox. Cs_{0.05}(FA_{0.83}MA_{0.17})_{0.95}Pb(I_{0.83}Br_{0.17})₃ perovskite was prepared from a precursor solution of FAI (1 M), PbI₂ (1.1 M), MABr (0.2 M) and PbBr₂ (0.2 M) in anhydrous DMF:DMSO 4:1 (v:v). Further, 5 mol-% CsI from a 1.5 M stock solution in DMSO was added to the precursor solution. The perovskite solution was spin coated in a two-step program at 1000 rpm for 10 s and 6000 rpm for 20 s. 5 s before to the end of the program, 160 µL of chlorobenzene was poured on the spinning substrate. Subsequently, the sample was annealed at 100 °C for 1 h. Next 36.2 mg of spiro-OMeTAD was dissolved in 1 mL of CBZ, 8.8 µL of a LiTFSI stock solution (520 mg/mL in acetonitrile), 14.5 µL of a FK209 stock solution (300 mg/mL in acetonitrile), and 14.4 µL of TBP. The doped spiro-OMeTAD solution was spin coated onto the samples at 1800 rpm for 30 s. Finally, 80 nm of gold were thermally evaporated at a base pressure of 10⁻⁶ mbar and a rate of 0.7 Å/s through shadow masks defining six active areas of 16 mm² per substrate.

Current Density–Voltage Characteristics, EQE_{PV} and 2-probe conductivity: J-V curves were measured under N₂ on a Keithley 2400 system in a 2-wire configuration with a scan speed of 0.1V/s and voltage step of 0.02V. One sun illumination at approximately 100mWcm⁻² of AM1.5G irradiation was provided by a Oriel class ABA sun simulator. The real illumination intensity was monitored during the measurement using a Si photodiode and the exact illumination intensity was used for efficiency calculations. The sun simulator was calibrated with a KG5 filtered silicon solar cell (certified by Fraunhofer ISE). The AM1.5G short-circuit current of devices matched the integrated product of the EQE spectrum within 5-10% error. The latter was recorded using a home build set-up utilizing a Philips Projection Lamp (Type7724 12 V 100 W) in front of a monochromator (Oriel Cornerstone 74100) and the light was mechanically chopped at 70 Hz. The photo-generated current was measured using a lock-in-amplifier (EG&G Princeton Applied Research Model 5302, integration times 300 ms) and evaluated after calibrating the lamp spectrum with an UV-enhanced Si photodetector (calibrated at Newport). The 2-probe conductivity was measured through current-voltage characteristics with an Agilent 4155C semiconductor parameter analyzer. The voltage was swept from positive to negative and the number of recorded points was kept at 201.

Absolute Photoluminescence: Excitation for the PL measurements was performed with a 445 nm CW laser (Insaneware) through an optical fibre into an integrating sphere. The intensity of the laser was adjusted to a 1 sun equivalent intensity by illuminating a 1 cm²-size perovskite solar cell under short-circuit and matching the current density to the J_{SC} under the sun simulator (22.0 mA/cm² at 100 mWcm⁻², or

1.375×10^{21} photons $\text{m}^{-2}\text{s}^{-1}$). A second optical fiber was used from the output of the integrating sphere to an Andor SR393i-B spectrometer equipped with a silicon CCD camera (DU420A-BR-DD, iDus). The system was calibrated by using a calibrated halogen lamp with specified spectral irradiance, which was shone into the integrating sphere. A spectral correction factor was established to match the spectral output of the detector to the calibrated spectral irradiance of the lamp. The spectral photon density was obtained from the corrected detector signal (spectral irradiance) by division through the photon energy (hf), and the photon numbers of the excitation and emission obtained from numerical integration using Matlab. In a last step, three fluorescent test samples with high specified PLQY ($\sim 70\%$) supplied from Hamamatsu Photonics were measured where the specified value could be accurately reproduced within a small relative error of less than 5%.

Time Resolved Photoluminescence: Time-resolved PL data was acquired with a TCSPC system (Berger & Lahr) after excitation with a pulse-picked and frequency-doubled output from a mode-locked Ti:sapphire oscillator (Coherent Chameleon) with nominal pulse durations ~ 100 fs and fluence of ~ 30 nJ/cm² at a wavelength of 470nm.

Energy Dispersive X-Ray maps were acquired by means of an Oxford Instruments Ultim Extreme windowless X-ray detector in a Zeiss UltraPlus scanning electron microscope (SEM). Measurements were performed with an acceleration voltage of 3 kV and a beam current of about 10 pA.

Cathodoluminescence intensity maps were acquired by means of a Zeiss MERLIN SEM equipped with a SPARC system from Delmic. An aluminium parabolic mirror positioned above the sample focused the light into a photomultiplier tube (Thorlabs, PMT1001) outside the SEM chamber. We minimized the effect of beam damage by measuring under mild beam conditions (50 pA and 3.5 kV) and reduced electron dose (10 nm pixel size and 15 μ s dwelling time per pixel).

Atomic Force Microscopy and Conductive Atomic Force Microscopy were performed with a Solver NT-MDT instrument with a hardware linearized 100 μ m scanner and scanning tip. The measurements were performed in contact mode by measuring both spreading resistance and topography. The tip used was a platinum NSG10/Pt.

Contact Angle: The contact angle profile of CMB-TA on perovskite MAPI thin film were determined by droplet shape profile analysis from OCA instrument, data physics ES, Germany, and drop shape analysis dsa1 V1.80 Krüss software.

Poly-Ionic Liquid Synthesis

Materials

1-Vinylimidazole, 1-methylimidazole, ethylbromide, 4-vinylbenzyl chloride, water-soluble nonionic azo-initiator VA86 (WakeChemicals), and lithium bis(trifluoromethylsulfonyl)imide (TFSI; Aldrich 97%) were used as received without further purifications. All solvents used were of analytic grade.

IL-monomer synthesis(1-ethyl-3-vinylimidazolium bromide)

1-Vinylimidazole (4.7 g 0.05 M) were dissolved in 100 mL of methanol in a round bottom flask. Slowly addition of Ethyl bromide (6.5 g 0.06 M) while stirring further 1 hour. Then the solution was heated to 40 °C for 24 h. After the solution was cooled to room temperature, the white precipitate was washed with diethyl ether several times. Finally the precipitate was dried in a vacuum (1×10^{-3} mbar) oven. (Yield 90% , 9.1 g)

Polymer synthesis

The IL monomer (5.0 g) was dissolved in deionized water (50 mL) in a round bottom flask. After the monomer was dissolved, water-soluble nonionic azo-initiator VA86 (120 mg) was added. The mixture was purged with argon for 30 minutes and then stirred and heated to 85 °C for 24 h. After cooling to room temperature, the solution was precipitated into ice cooled THF (50 mL). A beige powder was filtered off and washed several times with THF. The dry powder was dried at 80°C under vacuum for 10 h. (3.0 g, 60%).

Ionic Exchange

The anion metathesis was performed by adding an aqueous solution of Li-TFSI (5.63 g, 20 mmol) into the aqueous solution of Br contained polymer to replace Br by TFSI⁻. The resulting mixture was stirred for 1 h before filtering the solution using Por. 4 Buchner filter. The polymer was washed 5 times with water and dried in vacuum oven over night at 70 °C (2.1 g, 72%).

X-ray diffraction (XRD) patterns were obtained using Bruker D8 Advance X-ray diffractometer via Cu-K α radiation.

X-ray and ultraviolet photoemission (XPS and UPS) measurements were conducted using a JEOL (JPS-9030) photoelectron spectrometer, which is equipped with a monochromatized Al K α source (1486.6 eV) for XPS and hydrogen Lyman- α emission (10.2 eV) for UPS measurements.

12.6 Experimental Details Chapter 9

Energy Dispersive X-Ray maps were acquired by means of an Oxford Instruments Ultim Extreme windowless X-ray detector in a Zeiss UltraPlus scanning electron microscope (SEM). Measurements were performed with an acceleration voltage of 3 kV and a beam current of about 10 pA.

Cathodoluminescence intensity maps were acquired by means of a Zeiss MERLIN SEM equipped with a SPARC system from Delmic. An aluminium parabolic mirror positioned above the sample focused the light into a photomultiplier tube (Thorlabs, PMT1001) outside the SEM chamber. We minimized the effect of beam damage by

measuring under mild beam conditions (50 pA and 3.5 kV) and reduced electron dose (10 nm pixel size and 15 μ s dwelling time per pixel).

Absolute Photoluminescence: Excitation for the PL measurements was performed with a 445 nm CW laser (Insaneware) through an optical fibre into an integrating sphere. The intensity of the laser was adjusted to a 1 sun equivalent intensity by illuminating a 1 cm²-size perovskite solar cell under short-circuit and matching the current density to the J_{SC} under the sun simulator (22.0 mA/cm² at 100 mWcm⁻², or 1.375x10²¹ photons m⁻²s⁻¹). A second optical fiber was used from the output of the integrating sphere to an Andor SR393i-B spectrometer equipped with a silicon CCD camera (DU420A-BR-DD, iDus). The system was calibrated by using a calibrated halogen lamp with specified spectral irradiance, which was shone into to integrating sphere. A spectral correction factor was established to match the spectral output of the detector to the calibrated spectral irradiance of the lamp. The spectral photon density was obtained from the corrected detector signal (spectral irradiance) by division through the photon energy (hf), and the photon numbers of the excitation and emission obtained from numerical integration using Matlab. In a last step, three fluorescent test samples with high specified PLQY (~70%) supplied from Hamamatsu Photonics where measured where the specified value could be accurately reproduced within a small relative error of less than 5%.

Bibliography

- [1] E. Becquerel, *Comptes Rendus* **1839**, 561.
- [2] G. L. Pearson, *Semiconductor Signal Translating Device*, **1953**.
- [3] K. Yoshikawa, H. Kawasaki, W. Yoshida, T. Irie, K. Konishi, K. Nakano, T. Uto, D. Adachi, M. Kanematsu, H. Uzu, K. Yamamoto, *Nat. Energy* **2017**, 2, DOI 10.1038/nenergy.2017.32.
- [4] K. Yamamoto, K. Yoshikawa, H. Uzu, D. Adachi, *Jpn. J. Appl. Phys.* **2018**, 57, 1.
- [5] “NREL Solar Cell Efficiency Chart,” can be found under <https://www.nrel.gov/pv/cell-efficiency.html>, **n.d.**
- [6] M. Nakamura, K. Yamaguchi, Y. Kimoto, Y. Yasaki, T. Kato, H. Sugimoto, *IEEE J. Photovoltaics* **2019**, 9, 1863.
- [7] Q. Liu, Y. Jiang, K. Jin, J. Qin, J. Xu, W. Li, J. Xiong, J. Liu, Z. Xiao, K. Sun, S. Yang, X. Zhang, L. Ding, *Sci. Bull.* **2020**, 65, 272.
- [8] A. Kojima, K. Teshima, Y. Shirai, T. Miyasaka, *J. Am. Chem. Soc.* **2009**, 131, 6050.
- [9] M. M. Lee, J. Teuscher, T. Miyasaka, T. N. Murakami, H. J. Snaith, *Science* (80-.). **2012**, 338, 643.
- [10] H.-S. Kim, C.-R. Lee, J.-H. Im, K.-B. Lee, T. Moehl, A. Marchioro, S.-J. Moon, R. Humphry-Baker, J.-H. Yum, J. E. Moser, M. Grätzel, N.-G. Park, *Sci. Rep.* **2012**, 2, 591.
- [11] W.-J. Yin, T. Shi, Y. Yan, *Appl. Phys. Lett* **2014**, 104, 063903.
- [12] S. De Wolf, J. Holovsky, S. J. Moon, P. Löper, B. Niesen, M. Ledinsky, F. J. Haug, J. H. Yum, C. Ballif, *J. Phys. Chem. Lett.* **2014**, 5, 1035.
- [13] W.-J. Yin, J.-H. Yang, J. Kang, Y. Yan, S.-H. Wei, *J. Mater. Chem. A* **2015**, 3, 8926.
- [14] M. Cai, Y. Wu, H. Chen, X. Yang, Y. Qiang, L. Han, *Adv. Sci.* **2017**, 4, 1600269.
- [15] M. A. Green, A. Ho-Baillie, H. J. Snaith, *Nat. Photonics* **2014**, 8, 506.
- [16] V. M. Goldschmidt, *Naturwissenschaften* **1926**, 477.
- [17] B. L. Phoon, C. W. Lai, J. C. Juan, P. Show, W. Chen, *Int. J. Energy Res.* **2019**, 43, 5151.
- [18] Z. Xiao, Y. Yan, *Adv. Energy Mater.* **2017**, 7, 1.
- [19] G. Grancini, M. K. Nazeeruddin, *Nat. Rev. Mater.* **2019**, 4, 4.
- [20] L. Protesescu, S. Yakunin, M. I. Bodnarchuk, F. Krieg, R. Caputo, C. H. Hendon, R. X. Yang, A. Walsh, M. V. Kovalenko, *Nano Lett.* **2015**, 15, 3692.
- [21] D. P. Mcmeekin, G. Sadoughi, W. Rehman, G. E. Eperon, M. Saliba, M. T. Hörantner, A. Haghighirad, N. Sakai, L. Korte, B. Rech, M. B. Johnston, L. M. Herz, H. J. Snaith, *Science* (80-.). **2016**, 351, 151.
- [22] M. Saliba, T. Matsui, J.-Y. Seo, K. Domanski, J.-P. Correa-Baena, M. K. Nazeeruddin, S. M. Zakeeruddin, W. Tress, A. Abate, A. Hagfeldt, M. Grätzel, *Energy Environ. Sci.* **2016**, 9, 1989.

- [23] L. Qiu, S. He, L. K. Ono, Y. Qi, *Adv. Energy Mater.* **2019**, 1902726, 1.
- [24] T. Umebayashi, K. Asai, T. Kondo, A. Nakao, *Phys. Rev. B* **2003**, 67, 155405.
- [25] D. A. Egger, A. M. Rappe, L. Kronik, *Acc. Chem. Res.* **2016**, 49, 573.
- [26] W. J. Yin, T. Shi, Y. Yan, *Adv. Mater.* **2014**, 26, 4653.
- [27] F. Brivio, C. Caetano, A. Walsh, *J. Phys. Chem. Lett.* **2016**, 7, 1083.
- [28] J. H. Noh, S. H. Im, J. H. Heo, T. N. Mandal, S. Il Seok, *Nano Lett.* **2013**, 13, 1764.
- [29] W. S. Yang, J. H. Noh, N. J. Jeon, Y. C. Kim, S. Ryu, J. Seo, S. Il Seok, *Science (80-.)*. **2015**, 348, 1234.
- [30] M. Pazoki, T. J. Jacobsson, A. Hagfeldt, G. Boschloo, T. Edvinsson, *Phys. Rev. B* **2016**, 93, 144105.
- [31] J.-P. Correa-Baena, A. Abate, M. Saliba, W. Tress, T. Jesper Jacobsson, M. Grätzel, A. Hagfeldt, *Energy Environ. Sci.* **2017**, 10, 710.
- [32] N. Pellet, P. Gao, G. Gregori, T. Y. Yang, M. K. Nazeeruddin, J. Maier, M. Grätzel, *Angew. Chemie - Int. Ed.* **2014**, 53, 3151.
- [33] N. J. Jeon, J. H. Noh, W. S. Yang, Y. C. Kim, S. Ryu, J. Seo, & Sang, I. Seok, *Nature* **2014**, 517, 476.
- [34] D. J. Slotcavage, H. I. Karunadasa, M. D. McGehee, *ACS Energy Lett.* **2016**, 1, 1199.
- [35] E. T. Hoke, D. J. Slotcavage, E. R. Dohner, A. R. Bowring, H. I. Karunadasa, M. D. McGehee, *Chem. Sci.* **2015**, 6, 613.
- [36] T. Duong, H. K. Mulmudi, Y. Wu, X. Fu, H. Shen, J. Peng, N. Wu, H. T. Nguyen, D. Macdonald, M. Lockrey, T. P. White, K. Weber, K. Catchpole, *ACS Appl. Mater. Interfaces* **2017**, 9, 26859.
- [37] W. Mao, C. R. Hall, A. S. R. Chesman, C. Forsyth, Y.-B. Cheng, N. W. Duffy, T. A. Smith, U. Bach, *Angew. Chemie Int. Ed.* **2019**, 58, 2893.
- [38] S. J. Yoon, S. Draguta, J. S. Manser, O. Sharia, W. F. Schneider, M. Kuno, P. V. Kamat, *ACS Energy Lett.* **2016**, 1, 290.
- [39] S. Mahesh, J. M. Ball, R. D. J. Oliver, D. P. McMeekin, P. K. Nayak, M. B. Johnston, H. J. Snaith, *Energy Environ. Sci.* **2020**, 13, 258.
- [40] T. Elmelund, B. Seger, M. Kuno, P. V. Kamat, *ACS Energy Lett.* **2020**, 5, 56.
- [41] K. Suchan, A. Merdasa, C. Rehermann, E. L. Unger, I. G. Scheblykin, *J. Lumin.* **2020**, 221, 117073.
- [42] J. W. Lee, D. H. Kim, H. S. Kim, S. W. Seo, S. M. Cho, N. G. Park, *Adv. Energy Mater.* **2015**, 5, 1501310.
- [43] M. Saliba, T. Matsui, K. Domanski, J.-Y. Seo, A. Ummadisingu, S. M. Zakeeruddin, J.-P. Correa-Baena, W. R. Tress, A. Abate, A. Hagfeldt, M. Grätzel, *Science (80-.)*. **2016**, 354, 206.
- [44] M. Abdi-Jalebi, Z. Andaji-Garmaroudi, S. Cacovich, C. Stavrakas, B. Philippe, J. M. Richter, M. Alsari, E. P. Booker, E. M. Hutter, Andrew J. Pearson, S. Lilliu, T. J. Savenije, H. Rensmo, G. Divitini, C. Ducati, R. H. Friend, S. D. Stranks, *Nature* **2018**, 555, 497.
- [45] T. J. Jacobsson, M. Pazoki, A. Hagfeldt, T. Edvinsson, *J. Phys. Chem. C* **2015**, 119, 25673.

- [46] J. Navas, A. Sánchez-Coronilla, J. Jesús Gallardo, N. Cruz Hernández, J. Carlos Piñero, R. Alcántara, C. Fernández-Lorenzo, D. M. De los Santos, T. Aguilar, J. Martín-Calleja, *Nanoscale* **2015**, *7*, 6216.
- [47] R. L. Z. Hoye, R. E. Brandt, A. Osherov, V. Stevanovic, S. D. Stranks, M. W. B. Wilson, H. Kim, A. J. Akey, J. D. Perkins, R. C. Kurchin, J. R. Poindexter, E. N. Wang, M. G. Bawendi, V. Bulovic, T. Buonassisi, *Chem. - A Eur. J.* **2016**, *22*, 2605.
- [48] N. K. Noel, S. D. Stranks, A. Abate, C. Wehrenfennig, S. Guarnera, A.-A. Haghighirad, A. Sadhanala, G. E. Eperon, S. K. Pathak, M. B. Johnston, A. Petrozza, L. M. Herz, H. J. Snaith, *Energy Environ. Sci.* **2014**, *7*, 3061.
- [49] M. T. Klug, A. Osherov, A. A. Haghighirad, S. D. Stranks, P. R. Brown, S. Bai, J. T.-W. Wang, X. Dang, V. Bulovi, H. J. Snaith, A. M. Belcher, *Energy Environ. Sci.* **2017**, *236*, 236.
- [50] C. Grote, B. Ehrlich, R. F. Berger, *Phys. Rev. B* **2014**, *90*, 205202.
- [51] F. Wang, I. Grinberg, A. M. Rappe, *Appl. Phys. Lett* **2014**, *104*, 152903.
- [52] R. Lin, K. Xiao, Z. Qin, Q. Han, C. Zhang, M. Wei, M. I. Saidaminov, Y. Gao, J. Xu, M. Xiao, A. Li, J. Zhu, E. H. Sargent, H. Tan, *Nat. Energy* **2019**, *4*, 864.
- [53] A. F. Palmstrom, G. E. Eperon, T. Leijtens, R. Prasanna, S. N. Habisreutinger, W. Nemeth, E. A. Gaubing, S. P. Dunfield, M. Reese, S. Nanayakkara, T. Moot, J. Werner, J. Liu, B. To, S. T. Christensen, M. D. McGehee, M. F. A. M. van Hest, J. M. Luther, J. J. Berry, D. T. Moore, *Joule* **2019**, *3*, 2193.
- [54] J. Kim, S. H. Lee, J. H. Lee, K. H. Hong, *J. Phys. Chem. Lett.* **2014**, *5*, 1312.
- [55] A. Walsh, D. O. Scanlon, S. Chen, X. G. Gong, S.-H. Wei, *Angew. Chemie Int. Ed.* **2015**, *54*, 1791.
- [56] K. X. Steirer, P. Schulz, G. Teeter, V. Stevanovic, M. Yang, K. Zhu, J. J. Berry, *ACS Energy Lett.* **2016**, *1*, 360.
- [57] V. Adinolfi, M. Yuan, R. Comin, E. S. Thibau, D. Shi, M. I. Saidaminov, P. Kanjanaboos, D. Kopilovic, S. Hoogland, Z.-H. Lu, O. M. Bakr, E. H. Sargent, *Adv. Mater.* **2016**, *28*, 3406.
- [58] J. M. Ball, A. Petrozza, *Nat. Energy* **2016**, *1*, DOI 10.1038/nenergy.2016.149.
- [59] S. D. Stranks, V. M. Burlakov, T. Leijtens, J. M. Ball, A. Goriely, H. J. Snaith, *Phys. Rev. Appl.* **2014**, *2*, 034007.
- [60] M. Saba, M. Cadelano, D. Marongiu, F. Chen, V. Sarritzu, N. Sestu, C. Figus, M. Aresti, R. Piras, A. Geddo Lehmann, C. Cannas, A. Musinu, F. Quochi, A. Mura, G. Bongiovanni, *Nat. Commun.* **2014**, *5*, 1.
- [61] B. Chen, P. N. Rudd, S. Yang, Y. Yuan, J. Huang, *Chem. Soc. Rev.* **2019**, *48*, 3842.
- [62] Y. Yuan, T. Li, Q. Wang, J. Xing, A. Gruverman, J. Huang, *Sci. Adv.* **2017**, *3*, e1602164.
- [63] J. M. Azpiroz, E. Mosconi, J. Bisquert, F. De Angelis, *Energy Environ. Sci.* **2015**, *8*, 2118.
- [64] C. Eames, J. M. Frost, P. R. F. Barnes, B. C. O'Regan, A. Walsh, M. S. Islam, *Nat. Commun.* **2015**, *6*, 1.
- [65] W. Tress, N. Marinova, T. Moehl, S. M. Zakeeruddin, M. K. Nazeeruddin, M. Grätzel, *Energy Environ. Sci.* **2015**, *8*, 995.

- [66] D. J. Slotcavage, H. I. Karunadasa, M. D. McGehee, *ACS Energy Lett.* **2016**, *1*, 1199.
- [67] W. Li, M. U. Rothmann, A. Liu, Z. Wang, Y. Zhang, A. R. Pascoe, J. Lu, L. Jiang, Y. Chen, F. Huang, Y. Peng, Q. Bao, J. Etheridge, U. Bach, Y. B. Cheng, *Adv. Energy Mater.* **2017**, *7*, 1.
- [68] S. G. Motti, D. Meggiolaro, A. J. Barker, E. Mosconi, C. A. R. Perini, J. M. Ball, M. Gandini, M. Kim, F. De Angelis, A. Petrozza, *Nat. Photonics* **2019**, DOI 10.1038/s41566-019-0435-1.
- [69] B. Chen, P. N. Rudd, S. Yang, Y. Yuan, J. Huang, *Chem. Soc. Rev.* **2019**, *48*, 3842.
- [70] H. H. Fang, S. Adjokatse, H. Wei, J. Yang, G. R. Blake, J. Huang, J. Even, M. A. Loi, *Sci. Adv.* **2016**, *2*, e1600534.
- [71] N. K. Noel, A. Abate, S. D. Stranks, E. S. Parrott, V. M. Burlakov, A. Goriely, H. J. Snaith, *ACS Nano* **2014**, *8*, 9815.
- [72] L. Zuo, H. Guo, D. W. Dequilettes, S. Jariwala, N. De Marco, S. Dong, R. Deblock, D. S. Ginger, B. Dunn, M. Wang, Y. Yang, *Sci. Adv.* **2017**, *3*, e1700106.
- [73] I. L. Braly, D. W. Dequilettes, L. M. Pazos-Outón, S. Burke, M. E. Ziffer, D. S. Ginger, H. W. Hillhouse, *Nat. Photonics* **2018**, *12*, 355.
- [74] S. Lee, J. H. Park, B. R. Lee, E. D. Jung, J. C. Yu, D. Di Nuzzo, R. H. Friend, M. H. Song, *J. Phys. Chem. Lett.* **2017**, *8*, 1784.
- [75] C. M. Wolff, F. Zu, A. Paulke, L. P. Toro, N. Koch, D. Neher, *Adv. Mater.* **2017**, *29*, 1700159.
- [76] S.-H. Turren-Cruz, A. Hagfeldt, M. Saliba, *Science (80-)*. **2018**, *362*, 449.
- [77] V. Adinolfi, W. Peng, G. Walters, O. M. Bakr, E. H. Sargent, *Adv. Mater.* **2018**, *30*, 1.
- [78] S. D. Stranks, G. E. Eperon, G. Grancini, C. Menelaou, M. J. P. Alcocer, T. Leijtens, L. M. Herz, A. Petrozza, H. J. Snaith, *Science (80-)*. **2013**, *342*, 341.
- [79] Q. Dong, Y. Fang, Y. Shao, P. Mulligan, J. Qiu, L. Cao, J. Huang, *Science (80-)*. **2015**, *347*, 967.
- [80] C. S. Ponseca, T. J. Savenije, M. Abdellah, K. Zheng, A. Yartsev, T. Pascher, T. Harlang, P. Chabera, T. Pullerits, A. Stepanov, J. P. Wolf, V. Sundström, *J. Am. Chem. Soc.* **2014**, *136*, 5189.
- [81] J. S. Manser, J. A. Christians, P. V. Kamat, *Chem. Rev.* **2016**, *116*, 12956.
- [82] Y. Zhao, K. Zhu, *Chem. Soc. Rev.* **2016**, *45*, 655.
- [83] Y. Wu, A. Islam, X. Yang, C. Qin, J. Liu, K. Zhang, W. Peng, L. Han, *Energy Environ. Sci.* **2014**, *7*, 2934.
- [84] M. Xiao, F. Huang, W. Huang, Y. Dkhissi, Y. Zhu, J. Etheridge, A. Gray-Weale, U. Bach, Y.-B. Cheng, L. Spiccia, *Angew. Chemie Int. Ed.* **2014**, *53*, 9898.
- [85] P. S. Shen, J. S. Chen, Y. H. Chiang, M. H. Li, T. F. Guo, P. Chen, *Adv. Mater. Interfaces* **2016**, DOI 10.1002/admi.201500849.
- [86] Y. Li, J. K. Cooper, R. Buonsanti, C. Giannini, Y. Liu, F. M. Toma, I. D. Sharp, *J. Phys. Chem. Lett.* **2015**, DOI 10.1021/jz502720a.
- [87] M. M. Lee, J. Teuscher, T. Miyasaka, T. N. Murakami, H. J. Snaith, *Science (80-)*. **2012**, *338*, 643.

- [88] H. S. Kim, C. R. Lee, J. H. Im, K. B. Lee, T. Moehl, A. Marchioro, S. J. Moon, R. Humphry-Baker, J. H. Yum, J. E. Moser, M. Grätzel, N. G. Park, *Sci. Rep.* **2012**, 2, 1.
- [89] J. P. Correa Baena, L. Steier, W. Tress, M. Saliba, S. Neutzner, T. Matsui, F. Giordano, T. J. Jacobsson, A. R. Srimath Kandada, S. M. Zakeeruddin, A. Petrozza, A. Abate, M. K. Nazeeruddin, M. Grätzel, A. Hagfeldt, *Energy Environ. Sci.* **2015**, 8, 2928.
- [90] Y. Shao, Z. Xiao, C. Bi, Y. Yuan, J. Huang, *Nat. Commun.* **2014**, 5, 1.
- [91] J. Xu, A. Buin, A. H. Ip, W. Li, O. Voznyy, R. Comin, M. Yuan, S. Jeon, Z. Ning, J. J. McDowell, P. Kanjanaboos, J. P. Sun, X. Lan, L. N. Quan, D. H. Kim, I. G. Hill, P. Maksymovych, E. H. Sargent, *Nat. Commun.* **2015**, 6, 1.
- [92] S. Albrecht, B. Rech, *Nat. Energy* **2017**, 2, 16196.
- [93] Z. Xiao, Y. Yuan, Y. Shao, Q. Wang, Q. Dong, C. Bi, P. Sharma, A. Gruverman, J. Huang, **2015**, DOI 10.1038/NMAT4150.
- [94] Y. Zhao, W. Zhou, W. Ma, S. Meng, H. Li, J. Wei, R. Fu, K. Liu, D. Yu, Q. Zhao, *ACS Energy Lett.* **2016**, 1, 266.
- [95] P. Calado, A. M. Telford, D. Bryant, X. Li, J. Nelson, B. C. O'Regan, P. R. F. Barnes, *Nat. Commun.* **2016**, 7, 1.
- [96] M. Kim, G. H. Kim, T. K. Lee, I. W. Choi, H. W. Choi, Y. Jo, Y. J. Yoon, J. W. Kim, J. Lee, D. Huh, H. Lee, S. K. Kwak, J. Y. Kim, D. S. Kim, *Joule* **2019**, 3, 2179.
- [97] Z. Liu, L. Krückemeier, B. Krogmeier, B. Klingebiel, J. A. Márquez, S. Levchenko, S. Öz, S. Mathur, U. Rau, T. Unold, T. Kirchartz, *ACS Energy Lett.* **2019**, 4, 110.
- [98] M. Stolterfoht, C. M. Wolff, Y. Amir, A. Paulke, L. Perdigón-Toro, P. Caprioglio, D. Neher, *Energy Environ. Sci.* **2017**, 10, 1530.
- [99] X. Zheng, Y. Hou, C. Bao, J. Yin, F. Yuan, Z. Huang, K. Song, J. Liu, J. Troughton, N. Gasparini, C. Zhou, Y. Lin, D. J. Xue, B. Chen, A. K. Johnston, N. Wei, M. N. Hedhili, M. Wei, A. Y. Alsalloum, P. Maity, B. Turedi, C. Yang, D. Baran, T. D. Anthopoulos, Y. Han, Z. H. Lu, O. F. Mohammed, F. Gao, E. H. Sargent, O. M. Bakr, *Nat. Energy* **2020**, 5, 131.
- [100] J.-P. Correa-Baena, M. Saliba, T. Buonassisi, M. Grätzel, A. Abate, W. Tress, A. Hagfeldt, *Science* **2017**, 358, 739.
- [101] W. Tress, *Adv. Energy Mater.* **2017**, 7, 1602358.
- [102] K. Domanski, E. A. Alharbi, A. Hagfeldt, M. Grätzel, W. Tress, *Nat. Energy* **2018**, 3, 61.
- [103] N. K. Noel, A. Abate, S. D. Stranks, E. S. Parrott, V. M. Burlakov, A. Goriely, H. J. Snaith, **2014**, 8, 9815.
- [104] X. Zheng, B. Chen, J. Dai, Y. Fang, Y. Bai, Y. Lin, H. Wei, X. C. Zeng, J. Huang, *Nat. Energy* **2017**, 2, 17102.
- [105] W. Deng, X. Liang, P. S. Kubiak, P. J. Cameron, *Adv. Energy Mater.* **2018**, 8, 1.
- [106] P. Caprioglio, F. Zu, C. M. Wolff, J. A. Márquez Prieto, M. Stolterfoht, P. Becker, N. Koch, T. Unold, B. Rech, S. Albrecht, D. Neher, *Sustain. Energy Fuels* **2019**, 3, 550.
- [107] M. Abdi-Jalebi, Z. Andaji-Garmaroudi, S. Cacovich, C. Stavrakas, B. Philippe, J. Richter, M. Alsari, E. P. Booker, E. Hutter, Andrew J. Pearson, S. Lilliu, T. J.

- Savenije, H. Rensmo, G. Divitini, C. Ducati, R. Friend, S. D. Stranks, *Nature* **2018**, 555, 497.
- [108] D. Bi, C. Yi, J. Luo, J.-D. Décoppet, F. Zhang, S. M. Zakeeruddin, X. Li, A. Hagfeldt, M. Grätzel, *Nat. Energy* **2016**, 1, 16142.
- [109] Q. Wu, W. Zhou, Q. Liu, P. Zhou, T. Chen, Y. Lu, Q. Qiao, S. Yang, **2016**, DOI 10.1021/acsami.6b12683.
- [110] H. Zhang, H. Azimi, Y. Hou, T. Ameri, T. Przybilla, E. Spiecker, M. Kraft, U. Scherf, C. J. Brabec, *Chem. Mater.* **2014**, 26, 5190.
- [111] B.-E. El Cohen, M. Wierzbowska, L. Etgar, *Sustain. Energy Fuels* **2017**, 1, 1935.
- [112] L. Etgar, *Energy Environ. Sci.* **2018**, 11, 234.
- [113] K. T. Cho, Y. Zhang, S. Orlandi, M. Cavazzini, I. Zimmermann, A. Lesch, N. Tabet, G. Pozzi, G. Grancini, M. K. Nazeeruddin, *Nano Lett* **2018**, 18, DOI 10.1021/acs.nanolett.8b01863.
- [114] K. T. Cho, S. Paek, G. Grancini, C. Roldán N-Carmona, P. Gao, Y. Lee, M. K. Nazeeruddin, C. Roldán-Carmona, P. Gao, Y. Lee, M. K. Nazeeruddin, *Energy Environ. Sci.* **2017**, 10, 621.
- [115] G. Grancini, C. Roldán-Carmona, I. Zimmermann, E. Mosconi, X. Lee, D. Martineau, S. Narbey, F. Oswald, F. De Angelis, M. Graetzel, M. K. Nazeeruddin, *Nat. Commun.* **2017**, 8, 1.
- [116] R. Qiao, L. Zuo, *J. Mater. Res* **2019**, 33, 387.
- [117] C.-Y. Chang, Y.-C. Chang, W.-K. Huang, W.-C. Liao, H. Wang, C. Yeh, B.-C. Tsai, Y.-C. Huang, C.-S. Tsao, *J. Mater. Chem. A* **2016**, 4, 7903.
- [118] A. Al-Ashouri, A. Magomedov, M. Roß, M. Jošt, M. Talaikis, G. Chistiakova, T. Bertram, J. A. Márquez, E. Köhnen, E. Kasparavičius, S. Levenco, L. Gil-Escrig, C. J. Hages, R. Schlattmann, B. Rech, T. Malinauskas, T. Unold, C. A. Kaufmann, L. Korte, G. Niaura, V. Getautis, S. Albrecht, *Energy Environ. Sci.* **2019**, 12, 3356.
- [119] J. A. Christians, P. Schulz, J. S. Tinkham, T. H. Schloemer, S. P. Harvey, B. J. Tremolet De Villers, A. Sellinger, J. J. Berry, J. M. Luther, *Nat. Energy* **2018**, 3, 68.
- [120] N. J. Jeon, H. Na, E. H. Jung, T.-Y. Y. Yang, Y. G. Lee, G. Kim, H.-W. W. Shin, S. Il Seok, J. Lee, J. Seo, *Nat. Energy* **2018**, 3, 682.
- [121] W. Shockley, H. J. Queisser, *J. Appl. Phys.* **1961**, 32, 510.
- [122] C. M. Wolff, P. Caprioglio, M. Stollerfoht, D. Neher, *Adv. Mater.* **2019**, 31, 1902762.
- [123] J. M. Richter, M. Abdi-Jalebi, A. Sadhanala, M. Tabachnyk, J. P. H. Rivett, L. M. Pazos-Outón, K. C. Gödel, M. Price, F. Deschler, R. H. Friend, *Nat. Commun.* **2016**, 7, 13941.
- [124] S. D. Stranks, R. L. Z. Hoyer, D. Di, R. H. Friend, F. Deschler, *Adv. Mater.* **2019**, 31, 1803336.
- [125] M. B. Johnston, L. M. Herz, *Acc. Chem. Res.* **2016**, 49, 146.
- [126] W. Shockley, W. T. Read, *Phys. Rev.* **1952**, 87, 835.
- [127] M. Stollerfoht, C. M. Wolff, J. A. Márquez, S. Zhang, C. J. Hages, D. Rothhardt, S. Albrecht, P. L. Burn, P. Meredith, T. Unold, D. Neher, *Nat. Energy* **2018**, 3,

- [128] M. Stolterfoht, P. Caprioglio, C. M. Wolff, J. A. Márquez, J. Nordmann, S. Zhang, D. Rothhardt, U. Hörmann, Y. Amir, A. Redinger, L. Kegelmann, F. Zu, S. Albrecht, N. Koch, T. Kirchartz, M. Saliba, T. Unold, D. Neher, *Energy Environ. Sci.* **2019**, *12*, 2778.
- [129] E. M. Hutter, J. J. Hofman, M. L. Petrus, M. Moes, R. D. Abellón, P. Docampo, T. J. Savenije, *Adv. Energy Mater.* **2017**, *7*, 1.
- [130] V. Sarritzu, N. Sestu, D. Marongiu, X. Chang, S. Masi, A. Rizzo, S. Colella, F. Quochi, M. Saba, A. Mura, G. Bongiovanni, *Sci. Rep.* **2017**, *7*, 44629.
- [131] T. Kirchartz, U. Rau, *Phys. Status Solidi Appl. Mater. Sci.* **2008**, *205*, 2737.
- [132] U. Rau, D. Abou-Ras, T. Kirchartz, T. Unold, L. Gütay, *Adv. Charact. Tech. Thin Film Sol. Cells (Eds D. Abou-Ras, T. Kirchartz, U. Rau, 1st) Wiley VCH, Weinheim, Ger. 2011, pp. 151-175* **2011**.
- [133] P. Würfel, *J. Phys. C Solid State Phys.* **1982**, *15*, 3967.
- [134] G. H. Bauer, L. Gütay, R. Kniese, *Thin Solid Films* **2005**, *480–481*, 259.
- [135] G. El-Hajje, C. Momblona, L. Gil-Escrig, J. Ávila, T. Guillemot, J.-F. Guillemoles, M. Sessolo, H. J. Bolink, L. Lombez, *Energy Environ. Sci.* **2016**, *131*, 6050.
- [136] V. Sarritzu, N. Sestu, D. Marongiu, X. Chang, S. Masi, A. Rizzo, S. Colella, F. Quochi, M. Saba, A. Mura, G. Bongiovanni, *Sci. Rep.* **2017**, *7*, 44629.
- [137] I. L. Braly, H. W. Hillhouse, *J. Phys. Chem. C* **2016**, *120*, 893.
- [138] U. Rau, *Phys. Rev. B* **2007**, *76*, 085303.
- [139] K. Tvingstedt, C. K. Deibel, *Adv. Energy Mater.* **2016**, *6*, 1502230.
- [140] T. Kirchartz, F. Deledalle, P. S. Tuladhar, J. R. Durrant, J. Nelson, *J. Phys. Chem. Lett.* **2013**, *4*, 2371.
- [141] W. Tress, M. Yavari, K. Domanski, P. Yadav, B. Niesen, J. P. Correa Baena, A. Hagfeldt, M. Graetzel, *Energy Environ. Sci.* **2018**, *11*, 151.
- [142] W. S. Yang, B. W. Park, E. H. Jung, N. J. Jeon, Y. C. Kim, D. U. Lee, S. S. Shin, J. Seo, E. K. Kim, J. H. Noh, S. Il Seok, *Science (80-)*. **2017**, *356*, 1376.
- [143] L. M. Herz, *Annu. Rev. Phys. Chem.* **2016**, *67*, 65.
- [144] T. Leijtens, G. E. Eperon, A. J. Barker, G. Grancini, W. Zhang, J. M. Ball, A. R. S. Kandada, H. J. Snaith, A. Petrozza, *Energy Environ. Sci.* **2016**, *9*, 3472.
- [145] Z. Liu, L. Krückemeier, B. Krogmeier, B. Klingebiel, J. A. Márquez, S. Levchenko, S. Öz, S. Mathur, U. Rau, T. Unold, T. Kirchartz, *ACS Energy Lett.* **2018**, 110.
- [146] P. Caprioglio, F. Zu, C. M. Wolff, J. A. M. Prieto, M. Stolterfoht, N. Koch, T. Unold, B. Rech, S. Albrecht, D. Neher, J. A. Márquez Prieto, M. Stolterfoht, P. Becker, N. Koch, T. Unold, B. Rech, S. Albrecht, D. Neher, *Sustain. Energy Fuels* **2019**, *3*, 550.
- [147] D. Kiermasch, P. Rieder, K. Tvingstedt, A. Baumann, V. Dyakonov, *Sci. Rep.* **2016**, *6*, 39333.
- [148] B. Krogmeier, F. Staub, D. Grabowski, U. Rau, T. Kirchartz, *Sustain. Energy Fuels* **2018**, *00*, 1.
- [149] F. Staub, H. Hempel, J. Hebig, J. Mock, U. W. Paetzold, U. Rau, T. Unold, T. Kirchartz, *Phys. Rev. Appl.* **2016**, *6*, 044017.

- [150] J. Horn, I. Minda, H. Schwoerer, D. Schlettwein, *Phys. status solidi* **2019**, 256, 1800265.
- [151] B. Krogmeier, F. Staub, D. Grabowski, U. Rau, T. Kirchartz, *Sustain. Energy Fuels* **2018**, 2, 1027.
- [152] H. K. Gummel, *IEEE Trans. Electron Devices* **1964**, 11, 455.
- [153] T. S. Sherkar, C. Momblona, L. Gil-Escrig, J. Ávila, M. Sessolo, H. J. Bolink, L. J. A. Koster, *ACS Energy Lett.* **2017**, 2, 1214.
- [154] X. Zheng, B. Chen, J. Dai, Y. Fang, Y. Bai, Y. Lin, H. Wei, X. C. Zeng, J. Huang, *Nat. Energy* **2017**, 2, 17102.
- [155] W. S. Yang, B. Park, E. H. Jung, N. J. Jeon, Y. C. Kim, D. U. Lee, S. S. Shin, J. Seo, E. K. Kim, J. H. Noh, S. Il Seok, *Science (80-)*. **2017**, 356, 1376.
- [156] X. Li, D. Bi, C. Yi, J.-D. Décoppet, J. Luo, S. M. Zakeeruddin, A. Hagfeldt, M. Grätzel, *Science (80-)*. **2016**, 8060, 1.
- [157] J.-P. Correa-Baena, W. Tress, K. Domanski, E. H. Anaraki, S.-H. Turren-Cruz, B. Roose, P. P. Boix, M. Grätzel, M. Saliba, A. Abate, A. Hagfeldt, *Energy Environ. Sci.* **2017**, 10, 1207.
- [158] K. Tvingstedt, L. Gil-Escrig, C. Momblona, P. Rieder, D. Kiermasch, M. Sessolo, A. Baumann, H. J. Bolink, V. Dyakonov, *ACS Energy Lett.* **2017**, 2, 424.
- [159] Y. Yang, M. Yang, D. T. Moore, Y. Yan, E. M. Miller, K. Zhu, M. C. Beard, *Nat. Energy* **2017**, 2, 1.
- [160] E. Guillén, F. J. Ramos, J. A. Anta, S. Ahmad, E. Guille, F. J. Ramos, J. A. Anta, S. Ahmad, *J. Phys. Chem. C* **2014**, 118, 22913.
- [161] D. Kiermasch, A. Baumann, M. Fischer, V. Dyakonov, K. Tvingstedt, *Energy Environ. Sci.* **2018**, 11, 629.
- [162] A. Delamarre, L. Lombez, J.-F. Guillemoles, *Appl. Phys. Lett.* **2012**, 100, 131108.
- [163] P. Schulz, E. Edri, S. Kirmayer, G. Hodes, D. Cahen, A. Kahn, *Energy Environ. Sci.* **2014**, 7, 1377.
- [164] L. E. Polander, P. Pahnner, M. Schwarze, M. Saalfrank, C. Koerner, K. Leo, *APL Mater.* **2014**, 2, 081503.
- [165] I. Gelmetti, N. F. Montcada, A. Pérez-Rodríguez, E. Barrena, C. Ocal, I. García-Benito, A. Molina-Ontoria, N. Martín, A. Vidal-Ferran, E. Palomares, *Energy Environ. Sci.* **2019**, 12, 1309.
- [166] R. A. Belisle, P. Jain, R. Prasanna, T. Leijtens, M. D. McGehee, *ACS Energy Lett.* **2016**, 1, 556.
- [167] Y. Hou, X. Du, S. Scheiner, D. P. McMeekin, Z. Wang, N. Li, M. S. Killian, H. Chen, M. Richter, I. Levchuk, N. Schrenker, E. Spiecker, T. Stubhan, N. A. Luechinger, A. Hirsch, P. Schmuki, H.-P. Steinrück, R. H. Fink, M. Halik, H. J. Snaith, C. J. Brabec, *Science (80-)*. **2017**, 358, 1192.
- [168] Q. Wang, Q. Dong, T. Li, A. Gruverman, J. Huang, *Adv. Mater.* **2016**, 28, 6734.
- [169] C. C. Chueh, C. Z. Li, A. K. Y. Jen, *Energy Environ. Sci.* **2015**, 8, 1160.
- [170] H. Wei, Y. Fang, P. Mulligan, W. Chuirazzi, H.-H. Fang, C. Wang, B. R. Ecker, Y. Gao, M. A. Loi, L. Cao, J. Huang, *Nat. Photonics* **2016**, 10, 333.
- [171] S. Zhang, M. Stolterfoht, A. Armin, Q. Lin, F. Zu, J. Sobus, H. Jin, N. Koch, P.

- Meredith, P. L. Burn, D. Neher, *ACS Appl. Mater. Interfaces* **2018**, *10*, 21681.
- [172] L. Calió, S. Kazim, M. Grätzel, S. Ahmad, *Angew. Chemie - Int. Ed.* **2016**, *55*, 14522.
- [173] A. Gheno, S. Vedraïne, B. Ratier, J. Bouclé, *Metals (Basel)*. **2016**, *6*, 21.
- [174] Y. Shao, Y. Yuan, J. Huang, *Nat. Energy* **2016**, *1*, 1.
- [175] P. Tiwana, P. Docampo, M. B. Johnston, H. J. Snaith, L. M. Herz, *ACS Nano* **2011**, *5*, 5158.
- [176] W. Tress, N. Marinova, O. Inganäs, M. K. Nazeeruddin, S. M. Zakeeruddin, M. Graetzel, *Adv. Energy Mater.* **2015**, *5*, 1.
- [177] K. Tvingstedt, O. Malinkiewicz, A. Baumann, C. Deibel, H. J. Snaith, V. Dyakonov, H. J. Bolink, *Sci. Rep.* **2014**, *4*, 6071.
- [178] D. Luo, W. Yang, Z. Wang, A. Sadhanala, Q. Hu, R. Su, R. Shivanna, G. F. Trindade, J. F. Watts, Z. Xu, T. Liu, K. Chen, F. Ye, P. Wu, L. Zhao, J. Wu, Y. Tu, Y. Zhang, X. Yang, W. Zhang, R. H. Friend, Q. Gong, H. J. Snaith, R. Zhu, *Science (80-)*. **2018**, *360*, 1442.
- [179] M. Burgelman, P. Nollet, S. Degrave, *Thin Solid Films* **2000**, *361*, 527.
- [180] F. Zu, C. M. Wolff, M. Ralaiarisoa, P. Amsalem, D. Neher, N. Koch, *ACS Appl. Mater. Interfaces* **2019**, acsami.9b05293.
- [181] D. Kiermasch, L. Gil-Escrig, A. Baumann, H. J. Bolink, V. Dyakonov, K. Tvingstedt, *J. Mater. Chem. A* **2019**, *7*, 14712.
- [182] S. G. M. Wheeler, Bulk and Surface Recombination Limitations to High Voltage Solution Processed Solar Cells, **2017**.
- [183] S. Pisoni, M. Stolterfoht, J. Loekinger, T. Moser, P. Caprioglio, D. Neher, S. Buecheler, N. Ayodhya, **n.d.**, DOI 10.1080/14686996.2019.1633952.
- [184] F. Sahli, J. Werner, B. A. Kamino, M. Bräuninger, R. Monnard, B. Paviet-Salomon, L. Barraud, L. Ding, J. J. Diaz Leon, D. Sacchetto, G. Cattaneo, M. Despeisse, M. Boccard, S. Nicolay, Q. Jeangros, B. Niesen, C. Ballif, *Nat. Mater.* **2018**, *17*, 820.
- [185] S. Zhang, S. M. Hosseini, R. Gunder, A. Petsiuk, P. Caprioglio, C. M. Wolff, S. Shoaee, P. Meredith, S. Schorr, T. Unold, P. L. Burn, D. Neher, M. Stolterfoht, *Adv. Mater.* **2019**, 1901090.
- [186] H. Tsai, W. Nie, J. C. Blancon, C. C. Stoumpos, R. Asadpour, B. Harutyunyan, A. J. Neukirch, R. Verduzco, J. J. Crochet, S. Tretiak, L. Pedesseau, J. Even, M. A. Alam, G. Gupta, J. Lou, P. M. Ajayan, M. J. Bedzyk, M. G. Kanatzidis, A. D. Mohite, *Nature* **2016**, *536*, 312.
- [187] W. Tress, M. Yavari, K. Domanski, P. Yadav, B. Niesen, J. P. Correa Baena, A. Hagfeldt, M. Graetzel, *Energy Environ. Sci.* **2018**, *11*, 151.
- [188] M. Wolf, H. Rauschenbach, *Adv. Energy Convers.* **1963**, *3*, 455.
- [189] M. Stolterfoht, P. Caprioglio, C. M. Wolff, J. A. Márquez, J. Nordmann, S. Zhang, D. Rothhart, U. Hörmann, A. Redinger, L. Kegelmann, S. Albrecht, T. Kirchartz, M. Saliba, T. Unold, D. Neher, *ArXiv* **2018**, <http://arxiv.org/abs/1810.01333>.
- [190] Z. Wang, Q. Lin, B. Wenger, M. G. Christoforo, Y. H. Lin, M. T. Klug, M. B. Johnston, L. M. Herz, H. J. Snaith, *Nat. Energy* **2018**, *3*, 855.
- [191] S. W. Glunz, J. Nekarda, H. Mäckel, A. Cuevas, *Proc. 22nd Eur. Photovolt. Sol.*

Energy Conf. 3-7 Sept. 2007, Milan, Italy; 2007; pp 849–853 n.d.

- [192] O. Gunawan, T. Gokmen, D. B. Mitzi, *J. Appl. Phys.* **2014**, *116*, 510.
- [193] T. Kirchartz, B. E. Pieters, J. Kirkpatrick, U. Rau, J. Nelson, *Phys. Rev. B - Condens. Matter Mater. Phys.* **2011**, *83*, 1.
- [194] C. Van Berkel, M. J. Powell, A. R. Franklin, I. D. French, *J. Appl. Phys.* **1993**, *73*, 5264.
- [195] M. B. Johnston, L. M. Herz, *Acc. Chem. Res.* **2015**, 146.
- [196] S. D. Stranks, V. M. Burlakov, T. Leijtens, J. M. Ball, A. Goriely, H. J. Snaith, *Phys. Rev. Appl.* **2014**, 034007.
- [197] G. J. A. H. Wetzelaer, M. Scheepers, A. M. Sempere, C. Momblona, J. ??vila, H. J. Bolink, *Adv. Mater.* **2015**, *27*, 1837.
- [198] S. Ullbrich, A. Fischer, Z. Tang, J. Ávila, H. J. Bolink, S. Reineke, K. Vandewal, *Phys. Rev. Appl.* **2018**, *9*, 051003.
- [199] S. Olthof, K. Meerholz, *Sci. Rep.* **2017**, *7*, 40267.
- [200] F. Wang, S. Bai, W. Tress, A. Hagfeldt, F. Gao, *npj Flex. Electron.* **2018**, *2*, 22.
- [201] T. Kirchartz, F. Deledalle, P. S. Tuladhar, J. R. Durrant, J. Nelson, *J. Phys. Chem. Lett.* **2013**, *4*, 2371.
- [202] P. Calado, D. Burkitt, J. Yao, J. Troughton, T. M. Watson, M. J. Carnie, A. M. Telford, B. C. O. Regan, J. Nelson, P. R. F. Barnes, *Phys. Rev. Appl.* **2019**, *10*, 1.
- [203] Peter Würfel, *Physics of Solar Cells: From Principles to New Concepts*, Wiley, **2005**.
- [204] S. Wheeler, D. Bryant, J. Troughton, T. Kirchartz, T. Watson, J. Nelson, J. R. Durrant, *J. Phys. Chem. C* **2017**, *121*, 13496.
- [205] D. Kiermasch, L. Gil-Escrig, A. Baumann, H. J. Bolink, V. Dyakonov, K. Tvingstedt, *J. Mater. Chem. A* **2019**, *7*, 14712.
- [206] M. Stolterfoht, P. Caprioglio, C. M. Wolff, J. A. Márquez, J. Nordmann, S. Zhang, D. Rothhardt, U. Hörmann, Y. Amir, A. Redinger, L. Kegelmann, F. Zu, S. Albrecht, N. Koch, T. Kirchartz, M. Saliba, T. Unold, D. Neher, *Energy Environ. Sci.* **2019**, *12*, 2778.
- [207] P. Caprioglio, M. Stolterfoht, C. M. Wolff, T. Unold, B. Rech, S. Albrecht, D. Neher, *Adv. Energy Mater.* **2019**, *9*, 1901631.
- [208] D. Kiermasch, L. Gil-Escrig, A. Baumann, H. J. Bolink, V. Dyakonov, K. Tvingstedt, *J. Mater. Chem. A* **2019**, *7*, 14712.
- [209] O. Almora, K. T. Cho, S. Aghazada, I. Zimmermann, G. J. Matt, C. J. Brabec, M. K. Nazeeruddin, G. Garcia-Belmonte, *Nano Energy* **2018**, *48*, 63.
- [210] T. Kirchartz, J. Nelson, *Phys. Rev. B* **2012**, *86*, 165201.
- [211] K. Tvingstedt, † Lidón, L. Gil-Escrig, C. Momblona, P. Rieder, D. Kiermasch, M. Sessolo, A. Baumann, H. J. Bolink, V. Dyakonov, **2017**, DOI 10.1021/acsenergylett.6b00719.
- [212] L. M. Pazos-Outón, T. P. Xiao, E. Yablonovitch, *J. Phys. Chem. Lett.* **2018**, *9*, 1703.
- [213] R. Brenes, M. Laitz, J. Jean, D. W. Dequilettes, V. Bulović, *Phys. Rev. Appl.* **2019**, *12*, DOI 10.1103/PhysRevApplied.12.014017.

- [214] D. W. deQuilettes, S. Koch, S. Burke, R. K. Paranj, A. J. Shropshire, M. E. Ziffer, D. S. Ginger, *ACS Energy Lett.* **2016**, *1*, 438.
- [215] T. S. Sherkar, C. Momblona, L. Gil-Escrig, H. J. Bolink, L. J. A. Koster, *Adv. Energy Mater.* **2017**, *7*, DOI 10.1002/aenm.201602432.
- [216] S. Wheeler, F. Deledalle, N. Tokmoldin, T. Kirchartz, J. Nelson, J. R. Durrant, *Phys. Rev. Appl.* **2015**, *4*, DOI 10.1103/PhysRevApplied.4.024020.
- [217] T. Kirchartz, F. Deledalle, P. S. Tuladhar, J. R. Durrant, J. Nelson, *J. Phys. Chem. Lett.* **2013**, *4*, 2371.
- [218] B. Dänekamp, N. Droseros, D. Tsokkou, V. Brehm, P. P. Boix, M. Sessolo, N. Banerji, H. J. Bolink, *J. Mater. Chem. C* **2019**, *7*, 523.
- [219] T. Du, W. Xu, M. Daboczi, J. Kim, S. Xu, C.-T. Lin, H. Kang, K. Lee, M. J. Heeney, J.-S. Kim, J. R. Durrant, M. A. McLachlan, *J. Mater. Chem. A* **2019**, *7*, 18971.
- [220] W. Xiang, Z. Wang, D. J. Kubicki, W. Tress, J. Luo, D. Prochowicz, S. Akin, L. Emsley, J. Zhou, G. Dietler, M. Grätzel, A. Hagfeldt, *Joule* **2019**, *3*, 205.
- [221] G. Huang, C. Wang, H. Zhang, S. Xu, Q. Xu, Y. Cui, *J. Mater. Chem. A* **2018**, *6*, 2449.
- [222] A. D. Jodlowski, C. Roldán-Carmona, G. Grancini, M. Salado, M. Ralaiarisoa, S. Ahmad, N. Koch, L. Camacho, G. De Miguel, M. K. Nazeeruddin, *Nat. Energy* **2017**, *2*, 972.
- [223] D. Perez-del-Rey, D. Forgacs, E. M. Hutter, T. J. Savenije, D. Nordlund, P. Schulz, J. J. Berry, M. Sessolo, H. J. Bolink, *Adv. Mater.* **2016**, *28*, 9839.
- [224] C. F. J. Lau, M. Zhang, X. Deng, J. Zheng, J. Bing, Q. Ma, J. Kim, L. Hu, M. A. Green, S. Huang, A. Ho-Baillie, *ACS Energy Lett.* **2017**, 2319.
- [225] H. Zhang, H. Wang, S. T. Williams, D. Xiong, W. Zhang, C. C. Chueh, W. Chen, A. K. Y. Jen, *Adv. Mater.* **2017**, *29*, 1606608.
- [226] X. Shai, L. Zuo, P. Sun, P. Liao, W. Huang, E.-P. Yao, H. Li, S. Liu, Y. Shen, Y. Yang, M. Wang, *Nano Energy* **2017**, *36*, 213.
- [227] M.-C. Wu, W.-C. Chen, S.-H. Chan, W.-F. Su, *Appl. Surf. Sci.* **2018**, *429*, 9.
- [228] H. Cho, S.-H. Jeong, M.-H. Park, Y.-H. Kim, C. Wolf, C.-L. Lee, J. Hyuck Heo, A. Sadhanala, N. Myoung, S. Yoo, S. Hyuk Im, R. H. Friend, T.-W. Lee, *Science (80-.)*. **2015**, *350*, 1222.
- [229] D. Shi, V. Adinolfi, R. Comin, M. Yuan, E. Alarousu, A. Buin, Y. Chen, S. Hoogland, A. Rothenberger, K. Katsiev, Y. Losovyj, X. Zhang, P. A. Dowben, O. F. Mohammed, E. H. Sargent, O. M. Bakr, *Science (80-.)*. **2015**, *347*, 519.
- [230] Y. Yang, M. Yang, D. T. Moore, Y. Yan, E. M. Miller, K. Zhu, M. C. Beard, *Nat. Energy* **2017**, *2*, 16207.
- [231] P. Wurfel, *J. Phys. C Solid State Phys. J. Phys* **1982**, *15*, 3967.
- [232] D. Bi, W. Tress, M. I. Dar, P. Gao, J. Luo, C. Renevier, K. Schenk, A. Abate, F. Giordano, J.-P. Correa Baena, J.-D. Decoppet, S. M. Zakeeruddin, M. K. Nazeeruddin, M. Grätzel, A. Hagfeldt, *Sci. Adv.* **2016**, *2*, 1501170.
- [233] S. Olthof, *APL Mater.* **2016**, *4*, 091502.
- [234] E. M. Miller, Y. Zhao, C. C. Mercado, S. K. Saha, J. M. Luther, K. Zhu, V. Stevanović, C. L. Perkins, J. van de Lagemaat, *Phys. Chem. Chem. Phys.* **2014**, *16*, 22122.

- [235] M. F. Lo, Z. Q. Guan, T. W. Ng, C. Y. Chan, C. S. Lee, *Adv. Funct. Mater.* **2015**, *25*, 1213.
- [236] Z. Zhang, J. T. Yates, *Chem. Rev.* **2012**, *112*, 5520.
- [237] B. Conings, L. Baeten, C. De Dobbelaere, J. D'Haen, J. Manca, H. G. Boyen, *Adv. Mater.* **2014**, *26*, 2041.
- [238] F. S. Zu, P. Amsalem, I. Salzmann, R. Bin Wang, M. Ralaiarisoa, S. Kowarik, S. Duhm, N. Koch, *Adv. Opt. Mater.* **2017**, *5*, 1700139.
- [239] F. Zu, P. Amsalem, M. Ralaiarisoa, T. Schultz, R. Schlesinger, N. Koch, *ACS Appl. Mater. Interfaces* **2017**, *9*, 41546–41552.
- [240] J. F. L. Salas, S. J. Heise, M. Richter, V. Gerliz, M. S. Hammer, J. Ohland, I. Hammer-Riedel, *Thin Solid Films* **2017**, *633*, 40.
- [241] J. F. L. Salas, M. Richter, J. Parisi, S. J. Heise, *J. Appl. Phys.* **2017**, *122*, 203103.
- [242] J. Liqiang, S. Xiaojun, S. Jing, C. Weimin, X. Zili, D. Yaoguo, F. Honggang, *Sol. Energy Mater. Sol. Cells* **2003**, *79*, 133.
- [243] L. Kronik, Y. Shapira, *Surf. INTERFACE Anal. Surf. Interface Anal* **2001**, *31*, 954.
- [244] J. R. Harwell, T. K. Baikie, I. D. Baikie, J. L. Payne, C. Ni, J. T. S. Irvine, G. A. Turnbull, I. D. W. Samuel, *Phys. Chem. Chem. Phys. Phys. Chem. Chem. Phys* **2016**, *18*, 19738.
- [245] L. Barnea-Nehoshtan, S. Kirmayer, E. Edri, G. Hodes, D. Cahen, *J. Phys. Chem. Lett.* **2014**, *5*, 2408.
- [246] W. Zhang, S. Pathak, N. Sakai, T. Stergiopoulos, P. K. Nayak, N. K. Noel, A. A. Haghhighirad, V. M. Burlakov, D. W. Dequillettes, A. Sadhanala, W. Li, L. Wang, D. S. Ginger, R. H. Friend, H. J. Snaith, *Nat. Commun.* **2015**, *6*, 10030.
- [247] T. G. Kim, S. W. Seo, H. Kwon, J. Hahn, J. W. Kim, *Phys. Chem. Chem. Phys.* **2015**, *17*, 24342.
- [248] H. Xie, X. Liu, L. Lyu, D. Niu, Q. Wang, J. Huang, Y. Gao, *J. Phys. Chem. C* **2016**, *120*, 215.
- [249] Q. Wang, Y. Shao, H. Xie, L. Lyu, X. Liu, Y. Gao, J. Huang, *Appl. Phys. Lett.* **2014**, *105*, 163508.
- [250] A. Cuevas, D. Yan, *IEEE J. Photovoltaics* **2013**, *3*, 916.
- [251] J.-Y. Y. Seo, T. Matsui, J. Luo, J.-P. P. Correa-Baena, F. Giordano, M. Saliba, K. Schenk, A. Ummadisingu, K. Domanski, M. Hadadian, A. Hagfeldt, S. M. Zakeeruddin, U. Steiner, M. Grätzel, A. Abate, *Adv. Energy Mater.* **2016**, *6*, 1.
- [252] J. Wang, X. Ye, Y. Wang, Z. Wang, W. Wong, C. Li, *Electrochim. Acta* **2019**, *303*, 133.
- [253] R. Xia, Z. Fei, N. Drigo, F. D. Bobbink, Z. Huang, R. Jasiūnas, M. Franckevičius, V. Gulbinas, M. Mensi, X. Fang, C. Roldán-Carmona, M. K. Nazeeruddin, P. J. Dyson, *Adv. Funct. Mater.* **2019**, *29*, 1902021.
- [254] S. Bai, P. Da, C. Li, Z. Wang, Z. Yuan, F. Fu, M. Kawecki, X. Liu, N. Sakai, J. T.-W. Wang, S. Huettner, S. Buecheler, M. Fahlman, F. Gao, H. J. Snaith, *Nature* **2019**, *571*, 245.
- [255] D. Yang, X. Zhou, R. Yang, Z. Yang, W. Yu, X. Wang, C. Li, S. (Frank) Liu, R. P. H. Chang, *Energy Environ. Sci.* **2016**, *9*, 3071.
- [256] M. Li, C. Zhao, Z. Z.-K. Wang, C.-C. C. Zhang, H. K. H. Lee, A. Pockett, J. Barbé,

- W. C. Tsoi, Y. Y.-G. Yang, M. J. Carnie, X. X.-Y. Gao, W.-X. W. Yang, J. R. Durrant, L.-S. L. Liao, S. M. Jain, *Adv. Energy Mater.* **2018**, *8*, 1801509.
- [257] S. Wang, Z. Li, Y. Zhang, X. Liu, J. Han, X. Li, Z. Liu, S. Frank Liu, W. C. H. Choy, *Adv. Funct. Mater.* **2019**, 1900417.
- [258] W. Qian, J. Texter, F. Yan, *Chem. Soc. Rev.* **2017**, *46*, 1124.
- [259] M. R. Gao, J. Yuan, M. Antonietti, *Chem. - A Eur. J.* **2017**, *23*, 5391.
- [260] U. Würfel, D. Neher, A. Spies, S. Albrecht, *Nat. Commun.* **2015**, *6*, DOI 10.1038/ncomms7951.
- [261] S. Yang, J. Dai, Z. Yu, Y. Shao, Y. Zhou, X. Xiao, X. C. Zeng, J. Huang, *J. Am. Chem. Soc.* **2019**, *141*, 5781.
- [262] J. Yuan, M. Antonietti, *Polymer (Guildf)*. **2011**, *52*, 1469.
- [263] Q. Wang, F. Lin, C.-C. C. Chueh, T. Zhao, M. Eslamian, A. K. Y. K.-Y. Jen, *Mater. Today Energy* **2018**, *7*, 161.
- [264] M. Węclawik, A. Gağor, A. Piecha, R. Jakubas, W. Medycki, *CrystEngComm* **2013**, *15*, 5633.
- [265] M. Salado, M. A. Fernández, J. P. Holgado, S. Kazim, M. K. Nazeeruddin, P. J. Dyson, S. Ahmad, *ChemSusChem* **2017**, *10*, 3846.
- [266] C. Huang, P. Lin, N. Fu, K. Sun, M. Ye, C. Liu, X. Zhou, L. Shu, X. Hao, B. Xu, X. Zeng, Y. Wang, S. Ke, **2018**, DOI 10.1039/c8ta04131h.
- [267] J.-K. Tseng, S. Tang, Z. Zhou, M. Mackey, J. M. Carr, R. Mu, L. Flandin, D. E. Schuele, E. Baer, L. Zhu, *Polymer (Guildf)*. **2014**, *55*, 8.
- [268] F. Ganet, M. Q. Le, J. F. Capsal, P. Lermusiaux, L. Petit, A. Millon, P. J. Cottinet, *Sci. Rep.* **2016**, *5*, 18593.
- [269] N. Ahn, K. Kwak, M. S. Jang, H. Yoon, B. Y. Lee, J.-K. Lee, P. V. Pikhitsa, J. Byun, M. Choi, *Nat. Commun.* **2016**, *7*, 13422.
- [270] H. J. Snaith, *J. Phys. Chem. Lett.* **2013**, *4*, 3623.
- [271] D. Bryant, N. Aristidou, S. Pont, I. Sanchez-Molina, T. Chotchunangatchaval, S. Wheeler, J. R. Durrant, S. A. Haque, *Energy Environ. Sci.* **2016**, *9*, 1655.
- [272] A. J. Pearson, G. E. Eperon, P. E. Hopkinson, S. N. Habisreutinger, J. T. W. Wang, H. J. Snaith, N. C. Greenham, *Adv. Energy Mater.* **2016**, *6*, 1.
- [273] P. Gratia, G. Grancini, J. N. Audinot, X. Jeanbourquin, E. Mosconi, I. Zimmermann, D. Dowsett, Y. Lee, M. Grätzel, F. De Angelis, K. Sivula, T. Wirtz, M. K. Nazeeruddin, *J. Am. Chem. Soc.* **2016**, *138*, 15821.
- [274] A. J. Barker, A. Sadhanala, F. Deschler, M. Gandini, S. P. Senanayak, P. M. Pearce, E. Mosconi, A. J. Pearson, Y. Wu, A. R. Srimath Kandada, T. Leijtens, F. De Angelis, S. E. Dutton, A. Petrozza, R. H. Friend, *ACS Energy Lett.* **2017**, *2*, 1416.
- [275] E. L. Unger, L. Kegelmann, K. Suchan, D. Sörell, L. Korte, S. Albrecht, *J. Mater. Chem. A* **2017**, *5*, 11401.
- [276] R. A. Belisle, K. A. Bush, L. Bertoluzzi, A. Gold-Parker, M. F. Toney, M. D. McGehee, *ACS Energy Lett.* **2018**, *3*, 2694.
- [277] S. Draguta, O. Sharia, S. J. Yoon, M. C. Brennan, Y. V. Morozov, J. M. Manser, P. V. Kamat, W. F. Schneider, M. Kuno, *Nat. Commun.* **2017**, *8*, 1.
- [278] D. W. DeQuilettes, W. Zhang, V. M. Burlakov, D. J. Graham, T. Leijtens, A.

- Osherov, V. Bulović, H. J. Snaith, D. S. Ginger, S. D. Stranks, *Nat. Commun.* **2016**, 7, DOI 10.1038/ncomms11683.
- [279] J. Werner, G. Nogay, F. Sahli, T. C. J. Yang, M. Bräuninger, G. Christmann, A. Walter, B. A. Kamino, P. Fiala, P. Löper, S. Nicolay, Q. Jeangros, B. Niesen, C. Ballif, *ACS Energy Lett.* **2018**, 3, 742.
- [280] M. Yuan, L. N. Quan, R. Comin, G. Walters, R. Sabatini, O. Voznyy, S. Hoogland, Y. Zhao, E. M. Beauregard, P. Kanjanaboos, Z. Lu, D. H. Kim, E. H. Sargent, *Nat. Nanotechnol.* **2016**, 11, 872.
- [281] C. G. Bischak, C. L. Hetherington, H. Wu, S. Aloni, D. F. Ogletree, D. T. Limmer, N. S. Ginsberg, *Nano Lett.* **2017**, 17, 1028.
- [282] X. Tang, M. Van Den Berg, E. Gu, A. Horneber, G. J. Matt, A. Osvet, A. J. Meixner, D. Zhang, C. J. Brabec, *Nano Lett.* **2018**, 18, 2172.
- [283] C. Li, J. Wei, M. Sato, H. Koike, Z. Z. Xie, Y. Q. Li, K. Kanai, S. Kera, N. Ueno, J. X. Tang, *ACS Appl. Mater. Interfaces* **2016**, 8, 11526.
- [284] X. Zhou, W. Ye, X. Li, W. Zheng, R. Lin, F. Huang, D. Zhong, *Appl. Phys. Lett.* **2016**, 109, 233906.
- [285] S. Tao, I. Schmidt, G. Brocks, J. Jiang, I. Tranca, K. Meerholz, S. Olthof, *Nat. Commun.* **2019**, 10, 1.
- [286] C. M. Wolff, L. Canil, C. Rehermann, N. Ngoc Linh, F. Zu, M. Ralaiarisoa, P. Caprioglio, L. Fiedler, M. Stolterfoht, S. Kogikoski, I. Bald, N. Koch, E. L. Unger, T. Dittrich, A. Abate, D. Neher, *ACS Nano* **2020**, acsnano.9b03268.
- [287] M. Stolterfoht, M. Grischek, P. Caprioglio, C. M. Wolff, E. Gutierrez-Partida, F. Peña-Camargo, D. Rothhardt, S. Zhang, M. Raoufi, J. Wolansky, M. Abdi-Jalebi, S. D. Stranks, S. Albrecht, T. Kirchartz, D. Neher, *Adv. Mater.* **2020**, 32, 2000080.
- [288] W. Tress, *Adv. Energy Mater.* **2017**, 7, 1602358.
- [289] D. Luo, W. Yang, Z. Wang, A. Sadhanala, Q. Hu, R. Su, R. Shivanna, G. F. Trindade, J. F. Watts, Z. Xu, T. Liu, K. Chen, F. Ye, P. Wu, L. Zhao, J. Wu, Y. Tu, Y. Zhang, X. Yang, W. Zhang, R. H. Friend, Q. Gong, H. J. Snaith, R. Zhu, *Sci.* **2018**, 360, 1442.
- [290] L. M. Pazos-Outón, T. P. Xiao, E. Yablonovitch, *J. Phys. Chem. Lett.* **2018**, 9, 1703.
- [291] M. B. Johnston, L. M. Herz, *Acc. Chem. Res.* **2016**, 49, 146.
- [292] J. Hwang, A. Wan, A. Kahn, *Mater. Sci. Eng. R Reports* **2009**, 64, 1.
- [293] H. Wang, P. Amsalem, G. Heimel, I. Salzmänn, N. Koch, M. Oehzelt, *Adv. Mater.* **2014**, 26, 925.
- [294] R. Schlesinger, Y. Xu, O. T. Hofmann, S. Winkler, J. Frisch, J. Niederhausen, A. Vollmer, S. Blumstengel, F. Henneberger, P. Rinke, M. Scheffler, N. Koch, *Phys. Rev. B* **2013**, 87, DOI 10.1103/PhysRevB.87.155311.
- [295] M. Oehzelt, N. Koch, G. Heimel, *Nat. Commun.* **2014**, 5, DOI 10.1038/ncomms5174.
- [296] H. Ishii, N. Hayashi, E. Ito, Y. Washizu, K. Sugi, Y. Kimura, M. Niwano, Y. Ouchi, K. Seki, *Phys. Status Solidi Appl. Res.* **2004**, 201, 1075.
- [297] A. Delamarre, L. Lombez, J.-F. Guillemoles, *Appl. Phys. Lett.* **2012**, 1001, 131108.

